

AN ANALYTICAL MODEL FOR PREDICTING THE BEHAVIOUR OF Laterally
RESTRAINED REINFORCED CONCRETE BEAMS

by

Rami G. Mansour

A thesis submitted in conformity with the requirements
for the degree of Master of Applied Science
Graduate Department of Civil Engineering
University of Toronto

© Copyright 2016 by Rami G. Mansour

Abstract

An Analytical Model for Predicting the Behaviour of Laterally Restrained Reinforced Concrete Beams

Rami G. Mansour

Master of Applied Science

Graduate Department of Civil Engineering

University of Toronto

2016

In this thesis, an analytical model for predicting the response of laterally restrained, reinforced concrete beams and slab strips is proposed. This model is formulated using a sectional analysis approach that assumes plane sections remain plane, and accounts for both material nonlinearities and second-order effects. A refined version of the model is developed to account for varying support stiffness, diagonal compression field action, slip relative to the support, and bond deterioration. The refined model is shown to correlate well with test data from two existing experimental investigations on laterally restrained beams. Finally, a series of parametric studies are presented to illustrate the influence of concrete strength, mechanical reinforcement ratio, second-order effects, and slip at a support on the capacity of laterally restrained beams or slab strips. The proposed analytical model presented in this thesis provides the basis for the development of a simplified method that can be incorporated into design standards.

Acknowledgements

I would like to thank my supervisor, Professor D.P. Gauvreau. His encouragement and guidance at every step has been instrumental in the development of this thesis. In addition, his dedication to teaching and his industry experience has been paramount in developing my passion for bridge construction. I would also like to thank the second reader of this thesis, Professor F.J. Vecchio, who also provided assistance at times throughout the duration of this research.

Over the past two and a half years, I have had the privilege of working with a group of like minded individuals who share my passion for bridge construction. A special thanks to David Hubbell for always being willing to discuss the intricacies of arching action, and providing ideas and insight. I would also like to thank the following research students for their support and friendship: Amos Chen, Karl Shao, Luca Nagy, Samantha Hinz, Robert Botticchio, and Vahid Serara.

I would like to acknowledge the generous financial assistance provided by the National Sciences and Research Council of Canada Canadian Graduate Scholarship (NSERC CGS-M), the Queen Elizabeth II Graduate Scholarship in Science and Technology (QEII-GSST), and the University of Toronto.

Most importantly, I would like to thank my family, who have provided unconditional love and support throughout my entire education.

Contents

1	Introduction	1
1.1	Arching Action	1
1.2	Experimental Investigations of Membrane Action	4
1.3	Existing Analytical Formulations	5
1.3.1	Christiansen (1963)	5
1.3.2	Park (1964)	7
1.3.3	Rankin (1982)	9
1.3.4	Eyre (1997)	11
1.3.5	Finite Element Analysis	12
1.3.6	Wu (2013)	13
1.3.7	Botticchio (2014)	15
1.4	Implementation in Design Standards	16
1.4.1	Canadian Highway Bridge Design Code (CHBDC)	17
1.4.2	UK Design Codes	18
1.4.3	Discussion	18
1.5	Objectives and Content of Thesis	19
2	Proposed Model	22
2.1	Model Assumptions	22
2.2	Material Properties	23
2.2.1	Concrete Material Model	24
2.2.2	Steel Reinforcement Material Model	26
2.3	Compatibility Conditions	28
2.4	Equilibrium Requirements	32
2.5	Sectional Analysis	32
2.5.1	Bending Moment	33
2.5.2	Layered Analysis	34
2.5.3	Moment-Curvature Relation	37
2.5.4	Beam Deformation	38
2.6	Second-Order Effects	40
2.7	Proposed Analytical Procedure	41
2.8	Comparison of the Proposed Model to Wu (2013)	44
2.9	Softening due to Second-Order Effects	48

2.10	Optimization of the Numerical Integration Approach	52
2.10.1	Layered Analysis	53
2.10.2	Sectional Analysis	55
3	Supplementary Model Refinements	58
3.1	Support Stiffness	59
3.1.1	Overview	59
3.1.2	Compatibility Condition	60
3.1.3	Influence of Partial Restraint	61
3.1.4	Conclusion	64
3.2	Diagonal Compression Field Action	65
3.2.1	Laterally Unrestrained Beams	65
3.2.2	Laterally Restrained Beams	69
3.2.3	Influence of Diagonal Compression Field Action on Beam Response	70
3.2.4	Conclusion	74
3.3	Slip at Supports	75
3.3.1	Influence of Lateral Slip	76
3.3.2	Conclusion	78
3.4	Bond Deterioration	79
3.4.1	Simplified Bond Deterioration Model	81
3.4.2	Influence of Bond Deterioration	83
3.4.3	Conclusion	85
4	Experimental Validation	86
4.1	S-Series	87
4.1.1	Test Setup	87
4.1.2	Specimen Properties	89
4.1.3	Measured Response of the Test Specimens	90
4.1.4	Predicted Response using the Proposed Analytical Model	92
4.1.5	S-Series Conclusion	105
4.2	Y-Series	106
4.2.1	Test Setup	106
4.2.2	Specimen Properties	107
4.2.3	Measured Response of the Test Specimens	109
4.2.4	Predicted Response using the Proposed Analytical Model	113
4.2.5	Y-Series Conclusion	120
4.3	Discussion of Results and Concluding Remarks	120
5	Parametric Study	122
5.1	Concrete Compressive Strength	123
5.1.1	Unrestrained Beam Response	124
5.1.2	Restrained Beam Response	127
5.1.3	Influence of Lateral Restraint	130
5.1.4	Reinforcement Limits	133

5.1.5	Summary of Results and Conclusions	135
5.2	Mechanical Reinforcement Ratio	136
5.2.1	Unrestrained Beam Response	137
5.2.2	Restrained Beam Response	138
5.2.3	Influence of Lateral Restraint	140
5.2.4	Summary of Results and Conclusions	141
5.3	Second-Order Effects	141
5.3.1	Influence of Second-Order Effects on Bending Moment	142
5.3.2	Influence of Lateral Restraint	143
5.3.3	Influence of Second-Order Effects on Beam Response	144
5.3.4	Summary of Results and Conclusions	147
5.4	Lateral Slip at Supports	148
5.4.1	Restrained Beam Response	149
5.4.2	Influence of Lateral Restraint	151
5.4.3	Summary of Results and Conclusions	152
5.5	Diagonal Strut Inclination	152
5.5.1	Unrestrained Beam Response	154
5.5.2	Restrained Beam Response	155
5.5.3	Summary of Results and Conclusions	155
5.6	Discussion of Results and Concluding Remarks	156
6	Conclusions and Summary	158
6.1	Key Findings from this Thesis	158
6.2	Proposed Analytical Model	159
6.3	Experimental Validation of the Proposed Model	164
6.4	Final Conclusions and Recommendations for Future Work	166
	References	168
	Appendix A: Sample Calculations	171
	Appendix B: Additional Notes on the Proposed Model	179
	Appendix C: Proposed Experiment	185

List of Tables

4.1	S-Series beam properties, adapted from Su (2009).	89
4.2	S-Series reinforcement properties, adapted from Su (2009).	90
4.3	Y-Series reinforcement properties, adapted from Yu (2013).	109
A.1	Results from first iteration.	175
A.2	Results from second iteration.	175
A.3	Results from third iteration.	175
A.4	Results from final iteration.	176
A.5	Results from first iteration of layered analysis.	178
A.6	Results from final iteration of layered analysis.	178
C.1	Properties of the beams in the proposed experiment.	191

List of Figures

1.1	Lateral expansion of a simply supported beam.	1
1.2	Lateral expansion of a beam with rotational restraint.	2
1.3	Compression and tension stress fields, adapted from Gauvreau (1993).	3
1.4	M-H interaction diagram for a laterally restrained beam.	3
1.5	Plastic collapse mechanism of a slab, adapted from Christiansen (1963).	6
1.6	Plastic collapse mechanism of a slab, adapted from Park (1964).	7
1.7	Internal forces at either end of a slab segment, adapted from Park (1964).	8
1.8	Three hinged arch with elastic supports, adapted from Rankin (1982).	9
1.9	Predicted load-deflection response of beam B2, using Wu's method.	14
1.10	Predicted load-deflection response of beam B2, using Botticchio's method.	16
1.11	Potential limitations on efficiency, imposed by the EDM.	18
2.1	Typical response of a short and slender beam.	23
2.2	Constitutive material models of concrete in compression.	24
2.3	Numerical integration of compressive stresses.	24
2.4	Influence of confinement on concrete in compression.	26
2.5	Constitutive material model of steel reinforcement.	26
2.6	Concentration of strain at a crack, adapted from Mayer (1998).	28
2.7	Influence of lateral and rotational restraint on beam deformation.	29
2.8	Ratio of arc length to chord length of the centroidal axis.	30
2.9	Numerical integration used to calculate the arc length of the deflected shape.	30
2.10	Trapezoidal rule used to calculate the arc length of the centroidal axis.	31
2.11	Sections considered throughout a beam with a concentrated load.	32
2.12	Components of first-order and second-order bending moment.	34
2.13	Sectional forces derived from a plane of strain.	35
2.14	Numerical integration of compressive stress in concrete.	36
2.15	Proposed procedure for conducting a layered analysis.	37
2.16	Beam properties for the moment-curvature example.	38
2.17	Moment-curvature response with varying H , adapted from Wu (2013).	38
2.18	Bending moment and curvature in a restrained beam, at Q_{peak}	39
2.19	Axial compression in a column vs. a laterally restrained beam.	41
2.20	Proposed formulation for the analytical model.	44
2.21	Beam properties for the comparison with Wu's model.	45
2.22	Load-deflection response of beams F1 and F2.	46

2.23	Load-restraint response of beams F1 and F2.	46
2.24	Comparison of M_t and M_w in beams F1 and F2, at Q_{peak}	47
2.25	Beam properties for second-order effects example.	48
2.26	Load-deflection and restraint-deflection response of beam L1.	49
2.27	Bending moment diagram in beams L1-R and L1-N.	50
2.28	Properties of beam S1 from the S-Series validation.	51
2.29	$M-\phi$ illustrating the development of a numerical instability.	52
2.30	$\sigma-\varepsilon$ response for layered analysis optimization.	53
2.31	Concrete stress based on the Bi-linear and Popovics models.	53
2.32	Number of layers required for use with the Bi-linear $\sigma-\varepsilon$ response, at ε_{cu}	54
2.33	Number of layers required for use with the Popovics $\sigma-\varepsilon$ response, at ε_o	54
2.34	Number of layers required for use with the Popovics $\sigma-\varepsilon$ response, at $2 \cdot \varepsilon_o$	55
2.35	Beam properties for sectional analysis optimization.	55
2.36	Proposed layout of sections in a given beam.	56
2.37	Number of sections required, at $Q = 110$ kN.	56
3.1	Lateral and rotational spring supports.	59
3.2	Ratio of chord length, arc length, and deflection.	60
3.3	Properties of beam F2, used to study finite support stiffness.	62
3.4	Bending moment and curvature in beam F2.	62
3.5	Moment-curvature response of beam F2.	63
3.6	Load-deflection and load-restraint response of beam F2.	63
3.7	B and D-regions in a restrained beam, adapted from Schlaich (1987).	65
3.8	Sectional forces in a laterally unrestrained beam.	66
3.9	Truss model for a laterally unrestrained beam, with no web members.	66
3.10	Truss model for a laterally unrestrained beam, with web members.	67
3.11	Sectional forces in a laterally unrestrained beam, with consideration of D	67
3.12	Influence of H^* in laterally unrestrained beams, adapted from Gauvreau (1993).	68
3.13	Influence of H^* in laterally restrained beams, adapted from Gauvreau (1993).	70
3.14	Beam properties used to study the influence of DCFA.	71
3.15	Influence of H^* on the load-deflection response of a laterally unrestrained beam.	71
3.16	Influence of H^* on the curvature in a laterally unrestrained beam, at $Q = 25$ kN.	72
3.17	Influence of H^* on the $M-\phi$ response of sections A and B.	72
3.18	Influence of H^* on the response of a laterally restrained beam.	73
3.19	Influence of H^* on the curvature in a laterally restrained beam, at Q_{peak}	74
3.20	Lateral slip in a beam, relative to its supports.	75
3.21	Properties of the beam F2, used to study the influence of lateral slip.	76
3.22	Lateral force vs. slip response in beam F2- R_s	77
3.23	$M-\phi$ response of beam F2, considering slip at supports.	78
3.24	Influence of lateral slip on the response of beam F2.	78
3.25	Test setup for S-Series experiment, adapted from Su(2009)	79
3.26	Reinforcement layout in the column stubs, adapted from Su (2009).	80
3.27	Strain penetration in the column stubs.	81
3.28	Adjusted $\sigma-\varepsilon$ response of concrete in the column stubs.	83

3.29	Properties of beam BD, used to study the influence of bond deterioration.	83
3.30	Influence of bond deterioration on the response of beam BD.	84
3.31	Influence of bond deterioration on the curvature in beam BD, at $Q = 80$ kN.	85
4.1	Test setup for S-Series experiment, adapted from Su (2009).	88
4.2	Schematic of the setup for each specimen, adapted from Su (2009).	88
4.3	Geometric and reinforcement layout of specimens, adapted from Su (2009).	89
4.4	Response of specimens from S-Series experiment, adapted from Su (2009).	91
4.5	σ - ε response of concrete in specimen S1.	92
4.6	σ - ε response of reinforcement in specimen S1.	93
4.7	Lateral expansion and rotation of specimen S1.	93
4.8	Truss model representation of specimen S1.	94
4.9	Reinforcement layout in the column stubs, adapted from Su (2009).	95
4.10	Predicted vs. observed response of specimen S1.	96
4.11	M - ϕ response of specimen S1.	98
4.12	Material σ - ε response in specimen S2.	99
4.13	Lateral expansion and rotation of specimen S2.	99
4.14	Predicted vs. observed response of specimen S2.	100
4.15	Material σ - ε response in specimen S3.	101
4.16	Lateral expansion and rotation of specimen S3.	101
4.17	Predicted vs. observed response of specimen S3.	102
4.18	Material σ - ε response of specimen S4.	103
4.19	Lateral expansion and rotation of specimen S4.	104
4.20	Predicted vs. observed response of specimen S4.	104
4.21	Test setup for Y-Series, adapted from Yu (2013).	106
4.22	Schematic of the test setup for each specimen, adapted from Yu (2013).	107
4.23	Geometric and reinforcement layout of specimens, adapted from Yu (2013).	108
4.24	Typical beam layout and section, adapted from Yu (2013).	108
4.25	σ - ε response of concrete and steel, adapted from Yu (2013).	109
4.26	Response of specimens from Y-Series, adapted from Yu (2013).	110
4.27	Failure mode of middle stub, adapted from Yu (2013).	111
4.28	Lateral supports, adapted from Yu (2013).	111
4.29	Deflection of specimen Y1, at Q_{peak} , adapted from Yu (2013).	112
4.30	σ - ε response of concrete in specimen Y1.	113
4.31	σ - ε response of reinforcement in specimen Y1.	114
4.32	Lateral expansion and rotation of specimen Y1.	114
4.33	Reinforcement layout in the column stubs, adapted from Yu (2013).	116
4.34	Predicted vs. observed response of specimen Y1.	117
4.35	σ - ε response of concrete in specimen Y2.	118
4.36	Lateral expansion and rotation of specimen Y2.	118
4.37	Predicted vs. observed response of specimen Y2.	119
5.1	Beam layout for parametric studies.	123
5.2	Beam properties for the concrete parametric study.	123

5.3	σ - ε response of concrete in parametric studies.	124
5.4	Load-deflection response of A-Series beams, without restraint.	124
5.5	Section response of beams A1-U and A4-U, at failure.	125
5.6	Response of beams in the A and B-Series, with no lateral restraint.	126
5.7	Section response of beams B2-U and B4-U, at failure.	126
5.8	Response of A-Series beams, with lateral restraint.	127
5.9	M - ϕ response of beams A1-R and A4-R.	128
5.10	Section response of beams A1 and A4, at failure.	128
5.11	Section response of beams A1-R and A4-R, at failure.	129
5.12	Response summary of beams in the A and B-Series, with lateral restraint.	129
5.13	Influence of concrete strength on Q_{peak} in the A-Series.	130
5.14	Influence of reinforcement ratio on Q_{peak}	130
5.15	Section response of beams A4-U and A4-R.	131
5.16	Influence of concrete strength on α_c and α_d	132
5.17	Curvature throughout beams A1 and A4, with and without lateral restraint.	133
5.18	Reinforcement limits specified by the CHBDC (2006).	134
5.19	Beam properties for the mechanical reinforcement parametric study.	136
5.20	Load-deflection response of A-Series beams, without restraint.	137
5.21	Response of the beams in the A and B-Series, with no lateral restraint.	137
5.22	Response of B-Series beams, with lateral restraint.	138
5.23	Response summary of beams in the A and B-Series, with lateral restraint.	139
5.24	Midspan section response of beams A4-R and B2-R, at failure.	139
5.25	Influence of mechanical reinforcement ratio on α_c and α_d	140
5.26	Beam properties for the second-order effects parametric study.	142
5.27	Bending moment diagram in beams D2-R and D5-R, at Q_{peak}	143
5.28	Influence of second-order bending moment on α_c	143
5.29	Influence of second-order bending moment on Q_{peak}	144
5.30	Bending moment in beams C5-R and D5-R, at Q_{peak}	145
5.31	Influence of second-order bending moment on H_{peak} and $w_{t_{peak}}$	146
5.32	Bending moment and curvature throughout beam D5, at Q_{peak}	147
5.33	Beam properties for the slip parametric study.	148
5.34	Influence of slip on Q , H and w_t for beam A1.	149
5.35	Lateral restraint force vs. slip in beams A1-R1 and A1-R3.	150
5.36	Response summary of beams A1 and B4, with varying lateral slip.	150
5.37	Influence of lateral slip on α_c and α_d	151
5.38	Beam properties for the strut inclination parametric study.	153
5.39	Influence of strut inclination on L_{fan}	153
5.40	Influence of varying θ on the response of laterally unrestrained beams.	154
5.41	Influence of varying θ on the response of laterally restrained beams.	155
A.1	Layout of sections in beam F2.	172
A.2	Properties of beam F2, used for sample analysis.	172
A.3	Assumed initial deflected shape of beam F2.	173
A.4	Bending moment in beam F2, due to the applied load.	173

A.5	Bending moment in beam F2, due to second-order effects.	174
A.6	Total bending moment in beam F2.	174
A.7	Total curvature in beam F2.	174
A.8	Final deflected shape of beam F2	176
A.9	Properties of beam F2, used for layered sample analysis.	177
B.1	Geometrical properties of a confined core.	180
B.2	Beam deflection, based on Moment Area Theorem.	183
C.1	Lateral and rotational restraint schematic.	187
C.2	Proposed actuator supports, drawn by David Hubbell.	188
C.3	Options for the steel end block at each support.	189
C.4	Experimental support setup.	190
C.5	Steel end plates.	190
C.6	Predicted response of the beams in the proposed experiment.	192

List of Symbols

δ_o :	Lateral expansion at the end of a beam
ε_b :	Strain at the bottom of a section
ε_c :	Compressive strain in the concrete
ε_{cc} :	Confined peak compressive strain in concrete
ε_{ce} :	Concrete strain at the centroid
$\varepsilon_{c,s}$:	Strain in the concrete at the level of the reinforcement
$\varepsilon_{c,p}$:	Concrete strain at the onset of plastic behaviour
$\varepsilon_{c,u}$:	Ultimate strain of concrete
ε_o :	Peak compressive strain in concrete
ε_s :	Strain in the steel reinforcement
$\varepsilon_{s,h}$:	Strain in the steel reinforcement at the onset of strain hardening
$\varepsilon_{s,u}$:	Ultimate strain of the steel reinforcement
$\varepsilon_{s,y}$:	Yield strain in the steel reinforcement
ε_t :	Strain at the top of a section
ρ :	Reinforcement ratio
ϕ :	Curvature at a section
α_c :	Strength enhancement ratio, caused by lateral restraint
α_d :	Deflection reduction ratio, caused by lateral restraint
θ_o :	Rotation of a beam at its supports
θ_s :	Rotational slip between a beam and its supports
A_s :	Total cross-sectional area of reinforcement at the bottom of a beam or slab
A'_s :	Total cross-sectional area of reinforcement at the top of a beam or slab
b :	Width of a beam or slab strip
c :	Depth of concrete in compression at a section

C :	Force resultant in the compression chord of a truss model
d :	Effective depth of the bottom reinforcement, relative to the top of the section
d' :	Effective depth of the top reinforcement, relative to the top of the section
d_{st} :	Depth of strain penetration in the middle and end column stubs
D_x :	Horizontal component of the diagonal compression strut in a truss model
D_y :	Vertical component of the diagonal compression strut in a truss model
E_c :	Modulus of elasticity of concrete
E_s :	Modulus of elasticity of steel
E_{sh} :	Strain hardening modulus of elasticity of steel
e_c :	Eccentricity of the concrete compressive force resultant, relative to the centroid
$e_{s,b}$:	Eccentricity of the bottom steel force resultant, relative to the centroid
$e_{s,t}$:	Eccentricity of the top steel force resultant, relative to the centroid
F_c :	Resultant compressive force in concrete
$F_{s,b}$:	Resultant force in the reinforcement, located below the centroid
$F_{s,t}$:	Resultant force in the reinforcement, located above the centroid
f :	Total rise of a deflected shape
f_c :	Compressive stress in concrete
f'_c :	Compressive stress capacity of concrete
f'_{cc} :	Confined compressive stress capacity of concrete
f_s :	Stress in the steel reinforcement
$f_{s,u}$:	Ultimate rupture stress of the steel reinforcement
$f_{s,y}$:	Yield stress of the steel reinforcement
f'_t :	Tensile stress capacity of concrete
H :	Lateral restraint load
H_n :	Local axial compression force resultant at section n
h :	Thickness of a slab, or height of a beam
h_i :	Height of layer i in concrete
K_{axial} :	Stiffness of the support preventing lateral expansion
K_{rot} :	Stiffness of the support preventing rotation
K_{slip} :	Residual slip stiffness of a beam, relative to its support
L :	Initial undeformed length of a beam
$L_{a,ce}$:	Arc length of the centroidal axis, measured along the length of the beam

$L_{c,ce}$:	Chord length of the centroidal axis, measured along the length of the beam
L_n :	Length of beam segments in a two-bay frame
L_w :	Arc length of the deflected shape
M_n :	Bending moment at section n
M_o :	Bending moment applied at the supports
M_t :	Total bending moment in a beam or slab strip, accounting for second-order effects
$M_{t,o}$:	Total first-order bending moment in a beam or slab strip
M_Q :	Bending moment due to the applied point load
M_w :	Bending moment due to second-order effects
n :	Number of layers or sections used in a numerical integration Factor that accounts for the composition of concrete, used in Popovics (1973)
P :	Strain hardening power
Q :	Concentrated load applied at midspan
r :	Relationship between the tangent and secant stiffness of concrete
s_0 :	Initial slip of a beam, relative to the supports
s_1 :	Residual slip of a beam, relative to the supports
s_t :	Total slip of a beam, relative to the supports
T :	Force resultant in the tension tie of a truss model
V :	Shear force at a section
w_o :	Assumed deflection throughout a given beam, at the start of an iterative loop
w_t :	Resultant deflection throughout a given beam
$w_{t,m}$:	Resultant deflection of a given beam at section m
$w_{t,max}$:	Midspan deflection of a given beam
x_o :	Length of the beam or slab strip that remains uncracked
x :	Ratio of compressive strain to peak compressive strain Horizontal distance between two points in a beam or slab strip
y_i :	Distance from the center of layer i to the centroid of a section
z :	Lever arm of the compression and tension strut in a truss model

1

Introduction

This thesis presents an analytical model that predicts the behaviour of a reinforced concrete beam or slab strip with supports that prevent rotation and lateral expansion. In this thesis, lateral expansion and restraint occur along the longitudinal axis of a beam or slab strip. This model provides the basis for the development of a simplified analytical method that can be incorporated into current design standards. This thesis (1) introduces the concept of arching action and discusses the currently available analytical methods, (2) presents the proposed analytical model, (3) validates the approach using test data from two experiments available in the literature, and (4) presents the results of a parametric study conducted using the proposed model.

1.1 Arching Action

The response of an uncracked beam with linear elastic material properties, supported by rollers at both ends, is illustrated in Figure 1.1a.

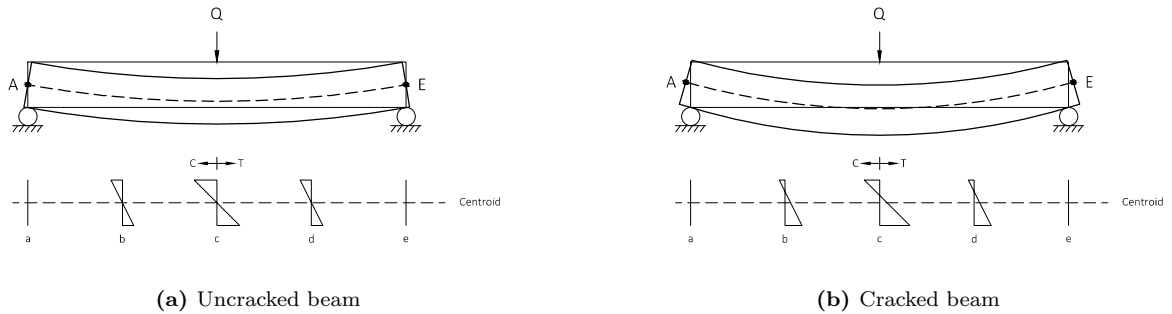


Figure 1.1: Lateral expansion of a simply supported beam.

When load is applied to this beam, the sum of the tensile strains between point a and e causes the bottom of the beam to expand, while the sum of the compressive strains from point a and e causes the top of the beam to shorten. Since the beam is uncracked, the strain at the centroid throughout the beam

is equal to zero. Therefore, the beam will not expand at its centroid, resulting in no outward expansion at points A and E . Alternatively if the beam cracks, then the sum of the tensile strain along the bottom of the beam between points a and e increases relative to the sum of the compressive strains at the top of the beam, as illustrated in Figure 1.1b. In this case, the strains at the centroid throughout the beam are tensile, causing the beam to expand outward at points A and E .

If the support at each end prevents rotation of an uncracked beam, as illustrated in Figure 1.2a, then the sum of the strains along the top and bottom of the beam between points a to b , and e to d , are equal and opposite to the sum of the strains between points b to c , and points d to c . Therefore, the sum of the strains, at both the top and bottom of the beam from point a to point e , is equal to zero. This indicates that no lateral expansion will occur at points A and E . However if the beam cracks, the net tensile strains at each section will increase relative to the compressive strains. As previously indicated, this causes the beam to expand outward at points A and E . This example, which is based on a first-order analysis, indicates that in some situations, a vertically applied load will cause lateral expansion of a beam, after cracking has occurred.

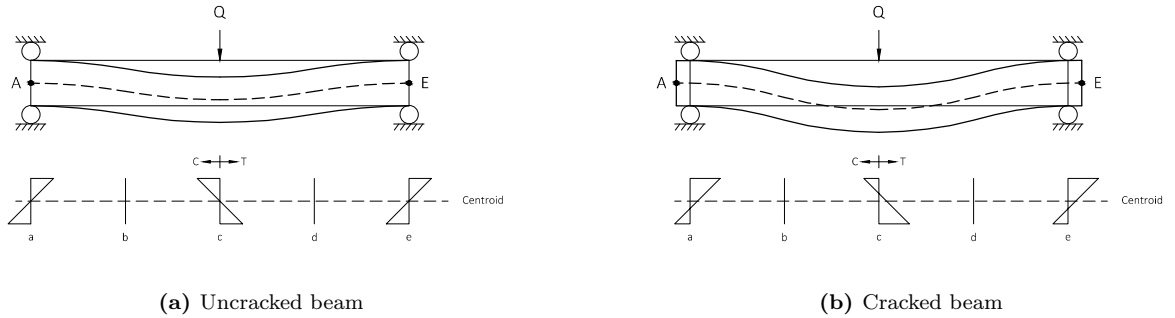


Figure 1.2: Lateral expansion of a beam with rotational restraint.

Arching action, or compressive membrane action, is a phenomenon that occurs in reinforced concrete beams and slabs with supports that limit or prevent lateral expansion. This thesis focuses on arching action in reinforced concrete beams. However, the same formulation can be adapted for use with slab strips. If a beam is rotationally restrained, as illustrated in Figure 1.2, then lateral expansion can only occur after the concrete has cracked. In laboratory tests, it was found that arching action commences prior to the formation of visible cracks at the surface of the concrete, suggesting that even micro-cracking can cause some lateral expansion (Liebenberg, 1966).

If this lateral expansion is limited by the supports, then a lateral restraint reaction force, H , develops at each end of the beam. This axial restraint force initially induces an axial compression force throughout the beam. If a given beam is unreinforced, then the compression resultant throughout the beam forms a single diagonal compression strut between the support and midspan, as illustrated in Figure 1.3a. Alternatively, if a given beam has longitudinal reinforcement and stirrups, then multiple diagonal compression struts will form throughout the beam, as illustrated in Figure 1.3b. In both cases, the axial compression resultant flows from the bottom of the beam near the support, to the top of the beam near the applied load, forming an internal arch.

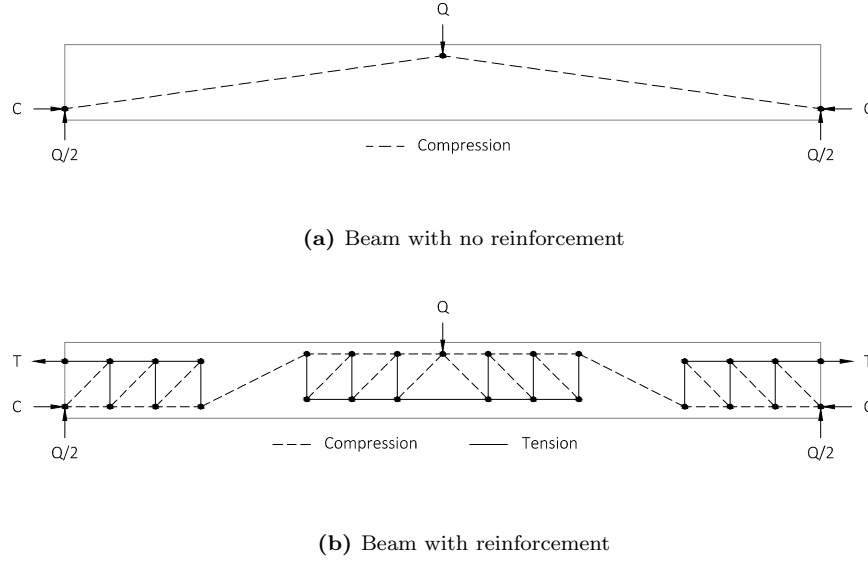


Figure 1.3: Compression and tension stress fields, adapted from Gauvreau (1993).

A qualitative bending moment vs. axial compression interaction diagram for a section of a reinforced concrete beam is presented in Figure 1.4.

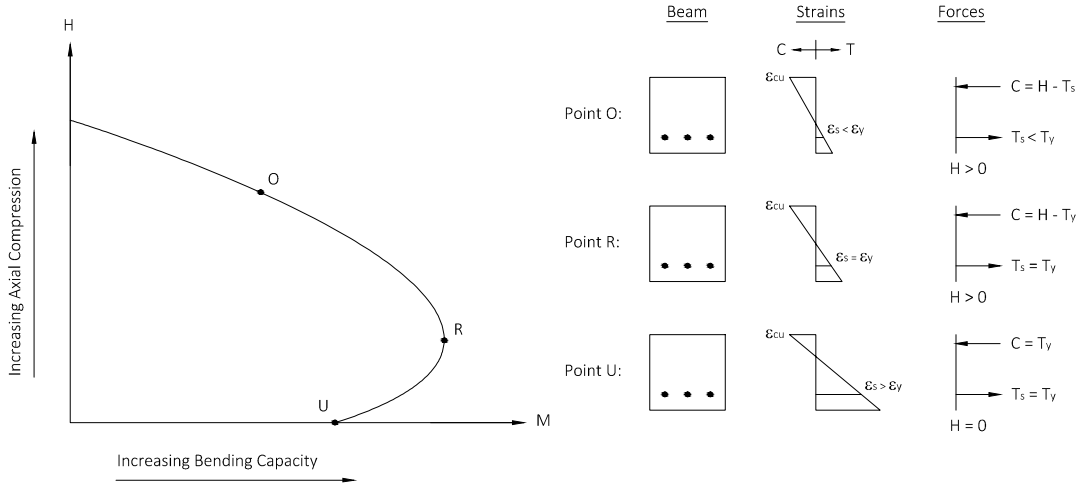


Figure 1.4: M-H interaction diagram for a laterally restrained beam.

The capacity of this section with no axial compression, at point U , is governed by the yield strength of the reinforcement, T_y . As the axial compression at this section increases from point U to point R , the tensile strain in the reinforcement reduces without altering the magnitude of T_s , and the magnitude of the compression resultant, C , increases. The increase in C increases the bending capacity of the beam. At point R , the axial compression resultant at the section causes the reinforcement to yield and the concrete to crush simultaneously. This maximizes the bending capacity of a beam by increasing the magnitude of C , without reducing the magnitude of $T_s = T_y$. However as the axial compression force at

the section continues to increase, the strain in the reinforcement when the concrete crushes is lower than the yield strain, reducing the force T_s , and reducing the bending capacity of the beam. Therefore, the benefits of lateral restraint are more efficient in cases where the reinforcement yields and the concrete crushes simultaneously.

1.2 Experimental Investigations of Membrane Action

For over a century, the behaviour of laterally restrained reinforced concrete beams and slabs has been studied experimentally. One of the earliest observations was made by Westergaard and Slater (1921) during the testing of flat slab panels with all four sides restrained against lateral expansion. These tests indicated that the ultimate capacity of a restrained slab is much larger than the capacity predicted based on flexural analysis. One of the first instances where the increased capacity in a slab was directly attributed to the development of membrane forces was during the demolition of the five storey Old Dental Hospital in Johannesburg (Ockleston, 1955). The dental hospital, constructed in 1942, was set for demolition in 1952 to allow for the remodeling of the Johannesburg railway station. The in-place load tests conducted on the recently built structure, first proposed by R. G. Ventress, provided an unusual opportunity to test the accuracy of the analytical techniques available at that time. In these historic tests, the capacity of the floor slabs with light reinforcement was three to four times higher than the capacity predicted using both flexural and plastic analysis. This finding has motivated more experimental investigations of both reinforced concrete slabs and beams with varying magnitudes of support stiffness.

Experimental studies have since identified various factors that can affect the response of a laterally restrained, reinforced concrete beam or slab. The importance of considering second-order effects, caused by the axial compression and the deformation of a concrete slab, was highlighted in the experimental investigation conducted by Vecchio and Tang (1990). The study, conducted in response to the 1978 collapse of a warehouse structure in Niagara Falls, Canada, consisted of two slab specimens with concentrated loads at midspan. By laterally restraining one of the slabs and allowing the other to expand freely, the influence of the membrane force developed in the slab could be determined. Similar to previous investigations, the addition of lateral restraint at the support was found to increase the stiffness and capacity of the slab. However, the capacity of the restrained slab was found to be limited by the increased bending moment caused by second-order effects. The importance of considering rotational restraint, in addition to lateral restraint, was highlighted in an experiment conducted by Guice and Rhomberg (1988). This test consisted of 16 one-way slab strips under uniform loading, and found that increasing the rotational stiffness of a support will reduce the deflection of a slab. The reduced rotation at each support increases the bending moment at the support, and reduces the bending moment at midspan. Therefore, limiting the rotation of a slab at a support can increase capacity.

The initial investigation of membrane action in reinforced concrete slabs also inspired a number of experiments that studied the effect of arching action in laterally restrained, reinforced concrete beams. In an experimental investigation conducted by Ruddle (1989), 22 rectangular and tee beams, axially and rotationally restrained at the supports, were tested. The amount of stirrups in each beam was varied to study both the flexural and shear strength enhancement caused by lateral restraint. It was found

that both flexure and shear critical beams benefit from the compressive resultant that develops as a result of the lateral supports. More recently, a series of experiments were conducted that investigate the progressive collapse resistance of a reinforced concrete beam in a two bay frame, after the removal of the middle column. When the middle column is removed, the lateral expansion of the beam is prevented by the stiffness of the supporting columns and adjacent beams, causing membrane forces to develop. In tests conducted by Su, Tian, and Song (2009) and Yu and Tan (2013), it was found that the capacity of each specimen was governed by a softening effect caused by second-order effects. It was also found that at large magnitudes of midspan deflection, the axial force in a beam transitions from compression to tension. The development of a tensile resultant force, known as catenary action, can increase the capacity of a beam beyond the initial peak load. This is discussed in detail later in this thesis.

Experimental investigations have also been conducted to study the influence of lateral restraint on the capacity of reinforced concrete slabs used in bridge construction. Tests on nine reinforced concrete slabs supported by I-beams were conducted by Batchelor, Hewitt, Csagoly, and Holowka (1985) to determine the increased load capacity provided by the lateral stiffness of the adjacent slabs. This study found that the axial compression force that develops in the transverse spans between the I-beam supports prevents the need for any tensile reinforcement. However, it was recommended that a minimal amount of reinforcement be specified to control cracking due to shrinkage and changes in temperature. The importance of reinforcement in bridge decks was also investigated in an experiment conducted by Khanna, Mufti, and Bakht (2000). As part of this investigation, a full scale model of a reinforced concrete bridge deck, supported by two steel girders, was constructed. This bridge deck consisted of four slab strips with varying amounts of reinforcement that were tested individually to determine the optimal arrangement. These tests suggested that the bottom transverse reinforcement has the greatest influence on the load capacity of a bridge deck slab, and that this capacity is governed by the stiffness and not the strength of the reinforcement.

1.3 Existing Analytical Formulations

Over the past few decades, a number of analytical formulations have been developed to quantify the influence of lateral restraint on the capacity of reinforced concrete beams and slabs. However, few have been successful in improving the understanding of the mechanics behind the increased capacity caused by lateral restraint. A brief overview of the more popular models is presented in this section to provide insight into the current state-of-the-art analytical techniques available in the literature.

1.3.1 Christiansen (1963)

One of the earliest formulations that accounted for the increased section capacity caused by lateral restraint was developed by Christiansen (1963). This formulation is based on the assumption that plastic hinges form at the locations of concentrated loads and at the support of a given slab. This is illustrated in Figure 1.5 for the case of a single concentrated load, Q , at midspan.

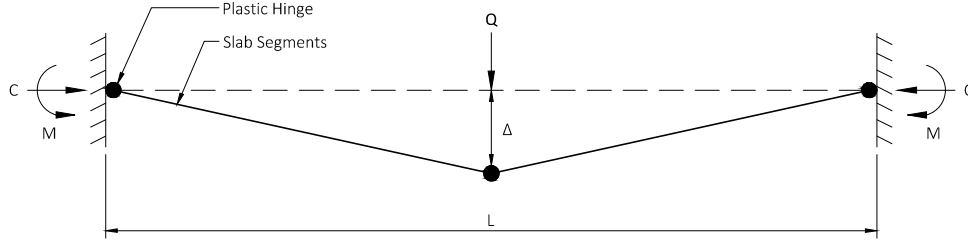


Figure 1.5: Plastic collapse mechanism of a slab, adapted from Christiansen (1963).

This formulation assumes that the vertical deflection at midspan is equal to,

$$\Delta = \Delta_e + \Delta_p \quad (1.1)$$

where Δ_e is the vertical deflection due to the elastic deformation of the slab segments, and Δ_p is the vertical deflection caused by rotations in the plastic hinges. The vertical deflection of the slab is dependent on the total axial compression force, C , caused by the rigid, lateral supports. Therefore, any small increase in the axial compression force, δC , will result in a small increase in the vertical deflection of the slab, $\delta \Delta$.

The compatibility condition in this analysis suggests that the total axial compression force applied at the supports is equal to the force required to counteract the total lateral expansion of the slab, X_t . Therefore, the magnitude of axial compression is determined by assuming that the total shortening is equal to the total expansion of the slab. The magnitude of this expansion is defined as,

$$X_t = X_{\delta \Delta} - X_{\delta C, e} - X_{\delta C, p} \quad (1.2)$$

where $X_{\delta \Delta}$ is the shortening caused by a rotation of the plastic hinges resulting from an incremental increase in the vertical deflection, $X_{\delta C, e}$ is the elastic shortening caused by the incremental increase in C , and $X_{\delta C, p}$ is the plastic shortening caused by the rotation of the hinges resulting from an incremental increase in C .

The increased bending capacity caused by arching, M_a , is equal to the product of the calculated axial compression force, C , and the vertical distance between the axial compression force at the support and at midspan. Therefore, the total bending capacity of a slab is defined as,

$$M = M_y + M_a \quad (1.3)$$

where M_y is the bending capacity governed by yielding of reinforcement, and M_a is the additional bending capacity resulting from arching.

Discussion

The development of this analytical method significantly improved the understanding of the influence of lateral restraint on the response of a reinforced concrete slab. This model has also motivated more extensive investigations of the topic, as discussed later in this chapter. However, this method is not very robust in nature. Firstly, it requires that the stiffness of the supports be known and applied using a dimensionless factor, which may limit its applicability in practical situations. Secondly, material nonlinearities are not accounted for in the analysis. Rather, a linear stress block is assumed for the concrete at each plastic hinge, and the reinforcement is assumed to have yielded. Therefore, this model cannot predict the full load-deflection response of a slab, and can only be used to predict its peak capacity in limited situations.

1.3.2 Park (1964)

An alternative model, developed by Park (1964), also incorporates the influence of membrane forces in the analysis of laterally restrained reinforced concrete slabs. Similar to the model developed by Christiansen (1963), the basis for the analysis is the assumption that a slab strip can be represented by rigid slab segments separated by plastic hinges. The case of a concentrated load applied at midspan is illustrated in Figure 1.6, where two slab segments are separated by plastic hinges at points a , b and c .

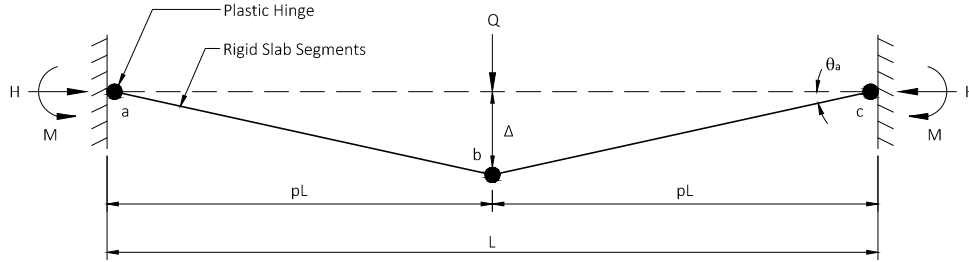


Figure 1.6: Plastic collapse mechanism of a slab, adapted from Park (1964).

The total vertical deflection of the slab strip, Δ , is governed by the rotation of the plastic hinges. The state of stress in the plastic hinge is approximated by assuming that plane sections remain plane. This assumption provides a means for calculating the force resultant in each material. The tension and compression forces in the reinforcement at each hinge, T_s and C_s , are assumed to be equal to the yield force of the reinforcement. The compressive force in the concrete, C_c , is based on a linear stress block assumed to act over the depth of the compression zone, c . The concrete is assumed to have no tensile strength. The state of equilibrium at the plastic hinges at either end of the slab segment $a-b$ is illustrated in Figure 1.7. Unlike the model developed by (Christiansen, 1963), each slab segment is assumed to remain rigid, and therefore the total length of each segment, pL , does not change after rotating.

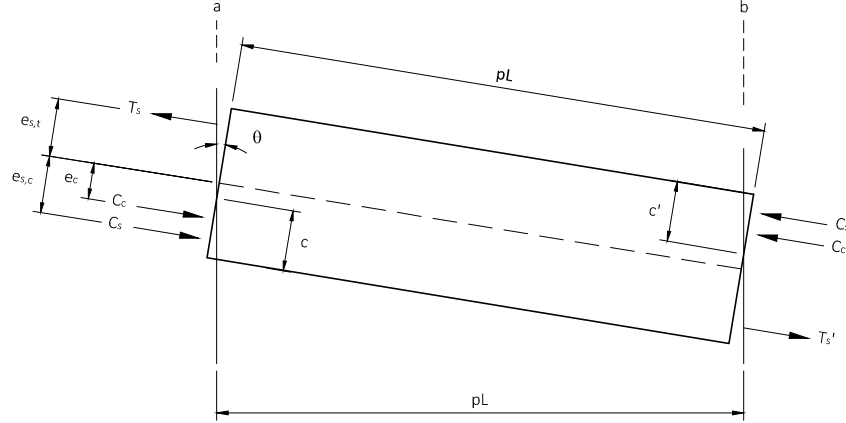


Figure 1.7: Internal forces at either end of a slab segment, adapted from Park (1964).

The depth of the neutral axis at each hinge is determined from the deflected shape and the geometry of the beam. This requires that the midspan deflection of the beam, and the depth of compression in the plastic hinges, be assumed prior to determining the force resultants in each plastic hinge. The axial compression resultant at each hinge can be determined based on horizontal equilibrium, using the following equation,

$$H = C_c + C_s + T_s \quad (1.4)$$

In addition, the total bending moment at each hinge can be defined based on rotational equilibrium, using the following equation,

$$M = C_c(e_c) + C_s(e_{s,c}) + T_s(e_{s,t}) \quad (1.5)$$

where $e_{s,c}$ is the eccentricity of the reinforcement in compression, $e_{s,t}$ is the eccentricity of the reinforcement in tension, and e_c is the depth of the compression resultant. The depth of the compression resultant is dependent on the depth of the neutral axis at each hinge, and is determined based on the assumed stress block.

The method of virtual work is employed, assuming a unit rotation of θ , to relate the applied load in the section to the midspan deflection in the slab strip. This can be expressed as,

$$(M_{supp} + M_{mid} - H\Delta)\theta \quad (1.6)$$

where M_{supp} is the bending moment at the support, M_{mid} is the bending moment at midspan, and $H\Delta$ is the bending moment due to second-order effects.

Discussion

The analytical method proposed by Park (1964) is an extension of the yield line method first proposed by Johansen (1962). The method is relatively straightforward and the response of a laterally restrained slab can be easily predicted as it is not computationally intensive. This method has been shown to accurately predict the ultimate capacity of experiments conducted by Taylor, Rankin, and Cleland (2001), and Su, Tian, and Song (2009). However, the assumption that the reinforcement has yielded will cause an over prediction of the rotation in the plastic hinge regions at low values of applied load. In addition, the influence of material nonlinearity is not considered. Therefore, despite being able to predict the ultimate capacity of a beam with stiff lateral supports, this method is unable to predict the relationship between the lateral restraint force and deflection at all values of applied load. This shortcoming was highlighted by Eyre and Kemp (1994), using test data from various experiments.

1.3.3 Rankin (1982)

The analytical model proposed by Rankin (1982) was developed by assuming that a restrained slab behaves similar to an arch. This formulation is based on an analytical model developed by McDowell, McKee, and Sevin (1956) for use with unreinforced masonry, and accounts for the material and sectional properties inherent in reinforced concrete slabs. The structural system, in this case, is based on the mechanics of a three hinged arch with elastic horizontal restraints, as illustrated in Figure 1.8. The stiffness of the lateral restraint, K_e , is dependent on the stiffness provided by the adjacent slab. The stiffness of each slab segment is based on an assumed bi-linear σ - ε response of concrete in compression.

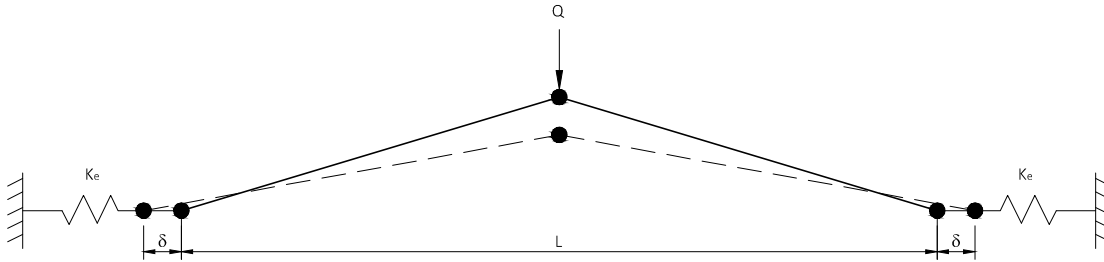


Figure 1.8: Three hinged arch with elastic supports, adapted from Rankin (1982).

Similar to the model developed by Christiansen (1963), the total bending capacity of a beam or slab strip is defined as,

$$M_p = M_b + M'_b + M_a \quad (1.7)$$

where $M_b + M'_b$ is the bending capacity assuming a plastic collapse mechanism, and M_a is the additional bending capacity resulting from arching action. If a single concentrated load is applied at the midspan

of a slab, the peak load capacity, Q_u , is defined as,

$$Q_u = \frac{4(M_b + M'_b + M_a)}{L} \quad (1.8)$$

where L is the undeformed length of the slab. The bending capacity resulting from arching action is defined as,

$$M_a = M_r \frac{0.85f'_c d_1^2}{4} \quad (1.9)$$

where f'_c is the compressive strength of concrete, d_1 is half the depth of arching in the section, and R is a unitless parameter that accounts for the geometric and material properties of a given slab or beam. The parameter M_r , which is dependent on R , is defined as,

$$M_r = \begin{cases} 0.3615/R & R \geq 0.26 \\ 4.3 - 16.1\sqrt{3.3 \times 10^{-4} + 0.1243R} & 0 < R < 0.26 \end{cases} \quad (1.10)$$

The parameter R is defined as,

$$R = \frac{\varepsilon_c L_r^2}{4d_1^2} \quad (1.11)$$

where ε_c is the plastic strain in the concrete, and L_r is half the span length of an equivalent rigidly restrained slab strip. This model assumes that a portion of the depth of the compression block is used to balance the tensile force in the reinforcement, with the remaining depth available for arching. This assumption, which was also used by Christiansen (1963), allows for half the depth of arching to be determined as,

$$2d_1 = h - (\rho - \bar{\rho}) \frac{f_y d}{0.85f'_c} \quad (1.12)$$

where ρ is the positive reinforcement ratio, $\bar{\rho}$ is the negative reinforcement ratio, h is the depth of the slab, and f_y is the yield stress of the reinforcement.

Discussion

The formulation proposed by Rankin (1982) has been used in numerous experimental studies to predict the load capacity of reinforced concrete beams and slabs with stiff lateral restraints. The majority of these studies, including those conducted by Rankin (1997), Taylor et al. (2001) and Ruddie (1989), have shown a good correlation between the predicted capacity and the measured capacity. However the basis for this model is not intuitive as it requires that a number of simplifying assumptions be made. These simplifications allow for the use of a single parameter to account for the geometric and material

properties in the slab, which may not accurately capture the state of stress at every section. This parameter reduces the transparency of the analysis, limiting the applications for which it can be used. In addition, the analysis can only be conducted at the peak applied load.

1.3.4 Eyre (1997)

All the previous analytical models developed to predict the influence of lateral restraint on reinforced concrete beams and slabs are too computationally intensive to implement for design purposes. The simplified analytical model, proposed by Eyre (1997), is an attempt at providing a lower bound estimate of the peak capacity of a slab slip, restrained against lateral expansion.

For each beam, the reinforced concrete section parameters, α and β , are defined as,

$$\alpha = \frac{a'}{z'} \quad (1.13) \quad \beta = \frac{b'}{z'} \quad (1.14)$$

where a' is the vertical distance between the centroid and the neutral axis, b' is the distance between the extreme fiber of the concrete on the compression side to the center of the compression zone, and z' is the distance between the center of the compression zone and the effective depth of the tensile reinforcement. The section parameters that are used to incorporate the material and section properties into the analysis, α_1 and β_1 , are defined as,

$$\alpha_1 = \frac{1}{2} \left(\frac{\alpha}{\beta} + 1 - \gamma \right) \quad (1.15) \quad \beta_1 = \frac{\alpha}{2\beta} + 1 \quad (1.16)$$

where γ is the ratio of tensile reinforcement at the support relative to midspan. The non-dimensional stiffness parameter, \bar{S} , allows a designer to estimate the influence of the support stiffness on the response of a given slab, and is defined as,

$$\bar{S} = \frac{2S}{T_o L} \left(\frac{h}{\beta_1} \right)^2 \quad (1.17)$$

where S is the lateral stiffness of the supports, T_o is the tensile yield force in the reinforcement per unit width of the slab, L is the undeformed length of the slab, and h is the total depth of the slab. The total strength enhancement of the beam, P/P_y , can be adopted in design practice to improve the prediction of the capacity of laterally restrained reinforced concrete slabs, and is defined as,

$$\frac{P}{P_y} = 1 + \frac{2\beta}{1 + \gamma_1} \left(\alpha_1 - \frac{\sqrt{1 + 4\alpha_1 \bar{S}} - 1}{2\bar{S}} \right)^2 \quad (1.18)$$

where P_y is the load capacity according to yield line theory, and P is the capacity of the restrained slab.

Discussion

This simplified design method is shown to give reasonable predictions of the capacity of reinforced concrete slabs with known magnitudes of lateral stiffness (Eyre, 1997). However, as indicated by Eyre (1997), the accuracy of this analysis is influenced by the assumed stiffness of the supports. As a result, it may be difficult for a design engineer to determine the appropriate stiffness to use unless a comprehensive list is generated. In addition, this lower bound prediction does improve the current predictions generated using a yield line method, but it does not provide a robust and transparent means to calculate the full load-deflection response of a reinforced concrete beam or slab strip. Finally, this method does not explicitly account for the state of stress in the reinforcement, or calculate the axial compression force in the section, which can be important design tools for engineers.

1.3.5 Finite Element Analysis

In recent years, nonlinear finite element methods have been developed to model the behaviour of laterally restrained reinforced concrete slabs and beams. These methods have been shown to be effective in predicting capacity, while also directly considering the state of stress in the concrete throughout the beam or slab. As a result, the finite element approach provides a more rational prediction of the influence of lateral restraint on a beam or slab.

A nonlinear finite element analysis program called Tempest, a precursor to the VecTor suite of finite element analysis software developed at the University of Toronto, was employed by Vecchio and Tang (1990) to predict the response of a lateral restrained slab strip. The program was found to correlate reasonably well with the load-deflection response of each specimen. However, the analysis over predicted the stiffness and peak capacity of the slab. The over prediction of capacity was attributed to difficulties in modeling the local two-way slab behaviour near column supports. Despite this, the software was able to account for second-order effects, as well as the internal state of stress and strain throughout each slab.

More recently, a number of commercially available software have been developed using the finite element method for reinforced concrete. A comprehensive validation of the more common programs was conducted by Zheng, Robinson, Taylor, Cleland, and Shaat (2009) for the case of a laterally restrained slab strip. The finite element method, which directly accounts for the lateral restraint force, was found to provide adequate predictions of the slab's capacity. However, these programs all over predict the stiffness, and as a result, under predict the deflection of the slab at failure. It was suggested by Einsfeld, Martha, and Bittencourt (2000) that the reason for this may be that the smeared crack model employed in this method causes stress-locking due to compatibility requirements between each element.

More recent studies have focused on developing one dimensional finite element models for predicting the influence of lateral restraint on reinforced concrete frame beams. As part of the investigation into the progressive collapse response of reinforced concrete frame beams with stiff end supports, Yu and Tan (2013) developed a one-dimensional, nonlinear finite element analysis method that provides an accurate prediction of the test specimens response at all magnitudes of applied load. This method requires the use of a joint model comprised of linear and shear springs that simulate the behaviour of bond

deterioration between the concrete and reinforcement at the supports and midspan. A similar analytical model, developed by Valipour, Vesali, Samali, and Foster (2014), correlates well with test data from an experiment conducted by FarhangVesali, Valipour, Samali, and Foster (2013). In this case however, bond deterioration is modeled using a nonlinear rotational spring at the supports and at midspan.

Discussion

The use of finite element analysis software to predict the influence of lateral restraint on the behaviour of a reinforced concrete slab or beam has been shown to be quite accurate (Vecchio & Tang, 1990). These programs directly account for the lateral restraint force applied at the supports, and can therefore provide a realistic representation of the state of stress and strain throughout a beam or slab. However, the current commercially available nonlinear finite element software often over predicts the stiffness and capacity of a restrained slab or beam. Finally, the creation and validation of a finite element analysis requires significant time and expertise, limiting its practicality for use in design practice.

1.3.6 Wu (2013)

A method for predicting the influence of lateral restraint on the response of reinforced concrete slab strips and beams was developed by Wu (2013). Unlike the previously developed analytical models, this method maintains equilibrium and compatibility throughout the entire beam, and uses nonlinear constitutive material models to relate the stress in each material to the strains at each section. The model is based on the assumption that plane sections remain plane, which provides a means for determining the resultant material forces at each section using a layered analysis approach. The axial force at each section is determined based on horizontal equilibrium, and is equal to,

$$H = F_c + F_{s,c} + F_{s,t} \quad (1.19)$$

where H is the axial compression force throughout the beam, F_c is the compressive force in the concrete, $F_{s,c}$ is the compressive force in the reinforcement, and $F_{s,t}$ is the tensile force in the reinforcement. Similarly, the bending moment at each section is determined based on rotational equilibrium, and is equal to,

$$M = F_c(e_c) + F_{s,c}(e_{s,c}) + F_{s,t}(e_{s,t}) \quad (1.20)$$

where e is the eccentricity of the force resultant of each material, relative to the centroid of each section. These equilibrium conditions are used to develop the moment-curvature response of each section, based on the magnitude of axial compression in the beam. This is discussed in detail in Chapter 2. The compatibility condition specified in this method states that there is to be no lateral expansion or rotation of the beam at its supports. This condition is defined as,

$$\int_0^L \varepsilon_t = \int_0^L \varepsilon_b = 0 \quad (1.21)$$

where ε_t is the strain at the top of each section, and ε_b is the strain at the bottom of each section. By integrating the strains at the top and bottom of each section throughout a beam, the total elongation, contraction and rotation of the ends of the beam can be determined.

The iterative procedure developed by Wu is summarized as:

1. Assume the total axial compression force H , applied at each support.
2. Determine the total bending moment in the beam, based on an assumed applied load, Q .
3. Determine the moment-curvature response, based on horizontal and rotational equilibrium.
4. Integrate the strains at the top and bottom of each section to determine the total elongation or contraction of the ends of the beam.
5. Adjust the magnitude of Q until the compatibility condition is achieved.

Test data from a series of experiments conducted by others was used to validate the proposed formulation (Wu, 2013). In most cases, the model developed Wu was able to provide a reasonable prediction of the capacity and axial compression developed in a laterally restrained beam. However, Wu's model over predicts the stiffness and under predicts the deflection of all of these experiments. The response of beam B2, from an experiment conducted by Su, Tian, and Song (2009) on reinforced concrete beams with stiff lateral restraints, is presented in Figure 1.9 alongside the response predicted using Wu's method.

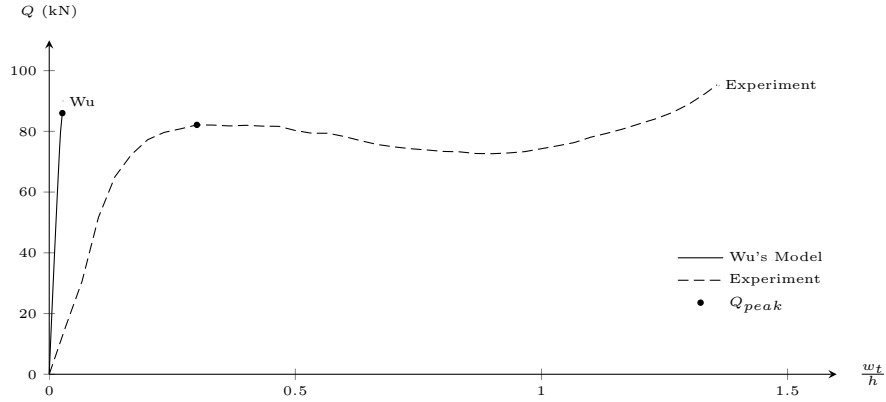


Figure 1.9: Predicted load-deflection response of beam B2, using Wu's method.

Although Wu's method does predict the capacity of the beam, it does not predict the softening of the load-deflection response that allows for the development of two peaks in applied load, and therefore under estimates the midspan deflection of the beam, at the first peak in the applied load, Q_{peak} , by a factor of 11.

Discussion

The model developed by Wu (2013) is the first to directly account for membrane forces in beams and slab strips using an analytical procedure where both equilibrium and compatibility conditions are based on the state of stress in the concrete and reinforcement throughout a beam. This method provides a

rational basis for predicting the relationship between the applied load, the axial compression force and the midspan deflection of a given beam or slab strip.

Despite providing a transparent formulation for predicting the strength enhancement due to arching action, this method makes some assumptions that limit its applicability to a small subset of beams and slab strips. First, the model assumes that the supports provide an infinite rotational and axial stiffness, causing it to over predict the response of beams or slab strips with a finite support stiffness. Second, the analysis does not account for second-order effects. As indicated by Vecchio and Tang (1990), these second-order effects can reduce the capacity and increase the deflection of a given beam or slab strip, particularly when large deformations occur prior to failure. Therefore, despite accurately predicting the load capacity of restrained reinforced concrete beams and slab strips from four experimental investigations, the model grossly under estimates stiffness and deflection. Therefore, Wu’s model can only be used for the analysis of short beams with very rigid supports. The definition of a short beam is discussed in detail later in this thesis.

1.3.7 Botticchio (2014)

Following the development of Wu’s model, Botticchio (2014) proposed a more intuitive approach to the analysis. This approach, which is mathematically equivalent to the method developed by Wu (2013), uses an iterative procedure to determine the required lateral restraint force in a beam for a given configuration of loading. The modified iterative procedure is summarized as:

1. Determine the total bending moment throughout the beam, based on the known applied load, Q .
2. Estimate the magnitude of the axial compression in the beam, H .
3. Determine the moment-curvature response, based on horizontal and rotational equilibrium.
4. Integrate the strains at the top and bottom of each section to determine the total elongation or contraction of the ends of the beam.
5. Adjust the assumed magnitude of H until the compatibility condition specified by Wu (2013) is achieved.

This alteration improves the transparency and logic in the procedure, and is a significant step in providing a more simplified approach for use in design. In addition, Botticchio developed a method to account for the elastic lateral and rotational stiffness of a support using a combination of a linear and rotational spring. The properties of these springs are incorporated into the method by specifying two compatibility conditions,

$$\int_0^{L/2} \varepsilon_t = \int_0^{L/2} \varepsilon_b = \frac{H}{K_{axial}} \quad (1.22)$$

$$\frac{\int \varepsilon_t + \int \varepsilon_b}{h} = \frac{M_o}{K_{rot}} \quad (1.23)$$

where K_{axial} is the axial stiffness of the spring that limits lateral expansion, K_{rot} is the rotational spring stiffness, and M_o is the bending moment at the support. These compatibility conditions allow the ends of a beam to displace and rotate based on the elastic stiffness of the support. Accounting for the measured elastic stiffness of the supports improves the correlation with test data from experiments by Su, Tian, and Song (2009), as illustrated in the load-deflection response of beam B2, presented in Figure 1.10. Despite the improvement, the model still grossly under predicts the stiffness and deflection of the beam by a factor of 5.

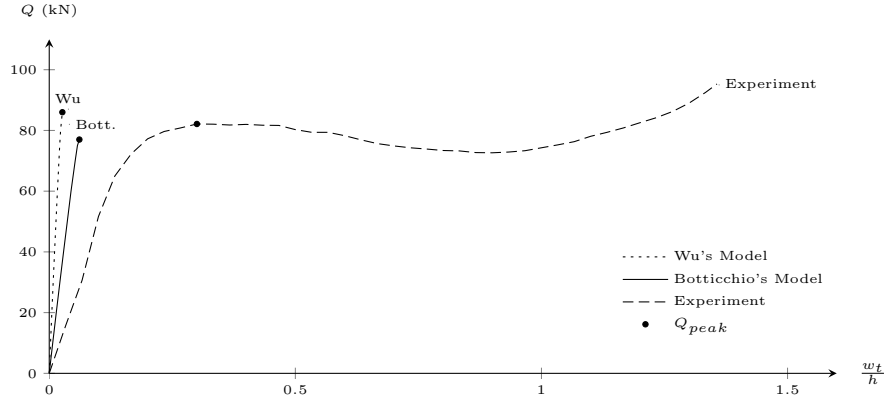


Figure 1.10: Predicted load-deflection response of beam B2, using Botticchio's method.

Discussion

The development of a more logical procedure, and the inclusion of the elastic stiffness of the supports increases the range of beams and slab strips that can be analyzed using the analytical method originally developed by Wu (2013). However, the second-order effects that are inherent in laterally restrained reinforced concrete beams and slab strips are not considered. In addition, the updated analytical model is unable to be validated using experimental data, as it over predicts the stiffness and under predicts the deflection measured in tests on restrained reinforced concrete beams, available in the literature. Therefore, this formulation cannot be used to predict the load-deflection response of a beam or slab strip with confidence, and further work is required to validate the analytical model before it can be simplified for use in design.

1.4 Implementation in Design Standards

There are very few simplified analytical techniques currently available for predicting the increased capacity of beams and slabs. The complexity that arises with the interaction of bending and axial compression, particularly when considering inelastic materials like concrete, has hindered progress. In addition, the uncertainty associated with the amount of lateral and rotational stiffness in various structural systems has, for the most part, precluded any analytical techniques from being incorporated into design standards. However, some design standards have taken steps to account for the influence of lateral restraint, particularly for bridge deck slabs.

1.4.1 Canadian Highway Bridge Design Code (CHBDC)

The experimental study conducted by Batchelor et al. (1985) found that conventionally reinforced deck slabs have large factors of safety against failure, and are therefore wastefully over reinforced. The report recommended, after consideration of shrinkage and temperature reinforcement requirements, that $\rho = 0.2\%$ isotropic reinforcement be prescribed for the range of bridge deck slabs studied. This study provided the basis for the Empirical Design Method (EDM), first implemented in the 1979 Ontario Highway Bridge Design Code (Ontario Ministry of Transportation and Communications, 1979), and later adopted in Section 8.18 of the Canadian Highway Bridge Design Code (Canadian Standards Association, 2006).

The Empirical Design Method reduces the top and bottom reinforcement running transverse between supporting girders to a reinforcement ratio of $\rho = 0.3\%$. The reinforcement ratio, ρ , is defined as the ratio of the cross sectional area of the reinforcement, A_s , to the effective depth of the reinforcement, d , and the width of the section, b . If approved by an engineer, this ratio can be reduced to $\rho = 0.2\%$. However, the empirical nature of this design method limits its applicability to the range of parameters considered in the original study by Batchelor et al. (1985). These limits include:

1. The thickness of the slab, h , must be greater than or equal to 175 mm.
2. The vertical distance between the top and bottom reinforcement must be greater than or equal to 55 mm.
3. The spacing of the transverse reinforcement must be less than or equal to 300 mm.
4. The ratio of the spacing between girders, S , to the thickness of the slab, must be less than or equal to 18.
5. The spacing between girders, S , must be less than or equal to 4 m.

If a bridge deck slab does not comply with all of these limitations, it must be designed using a flexural analysis approach. As previously discussed, flexural methods under predict the capacity of laterally restrained beams and slabs (Khanna et al., 2000). The additional material required as a result of the under predicted capacity can increase material costs and reduce the efficiency of materials. These limits prevent the design engineer from exploring options outside the scope of the EDM. For example, in some cases it may be more economically viable to increase the size and therefore spacing of girders. This would reduce the number of girders, potentially reducing construction costs. A schematic illustrating this concept is presented in Figure 1.11.

As indicated in this schematic, if girders are spaced within 4 m, then the slab can be design economically using the Empirical Design Method. However, if girder spacing exceeds this limit, flexural analysis techniques are required, resulting in a significant jump in the amount of reinforcement required in the slab. Therefore, the code provisions can limit the potential economy of a bridge design by limiting the ability of a design engineer to explore more economical designs, such as increasing girder spacing.

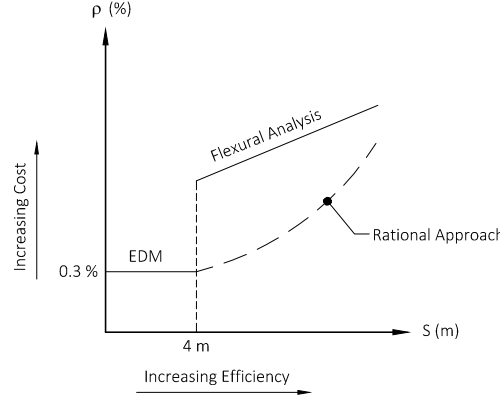


Figure 1.11: Potential limitations on efficiency, imposed by the EDM.

If an analytical model that can accurately predict the influence of lateral restraint on the capacity of reinforced concrete slabs is developed, then the geometrical limitations imposed by the empirical method can be removed. The potential for increasing the girder spacing, without having to over-design the deck slab, can result in cost savings, as indicated in Figure 1.11,

1.4.2 UK Design Codes

Following the implementation of the Empirical Design Method in Canada, other design standards have implemented provisions for reducing the transverse reinforcement required for bridge deck slabs. The Department of Regional Development for Northern Ireland (1986) created an amendment to the United Kingdom Bridge Design Code in 1986. This amendment adopts an empirical design procedure, similar to that proposed in the CHBDC. However, this design code prescribes a minimum transverse reinforcement ratio of $\rho = 0.6\%$, for both top and bottom reinforcement. In addition, it limits the spacing of girders to 2 m or less. Although these provisions do drastically increase the efficiency of bridge designs, they impose severe limitations on the geometry of a slab.

More recently, the UK Highway Agency Standard BD 81/02 (UK Highways Agency, 2002) included provisions for the use of a simplified design method that directly calculates the transverse reinforcement required in bridge deck slabs. Although these calculations are straightforward, there are still significant limitations on their use, as the model was developed using empirical factors. In particular, the spacing of girders cannot exceed 3.7 m, the span length to thickness ratio cannot exceed 15, and the slab thickness must be greater than or equal to 160 mm. Similar to the CHBDC, this empirical design method also limits the minimum amount of reinforcement in a deck slab to $\rho = 0.3\%$.

1.4.3 Discussion

There are currently no design standards that account for the increase in capacity of transverse deck slabs with stiff lateral supports provided by adjacent slabs. This highlights the lack of confidence in the current

understanding of membrane action. The analytical models that do provide a reasonable correlation with test data require a lot of computational effort, and are not derived on the basis of a transparent and rational procedure. The model proposed by Wu (2013), and further developed by Botticchio (2014), are based purely on the fundamentals used in traditional reinforced concrete analysis. This model provides the greatest potential for developing a simplified analytical method that can be implemented in design standards without the severe geometrical limitations that currently exist. Therefore, the model developed by Wu (2013) and Botticchio (2014) are used as the basis for the analytical model proposed in this thesis.

1.5 Objectives and Content of Thesis

The primary objectives of this thesis are:

1. Improve the analytical model developed by Wu (2013) and Botticchio (2014) by accounting for second-order effects.
2. Validate the proposed analytical model using the results of load tests on restrained, reinforced concrete beams.

In addition to these, the secondary objectives of this thesis are:

1. Develop supplementary refinements to the proposed model to account for the effects of partial restraints, compression carried in diagonal compression struts, slip at supports, and bond deterioration in regions with geometric irregularities.
2. Conduct a detailed parametric investigation to study the influence of concrete compressive strength, mechanical reinforcement ratio, second-order effects, lateral slip at supports, and the spreading of load through diagonal compression struts.

The primary and secondary objectives are addressed in this thesis following a logical progression in the development and implementation of the proposed analytical model. The focus of this thesis is to improve the model developed by Wu (2013) by accounting for second-order effects, which will allow for the accurate prediction of stiffness, capacity, and deflection of a reinforced concrete beam or slab strip with varying magnitudes of restraint stiffness.

In Chapter 2, the proposed analytical model is presented. The nonlinear constitutive material models adopted for concrete and steel are implemented into a layered analysis approach. The compatibility and equilibrium conditions originally developed by Wu (2013), which form the basis for the model, are updated to account for second-order effects. Based on this, an iterative procedure for conducting sectional analysis throughout the beam is proposed. The differences between the proposed analytical model and Wu's model are highlighted by examining two beams with varying span-to-depth ratios. Following this, the influence of second-order effects is highlighted by comparing the predicted load-deflection and restraint-deflection response of a slender beam using the proposed analytical model, with and without consideration of second-order effects.

In Chapter 3, four supplementary refinements are developed to account for potential internal and external factors that can alter the behaviour of a laterally restrained, reinforced concrete beam. These refinements are developed using test data from the experiments conducted by Su, Tian, and Song (2009) and Yu and Tan (2013). The first modification accounts for the finite rotational and axial stiffness of a support. The second modification accounts for the influence of the horizontal component of the diagonal compression strut that transfers the shear force throughout the beam. The diagonal compression field action model is developed using a truss analogy, and implemented into the proposed analytical model. The third modification accounts for any potential lateral or rotational slip that can occur between the ends of a beam and the support. Finally, the fourth modification accounts for the influence of bond deterioration in regions where significant geometric irregularities occur. To avoid implementing an empirically developed bond-slip model, a simplified method for accounting for bond deterioration, specific to the experiments conducted by Su, Tian, and Song (2009) and Yu and Tan (2013), is proposed.

In Chapter 4, the experiments conducted by Su, Tian, and Song (2009) and Yu and Tan (2013) are presented. The influence of the test setup on the response of the reinforced concrete beams is discussed and accounted for using the supplementary refinements developed in Chapter 3. Following this, the test data is presented and discussed, with particular emphasis on the load-deflection and restraint-deflection response of each specimen. Finally, the proposed analytical model used for the validation is presented, and the predicted response is compared to the test data.

In Chapter 5, the proposed analytical model is used to study the influence of various parameters on the behaviour of laterally restrained, reinforced concrete beams and slab strips. The parameters considered as part of this study include concrete strength, mechanical reinforcement ratio, span-to-depth ratio, slip at supports, and inclination of diagonal compression struts. The influence of lateral restraint is determined by comparing the response of each beam to the response of a laterally unrestrained beam. In addition, the influence of second-order effects on the response of laterally restrained beams and slab strips is studied by comparing the response of the proposed analytical model, with and without second-order effects.

The most important findings of this thesis are:

1. The validated analytical model provides a comprehensive, rational method that can be used to predict the full load-deflection response of a restrained, reinforced concrete beam or slab strip, with a wide range of geometry and boundary conditions.
2. In some cases, second-order effects can cause significant softening to occur, which can reduce the stiffness and capacity of a given beam or slab strip, while increasing deflection prior to failure.
3. The softening associated with second-order effects causes the peak axial compression to occur after the first peak in the applied load. Contrary to the conclusion by Su, Tian, and Song (2009), the peak axial compression is governed by the geometry of a beam, and does not correspond with the crushing of concrete.
4. Increasing the strength of concrete, and reducing the mechanical reinforcement ratio, increases the beneficial influence of lateral restraint.
5. A small magnitude of slip between a beam and its support can significantly reduce the capacity of

a laterally restrained beam.

6. Bond degradation in beams with geometric irregularities can have a significant impact on the stiffness and capacity of laterally restrained, reinforced concrete beams.

The rational analytical model presented in this thesis provides the basis for the development of a simplified approach that can be incorporated into design standards, in the hopes of increasing the efficiency and economy of bridge construction.

2

Proposed Model

This chapter presents an analytical model that predicts the response of a given reinforced concrete beam or slab strip with rigid supports that prevent lateral expansion and rotation. This model is based on a sectional analysis approach which assumes that plane sections remain plane, and accounts for material nonlinearities and second-order effects. Considering the compatibility of strain along the length of the beam provides a rational basis for predicting the axial restraint force associated with arching action. In this chapter, the components that form the basis for the analytical model are presented. These include key assumptions, constitutive material models assumed for concrete and steel, as well as the specified compatibility and equilibrium conditions. Next, a sectional analysis formulation used to predict the relationship between the bending moment and curvature in a given beam, is presented. Following this, the procedure for incorporating second-order effects is described. Finally, the iterative analytical procedure is proposed. To provide insight into the capabilities of the proposed model, the response of two beams with varying span-to-depth ratios are presented and compared to the response predicted by the model developed by Wu (2013). Following this, the importance of considering second-order effects is highlighted by comparing the predicted load-deflection and restraint-deflection response of a slender beam using the proposed analytical model, with and without consideration of second-order effects. Finally, a sensitivity study of the numerical integration approach adopted for the layered and sectional analysis approach is presented.

2.1 Model Assumptions

The proposed analytical model is based on the layered, sectional analysis approach first developed by Wu (2013). Both models make a number of assumptions that simplify the analysis. These assumptions include:

1. Plane sections remain plane during bending (i.e. strains at a given cross-section are linearly related to each other).
2. Reinforcement is bonded perfectly to the concrete, with $\varepsilon_s = \varepsilon_{c,s}$.

3. A σ - ε model can be assumed for the concrete and steel reinforcement.
4. The concrete is assumed to have zero tensile strength. As a result, a section is considered to be cracked when $\varepsilon_c > 0$.

The first assumption that plane sections remain plane is based on the Euler-Bernoulli beam formulation, and provides the basis for relating the applied load to the deflected shape. This assumption ignores any deflections that may result from shear deformation. Therefore, the proposed model is limited to applications where the response of the beam is governed by flexure.

The second assumption states that there is no loss of bond between the concrete and the reinforcement at any point along the length of the beam. The proposed analytical model, which uses a smeared crack formulation, assumes that cracking in the concrete is spread out over the length of each section.

The third and fourth assumptions provide a means to relate the strains at each section to the stress in each material. The stress-strain relation for each material is based on a predefined constitutive material model. The material models proposed for use in this formation are presented in Section 2.2.

The failure of a beam can be defined by considering the potential applied load vs. midspan deflection response of a restrained beam, presented in Figure 2.1. For the majority of short beams or slab strips, failure will occur as a result of crushing of concrete, labeled as point A. However in some slender beams, the applied load can develop two peaks. The term slender is used throughout this thesis to describe beams with large span-to-depth ratios that develop large deformations prior to failure. This is discussed in detail later in this chapter.

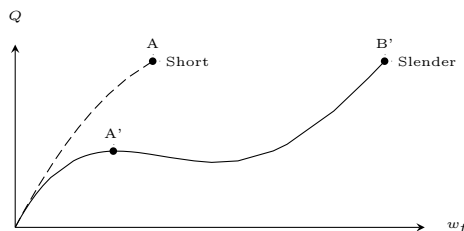


Figure 2.1: Typical response of a short and slender beam.

Throughout this thesis, failure is defined as:

Peak capacity: crushing of the concrete causing failure (A), or the first peak in the applied load of a slender beam (A').

Maximum capacity: the second peak in the applied load of a slender beam (B').

2.2 Material Properties

This section summarizes the nonlinear constitutive material models used as part of the proposed analysis. These models are typically established using experimental data, and provide the basis for relating the stress and strain in each material. First, the constitutive material models used to predict the behaviour

concrete in compression are presented. This includes a formulation that considers the influence of confinement provided by stirrups. Following this, the behaviour of steel reinforcement is defined using a material model that considers the effects of strain hardening.

2.2.1 Concrete Material Model

The following material models, illustrated in Figure 2.2, are considered for concrete in compression:

Bi-linear: The bi-linear σ - ε response of concrete is defined based on the provisions provided in the Federation Internationale du Beton (fib) (2010) model code. This model is used for all ranges of concrete strength.

Popovics: The σ - ε response of concrete is defined based on the provisions provided by Popovics (1973). This model is used for all ranges of concrete strength for which the post-peak response of the concrete is considered.

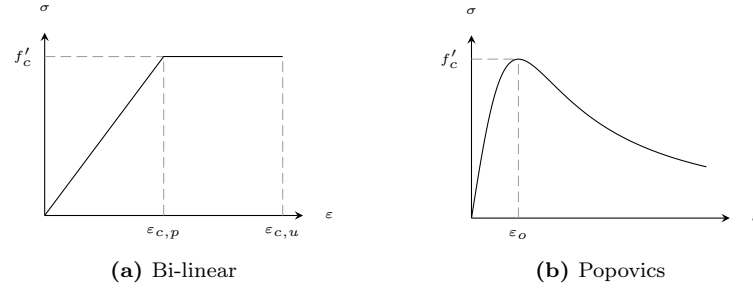


Figure 2.2: Constitutive material models of concrete in compression.

These constitutive material models relate the strain at each layer i to the stress in the concrete, as illustrated in Figure 2.3. The layered analysis approach adopted for the proposed analytical model is discussed in detail later in this chapter.

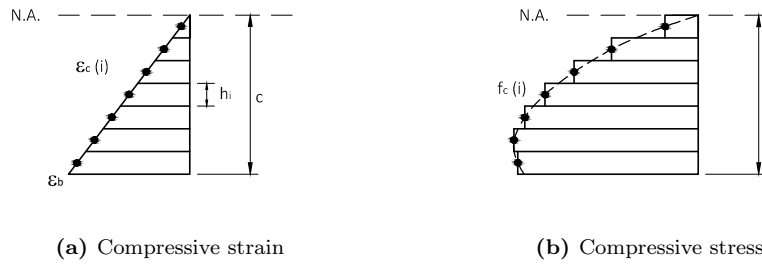


Figure 2.3: Numerical integration of compressive stresses.

The bi-linear response assumes that the concrete remains linear elastic up to the initial plastic strain, $\varepsilon_{c,p}$, defined as,

$$\varepsilon_{c,p} = 1.75 + 0.55 \left(\frac{f'_c - 50}{40} \right) \geq 1.75 \quad (2.1)$$

where f'_c is the compressive strength of the concrete. The stiffness of the concrete prior to any plastic deformation is defined as,

$$E_c = \frac{f'_c}{\varepsilon_{c,p}} \quad (2.2)$$

After the strain exceeds $\varepsilon_{c,p}$, the concrete remains perfectly plastic up to the ultimate strain, $\varepsilon_{c,u}$, defined as,

$$\varepsilon_{c,u} = 2.6 + 35 \left(\frac{90 - f'_c}{100} \right)^4 \leq 3.5 \quad (2.3)$$

Based on this, the compressive stress in the concrete, $f_{c,i}$, can be related to the compressive strain in the concrete, $\varepsilon_{c,i}$, at a depth of i , using the following equation,

$$f_{c,i} = \begin{cases} E_c \cdot \varepsilon_{c,i} & \text{if } \varepsilon_{c,i} < \varepsilon_{c,p} \\ f'_c & \text{if } \varepsilon_{c,p} \leq \varepsilon_{c,i} < \varepsilon_{c,u} \\ 0 & \text{if } \varepsilon_{c,i} \geq \varepsilon_{c,u} \end{cases} \quad (2.4)$$

Alternatively, the constitutive material model developed by Popovics (1973) can be used to model both the pre-peak and post-peak response of concrete in compression. The relationship between the compressive stress and strain in concrete is defined as,

$$f_{c,i} = f'_c \left(\frac{\varepsilon}{\varepsilon_o} \right) \left(\frac{n}{n - 1 + (\varepsilon/\varepsilon_o)^n} \right) < 0 \quad (2.5)$$

where n is an empirically developed factor that is defined for normal strength concrete as,

$$n = (0.058 \cdot f'_c) + 1.0 \quad (2.6)$$

If a uniaxial compressive stress is applied to concrete, it will expand outwards in the out-of-plane direction, perpendicular to the applied compression. If stirrups are provided in a beam, this out-of-plane expansion will be limited. The resulting confinement increases the compressive stress and strain capacity of the concrete within the confined core. Therefore, accurately predicting the behaviour of confined concrete will improve the predicted response of a reinforced concrete beam. The influence of confinement on the σ - ε response of concrete in compression is presented in Figure 2.4. Confining concrete increases the peak compressive stress, and allows the concrete to maintain higher magnitudes of stress after peak strain.

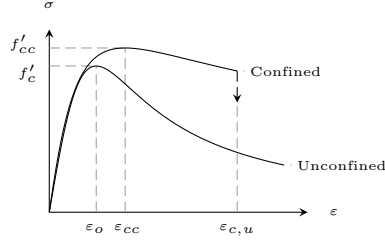


Figure 2.4: Influence of confinement on concrete in compression.

The influence of confinement on the σ - ε response of concrete can be quantified using the procedure developed by Mander, Priestley, and Park (1988). Based on this model, the compressive stress of confined concrete can be defined as,

$$f_c = \frac{f'_{cc} x r}{r - 1 + x^r} \quad (2.7)$$

where f'_{cc} is the peak compressive strength defined based on the geometry of the confined core and the amount of confining reinforcement, x is based on the ratio of the peak compressive strain in the unconfined and confined concrete, and r is based on the tangent and secant stiffness of the concrete. The increased peak strain in the confined concrete, ε_{cc} , is defined as,

$$\varepsilon_{cc} = \varepsilon_o \left[1 + 5 \left(\frac{f'_{cc}}{f'_c} - 1 \right) \right] \quad (2.8)$$

where ε_o is the peak strain in the unconfined concrete. The details regarding this formulation are presented in Appendix B.

2.2.2 Steel Reinforcement Material Model

The constitutive material model used for steel reinforcement is based on the model developed by Mander (1983). The σ - ε response of reinforcement is illustrated in Figure 2.5, and defines the response for both tension and compression.

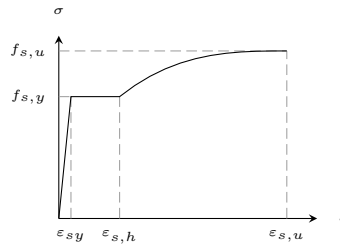


Figure 2.5: Constitutive material model of steel reinforcement.

Prior to yield, the stiffness of the reinforcement is equal to,

$$E_s = \frac{f_{s,y}}{\varepsilon_{s,y}} \quad (2.9)$$

where $f_{s,y}$ is the yield stress of the reinforcement, and $\varepsilon_{s,y}$ is the strain at the onset of yielding. After the reinforcement has yield, it remains perfectly plastic, defined as an increase in strain without an increase in stress. At a strain of $\varepsilon_{s,h}$, the reinforcement begins to strain-harden. Failure of the reinforcement is considered to occur when the strain in the reinforcement exceeds rupture strain, $\varepsilon_{s,u}$. Based on this response, the stress in the reinforcement is defined as,

$$f_s(i) = \begin{cases} E_s \cdot \varepsilon_s & \text{if } \varepsilon_s < \varepsilon_{s,y} \\ f_{s,y} & \text{if } \varepsilon_{s,y} \leq \varepsilon_s < \varepsilon_{s,h} \\ f_{s,u} + (f_{s,y} + f_{s,u}) \left(\frac{\varepsilon_{s,u} - \varepsilon_s}{\varepsilon_{s,u} - \varepsilon_{s,h}} \right)^P & \text{if } \varepsilon_{s,h} \leq \varepsilon_s < \varepsilon_{s,u} \end{cases} \quad (2.10)$$

where $f_{s,u}$ is the ultimate stress in the reinforcement. The strain-hardening power, P , is defined as,

$$P = E_{sh} \left(\frac{\varepsilon_{s,u} - \varepsilon_{s,h}}{f_{s,u} - f_{s,y}} \right) \quad (2.11)$$

where E_{sh} is the strain hardening modulus. The strain hardening modulus is defined as,

$$E_{sh} = \begin{cases} 0.02 \cdot E_s & \text{for mild steel} \\ 0.05 \cdot E_s & \text{for high strength steel} \end{cases} \quad (2.12)$$

The importance of considering strain hardening is illustrated in the experiment conducted by Mayer and Eligehausen (1998). In this experiment, a uniaxial tensile load was applied to a reinforced concrete rectangular prism. A single crack was formed at the middle of each specimen, prior to loading, to control the location where the reinforcement would first yield. To measure the distribution of strain near the crack, strain gauges were installed on the longitudinal reinforcement at various distances from the preformed crack. The measured strains throughout the specimen are presented in Figure 2.6.

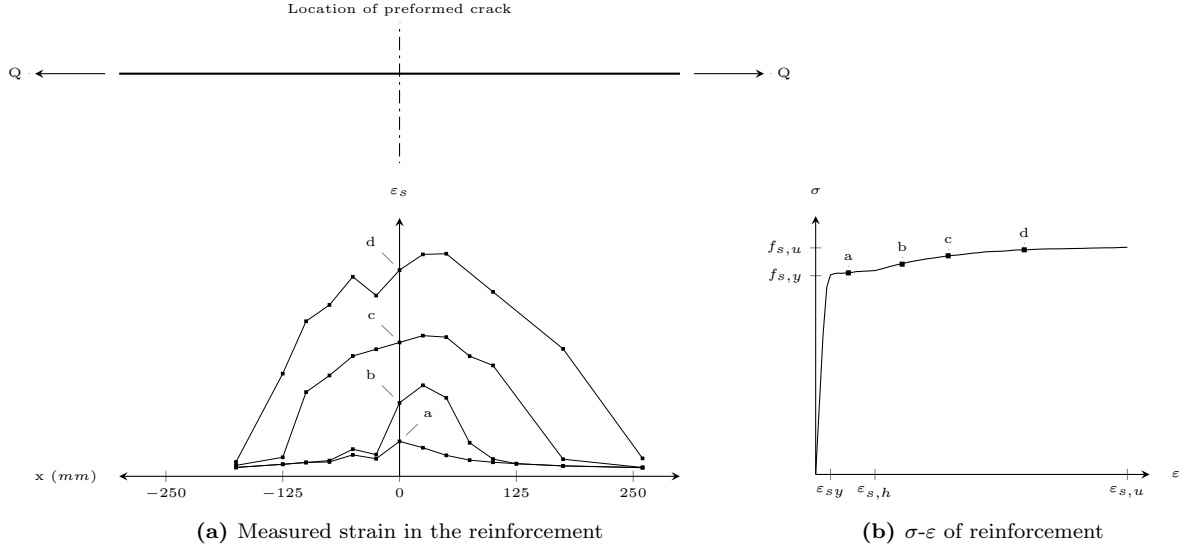


Figure 2.6: Concentration of strain at a crack, adapted from Mayer (1998).

At point a , the reinforcement has yield, causing the strain in the reinforcement to concentrate near the crack. As the strain increases from point a to b , the peak strain increases without significantly increasing the length over which the reinforcement has yield. However as the strain in the steel increases from b to c , the reinforcement undergoes strain hardening which allows the yielding of the reinforcement to spread out from the crack. Increasing the strain from c to d further increases this spreading. This experiment highlights the importance of accounting for strain hardening in reinforcement, particularly in a beam where the reinforcement is expected to develop large inelastic strains.

2.3 Compatibility Conditions

A fully rigid support condition can be defined using the following compatibility conditions,

1. No lateral expansion of the beam at a support.
2. No rotation of the beam at a support.

The influence of these compatibility conditions on the behaviour of a reinforced concrete beam can be understood by first considering a beam with simple supports, as illustrated in Figure 2.7a. When a vertical load Q is applied at midspan, the ends of the beam will both rotate about the support, θ_o , and displace laterally, δ_o . The first condition of compatibility can be met by applying a horizontal force, H , at each end of the beam. The magnitude of the horizontal force will depend on the magnitude of the lateral outward displacement of the beam. As this outward displacement increases, a larger force is required to maintain the first compatibility condition. The second condition of compatibility can be met by applying a negative bending moment, M_o , at both ends of the beam. The magnitude of this bending moment is governed by the amount of rotation at the support. To simultaneously provide rotational and lateral restraint, the interaction between these two conditions must be considered, as illustrated in Figure 2.7b.

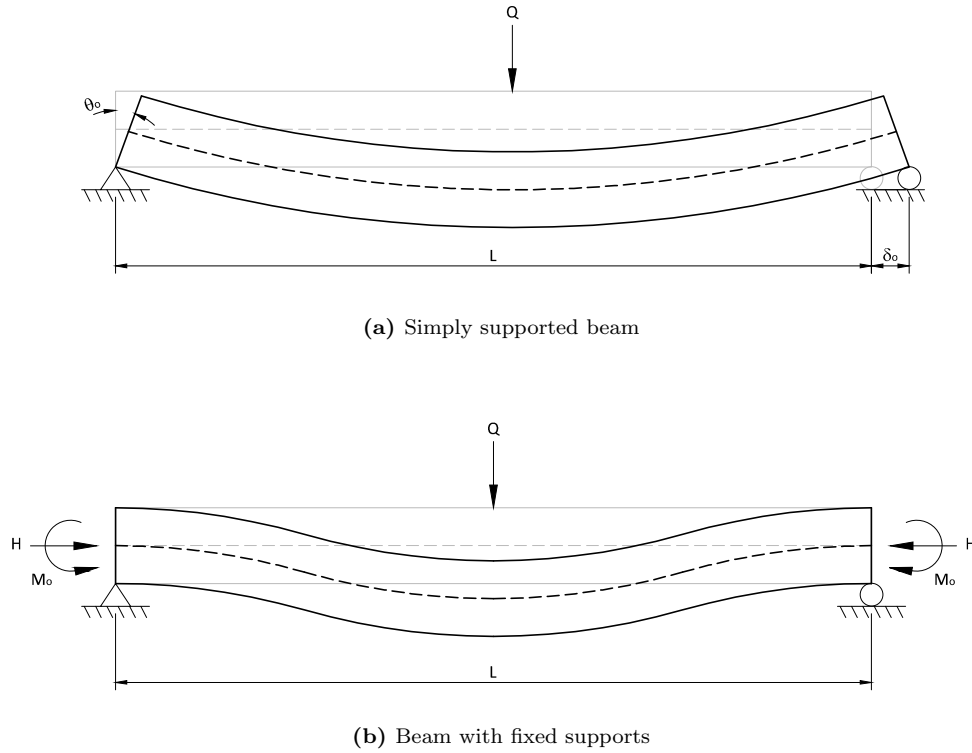


Figure 2.7: Influence of lateral and rotational restraint on beam deformation.

The total deflection of a beam at any point along its length, w_t , is defined as the vertical distance between the centroidal axis of the undeformed and deformed beam. When a beam is undeformed, the chord length of the centroidal axis, $L_{c,ce}$, and the arc length of the centroidal axis, $L_{a,ce}$, are both equal to the undeformed length of the beam, L . If some load is applied to a beam, the fixed supports prevent lateral expansion, resulting in a net-zero change in the chord length of the centroid. However, the deformation of the beam causes an increase in the arc length of the centroid. In the model developed by Wu (2013), the arc length of the centroid is always assumed to be equal to the chord length of the centroid. If the magnitude of the midspan deflection is small, ignoring this difference will have a minimal impact on the predicted response. As the magnitude of the deflection increases, the arc length of the centroid will deviate from the chord length of the centroid, resulting in the over-prediction of the axial compression force in the beam.

The proposed analytical method considers the difference between the arc and chord length caused by beam deformations. If a beam has infinitely rigid supports, the ratio between the chord length of the centroid, $L_{c,ce}$, and the arc length of the centroid, $L_{a,ce}$, will always be equal to the ratio of the undeformed length of the beam, L_o , and the arc length of the deflected shape, L_w . The equality of these two ratios, illustrated in Figure 2.8, is defined as,

$$\frac{L_{c,ce}}{L_{a,ce}} = \frac{L}{L_w} \quad (2.13)$$

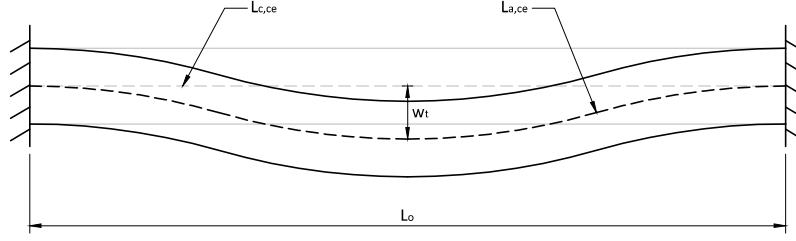


Figure 2.8: Ratio of arc length to chord length of the centroidal axis.

The relationship between the chord and arc length, defined here along the centroid, can also be used to define the chord and arc length at the top and bottom of a beam. The arc length of the deflected shape can be determined using the following equation,

$$\begin{aligned}
 L_w &= \int_0^L \sqrt{1 + \left(\frac{dw_t}{dx} \right)^2} \\
 &= \sum_{i=2}^n \sqrt{(w_t(i) - w_t(i-1))^2 + (x(i) - x(i-1))^2}
 \end{aligned} \tag{2.14}$$

where n is the total number of sections in the beam, and x is the horizontal distance between section i and the support. The deflected shape of a restrained beam is illustrated in Figure 2.9. The ideal number of sections defined for each beam is discussed in Section 2.10.

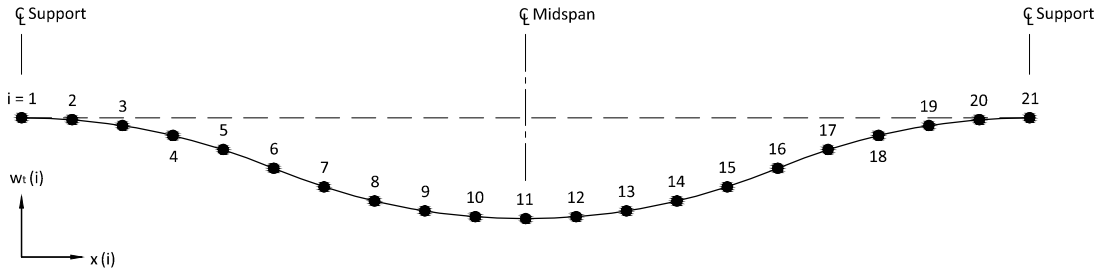


Figure 2.9: Numerical integration used to calculate the arc length of the deflected shape.

The arc length of the centroidal axis can be calculated by integrating the strains at the centroid of each section, along the length of the beam. This integration can be conducted using the trapezoidal rule, defined as,

$$\begin{aligned}
L_{a,ce} &= L + \int_0^L \varepsilon_{ce} dx \\
&= L + \sum_{i=2}^n \left(\frac{\varepsilon_{ce}(i) + \varepsilon_{ce}(i-1)}{2} \right) (x(i) - x(i-1))
\end{aligned} \tag{2.15}$$

The trapezoidal rule used for this calculation is illustrated in Figure 2.10.

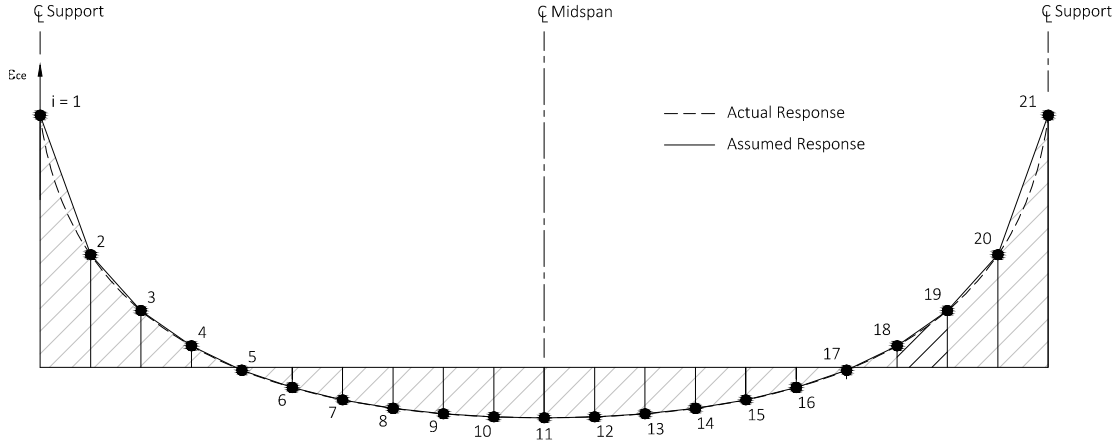


Figure 2.10: Trapezoidal rule used to calculate the arc length of the centroidal axis.

The two compatibility conditions required to provide fully fixed end supports can be formulated as,

1. No lateral expansion at the supports:

$$L_{c,ce} = L \tag{2.16}$$

2. No rotation at the supports:

$$\int_0^L \varepsilon_t = \int_0^L \varepsilon_b \tag{2.17}$$

where ε_t is the strain along the top of a beam, and ε_b is the strain along the bottom of a beam.

The first compatibility condition requires that the chord length of the centroidal axis be equal to the undeformed length of the beam, preventing lateral expansion at the supports. The second compatibility condition requires that the integral of the strains along the top and bottom of the beam be equal, preventing any rotation at the ends of the beam. Alternatively, the second compatibility condition can be met by calculating the rotation of the ends of the beam using the moment area method, which is discussed in Section 2.5.

2.4 Equilibrium Requirements

The proposed analytical model requires that the following equilibrium conditions be maintained,

1. The sum of the forces in the x-axis, defined along the length of a beam, must be equal to zero.

$$\sum F_x = 0 \quad (2.18)$$

2. The sum of the forces in the y-axis, defined along the depth of a beam, must be equal to zero.

$$\sum F_y = 0 \quad (2.19)$$

3. The sum of the bending moments at every section in a beam must be equal to zero.

$$\sum M = 0 \quad (2.20)$$

2.5 Sectional Analysis

The proposed analytical model is formulated based on a sectional analysis approach. This approach requires that the response of a given beam be considered at a number of sections taken along the length of the beam, as illustrated in Figure 2.11.

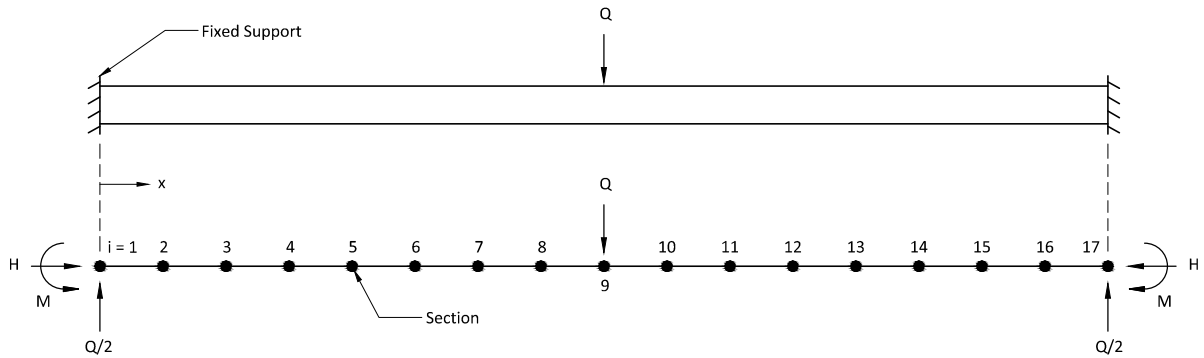


Figure 2.11: Sections considered throughout a beam with a concentrated load.

A layered analysis approach is used to relate the total bending moment and axial compression force at each section to the curvature. The curvature provides information regarding the deformation of a beam. Increasing the number of sections in a beam increases accuracy but reduces the speed and efficiency of

the analysis. Therefore, an optimal arrangement and number of sections is suggested in Section 2.10, based on the results of a numerical optimization study.

In this section, the sectional analysis approach adopted in the proposed analytical model is outlined. First, the total bending moment in a beam is determined by considering the applied load, support conditions and second-order effects. Following this, an iterative layered analysis approach is proposed to relate the bending moment and axial force resultant to the strain profile at each section. This provides a rational basis for determining the stress in both the concrete and reinforcement throughout a beam. The layered analysis approach is then used to develop a family of moment-curvature diagrams with varying magnitudes of axial compression. These diagrams provide insight into the influence of the axial compression force on the response at each section. Finally, the method for determining the deformation of a beam is discussed.

2.5.1 Bending Moment

The first step in conducting a sectional analysis is determining the total bending moment at each section, M_t . The total bending moment is comprised of three components. The first component is the bending moment due to the applied loading, M_Q , which defines the statically determinate primary system. For a beam with a concentrated load applied at midspan, the peak bending moment is defined as,

$$M_Q = \frac{QL}{4} \quad (2.21)$$

The second component is the negative bending moment applied at the supports, M_o , which is based on the compatibility conditions presented earlier in this chapter. The magnitude of this bending moment is initially unknown, and must be determined through an iterative procedure, which will be discussed later in this chapter.

The third component is the bending moment due to second-order effects, M_w . The magnitude of this bending moment, which is the only non-linear component, is dependent on both the deflected shape, w_t , and the lateral restraint force, H .

$$M_w = H \cdot w_t \quad (2.22)$$

The first-order bending moment in a beam is defined as,

$$M_{t_o} = M_Q + M_o \quad (2.23)$$

In the model developed by Wu (2013), the total bending moment in a given beam is equal to the first-order bending moment. The proposed analytical method considers the influence of second-order effects. Therefore, the total bending moment in a given beam, accounting for second-order effects, is defined as,

$$M_t = M_Q + M_o + M_w \quad (2.24)$$

The first-order and second-order bending moment of beam D5-R from the parametric study conducted in Section 5.3, is presented in Figure 2.12. This response indicates that when the second-order bending moment is large, relative to the total bending moment in a beam, then consideration of second-order effects increases the accuracy of the predicted response. Therefore, the proposed analytical model considers the second-order bending moment, M_t , in a beam. The influence of second-order effects is discussed in detail in Section 5.3.

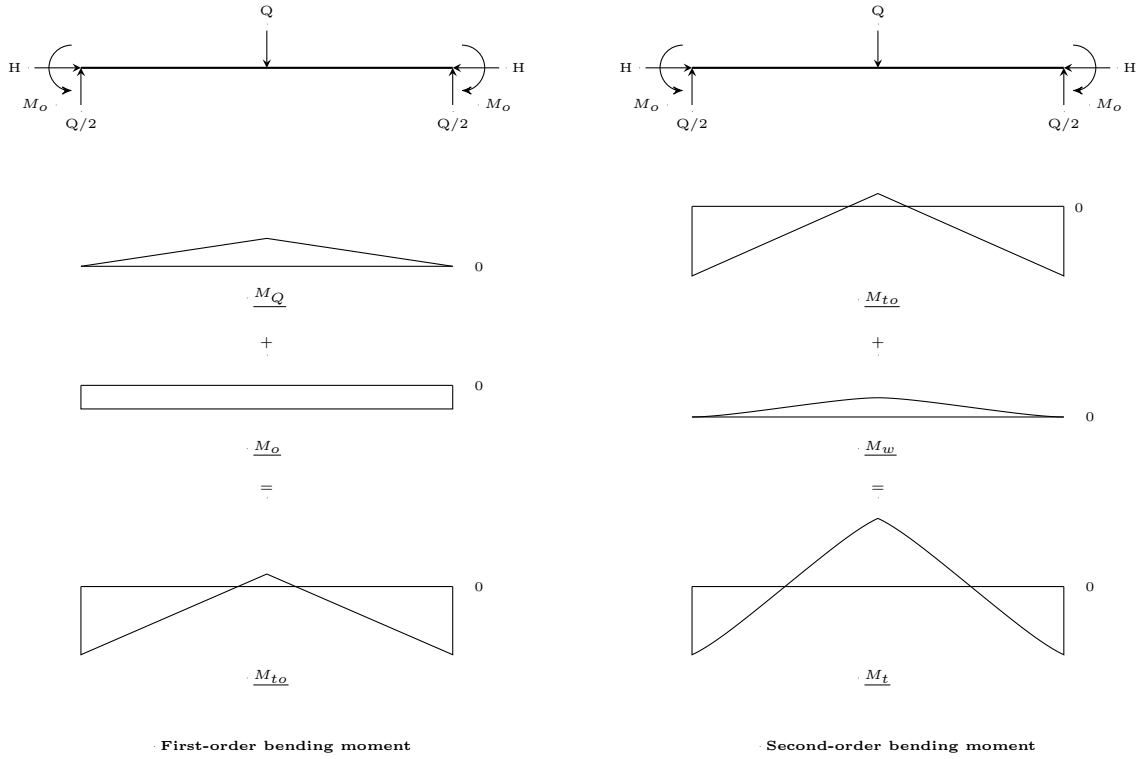


Figure 2.12: Components of first-order and second-order bending moment.

2.5.2 Layered Analysis

If the total bending moment and axial force at a section is known, then a layered analysis approach can be used to determine the strain profile at each section. This approach is predicated on the assumption that plane sections remain plane. Using this assumption, the strain throughout the depth of each section can be determined by defining the strain at the top and bottom, as illustrated in Figure 2.13. The strain profile at each section can be used in conjunction with the defined constitutive material models to determine the stress and force resultant in each material.

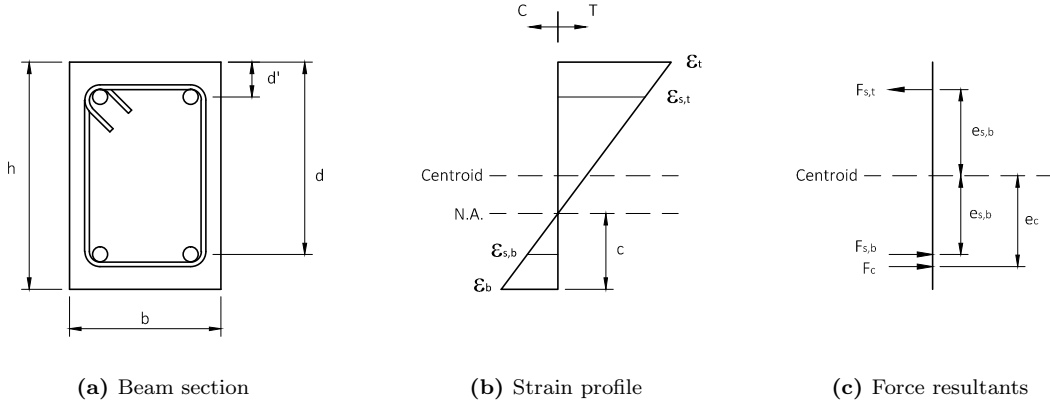


Figure 2.13: Sectional forces derived from a plane of strain.

The depth of compression in the concrete, c , is equal to the distance between the neutral axis and the extreme compression fiber. The compressive force resultant in the concrete can be calculated by integrating the compressive stresses along the depth of this compression zone. If the stress profile is nonlinear, a numerical integration approach can be defined as,

$$\begin{aligned}
 F_c &= b \cdot \int_0^c f_{c,i} dy \\
 &= b \cdot \sum_{i=1}^n f_{c,i} h_i
 \end{aligned} \tag{2.25}$$

where $f_c(i)$ is the stress in layer i , n is the total number of layers in the compression zone, h_i is the height of each layer, and b is the width of the beam. The eccentricity of the compressive force resultant, defined as the distance between the compressive force resultant and the centroid of the section, is defined as,

$$e_c = \frac{\sum_{i=1}^n f_{c,i} y_i}{\sum_{i=1}^n f_{c,i}} \tag{2.26}$$

where y_i is the distance between the center of layer i and the centroid. The layered analysis approach, used to determine F_c and e_c , is illustrated in Figure 2.14.

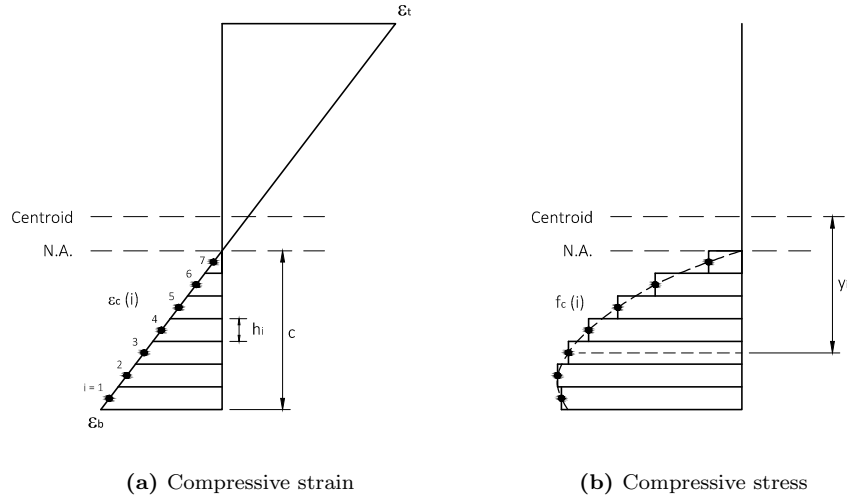


Figure 2.14: Numerical integration of compressive stress in concrete.

In a layered analysis approach, increasing the number of layers improves the accuracy of the analysis but also increases the required computational effort. Therefore, an optimized number of layers is suggested in Section 2.10, based on the results of a sensitivity study.

The force resultant in each layer of reinforcement, F_s , is defined as

$$F_s = f_s A_s \quad (2.27)$$

where f_s is the stress in the layer of reinforcement, and A_s is the total cross sectional area of the reinforcement. The eccentricity of the force resultant in the reinforcement, e_s , is equal to the vertical distance from the steel reinforcement to the centroid of the section.

The axial resultant at a section is defined as,

$$H_n = F_c + \sum F_s \quad (2.28)$$

The bending moment at a section is defined as,

$$M_n = (F_c e_c) + \sum (F_s e_s) \quad (2.29)$$

In the proposed analytical model, the strain profile corresponding to the total bending moment, M_t and axial force, H , can be determined using the iterative approach presented in Figure 2.15.

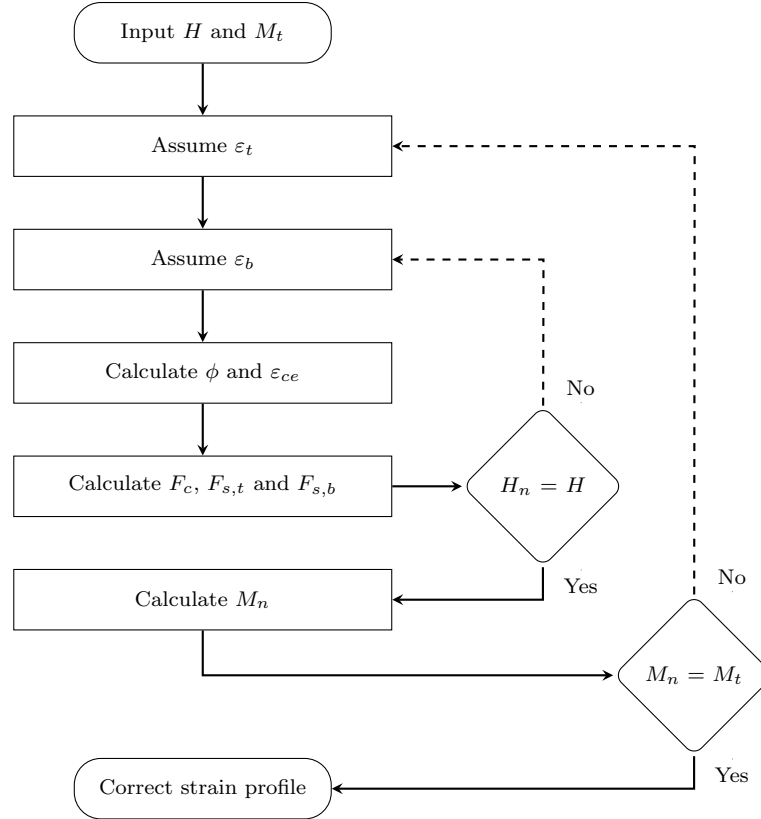


Figure 2.15: Proposed procedure for conducting a layered analysis.

This approach first requires that the strain at the top and bottom of a section be assumed. Using this strain profile, the force resultant and eccentricity in each material is calculated using the layered analysis approach. Following this, the axial force and bending moment at each section are calculated. The assumed bottom strain is adjusted until the axial force, H_n , is equal to the global axial force in the beam, H . Similarly, the assumed top strain is adjusted until the bending moment at each section, M_n , is equal to the global bending moment in the beam, M_t . The deformation of each beam is based on the strain profile at each section, which can be defined based on curvature, ϕ , and the centroidal strain, ε_{ce} .

2.5.3 Moment-Curvature Relation

The influence of axial compression on the moment-curvature response of a beam can be understood by considering the response of the beam with properties summarized in Figure 2.16.

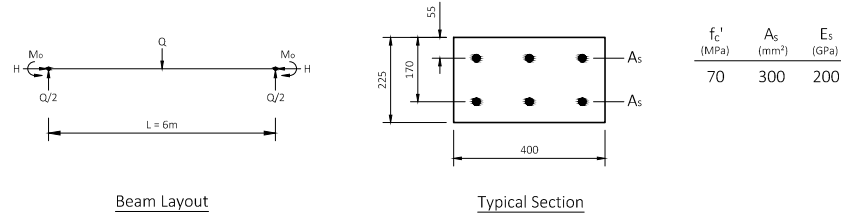
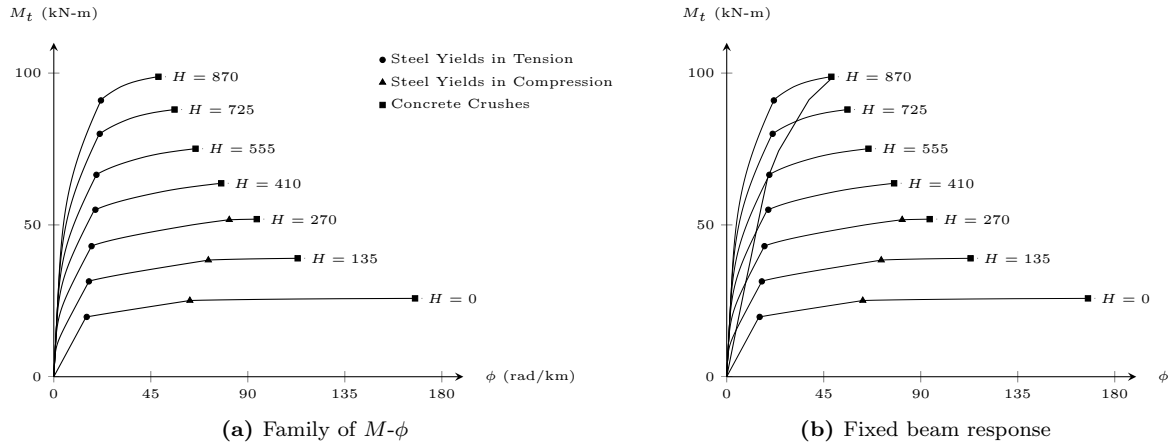


Figure 2.16: Beam properties for the moment-curvature example.

A family of moment-curvature responses can be developed by varying the magnitude of axial compression in the beam, as illustrated in Figure 2.17a. Since the reinforcement is the same at the top and bottom of the beam, the relationship for negative bending will be equivalent to that of positive bending. Increasing the magnitude of axial compression in the beam increases stiffness and capacity, and reduces the peak curvature.

Figure 2.17: Moment-curvature response with varying H , adapted from Wu (2013).

In a restrained beam, the axial compression force is a reaction to the applied load. As a result, the magnitude of axial compression will increase in conjunction with increasing bending moment, as illustrated in Figure 2.17b. Initially, there is no axial compression in the beam, causing cracking to occur immediately. Cracking causes the mobilization of the axial compression force, which allows the response to jump from one moment-curvature response to the next. For this beam, failure is caused by crushing of the concrete. Therefore, as indicated by Wu (2013), a family of moment-curvature responses can be derived to provide insight into the influence of axial compression on the response of a reinforced concrete beam or slab strip.

2.5.4 Beam Deformation

If the bending moment and axial compression at a section is known, a layered analysis approach can be used to determine the corresponding strain profile. The moment-curvature response, developed in the previous section, can be used to relate the bending moment to the curvature at every section in a

beam. This is illustrated in Figure 2.18 for the failure load of the sample beam presented in the previous section, where $H = 870$ kN.

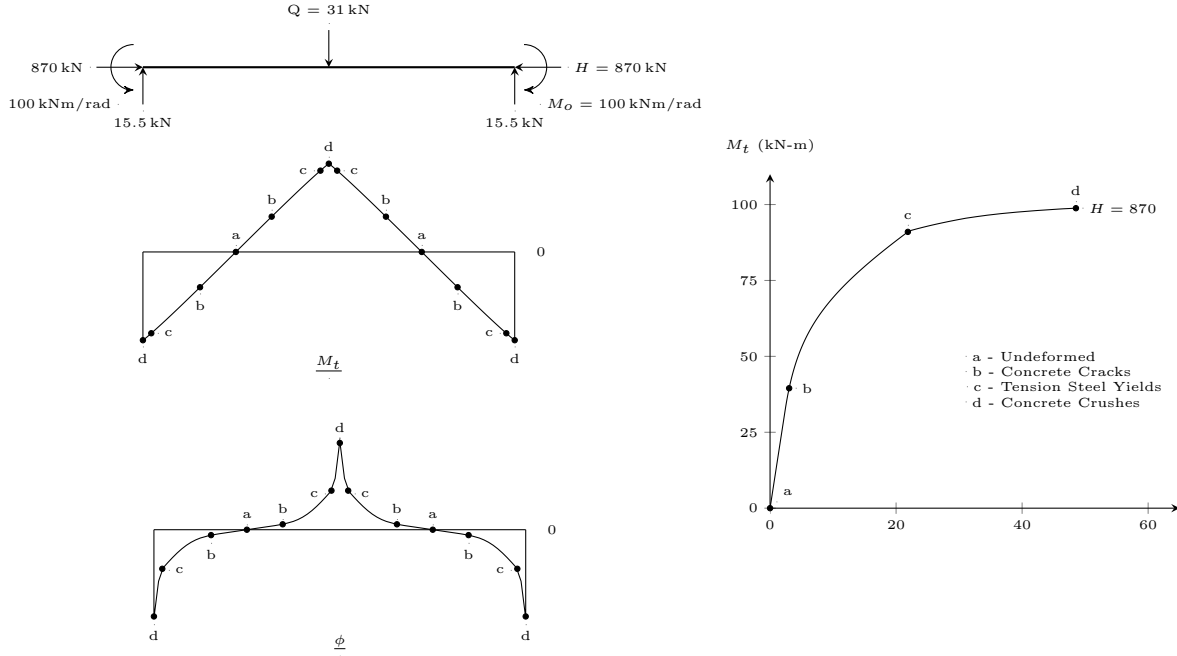


Figure 2.18: Bending moment and curvature in a restrained beam, at Q_{peak} .

Four significant points are labeled in the beam presented in Figure 2.18 to illustrate the influence of cracking, yielding and crushing on the curvature in a restrained beam. At sections where the concrete is uncracked, between points a and b , the magnitude of curvature is relatively small, and will have little impact on the deformation of the beam. In regions where cracking has occurred, between points b and c , the magnitude of curvature increases relative to the uncracked region, causing larger deformations in the beam. Finally, in regions where the reinforcement has yielded, between points c and d , the curvature drastically increases causing significant deformations to occur.

The deflection of a given beam can be determined based on the curvature diagram presented in Figure 2.18 using the moment area theorem. For reference, a detailed explanation of the moment area theorem is included in Appendix B. The midspan deflection of a beam can be calculated as,

$$w_{t,max} = \sum_{i=1}^{n-1} \left(\frac{\phi(i) + \phi(i+1)}{2} \right) \left(x(i+1) - x(i) \right) \left(\left(\frac{x(i+1) + x(i)}{2} \right) \right) \quad (2.30)$$

where n is the total number of sections, ϕ is the curvature at each section, and x is the distance from each section to the support. Similarly, the magnitude of deflection at each section can be calculated as,

$$w_{t,m} = w_{t,max} + \sum_{i=m}^{n-1} \left(\frac{\phi(i) + \phi(i+1)}{2} \right) \left(x(i+1) - x(i) \right) \left(\left(\frac{x(i+1) + x(i)}{2} \right) - x(m) \right) \quad (2.31)$$

where m is the section under consideration. The moment area theorem can also be used to determine the rotation of a beam at the support, θ , which can be used to satisfy the second compatibility condition presented in Section 2.3. This rotation can be calculated as,

$$\theta_o = \sum_{i=1}^{n-1} \left(\frac{\phi(i) + \phi(i+1)}{2} \right) (x(i+1) - x(i)) \quad (2.32)$$

2.6 Second-Order Effects

The analytical model developed by Wu (2013) does not account for the second-order effects that can occur in laterally restrained reinforced concrete beams. For the proposed analytical model, the bending moment due to second-order effects is defined as,

$$M_w = H \cdot w_t \quad (2.33)$$

where H is the axial force in the beam, and w_t is the deflection of the beam at each section. When the magnitude of M_w is small relative to the total bending moment, consideration of second-order effects will have a minimal impact on the response of a beam. However as the magnitude of M_w increases relative to the total bending moment, the influence of second-order effects increases.

An exact second-order analysis, assuming linear and elastic material properties, requires the solution of a fourth-order differential equation (Menn, 1990). According to Menn (1990), if material nonlinearities are considered and the flexural stiffness of the column is not constant, then solving the differential equation becomes complex and impractical. Therefore, an approximate method of calculation, called Vianello's Method, can be used to predict the response of either statically determinate or indeterminate columns with variable flexural stiffness. However, this formulation is based on the assumption that the axial load is equal to the applied load, Q , as illustrated in 2.19a. For the case of a laterally restrained beam, the axial load is a reaction of the applied load, as illustrated in Figure 2.19b. Therefore, Vianello's method cannot be incorporated into the proposed analytical model to account for second-order effects.

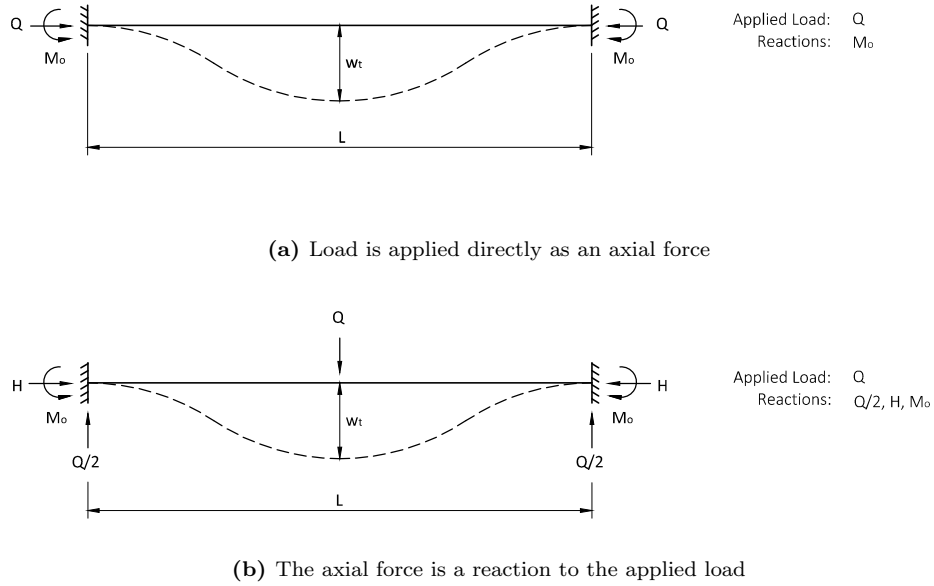


Figure 2.19: Axial compression in a column vs. a laterally restrained beam.

Alternatively, second-order effects can be incorporated into the proposed analytical method using an iterative approach. This procedure is summarized in the following steps:

1. Assume an initial deflected shape, w_o .
2. Determine the total bending moment at each section, accounting for M_w .
3. Calculate the deflected shape, w_t , based on the moment-curvature relation at each section.
4. If $w_t \neq w_o$, return to Step 1 and set $w_o = w_t$.
5. If $w_t \approx w_o$, within a tolerance of $\pm 1\%$, then the correct solution is attained.

The number of iterations required to determine the second-order deflected shape of the beam is dependent on the relative influence of the second-order bending moment on the response. If the magnitude of M_w is small relative to the total bending moment, then few iterations are required. As the magnitude of M_w increases relative to the total bending moment, then the number of iterations required to converge the deflected shape increases.

2.7 Proposed Analytical Procedure

This section summarizes the procedure used for the proposed analytical model, which can be adapted for use with various configurations of applied loading. The supports are assumed to be infinitely rigid, preventing any rotation or lateral displacement of the beam at the supports. The proposed analytical model can be used to determine the complete load-deflection and load-restraint response of a restrained

beam with a monotonically increasing applied load. Alternatively, the procedure can be used to determine the response of a given beam at any load stage, without consideration of the previous load stages. However, the number of iterations required to converge each of the three levels of iteration can be reduced by better predicting the initial deflected shape, w_o , the bending moment at the support, M_o , and the lateral restraint force, H . These initial predictions can be based on either a previous load stage, or a previous iteration conducted for the current load stage.

The procedure requires the convergence of three levels of iterations:

Iteration # 1: Determine w_o , such that $w_o \approx w_t$, within a tolerance of $\pm 1\%$.

Iteration # 2: Determine M_o , such that $\theta_o \approx 0$, within a tolerance of $\pm 1\%$.

Iteration # 3: Determine H , such that $L_{c,ce} \approx L$, within a tolerance of $\pm 1\%$.

The required inputs for the analytical formulation include:

Applied loads: Q , H and M_o

Beam geometry: L , h , b , d , d' and w_o

Material properties: f'_c , f_y , f_u , ε_s , ε_y , ε_{sh} , ε_{su} , A_s , A'_s

The procedure for determining the response of a restrained beam, using the proposed analytical formulation, is summarized below for a monotonically increasing load Q :

1. Assume an initial deflected shape, $w_o(x)$.
2. Assume an end restraint moment, M_o .
3. Assume a lateral restraint load, H .
4. Calculate the bending moment of the statically determinate, primary system, $M_Q(x)$.
5. Calculate the bending moment due to geometric nonlinearities, $M_w(x)$, defined as,

$$M_w(x) = H \cdot w_o(x) \quad (2.34)$$

6. Calculate the total bending moment in the system, $M_t(x)$, defined as,

$$M_t(x) = M_Q(x) + M_o(x) + M_w(x) \quad (2.35)$$

7. Using a sectional analysis approach, determine the curvature, $\phi(x)$, at each section along the length of the beam.
8. Using moment area theorem, determine the vertical deflection, $w_t(x)$, of each section throughout the beam
9. Calculate the arc length of the deflected shape, L_w , defined as,

$$L_w = \sum_{i=2}^n \sqrt{(w_t(i) - w_t(i-1))^2 + (x(i) - x(i-1))^2} \quad (2.36)$$

10. Calculate the arc length of the centroidal axis, L_a , defined as,

$$L_{a,ce} = L_o + \sum_{i=2}^n \left(\frac{\varepsilon_{ce}(i) + \varepsilon_{ce}(i-1)}{2} \right) (x(i) - x(i-1)) \quad (2.37)$$

11. Calculate the chord length of the centroidal axis, $L_{c,ce}$, defined as,

$$L_{c,ce} = \frac{L_o}{L_w} L_{a,ce} \quad (2.38)$$

12. Check the assumed lateral restraint load, H , based on the first compatibility condition proposed in Section 2.3.

$$\text{If } \begin{cases} L_{c,ce} > L_o & \text{increase estimate of } H \text{ and return to Step 3} \\ L_{c,ce} < L_o & \text{reduce estimate of } H \text{ and return to Step 3} \\ L_{c,ce} \approx L_o & \text{estimate of } H \text{ is adequate, proceed to next step} \end{cases}$$

13. Calculate the rotation of the beam at the support, θ_o , defined as,

$$\theta_o = \sum_{i=1}^{n-1} \left(\frac{\phi(i) + \phi(i+1)}{2} \right) (x(i+1) - x(i)) \quad (2.39)$$

14. Check the assumed bending moment at each support, M_o , based on the second compatibility condition proposed in Section 2.3.

$$\text{If } \begin{cases} \theta_o > 0 & \text{increase estimate of } M_o \text{ and return to Step 2} \\ \theta_o < 0 & \text{reduce estimate of } M_o \text{ and return to Step 2} \\ \theta_o \approx 0 & \text{estimate of } M_o \text{ is adequate, proceed to next step} \end{cases}$$

15. Check the initially assumed deflected shape.

$$\text{If } \begin{cases} w_t \neq w_o & \text{set } w_o = w_t \text{ and return to Step 1} \\ w_t \approx w_o & \text{estimate of } w_o \text{ is adequate} \end{cases}$$

This procedure is summarized in the flow chart presented in Figure 2.20.

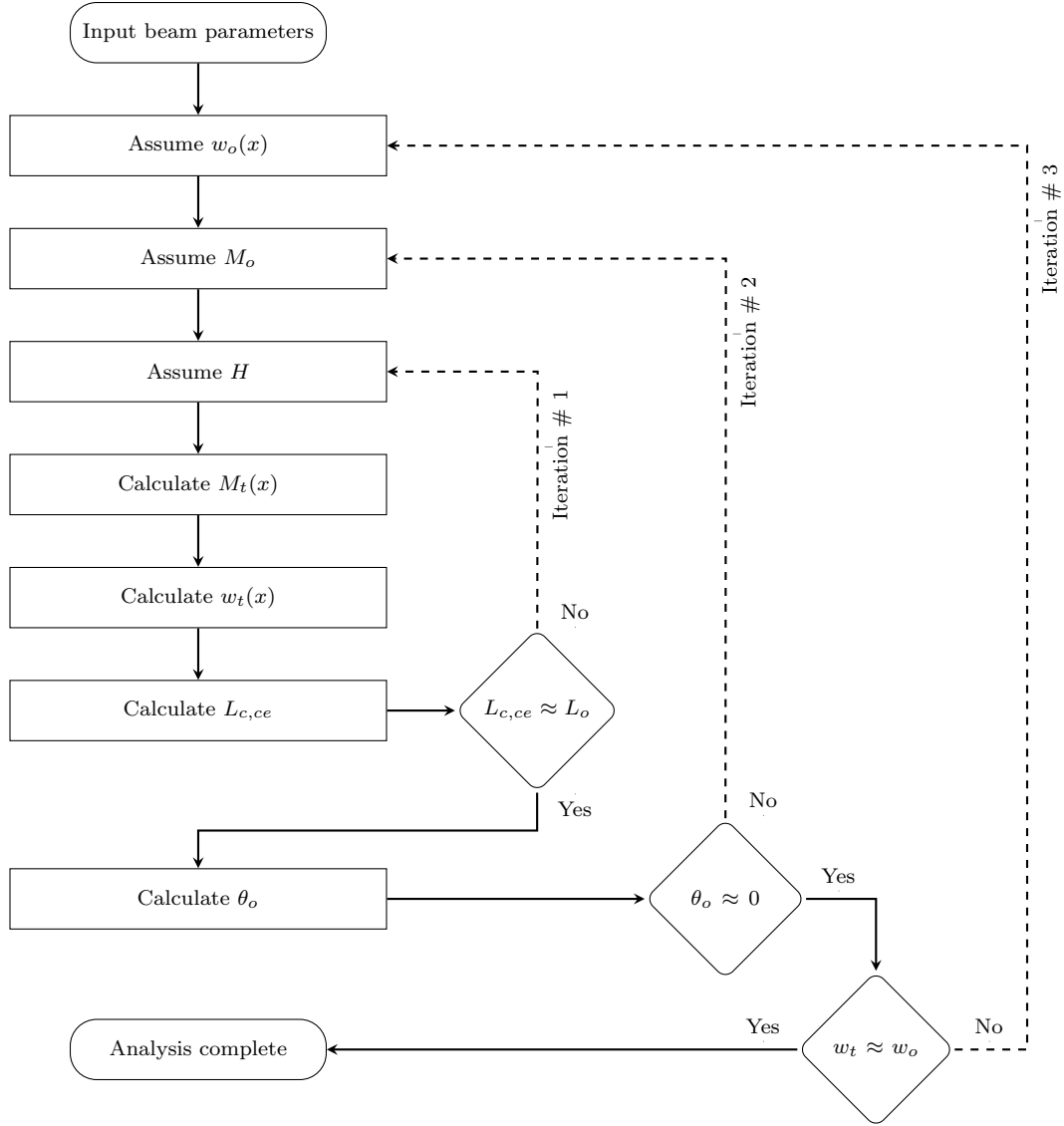


Figure 2.20: Proposed formulation for the analytical model.

2.8 Comparison of the Proposed Model to Wu (2013)

The analytical model proposed in this thesis is based on the model developed by Wu (2013). Both models use the plane sections hypothesis to determine the moment-curvature response for various magnitudes of axial compression developed as a result of the lateral restraint. The two major differences between the proposed analytical model and Wu's method are:

1. The arc and chord length along the centroid of a given beam.
 - (a) Wu: Assumes that the arc length along the centroidal axis, $L_{a,ce}$, is always equal to the chord length along the centroidal axis, $L_{c,ce}$.

- (b) Proposed: Assumes that vertical deflections cause the arc length along the centroidal axis, $L_{a,ce}$, to increase relative to the chord length along the centroidal axis, $L_{c,ce}$.
2. The second-order bending moment, M_w .
- (a) Wu: Does not account for the bending moment caused by second-order effects, $M_w = 0$.
- (b) Proposed: Accounts for the bending moment caused by second-order effects, $M_w = H \cdot w_t$.

To compare the response of the proposed model and Wu's model, the two beams with properties summarized in Figure 2.21 are considered. Both beams have the same cross-section and material properties. The only difference between these two beams is the span length, which is equal to 2 m in beam F1 and 6 m in beam F2. The σ - ε response of the concrete and steel reinforcement used in the analysis is included in Figure 2.21. The response of the steel reinforcement is shown up to a strain of 8 mm/m, as the maximum tensile strain in the reinforcement is too low to develop any strain hardening.

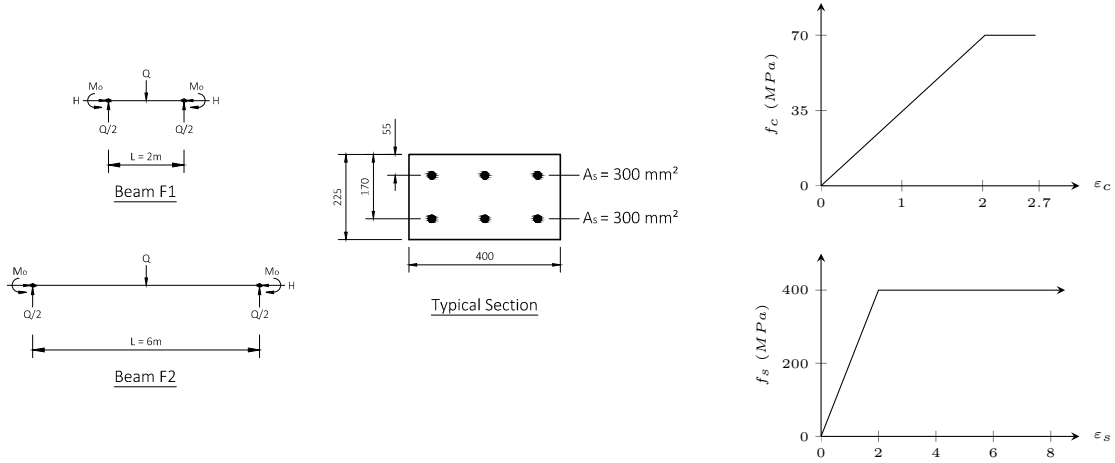


Figure 2.21: Beam properties for the comparison with Wu's model.

Each beam is labeled based on the type of analysis conducted, which include:

R: The analysis is conducted using the proposed analytical model.

W: The analysis is conducted using Wu's method.

U: The analysis is conducted without consideration of lateral restraint.

The applied load vs. midspan deflection response of beam F1, presented in Figure 2.22a, is developed using the proposed analytical method, Wu's method, and without consideration of lateral restraint. The capacity of beam F1-R, equal to 400 kN, is 1.02 times lower than the capacity of beam F1-W, equal to 406 kN. In addition, the peak midspan deflection of beam F1-R, equal to 3.2 mm, is equal to the peak midspan deflection of beam F1-W. For both beam F1-R and F1-W, accounting for lateral restraint increases the capacity of the beam by a factor of 3.9.

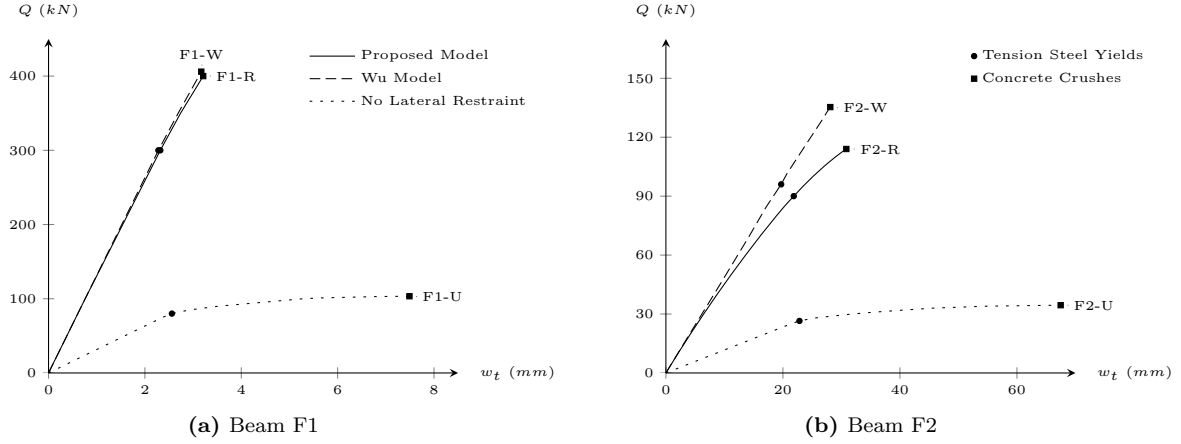


Figure 2.22: Load-deflection response of beams F1 and F2.

The applied load vs. midspan deflection of beam F2, developed using the proposed analytical model, Wu's method and without consideration of lateral restraint, is presented in Figure 2.22b. The capacity of beam F2-R, equal to 114 kN, is 1.2 times lower than the capacity of beam F2-W, equal to 135 kN. In addition, the peak midspan deflection of beam F2-R, equal to 31 mm, is 1.1 times higher than the peak midspan deflection of beam F1-W, equal to 28 mm. For beam F1-R accounting for lateral restraint increases the capacity of the beam by a factor of 3.3, while for beam F1-W, accounting for lateral restraint increases the capacity of the beam by a factor of 3.9.

The applied load vs. axial compression force of beam F1 and F2 is presented in Figure 2.23. The peak axial compression in beam F1-R, equal to 912 kN, is approximately equal to the peak axial compression in beam F1-W. In contrast, the peak axial compression in beam F2-R, equal to 872 kN, is 1.04 times smaller than the peak axial compression developed in beam F2-W, equal to 910 kN.

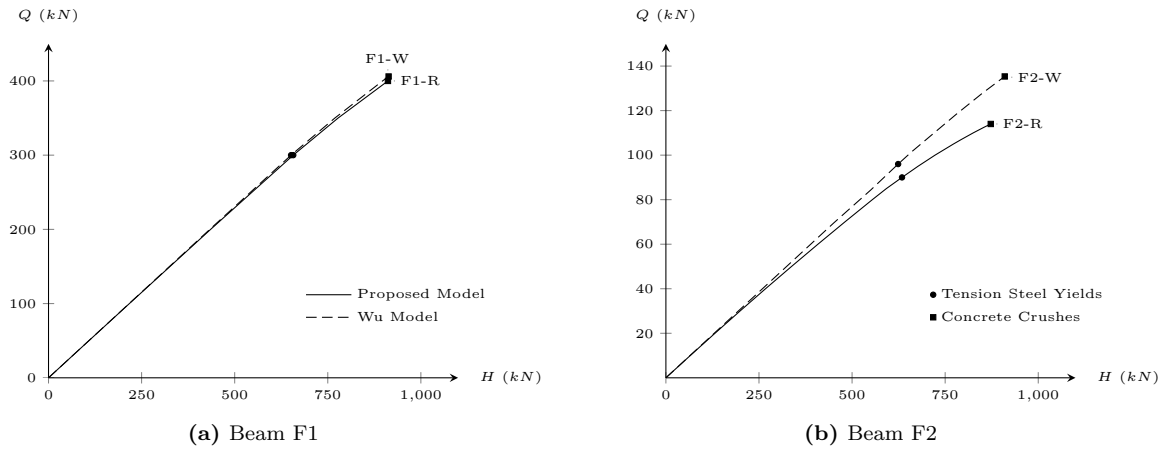


Figure 2.23: Load-restraint response of beams F1 and F2.

When considering Wu's method, varying the length of a given beam does not alter the axial compression developed at failure. In contrast, the proposed analytical model predicts that increasing the span length of the beam from 2 m to 6 m reduces the axial compression force by a factor of 1.05. In addition, Wu's

model predicts that increasing the span length from 2 m to 6 m reduces the capacity by a factor 3.0. However, the proposed analytical model predicts that increasing the undeformed length of the beam reduces the capacity by a factor of 3.5.

The influence of second-order effects on the predicted response of beams F1-R and F2-R can be understood by considering the bending moment response at each beam's respective peak applied load, presented in Figure 2.24. In beam F1-R, the bending moment due to second-order effects at midspan, equal to 3 kN m, is only three percent of the total bending moment at midspan, equal to 102 kN m. However in beam F2-R, the bending moment due to second-order effects at midspan, equal to 27 kN m, is 27 percent of the total bending moment at midspan, equal to 99 kN m. The increase in M_w , relative to M_t , increases the influence of second-order effects.

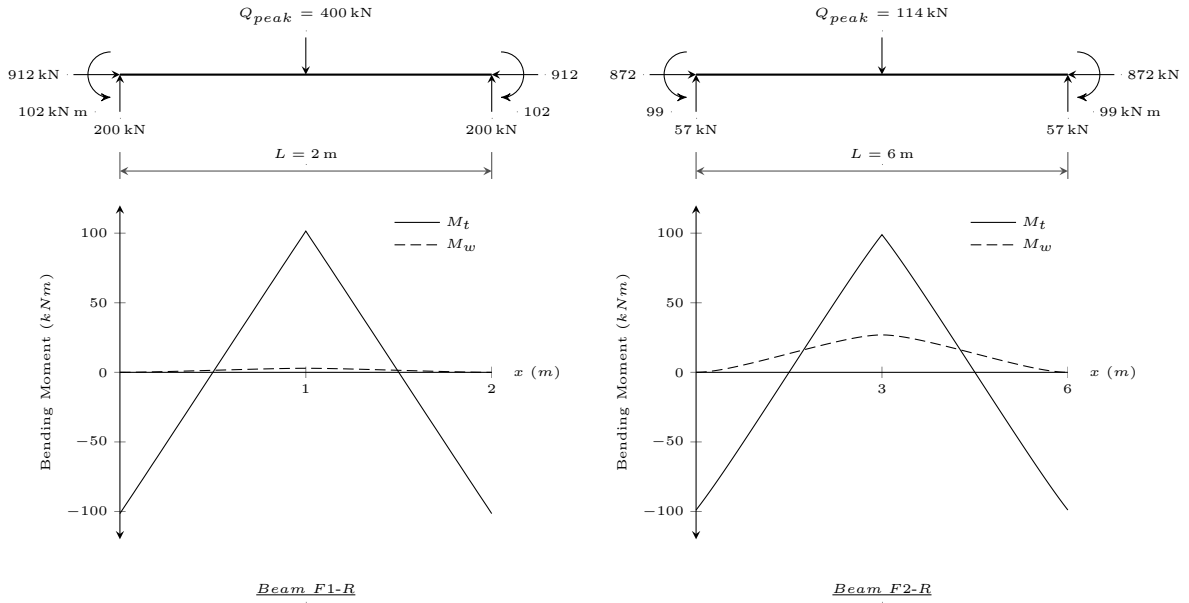


Figure 2.24: Comparison of M_t and M_w in beams F1 and F2, at Q_{peak} .

Based on the results of this analysis, the following conclusions can be made:

1. The model developed by Wu has a limited range of applicability, as it can only accurately predict the response of beams with minimal second-order effects.
2. The proposed analytical model, which directly accounts for second-order effects, can be used for the analysis of a wide range of beams, relative to Wu's model.
3. Accounting for second-order effects in a laterally restrained beam reduces capacity and increases the peak midspan deflection.

The importance of considering second-order effects is studied in Section 5.3 using a wider range of beams, providing additional insight into the capabilities of the proposed analytical method.

2.9 Softening due to Second-Order Effects

In the experiments conducted by Su, Tian, and Song (2009) and Yu and Tan (2013), the beam specimens exhibit a softening effect at relatively large magnitudes of deflection. This softening is caused by the second-order bending moment that develops in laterally restrained beams. For the majority of these beams, this softening causes a peak in the applied load to form prior to the failure of the specimen. In some cases, a second peak in the applied load occurs at a much larger deflection, which can occur after the axial force in the beam has transitioned from compression to tension. The response of these specimens is discussed in detail in Chapter 4.

The softening caused by second-order effects can be understood by considering the response of beam L1, with properties summarized in Figure 2.25. For this example, the concrete and steel reinforcement is assumed to remain linear elastic, as illustrated in the σ - ϵ response presented in Figure 2.25. Similar to the analysis conducted in the previous section, cracking is considered to occur when the concrete strain becomes tensile. The assumption of linear material properties isolates the influence of second-order effects from material nonlinearities.

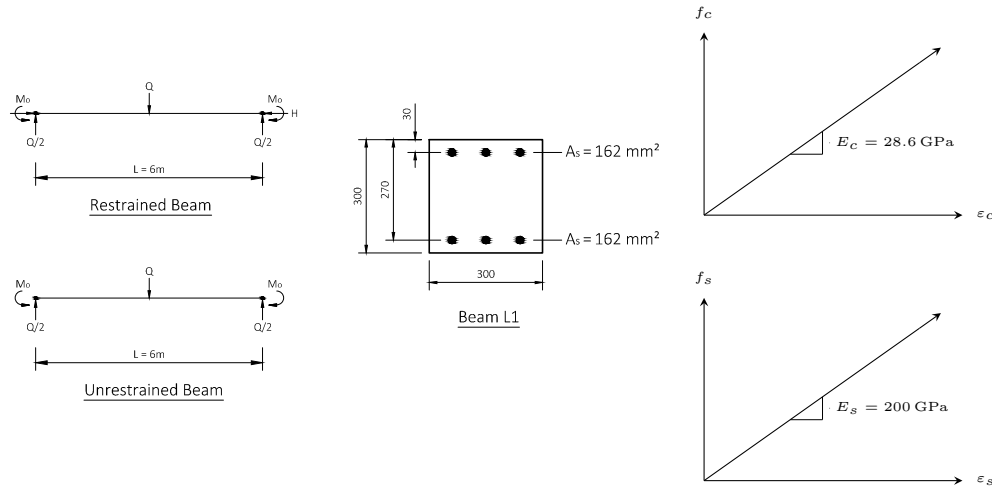


Figure 2.25: Beam properties for second-order effects example.

Beam L1 is labeled based on the type of analysis conducted:

R: The analysis is conducted using the proposed analytical model.

N: The analysis is conducted using the proposed analytical model, without considering second-order effects ($M_w = 0$).

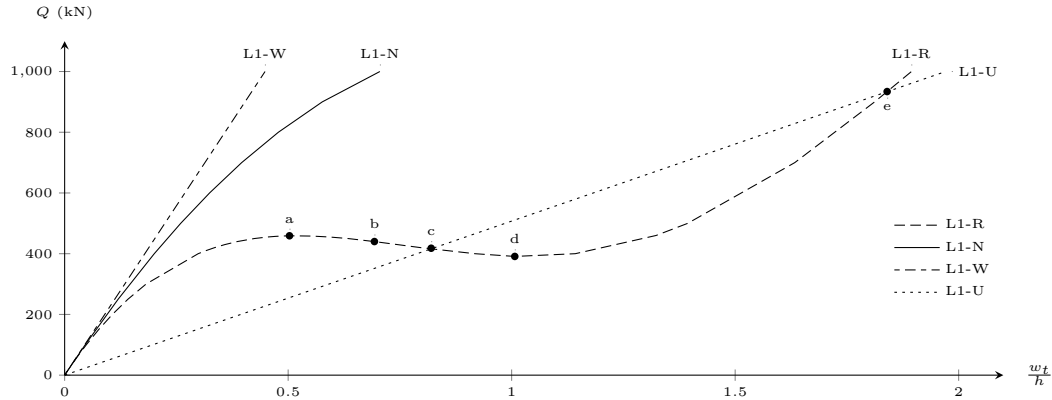
W: The analysis is conducted using Wu's method.

U: The analysis is conducted without consideration of lateral restraint.

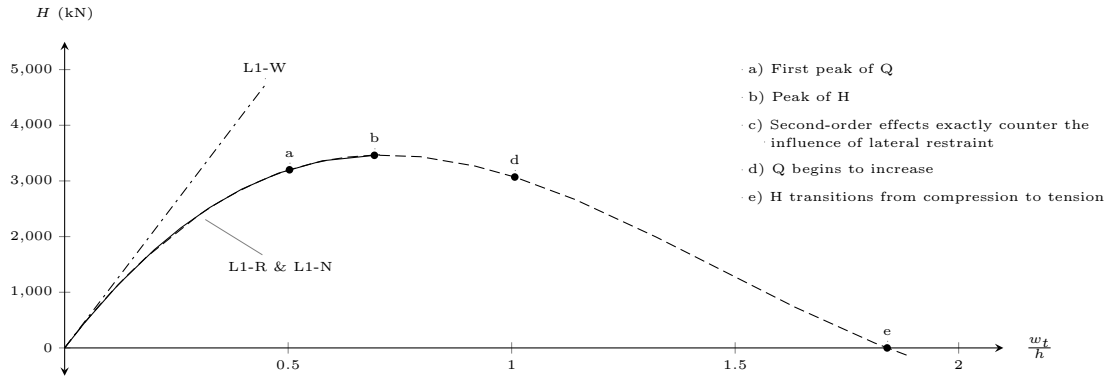
The applied load vs. midspan deflection of beam L1 is presented in Figure 2.26a, and the axial force vs. midspan deflection of beam L1 is presented in Figure 2.26b. The material linearity assumed in this analysis prevents the development of failure. Therefore, the analysis is conducted up to a maximum

load of 1000 kN. The response of beam L1-R, developed using the proposed analytical model, exhibits a softening in stiffness caused by second-order effects. This softening can be understood by considering four significant points in the response, described in Figure 2.26b. Based on the response of Beam L1-R, a number of observations can be made:

1. At point b, the peak axial compression force in beam L1-R corresponds with an inflection point in the load-deflection response.
2. At point c, the relationship between the applied load and deflection of beam L1-R is exactly equal to that of beam L1-U. This indicates that at point c, the reduction in load caused by second-order effects exactly counter acts the increased capacity caused by lateral restraint.
3. At point d, the applied load begins to increase in magnitude while the axial force in the beam is still in compression.
4. At point e, the axial force in beam L1-R is equal to zero, and the response is exactly equal to the response of beam L1-U.



(a) Applied load vs. midspan deflection



(b) Axial restraint force vs. midspan deflection

Figure 2.26: Load-deflection and restraint-deflection response of beam L1.

The influence of second-order effects can be determined by comparing the response of beams L1-R and L1-N. Beam L1-N, which assumes $M_w = 0$, predicts a midspan deflection of 212 mm at an applied load of 1000 kN. Beam L1-R however, which accounts for second-order effects, predicts a midspan deflection

of 568 mm, at the same magnitude of applied load. This indicates that for an applied load of 1000 kN, accounting for second-order effects increases the midspan deflection in beam L1 by a factor of 2.7. The difference between the deflection in each beam is the result of the softening effect caused by second-order effects.

However, beam L1-R has the same axial force vs. midspan deflection response as L1-N, indicating that second-order effects have minimal influence on the axial compression developed in a beam at a given magnitude of midspan deflection. The bending moment in beams L1-R and L1-N at point a , which corresponds with a midspan deflection of 151 mm, is presented in Figure 2.27. Although the second-order effects in beam L1-R cause the bending moment to become nonlinear, the total bending moment in both beams is very similar in magnitude. In beam L1-R, the total bending moment includes M_Q , M_o and M_w . However in beam L1-N, $M_w = 0$. Therefore for the same M_t , beam L1-N will have a larger magnitude of M_Q , relative to beam L1-R. Since both beams have identical sectional properties and a similar total bending moment at each section, the strain profile throughout both beams will be similar. Therefore the first compatibility condition in the proposed analytical model requires that beams L1-R and L1-N have approximately the same axial compression force, H .

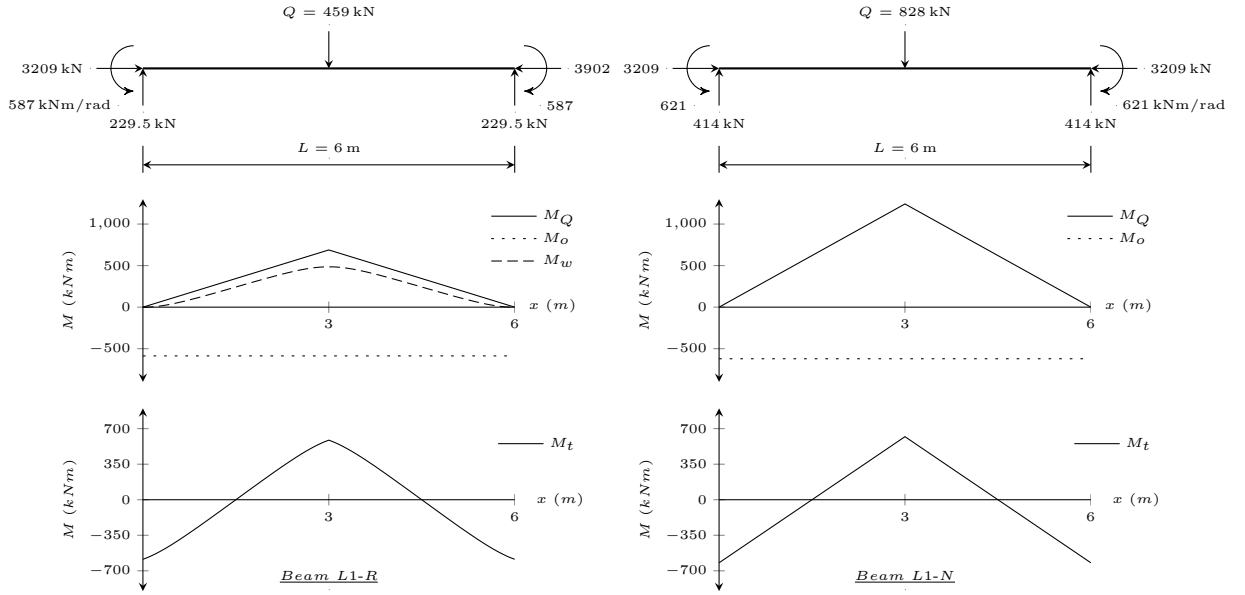


Figure 2.27: Bending moment diagram in beams L1-R and L1-N.

A similar comparison can be made between beams L1-N and L1-W. The analysis conducted for beam L1-W uses Wu's method, which assumes that the chord length of the centroidal axis is always equal to the arc length of the centroidal axis. The analysis conducted for beam L1-N is equivalent to Wu's method, but does account for the difference between the chord and arc length of the centroidal axis. Accounting for this difference increases the midspan deflection of beam L1, at an applied load of 1000 kN, by a factor of 1.6, from 135 mm in beam L1-W to 212 mm in beam L1-N. In addition, accounting for the difference between the arc length and chord length reduces the axial compression developed in the beam, at an applied load of 1000 kN, by a factor of 1.4, from 4721 kN in beam L1-W to 3470 kN in beam L1-N. This highlights the importance of considering the difference between the arc and chord length in

a laterally restrained beam.

The following conclusions can be made regarding the difference between beams L1-R, L1-N and L1-W:

1. Second-order effects in beam L1-R cause a softening of the load-deflection response. At an applied load of 1000 kN, accounting for second-order effects increases the midspan deflection of beam L1-R by a factor of 2.7, relative to beam L1-N.
2. Second-order effects in beam L1-R have a minimal influence on M_t , as accounting for M_w causes M_Q and M_o to decrease. Therefore, the axial compression vs. midspan deflection response of beams L1-R and L1-N is identical.
3. Accounting for the difference between the arc and chord length of a laterally restrained beam increases the midspan deflection of beam L1-N by a factor of 1.6, relative to beam L1-W.
4. At an applied load of 1000 kN, the proposed analytical model predicts a midspan deflection that is 4.2 times larger than the deflection predicted by Wu's model.

The proposed analytical model is able to simultaneously account for both material nonlinearities and second-order effects, as illustrated in the experimental validation presented in Chapter 4. However in cases where second-order effects cause a softening of the load-deflection response, modeling the response of the beam after the first peak in the applied load causes a numerical instability in the analysis. The section properties of beam S1, from the S-Series validation presented in Chapter 4, are summarized in Figure 2.28. The behaviour of the concrete is based on the constitutive material model developed by Popovics (1973). The behaviour of the reinforcement is based on the constitutive material model developed by Mander (1983), with and without a yield plateau.

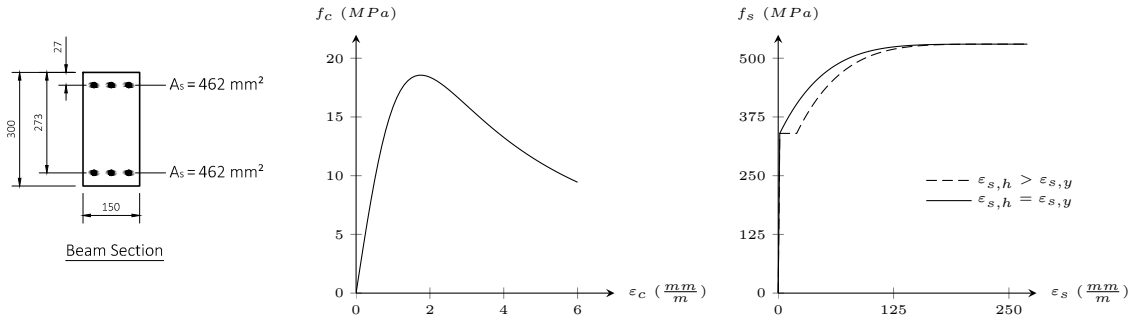


Figure 2.28: Properties of beam S1 from the S-Series validation.

The moment-curvature response of beam S1 is presented in Figure 2.29. Since the σ - ϵ response of the reinforcement is not provided by Su, Tian, and Song (2009), it is unclear if a yield plateau exists. Therefore, the moment-curvature response is presented with and without considering of a yield plateau in the response of the reinforcement. The procedure developed for the proposed analytical model assumes that the applied load is increased monotonically. Therefore the curvature is determined based on the bending moment and axial force at each section. When the reinforcement does not have a yield plateau, the curvature in the beam can be found for any value of bending moment. If however the reinforcement

does have a yield plateau, the range of curvatures that exist between point i and ii cannot be attained. Instead, increasing the bending moment at point i causes the curvature to jump to point ii .

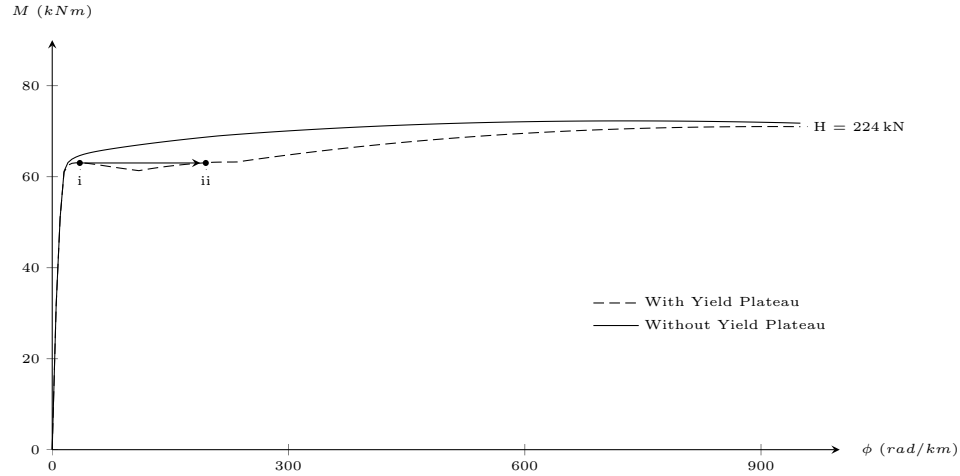


Figure 2.29: M - ϕ illustrating the development of a numerical instability.

This numerical instability, caused by consideration of material nonlinearities and second-order effects, limits the ability of the proposed analytical model to predict the post-peak load-deflection response of a given beam. If the procedure is altered to allow for a monotonically increasing midspan deflection, the bending moment at each section could be determined based on the curvature, allowing the model to predict the full post-peak response. However, the main consideration in this thesis is the response up to failure, which is typically defined as the first peak in the applied load. Therefore, consideration of a displacement controlled procedure is outside the scope of this thesis.

2.10 Optimization of the Numerical Integration Approach

The proposed analytical model requires that a numerical integration approach be adopted in two parts of the procedure. The first part requires the evaluation of a numerical integral for the layered analysis formulation, which calculates the compressive force resultant of the concrete, based on the strain profile at each section. The second part requires the evaluation of a numerical integral for the sectional analysis formulation, which calculates the deformation in a beam based on the curvature and centroidal strain at each section.

The accuracy of the analysis is dependent on the number of intervals used in the integration. Increasing the number of intervals increases the accuracy of the response, but also increases computational effort. Therefore, an appropriate number of sections can be determined by defining an acceptable magnitude of error. In both cases, a solution is considered accurate if it is within one percent of the correct solution. The correct solution is determined by increasing the number intervals used in the integration until the solution no longer changes. The results of an optimization study of the numerical integrals, evaluated as part of the proposed analytical model, are presented in this section.

2.10.1 Layered Analysis

To determine the number of layers required to provide an accurate estimation of the resultant force and eccentricity of the concrete, an optimization study is conducted using both the Bi-linear and Popovics constitutive material models. For both models, the strength of concrete is assumed to be either 20 MPa or 100 MPa, representing the range of concrete strengths considered throughout this thesis. The σ - ε response of the concrete considered for this study is presented in Figure 2.30

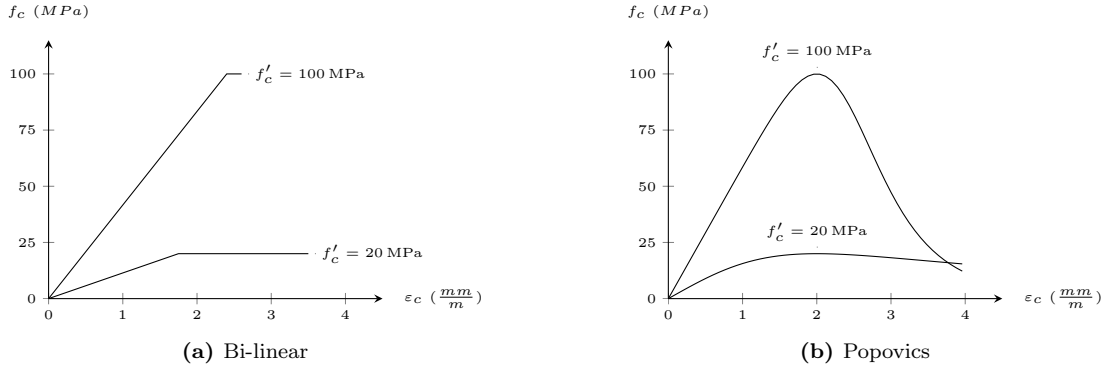


Figure 2.30: σ - ε response for layered analysis optimization.

The compressive strain profile used in this study, illustrated in Figure 2.31a, is defined based on the peak compressive strain ε_c , and the depth of the compression zone, c . The thickness of each layer, h_i , is dependent on the number of layers, n , considered through the depth of the compression zone. The compressive stress block for both the Bi-linear and Popovics material models is presented in Figures 2.31b and 2.31c, respectively.

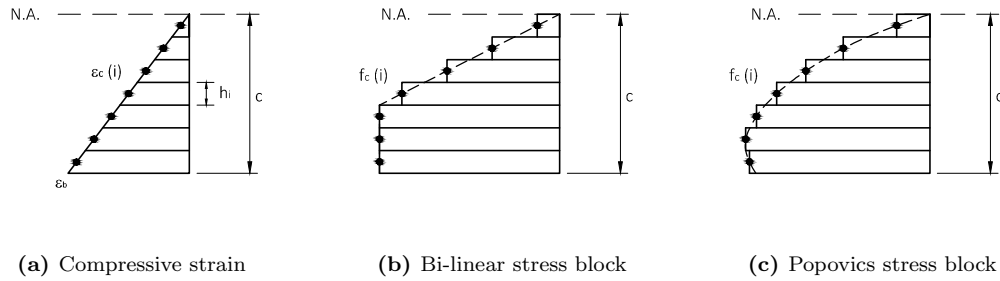


Figure 2.31: Concrete stress based on the Bi-linear and Popovics models.

The combinations of constitutive material models and peak compressive strain, ε_b , considered in this study are chosen to replicate the conditions that require the largest number of layers. These are:

1. Bi-linear material model, with $\varepsilon_b = \varepsilon_{c,u}$
2. Popovics material model, with $\varepsilon_b = \varepsilon_o$
3. Popovics material model, with $\varepsilon_b = 2 \cdot \varepsilon_o$

The influence of varying the number of layers in the compressive stress block developed using a Bi-linear material model, for concrete with a strength of 20 MPa and 100 MPa, is presented in Figure 2.32. To ensure that the resultant compressive force and eccentricity is accurate to within one percent, at least six layers should be used throughout the depth of a beam.

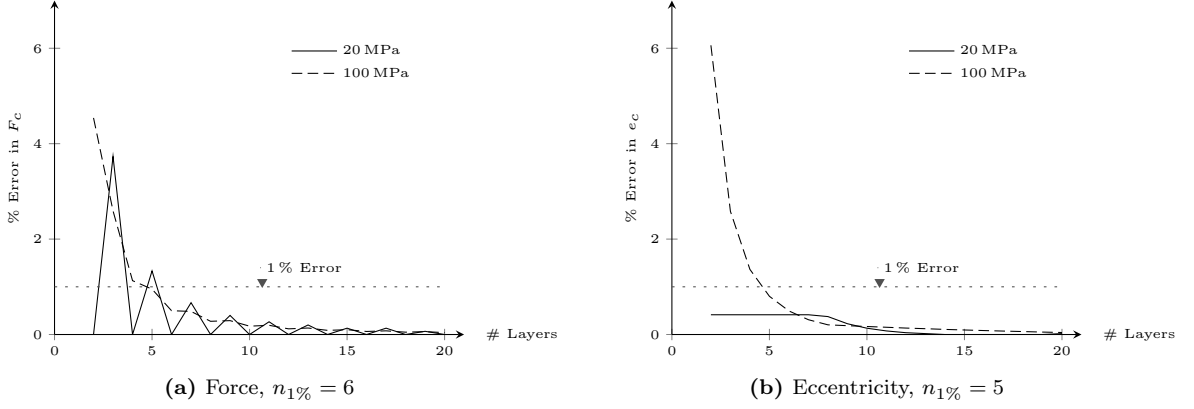


Figure 2.32: Number of layers required for use with the Bi-linear σ - ε response, at ε_{cu} .

Similarly, the influence of varying the number of layers in the compressive stress block developed using a Popovics material model, for concrete with a strength of 20 MPa and 100 MPa, is presented in Figure 2.33. This response is based on the assumption that the peak compressive strain in the section is equal to the peak compressive strain defined in the constitutive material model. To ensure that the resultant compressive force and eccentricity is accurate to within one percent, at least five layers should be used throughout the depth of a beam.

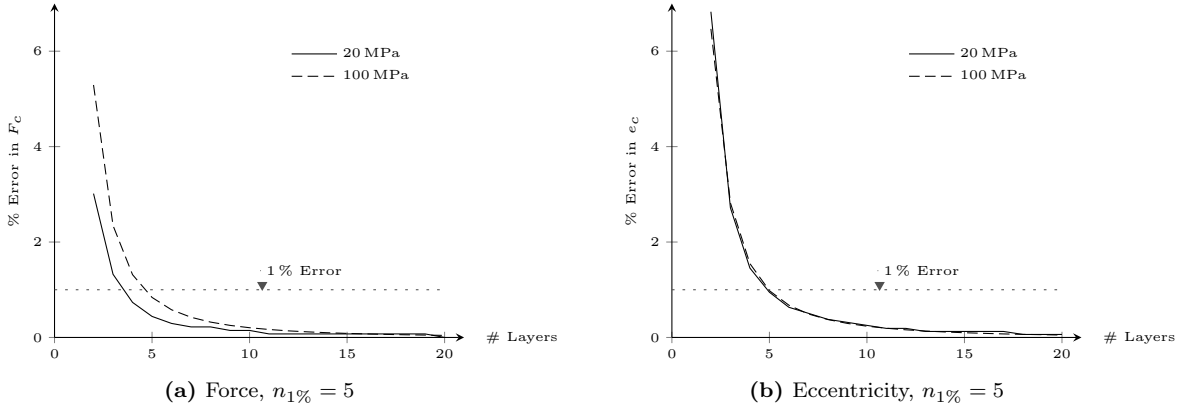


Figure 2.33: Number of layers required for use with the Popovics σ - ε response, at ε_o .

Finally, the influence of varying the number of layers in the compressive stress block developed using a Popovics material model, for concrete with a strength of 20 MPa and 100 MPa, is presented in Figure 2.34. This response is based on the assumption that the peak compressive strain in the section is equal to twice the peak compressive strain defined in the constitutive material model. For this case, to ensure that the resultant compressive force and eccentricity is accurate to within one percent, at least five layers should be used throughout the depth of a beam.

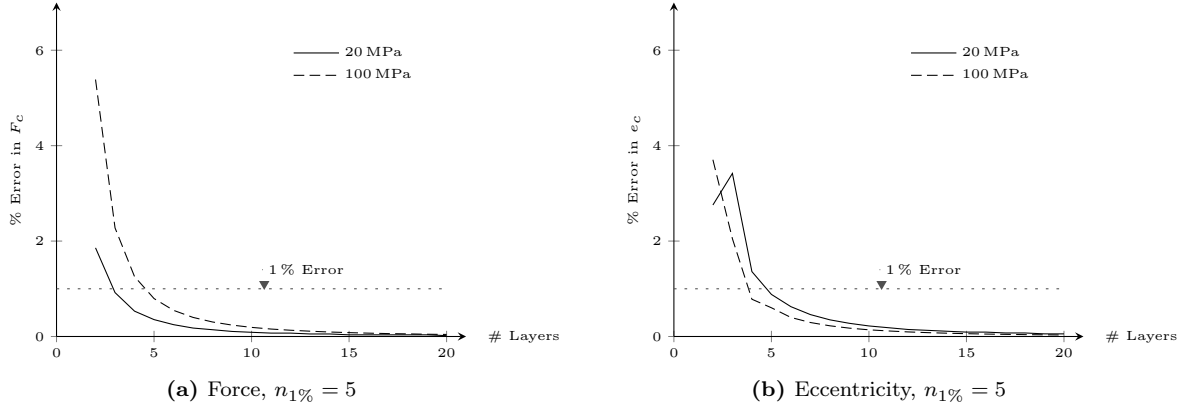


Figure 2.34: Number of layers required for use with the Popovics σ - ε response, at $2 \cdot \varepsilon_o$.

Based on the results of this optimization study, it can be concluded that providing at least six layers through the depth of the compression zone at a given section, will provide a result that is accurate to within one percent.

2.10.2 Sectional Analysis

The deformed shape of a beam is dependent on the curvature and centroidal strain at each section. As previously discussed, the curvature throughout a given beam, with a known bending moment and axial force distribution, can be determined using a sectional analysis approach. The beam, with properties summarized in Figure 2.35, is used to study the influence of varying the number of sections considered in the analysis of a laterally restrained and unrestrained beam.

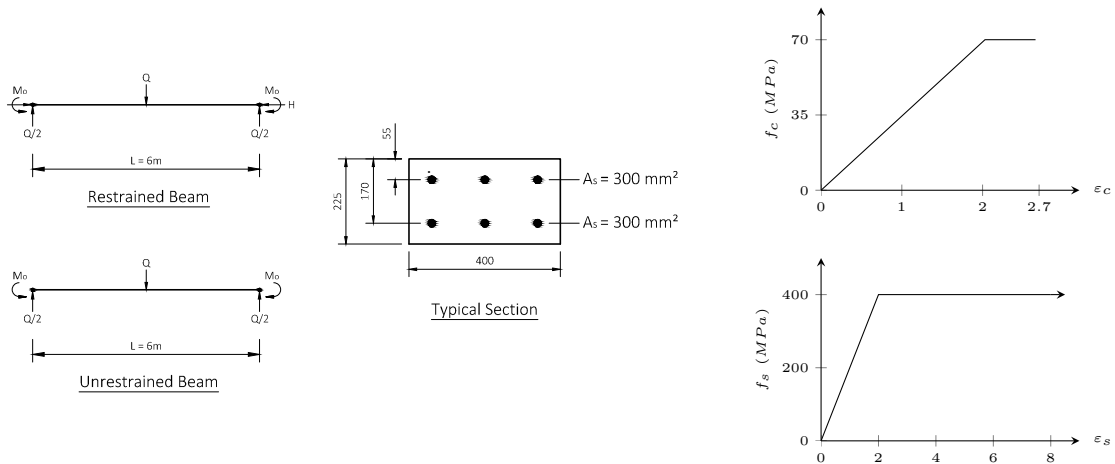


Figure 2.35: Beam properties for sectional analysis optimization.

The curvature throughout the restrained and unrestrained beam at $0.95 \cdot Q_{peak}$, determined using a total of 31 sections, is presented in Figure 2.36. In regions near the midspan and the support, the reinforcement yields, causing the curvature to increase. The response at each section governs the calculated axial load,

H , and the deflected shape, w_t . Therefore the accuracy of this analysis is influenced by the ability to predict the response in regions where curvatures concentrate. Increasing the number of sections in regions where the reinforcement yields will increase the accuracy of the predicted deformed shape, but will also increase the computational effort required.

The layout of sections presented in Figure 2.36 provides twice the number of sections within $L/8$ of the midspan and the supports. A more efficient layout could be developed by increasing the number of sections in the regions near the midspan and support based on the response of each beam. However for simplicity, the layout proposed in Figure 2.36 is considered in this study, and is used throughout this thesis, in conjunction with a varying number of sections.

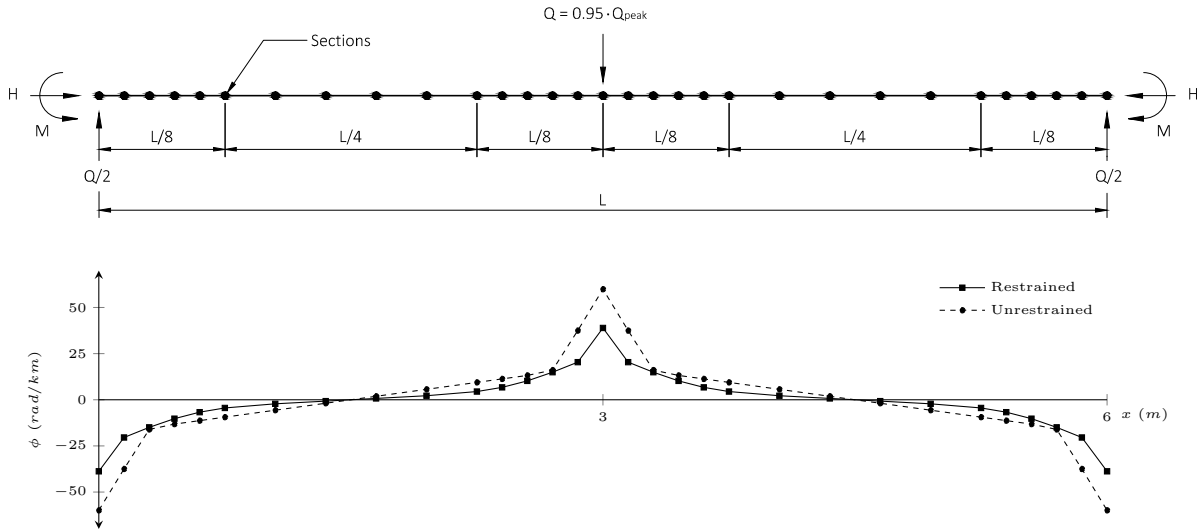


Figure 2.36: Proposed layout of sections in a given beam.

The error in determining the axial force and midspan deflection, relative to the number of sections used in the analysis of the beam presented in Figure 2.35, assuming $Q = 0.95 \cdot Q_{peak}$, is illustrated in Figures 2.37a and 2.37b, respectively.

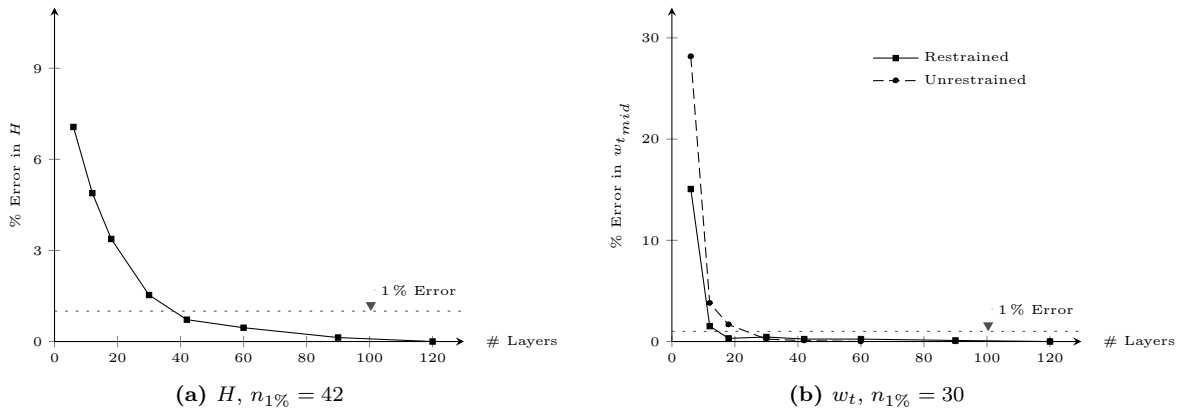


Figure 2.37: Number of sections required, at $Q = 110$ kN.

An acceptable threshold for error is defined as any solution within one percent of the solution provided by the analysis using 120 sections. As illustrated in Figure 2.37, increasing the number of sections from 90 to 120 does not significantly alter the results, and can therefore be assumed to be the correct solution. Based on the layout provided in Figure 2.36, a total of 42 sections are required to provide an accurate solution. This solution is specific to this beam, but can be used as a guideline for determining the number of sections required to provide accuracy in the analysis of other beams. Therefore, when conducting the analysis of a beam using the proposed analytical model, it is recommended that the number of sections be increased until the variation in H and w_t is within an acceptable limit.

3

Supplementary Model Refinements

The proposed analytical model presented in Chapter 2 provides a means for predicting the behaviour of laterally restrained, reinforced concrete beams and slab strips. For the remainder of this thesis, the model presented in Chapter 2 will be defined as the “base model”. The base model formulation:

1. Uses the plane sections hypothesis and nonlinear constitutive material models.
2. Is based on two compatibility conditions that prevent rotation and lateral expansion at each support.
3. Uses a layered analysis approach to determine the M - ϕ response, based on the axial force, at a given section.
4. Uses a sectional analysis approach to determine the restraint force and deformation of a given beam.
5. Uses an iterative procedure to account for second-order effects.

This chapter presents four refinements that can be applied to the base model to account for internal and external factors that can influence the response of a reinforced concrete beam or slab strip. These refinements were developed to validate the proposed model using test data from the experiments conducted by Su, Tian, and Song (2009) and Yu and Tan (2013). The validation of the proposed model, based on these two experiments, is presented in Chapter 4. Therefore, these refinements broaden the range of beams and slab strips that can be analyzed using the proposed analytical model. The refined model formulation:

1. Accounts for the actual stiffness of a support using an axial and rotational spring.
2. Accounts for the horizontal resultant of the diagonal compression struts, defined using a truss model formulation.

3. Accounts for lateral and rotational slip, between the beam and supporting structure, prior to developing the stiffness of the supports.
4. Accounts for the influence of bond deterioration, or strain penetration, in regions with geometric irregularities.

3.1 Support Stiffness

A reinforced concrete beam or slab strip, restrained from lateral displacement and rotation at each support, will develop an axial compression force that increases its stiffness and capacity. In the proposed analytical method, the restraint provided by the supports is assumed to be infinitely stiff. In some cases, the supports will have a finite stiffness, allowing for some lateral expansion and rotation at the ends of a given beam. Therefore, the proposed analytical model can be updated to provide a more accurate prediction of the response of a beam or slab strip with a finite support stiffness.

3.1.1 Overview

The stiffness of a support can be simulated using an axial and rotational spring, as illustrated in Figure 3.1. The representation of the support stiffness using a two spring system was adapted by Botticchio (2014) for use with the analytical model proposed by Wu (2013). The first spring resists lateral expansion, causing an axial compression force to develop in the beam. The second spring resists the rotation of the beam at the supports, reducing the positive bending moment at midspan and increasing the stiffness and capacity of a given beam.

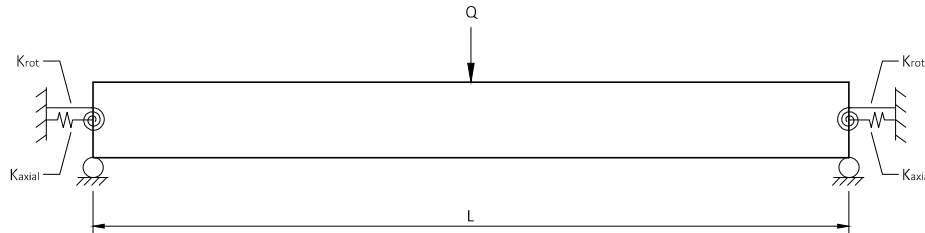


Figure 3.1: Lateral and rotational spring supports.

The lateral stiffness of each support is defined as the axial compression force causing a unit displacement, and is determined as,

$$K_{axial} = \frac{H}{\delta_o} \quad (3.1)$$

where H is the axial restraint force and δ_o is the lateral expansion at a support. The rotational stiffness of a support is defined as the bending moment causing a unit rotation, and is determined as,

$$K_{rot} = \frac{M_o}{\theta_o} \quad (3.2)$$

where M_o is the negative bending moment at a support and θ_o is the rotation at the ends of a given beam. If a beam is monolithically cast to an adjacent beam or slab, then the stiffness of the support can be estimated using elastic section properties (Botticchio, 2014). Alternatively, the support stiffness provided in an experiment can be determined by isolating and measuring the support reactions and end displacements.

3.1.2 Compatibility Condition

If a support prevents the lateral expansion of a beam, the chord length along the centroidal axis will always be equal to the undeformed length of the beam. Therefore, the arc length along the centroidal axis will be equal to the arc length of the deflected shape. However, if the supports allow for some lateral expansion, then the chord length of the centroidal axis will be greater than the undeformed length of the beam. The deflected shape of a beam is determined by assuming that the chord length of the beam does not change. Therefore increasing the chord length of the beam will cause an under prediction of the deflected shape.

This concept is illustrated in Figure 3.2 using two simplified shapes. When the chord length of the shape is increased from Figure 3.2a to Figure 3.2b, the vertical distance between the chord and arc length, f , increases.

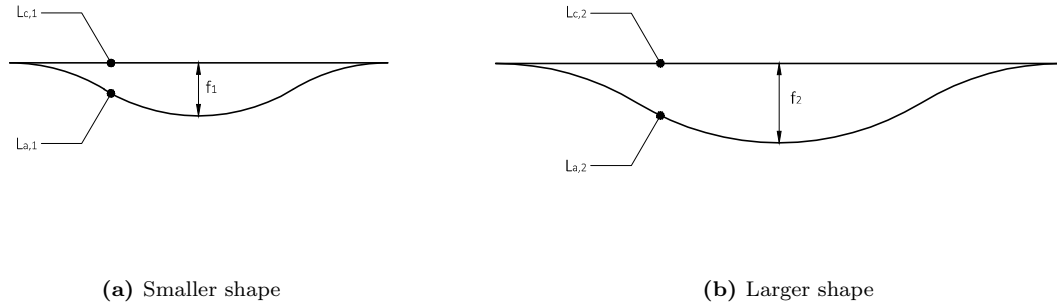


Figure 3.2: Ratio of chord length, arc length, and deflection.

As indicated in Chapter 2, the ratio of the two chord lengths will always be equal to the ratio of the two arc lengths. Therefore, the ratio of the deflection, f , in each shape will increase proportionally, as suggested in the following relation,

$$\frac{L_{a,1}}{L_{a,2}} = \frac{L_{c,1}}{L_{c,2}} = \frac{f_1}{f_2} \quad (3.3)$$

If the lateral displacement at the support is small relative to the undeformed length of the beam, then the difference between the calculated and actual deflection will be negligible. In the laterally unrestrained beams considered for comparison with Wu's method in Chapter 2, the magnitude of lateral expansion never exceeds one percent of the total length of the undeformed beam. Similarly in the experiments conducted by Su, Tian, and Song (2009) and Yu and Tan (2013), the total lateral expansion of each test specimen is less than one percent of the total undeformed length. Therefore, the magnitude of deflection calculated using the moment area theorem can be assumed to be approximately equal to the actual deformation of a beam.

The lateral and rotational stiffness of a support, defined using two springs with finite stiffness, can be incorporated into the proposed model by altering the compatibility conditions proposed in Section 2.3. The adjusted compatibility conditions are,

1. The chord length of a beam is equal to the sum of the undeformed length of the beam and the total lateral expansion at each support:

$$L_{c,ce} = L_o + \delta_o \quad (3.4)$$

where δ_o is the total lateral expansion, K_{axial} is the axial support stiffness, and H is the lateral restraint force. The magnitude of the lateral expansion is equal to, $\delta_o = H/K_{axial}$.

2. The total rotation of the ends of a beam is equal to the rotation of the elastic support:

$$\theta_o = \frac{M_o}{K_{rot}} \quad (3.5)$$

where θ_o is the rotation of the ends of a beam, M_o is the bending moment at the supports, and K_{rot} is the rotational stiffness of the supports.

3.1.3 Influence of Partial Restraint

The influence of altering the stiffness of the supports on the response of a given beam can be illustrated by considering beam F2, presented in Figure 3.3. In this section, the analysis of beam F2 is conducted as:

R: Base model, assuming support prevents all lateral expansion and rotation.

R₁: Base model, assuming $K_{axial} = 500 \text{ kN/mm}$ and $K_{rot} = \infty$.

R₂: Base model, assuming $K_{axial} = \infty$ and $K_{rot} = 5000 \text{ kNm/rad}$.

R_P: Base model, assuming $K_{axial} = 500 \text{ kN/mm}$ and $K_{rot} = 5000 \text{ kNm/rad}$.

S: Simply supported beam, assuming $K_{axial} = 0$ and $K_{rot} = 0$.

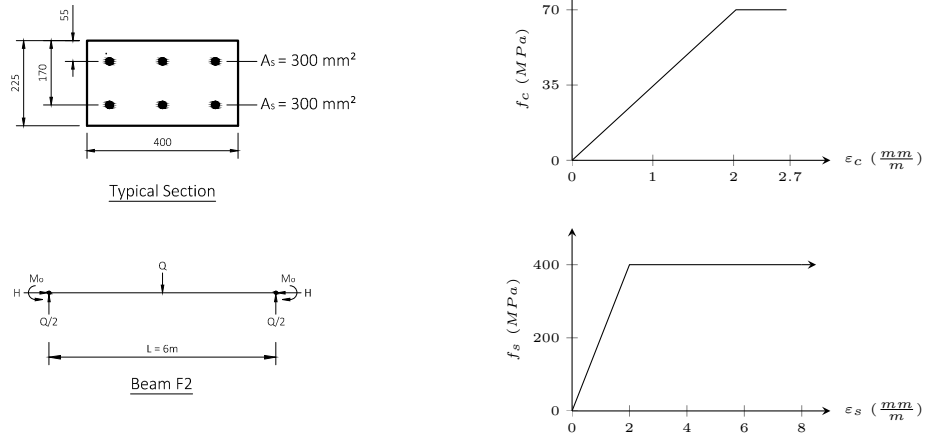


Figure 3.3: Properties of beam F2, used to study finite support stiffness.

The influence of varying rotational restraint on the response of beam F1 is illustrated in the moment and curvature response of beam F2- R and F2- R_2 , presented in Figure 3.4. The finite rotational stiffness in beam F2- R_2 reduces M_0 , which increases the bending moment at midspan relative to the support. This shift in the bending moment diagram reduces the capacity of the beam by a factor of 1.5, and reduces the peak axial compression in the beam by a factor of 1.4. In addition, the increased bending moment at midspan, relative to the supports, increases the curvature at midspan. This increased curvature increases the peak midspan deflection of the beam by a factor of 1.4, from 31 mm in beam F2- R to 42 mm in beam F2- R_2 .

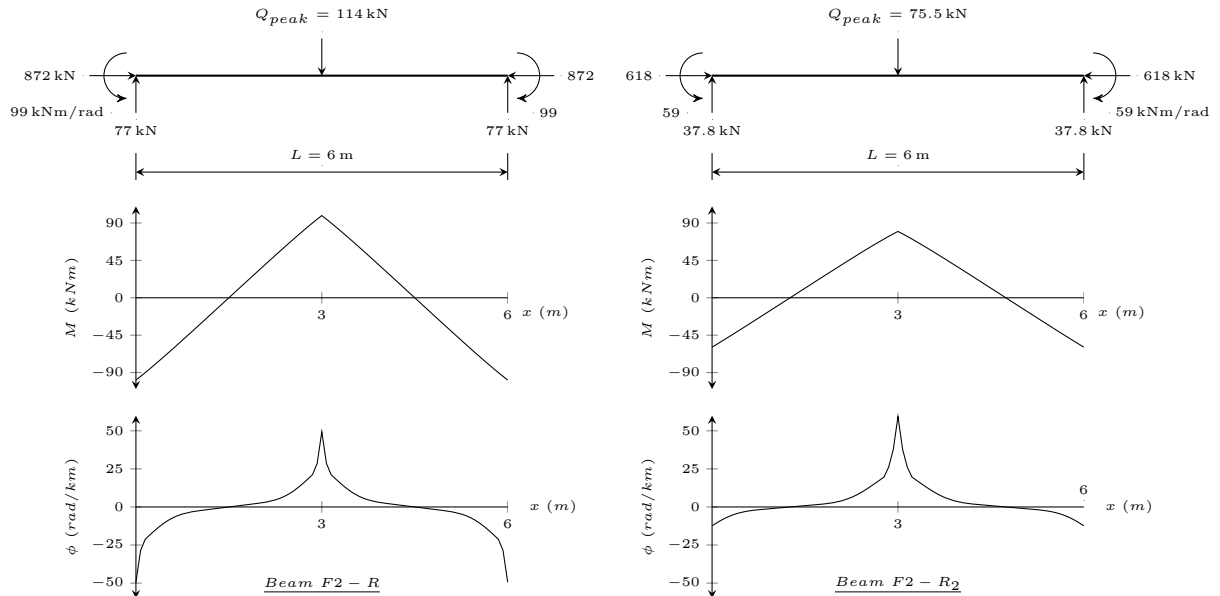


Figure 3.4: Bending moment and curvature in beam F2.

In contrast, accounting for a finite magnitude of lateral stiffness at a support does not shift the bending moment diagram. Instead, the increased lateral expansion of the beam reduces the lateral restraint force developed at the support, reducing stiffness and capacity. This is evident in the moment-curvature response of beams F2- R and F2- R_1 , presented in Figure 3.5. The plot is based on a family of moment-curvature diagrams that can be developed using the sectional properties of beam F1, for varying magnitudes of axial compression.

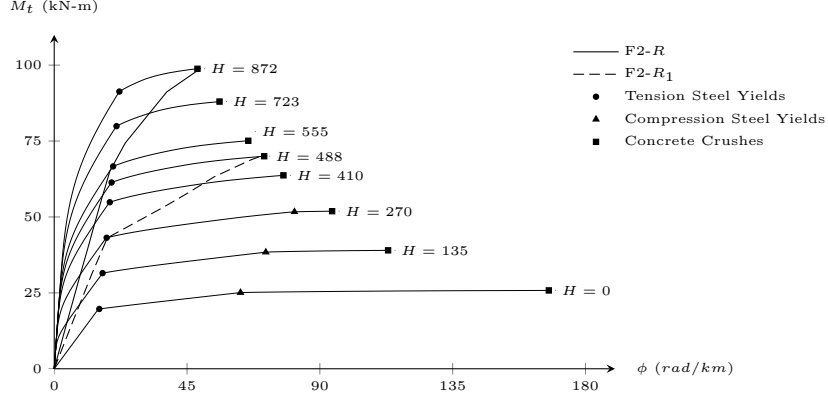


Figure 3.5: Moment-curvature response of beam F2.

The finite lateral stiffness of the support allows the beam to expand, reducing the peak axial compression force by a factor of 1.8, from 870 kN in beam F2- R to 488 kN in beam F2- R_1 . This reduced axial compression developed in beam F2- R_1 reduces the capacity of the beam by a factor of 1.4, from 114 kN in beam F2- R to 81 kN in beam F2- R_1 . In addition, the reduced axial compression increases the peak midspan deflection of the beam by a factor of 1.2, from 31 mm in beam F2- R to 37 mm in beam F2- R_1 .

The combined influence of considering K_{axial} and K_{rot} is illustrated in the applied load vs. midspan deflection response presented in Figure 3.6a, for beams F2- R , F2- R_P and F2- S .

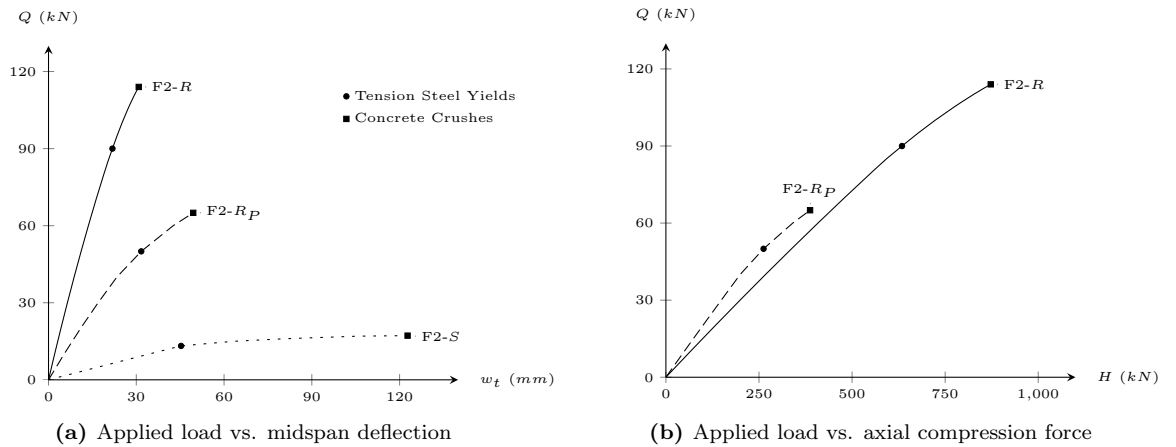


Figure 3.6: Load-deflection and load-restraint response of beam F2.

Allowing some rotation and lateral expansion to occur at the supports reduces the capacity of beam F2 by a factor of 1.8, from 114 kN in beam F2-*R* to 65 kN in beam F2-*R_P*. In addition, the partial restraint increases the peak midspan deflection by a factor of 1.6, from 31 mm in beam F2-*R* to 49 mm in beam F2-*R_P*. In contrast, providing no rotational or lateral stiffness at the supports of beam F2-*S* reduces the capacity by a factor of 6.6, and increases the peak midspan deflection by a factor of 4.0.

The influence of partial restraint is also illustrated in the applied load vs. axial compression plot, presented in Figure 3.6b. Reducing the rotational and lateral stiffness of the support reduces the peak axial compression by a factor of 2.2, from 872 kN in beam F2-*R* to 388 kN in beam F2-*R_P*. The reduced axial compression is the result of the combination of increased lateral expansion at the supports, and the increased deformation of the beam near midspan caused by rotation of the beam at the supports.

3.1.4 Conclusion

The base model, developed in Chapter 2, assumes that the supports of a beam or slab strip will prevent lateral expansion and rotation. For some beams and slab strips, the stiffness of the support will not be infinite. Therefore, this section presents updated compatibility conditions that simulate the stiffness of a support using a combination of a rotational and linear spring. As indicated through the sample analysis, allowing for some rotation of the beam at each support increases the deformation of the beam near midspan. This causes the concrete to crush at a lower applied load, relative to a beam with full rotational restraint. In addition, allowing for lateral expansion of a beam at the supports reduces the magnitude of axial compression developed in the beam, which reduces the influence of arching action on capacity.

Considering the combination of a lateral and rotational restraint, equal to $K_{axial} = 500 \text{ kN/mm}$ and $K_{rot} = 5000 \text{ kNm/rad}$, respectively, provides a means for highlighting the influence of partial restraint on the response of a restrained beam. Accounting for partial restraint in beam F2-*R_P*, relative to beam F2-*R*:

1. Reduces the capacity by a factor of 1.8.
2. Reduces the peak axial compression force by a factor of 2.2.
3. Increases the peak midspan deflection by a factor of 1.6.

In addition, allowing the beam to freely expand laterally and rotate at the supports:

1. Reduces the capacity by a factor of 6.6.
2. Increases the peak midspan deflection by a factor of 4.0.

These results indicate that varying both the lateral and rotational stiffness of the support can significantly influence the capacity and deflection of a restrained beam or slab strip. Therefore, providing an accurate estimate of restraint stiffness increases the accuracy of the proposed analytical model.

3.2 Diagonal Compression Field Action

In this section, a truss model formulation is used to understand the influence of the diagonal compression struts that form in a reinforced concrete beam with a concentrated load. The proposed analytical model does not account for the influence of these struts, and as a result, over predicts the concentration of curvature near the locations of peak bending moment. Therefore, a method of accounting for the diagonal compression field action is developed and implemented into the proposed analytical method.

A truss model, also known as a strut and tie model, provides a rational basis for analyzing cracked, reinforced concrete structures. The truss model can be developed by predicting the various fields of stress throughout the structure and representing the compressive and tensile forces as a series of struts and ties connected by nodal regions. The assumption of plane sections is valid for regions, defined as B-regions, where the strain distribution is not significantly nonlinear. However regions with highly nonlinear strains, defined as D-regions, are typically located near concentrated loads or geometric discontinuities. Figure 3.7 depicts both the B-regions and D-regions expected in a reinforced concrete beam.

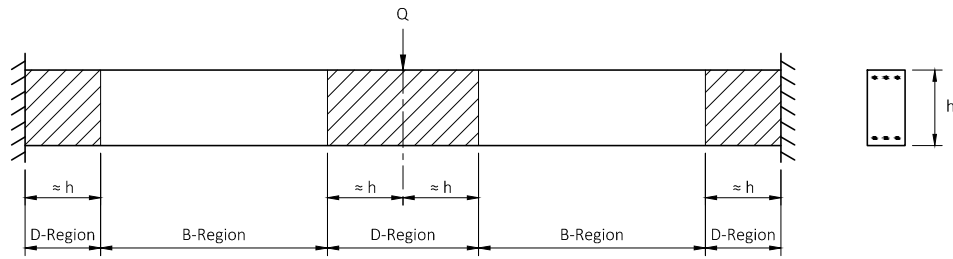


Figure 3.7: B and D-regions in a restrained beam, adapted from Schlaich (1987).

A rational approach to graphically represent both the B and D-regions of a structure was developed by Schlaich, Schafer, and Jennewein (1987), and is adapted for use in this section. This approach uses elastic stress trajectories to optimize the location and distribution of struts and ties throughout the structure.

3.2.1 Laterally Unrestrained Beams

In the proposed analytical model, the internal forces at each section can be represented as the compression resultant, C , and the tension resultant, T , separated by a lever arm, z . The shear force at each section, V , is assumed to be vertical at each section, and does not influence C or T . The sectional forces and internal forces in a laterally unrestrained beam are presented in Figure 3.8.

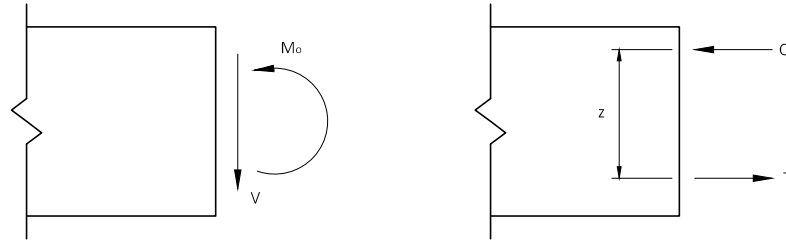


Figure 3.8: Sectional forces in a laterally unrestrained beam.

A truss model representation of a rotationally restrained, laterally unrestrained beam with a funicular top chord and no web members, is presented in Figure 3.9. The horizontal component of the funicular compression chord represents the compression resultant C , and the vertical component represents the shear force V , as assumed in the proposed analytical model. In Figure 3.9, and throughout this section, only half of each beam is depicted for clarity, and is assumed symmetric about midspan.

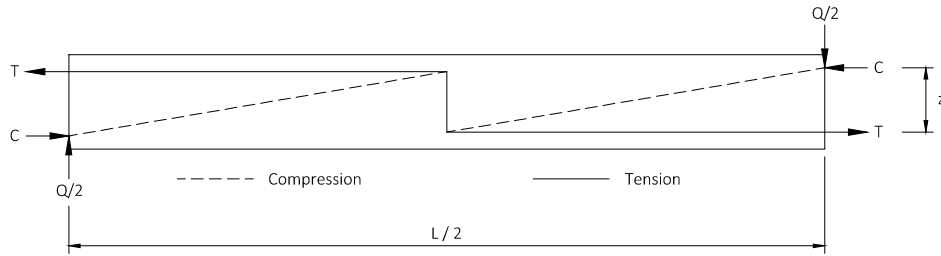


Figure 3.9: Truss model for a laterally unrestrained beam, with no web members.

A truss model without web members would indicate that the tension force in the reinforcement does not vary throughout the length of the beam. This finding contradicts the plane sections hypothesis, which predicts that the stress in the tension chord varies along the length of a beam. Therefore, the truss model presented in Figure 3.9 is not a valid representation of a reinforced concrete beam with bonded reinforcement (Gauvreau, 1993).

The stress in the tension chord can be varied by assuming that the shear force in the beam is transferred through diagonal compression struts, as illustrated in the truss model presented in Figure 3.10. The inclination of the diagonal struts, θ , governs the variation of stress in the top and bottom chords of the truss model.

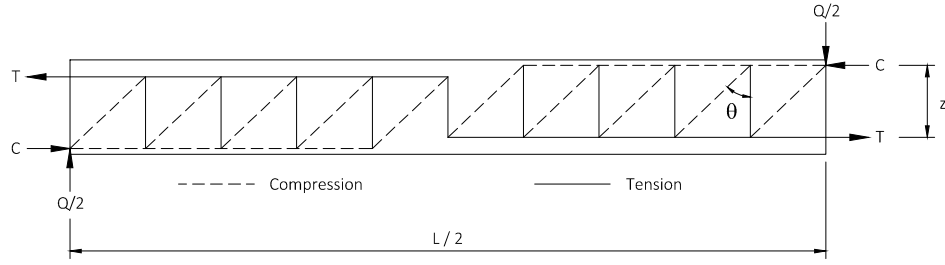


Figure 3.10: Truss model for a laterally unrestrained beam, with web members.

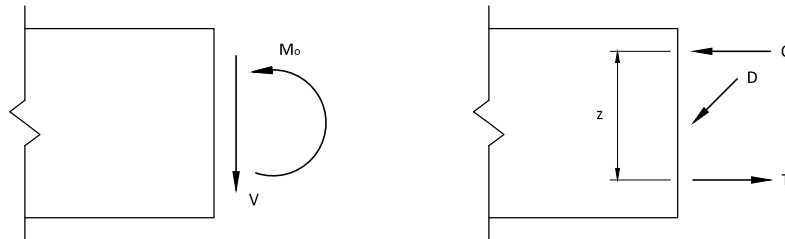
The updated truss model is in better agreement with the plane sections hypothesis, as it accounts for the variation of stress in the tension chord throughout the beam. The vertical component of each diagonal compression strut, D_y , is equal to the shear force at each section. For a beam with a concentrated load at midspan,

$$D_y = \frac{Q}{2} \quad (3.6)$$

The horizontal component of each diagonal compression strut, D_x , is dependent on the magnitude of the shear force and the inclination of the diagonal strut. Therefore for a beam with a concentrated load applied at midspan,

$$D_x = \frac{Q}{2 \tan \theta} \quad (3.7)$$

where θ is defined relative to the horizontal chord. The internal forces at each section can be updated to include the contribution of the diagonal compression strut, as illustrated in Figure 3.11. In a truss model, the location of D_x varies between nodes to account for the varying bending moment. In the proposed model, the magnitude of C and T vary between node locations to account for the change in bending moment. Therefore, D_x can be assumed to act directly at the centroid of each section.

Figure 3.11: Sectional forces in a laterally unrestrained beam, with consideration of D .

The equilibrium conditions at each section, with consideration of a diagonal compression strut, be-

comes,

$$\sum F_x = C + D_x - T = 0 \qquad \sum M = \frac{C}{z} = \frac{T}{z} = M_t$$

where M_t is the bending moment at each section. Since the magnitude of D_x is based on the shear force in the beam, and not the strain profile, it can be represented as an axial force, H^* , acting at the centroid of each section. Based on this, the horizontal equilibrium condition becomes,

$$\sum F_x = C - T = H^*$$

where H^* is equal to $-D_x$. In regions near a concentrated load, the diagonal compression struts will likely form a fan to spread out the load (Gauvreau, 1993). A refined truss model of a laterally unrestrained beam is presented in Figure 3.12, with each fan region represented by four diagonal struts with varying inclination. Each of these struts is assumed to carry a quarter of the shear force.

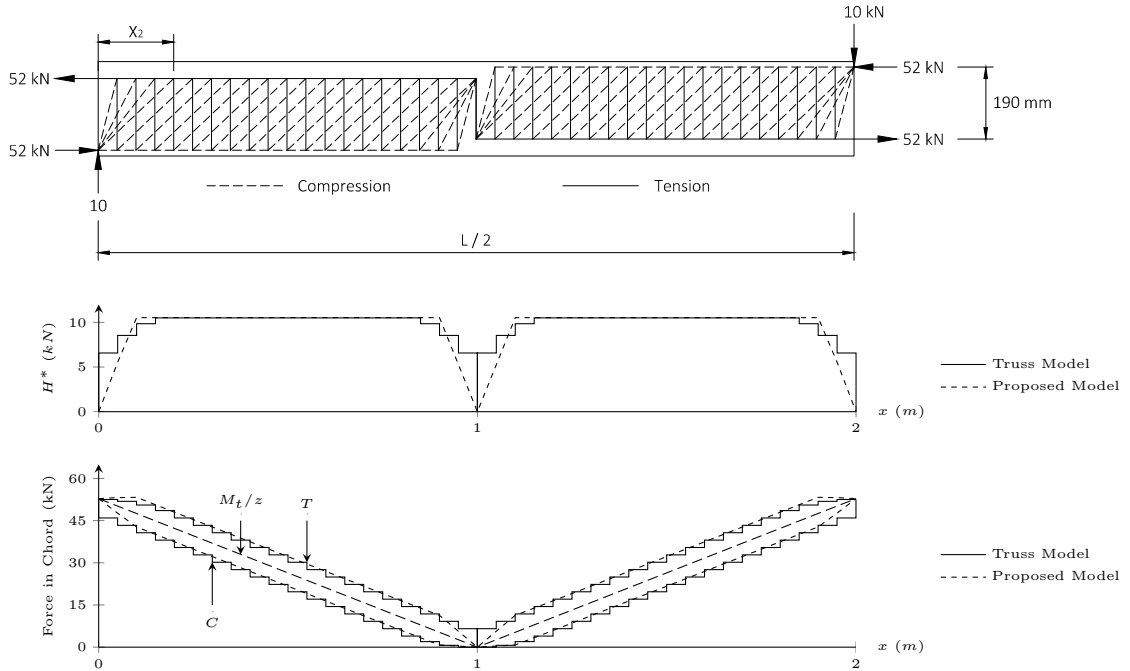


Figure 3.12: Influence of H^* in laterally unrestrained beams, adapted from Gauvreau (1993).

The magnitude of H^* increases from zero at the start of each fan, to a peak at the end of each fan region, as illustrated in Figure 3.12. For this analysis, the influence of compression reinforcement is ignored. The truss model assumes that the magnitude of H^* is constant between nodes, and will increase in steps at each node. For the proposed analytical method, the increased magnitude of H^* can be assumed to linearly increase over half of the length of the fan region, x_2 , defined as,

$$x_2 = \frac{z}{\tan \theta} \tag{3.8}$$

The variation of force in the compression and tension chords is presented in Figure 3.12, for the truss model and the proposed analytical model. When the diagonal compression struts are not considered, the force in each chord is equal to, $C = T = M_t/z$. When the diagonal compression struts are considered, the force in the compression chord reduces and the force in the tension chord increases. This provides a more realistic representation of the behaviour of a beam with a concentrated load. In addition, the response from the proposed analytical model, included in Figure 3.12, indicates that the assumed linear variation of H^* correlates well with the stepped variation assumed in the truss model.

3.2.2 Laterally Restrained Beams

A similar procedure to the one presented in the previous subsection can be adopted to incorporate the influence of diagonal compression struts in laterally restrained beams. For laterally restrained beams, the horizontal equilibrium condition is defined as,

$$H + H^* = F_c + \sum F_s \quad (3.9)$$

where H is the axial resultant force in each section, imposed by the lateral restraint. This axial compression force causes the beam to remain uncracked in regions with lower bending moment, where the full depth of the beam is in compression. The length of the beam that is uncracked, x_o , is defined as,

$$x_o = \frac{H(e_{cs} + e_{cm})}{Q/2} \quad (3.10)$$

where e_c is the distance between the compression chord and the centroid at the support, s , and at midspan, m . A refined truss model accounting for the uncracked region, x_o , is presented in Figure 3.13. The variation of H^* in regions with diagonal compression struts is presented in Figure 3.13, for the assumed truss model and the proposed analytical model. Similar to the unrestrained beam, the magnitude of H^* is assumed to increase linearly over half the length of the fan region, x_2 . In the uncracked region of concrete, the axial compression force is carried by a single diagonal strut defined based on the shear force in the section. Therefore, the magnitude of H^* is considered to be equal to zero throughout this region.

The variation of the force in the tension chord is presented in Figure 3.13 for both the truss model and proposed analytical model. When the diagonal compression struts are not considered, labeled as $H^* = 0$, the model under predicts the magnitude of tension force near the support and midspan. When the diagonal compression struts are considered, labeled as $H^* \geq 0$, the proposed model better predicts the tension force in the reinforcement, particularly in regions where the bending moment, and curvature, are at a peak. The curvature of the beam in regions near the peak bending moment will have more of an influence on deformation than the curvature located near or within the uncracked region. Therefore, accounting for the effects of the diagonal compression struts can improve the accuracy of the predicted deformations of a beam.

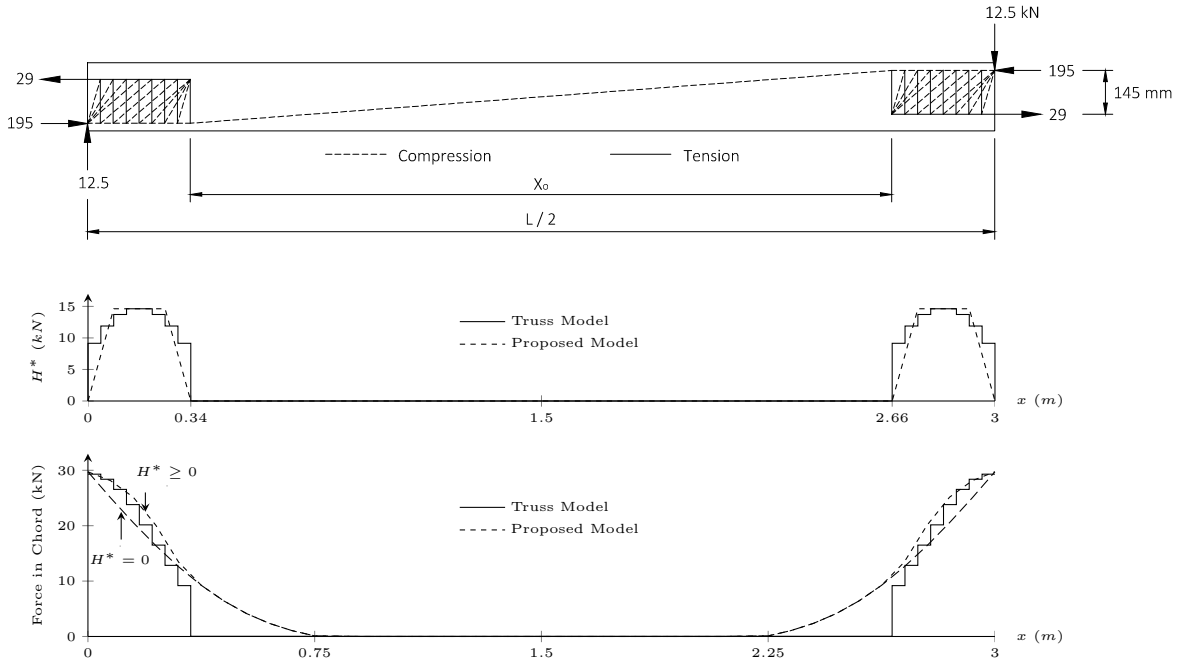


Figure 3.13: Influence of H^* in laterally restrained beams, adapted from Gauvreau (1993).

If the loading is symmetrical about the midspan of a beam, the middle of the uncracked region will always coincide with the location of zero bending moment. This requires that an iterative approach be adopted to determine the center of the uncracked region, as altering the location of the center of the uncracked region will affect the bending moment in the beam. Therefore, diagonal compression field action can be implemented into the proposed analytical method using the following iterative procedure:

- A. Complete Steps 1 to 6 from the proposed procedure outlined in Section 2.7.
- B. Using the computed bending moment diagram, determine the location of zero bending moment and the length over which the beam is uncracked, x_o .
- C. Complete Steps 7 to 15 from the proposed procedure outlined in Section 2.7 using the updated equilibrium equations presented in this section.
- D. Check the assumed location of zero bending moment. If the location has changed, return to step B and change the location of the center of the uncracked region. If the location has not changed, then the estimated location of zero bending moment is correct.

3.2.3 Influence of Diagonal Compression Field Action on Beam Response

The influence of the horizontal component of the diagonal compression struts can be understood by considering the response of a laterally unrestrained and restrained reinforced concrete beam. The beams considered in this comparison are presented in Figure 3.14.

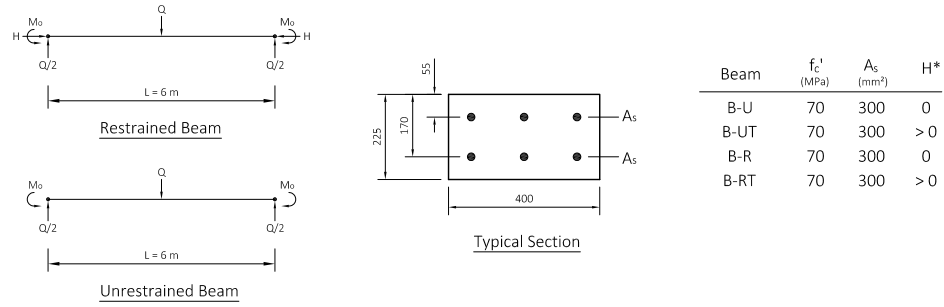


Figure 3.14: Beam properties used to study the influence of DCFA.

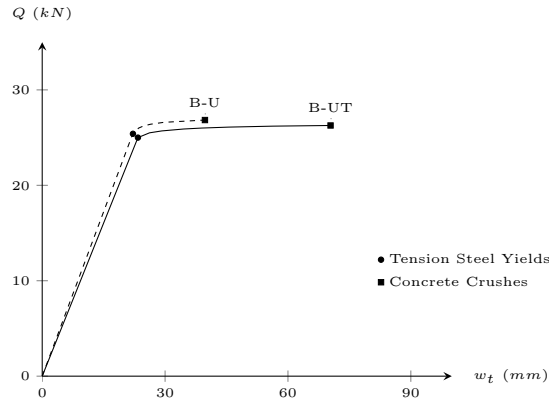
In this section, the analysis of beam B is conducted as:

U: Beam has no lateral restraint, and the influence of compression reinforcement is ignored.

R: Beam has an infinitely stiff lateral restraint.

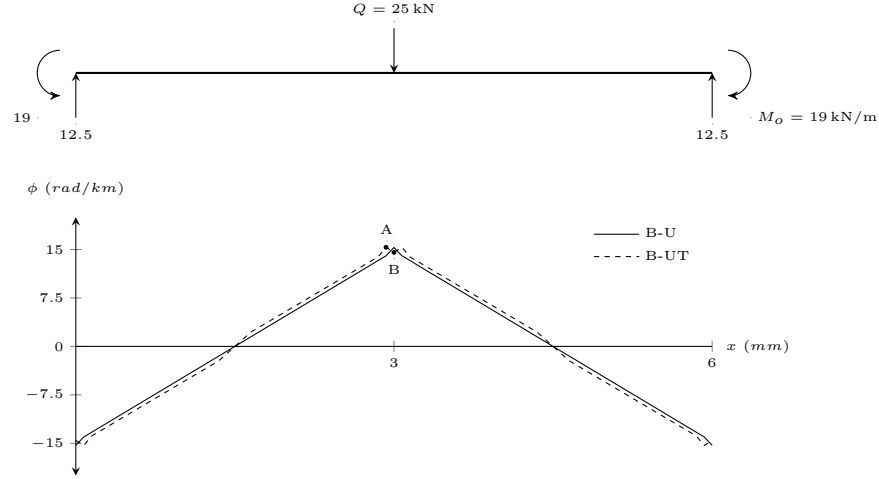
T: The influence of diagonal compression field action is included.

The applied load vs. midspan deflection response of a laterally unrestrained beam, with and without consideration of diagonal compression field action, is presented in Figure 3.15. Accounting for diagonal compression field action causes the capacity of beam B-U to decrease by a factor of 1.02, from 26.8 kN in beam B-U to 26.3 kN in beam B-UT. In contrast, accounting for H^* increases the peak midspan deflection in the beam by a factor of 1.8, from 40 mm in beam B-U to 70 mm in beam B-UT. This indicates that for laterally unrestrained beams, accounting for the diagonal compression struts throughout the beam has a minimal influence on capacity, but a significant influence on the midspan deflection at failure.

Figure 3.15: Influence of H^* on the load-deflection response of a laterally unrestrained beam.

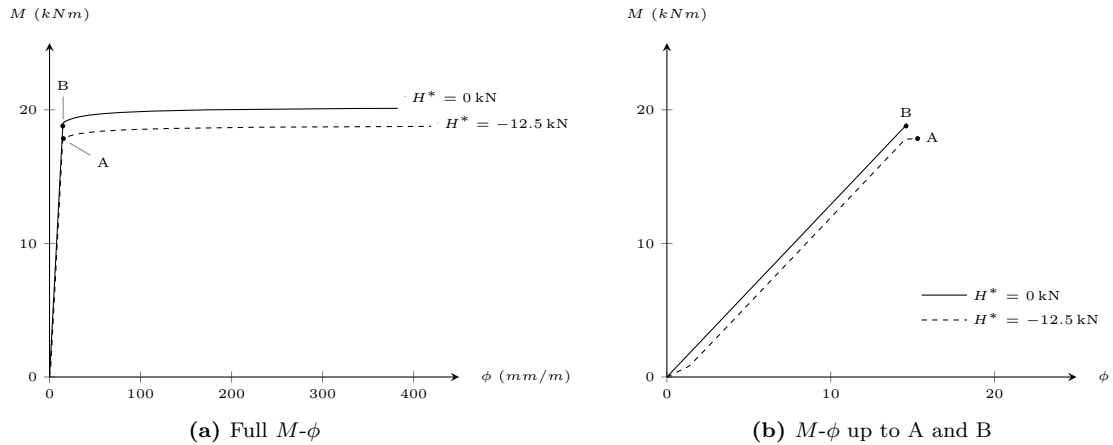
Prior to yielding, the midspan deflection of beams B-U and B-UT are similar. However once the reinforcement yields, the response of B-UT diverges from that of B-U. This can be explained by considering the curvature along each beam, just after the reinforcement first yields at $Q_{yield} = 25$ kN, presented in

Figure 3.16.

Figure 3.16: Influence of H^* on the curvature in a laterally unrestrained beam, at $Q = 25$ kN.

In beam B-U, the peak curvature and location where the reinforcement first yields is at the location of peak bending moment, labeled as point B . As previously indicated, accounting for diagonal compression field action increases the tensile force in the reinforcement and reduces the compressive force in the concrete. Therefore, increasing H^* will increase the curvature at each section, as illustrated in the response of beam B-UT. However, this causes the peak curvature in the beam to shift away from the location of peak bending moment at point B , to point A . This causes the midspan deflection of beam B-UT to exceed that of beam B-U.

The shift in the location of peak curvature can be understood by considering the moment-curvature response of the beam at point A and point B , presented in Figure 3.17. When $Q = 25$ kN, the bending moment at point A is equal to 19 kNm, while the bending moment at point B is 18 kNm. The axial resultant H^* , which is zero at point A , increases to -12.5 kN at point B . In this case, a negative axial resultant indicates that the section has a tensile resultant.

Figure 3.17: Influence of H^* on the M - ϕ response of sections A and B.

The moment-curvature response up to section A and B , presented in Figure 3.17b, indicates that despite the lower bending moment at section B , the curvature is larger. Therefore, consideration of diagonal compression struts can cause the location of first yield to occur away from the location of the peak bending moment. Crushing failure in beam B-UT occurs at 75 mm away from the concentrated load, which is exactly equal to half the length of the assumed fan region. In this example, the length of the fan region is assumed to be approximately equal to the lever arm between the compressive and tensile force at each section, z . A sensitivity study of the angle of inclination of the strut, as well as the length of the fan region, is presented as part of a parametric study in Chapter 5.

The load-deflection and load-restraint response of a laterally restrained beam, with and without consideration of diagonal compression field action, is presented in Figure 3.18. Similar to the laterally unrestrained beam, consideration of H^* does not alter the stiffness of the beam prior to yielding of the reinforcement in tension. However once the reinforcement yields, the lateral restraint prevents the same degradation of stiffness exhibited in the unrestrained beams. For beam B-R, accounting for H^* increases the capacity by a factor of 1.05, from 114 kN in beam B-R to 120 kN in beam B-RT. In addition, accounting for H^* increases the axial compression force developed at failure by a factor of 1.14, from 872 kN to 993 kN, and increases the peak midspan deflection in the beam by a factor of 1.13, from 31 mm to 35 mm.

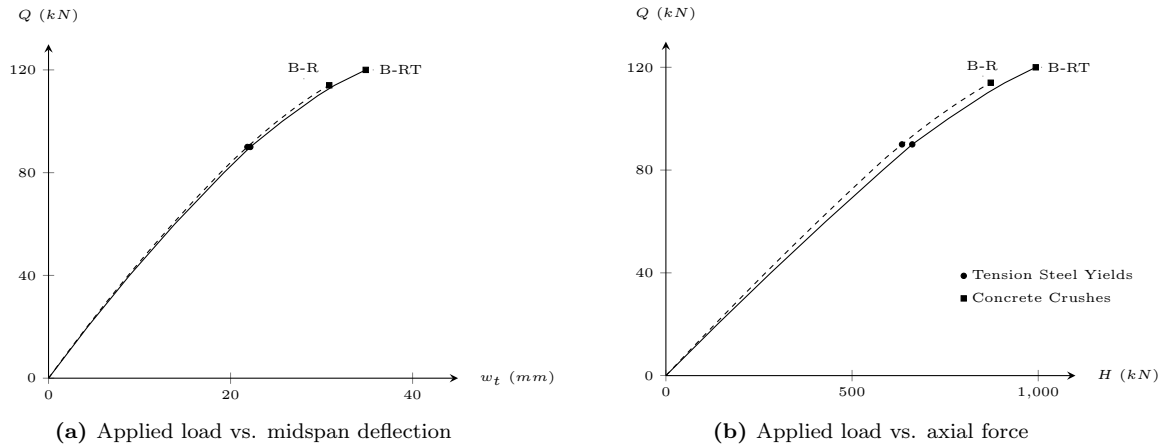


Figure 3.18: Influence of H^* on the response of a laterally restrained beam.

The influence of H^* on the peak midspan deflection of each beam can be understood by considering the curvature throughout beams B-R and B-RT, at their respective failure loads. The peak midspan bending moment in beam B-RT, equal to 99 kN m, is 1.08 times smaller than the peak bending moment in beam B-R, equal to 107 kN m. However as previously indicated, increasing the axial compression force developed in a beam reduces peak curvature. Therefore, accounting for H^* reduces the peak curvature by a factor of 1.1, from 0.50 rad/km in beam B-R to 0.45 rad/km in beam B-RT.

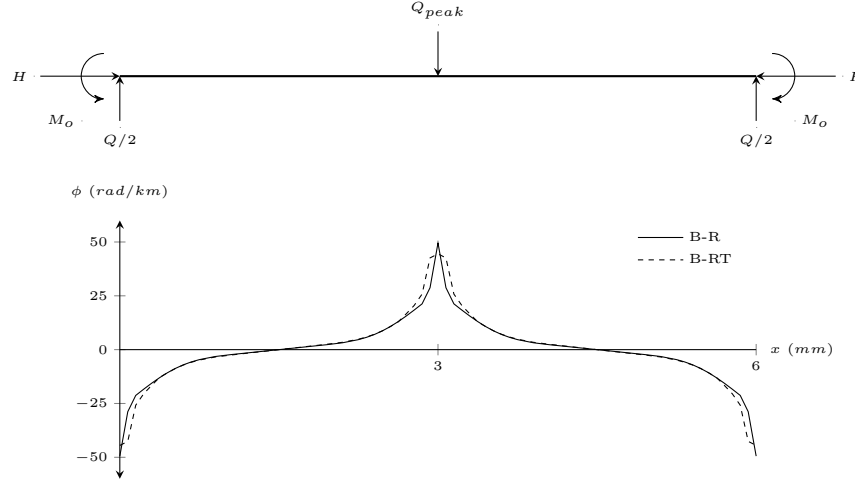


Figure 3.19: Influence of H^* on the curvature in a laterally restrained beam, at Q_{peak} .

Despite having a lower peak curvature, the implementation of diagonal compression field action in the analysis of beam B-RT increases the curvature in regions near the location of peak bending moment. This prevents the concentration of curvature near concentrated loads by accounting for spreading of load through diagonal compression struts. The increased curvature in beam B-RT results in a larger peak midspan deflection, relative to beam B-R.

3.2.4 Conclusion

The proposed analytical model presented in Chapter 2 does not directly account for the influence of diagonal compression field action. As illustrated throughout this section using a truss model formulation, the horizontal component of compression in the diagonal struts reduces the axial compression at each section located away from the concentrated load and supports. In a laterally unrestrained beam, accounting for diagonal compression field action:

1. Reduces the capacity of a beam by a factor of 1.02.
2. Increases the peak midspan deflection by a factor of 1.8.

For a laterally restrained beam, accounting for diagonal compression field action:

1. Increases the capacity of a beam by a factor of 1.05.
2. Increases the peak axial compression of a beam by a factor of 1.14.
3. Increases the peak midspan deflection by a factor of 1.13.

Based on the results obtained in this section, incorporating the diagonal compression field action model into the proposed analytical model does provide a better representation of the state of stress within a beam, and as a result, provides a more realistic prediction of a beam's response. Unless otherwise noted, the assumed inclination of the diagonal struts is assumed to be equal to 45° , and the length of the fan

region is assumed equal to z . The influence of this assumption on the response of laterally unrestrained and restrained beams is discussed in Chapter 5.

3.3 Slip at Supports

In the reinforced concrete slab of either a bridge deck or a building, the exterior and cantilever slabs prevent lateral expansion, causing membrane forces to develop. Similarly in a reinforced concrete frame, a beam that spans between columns is laterally restrained by the supporting columns and adjacent beams. If the slab or beam is cast monolithically to its supports, the stiffness of the lateral restraint is dependent on the elastic stiffness of the adjacent members (Botticchio, 2014).

Alternatively, if a beam is precast and mechanically connected to its supports, it may exhibit an initial softness prior to the development of the elastic stiffness of the support. This softness, which is evident in the experiments conducted by Su, Tian, and Song (2009) and Yu and Tan (2013), delays the mobilization of the lateral restraint force, which delays the onset of arching action. This can alter the response of a beam, and must therefore be incorporated into the proposed analytical model to provide a more accurate estimate of a given beam's behaviour.

The softness exhibited in the connection between the ends of a beam or slab and the support can be modeled by quantifying the amount of lateral slip. The total slip in the system, s_t , is determined by considering the two distinct slip components illustrated in Figure 3.20.

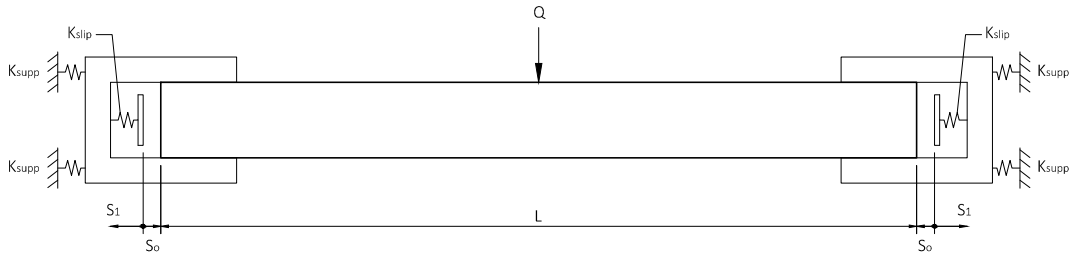


Figure 3.20: Lateral slip in a beam, relative to its supports.

The total slip in the system is defined as,

$$s_t = s_o + s_1 \quad (3.11)$$

where s_o is the initial slip, and s_1 is the residual slip of the beam relative to the support. The initial slip represents the settlement of the beam relative to the supports, and occurs without any lateral stiffness. This allows the specimen to freely expand outwards inside the support until the lateral restraint of the support is engaged. The residual slip is dependent on the type of connection that exists between the end of the beam and the support. When a friction connection is provided by clamping the ends of the

beam, the axial compression force that develops in the beam will cause some residual slip to occur. This slip is therefore governed by the stiffness of the friction connection and the axial compression force, H . If the ends of the concrete beam are bearing on the support after the initial slip, the system will not exhibit any residual slip.

The total slip can be incorporated into the proposed analytical method by altering the first compatibility condition,

$$L_{c,ce} = L + \left(\frac{H}{K_{axial}} \right) + s_t \quad (3.12)$$

where $L_{c,ce}$ is the chord length of the centroidal axis, (H/K_{axial}) is the elastic stiffness of the support, and s_t is the total slip of the beam relative to the support. Similarly, slip can cause a beam to rotate relative to the support, and can be defined as the rotation of the ends of the beam prior to the development of the supports elastic rotational stiffness. This rotational slip can be accounted for by altering the second compatibility condition used in the proposed analysis,

$$\theta_o = \frac{M_o}{K_{rot}} + \theta_s \quad (3.13)$$

where θ_o is the total rotation of the ends of a given beam, $\frac{M_o}{K_{rot}}$ is the elastic rotation of the support, and θ_s is the additional rotation of the ends of a beam caused by slip relative to the support.

3.3.1 Influence of Lateral Slip

The lateral slip of a beam, relative to its supports, will delay the mobilization of the lateral restraint force, and will therefore have a unique influence on the response of a laterally restrained beam. To highlight this influence, the results of an analysis conducted using beam F2, illustrated in Figure 3.21, is presented in this section.

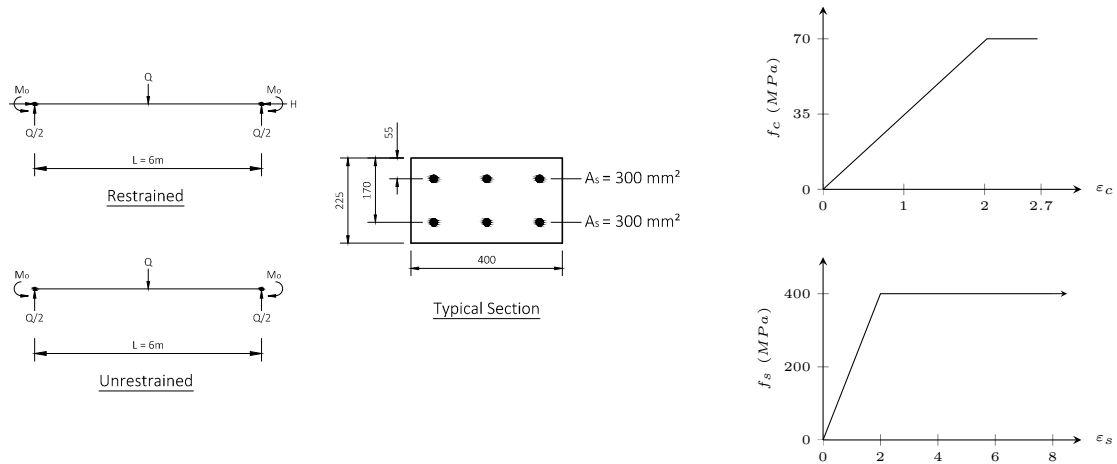


Figure 3.21: Properties of the beam F2, used to study the influence of lateral slip.

In this section, the analysis of beam F2 is conducted as:

R: Base model.

R_s : Base model, assuming $s_t = (0.5 \text{ mm}) + (H/(1000 \text{ kN/mm}))$.

U: Laterally unrestrained beam.

The influence of slip on the axial compression force developed in beam F2- R_s is illustrated in Figure 3.22. The amount of slip is represented as a ratio of the total slip to the undeformed length of the beam, s_t/L . The initial lateral slip, up to a total of 0.08 mm/m, occurs without the development of any axial compression. However once the lateral expansion exceeds 0.08 mm/m, the elastic stiffness of the support is engaged, allowing some axial compression to develop in the beam. In contrast, beam F2-R exhibits no lateral slip, and beam F2-U is free to laterally expand without the development of any axial compression.

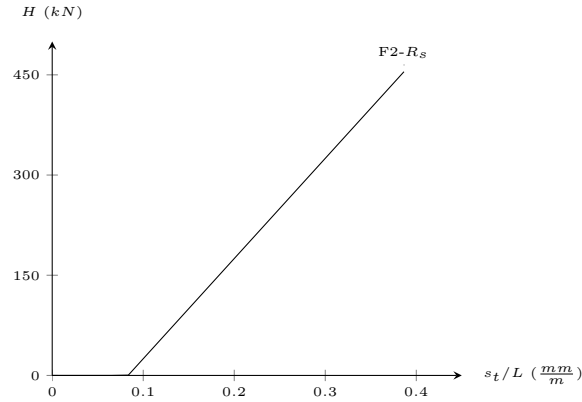
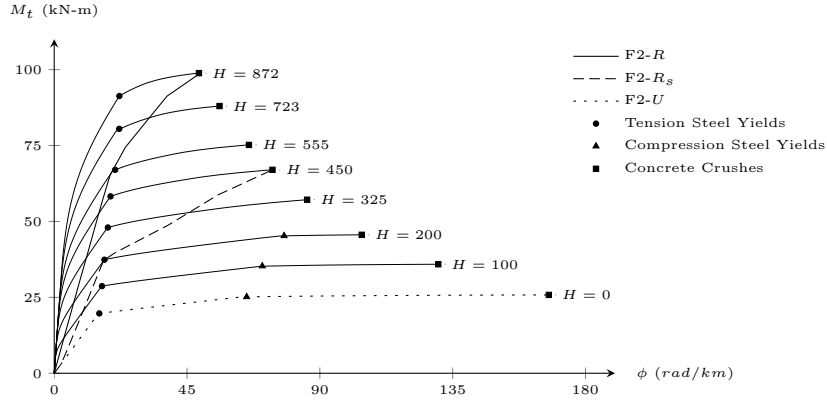


Figure 3.22: Lateral force vs. slip response in beam F2- R_s .

The moment-curvature response of beams F2-R, F2- R_s , and F2-U is presented in Figure 3.23. When there is no slip between the ends of a beam and its support, the axial compression force develops immediately. As previously indicated, the development of this axial compression force increases the stiffness and capacity of a given beam, and reduces the midspan deflection at failure. If the ends of the beam slip relative to the support, as in beam F2- R_s , then the initial response of the beam, prior to the development of axial compression, will be identical to the response of beam F2-U. However once the total lateral slip exceeds 0.08 mm/m, then an axial compression force will develop in beam F2- R_s , causing an increase in the stiffness of the beam. The initial softness due to slip causes the beam to yield at a much lower bending moment, which reduces the capacity of the beam. This indicates that even if the lateral slip is less than half a percent of the total length of the beam, it can cause a significant change in the response.

Figure 3.23: M - ϕ response of beam F2, considering slip at supports.

The load-deflection and load-restraint response of beam F2- R , F2- R_s and F2- U is presented in Figure 3.24a and Figure 3.24b, respectively. The lateral slip in beam F2- R_s reduces the axial compression developed in the beam by a factor of 1.9, from 872 kN in beam F2- R to 455 kN in beam F2- R_s . This reduction in axial compression causes the capacity to decrease by a factor of 1.5, from 114 kN in beam F2- R to 78 kN in beam F2- R_s . In addition, this slip increases the midspan deflection of beam F2 at failure by a factor of 1.3, from 31 mm in beam F2- R to 40 mm in beam F2- R_s . The response of F2- U , which is discussed in Chapter 2, illustrates how significant the lateral slip considered in this example can be, even though it is less than half a percent of the total length of the beam. The influence of lateral slip is studied in detail in a parametric study presented in Chapter 5.

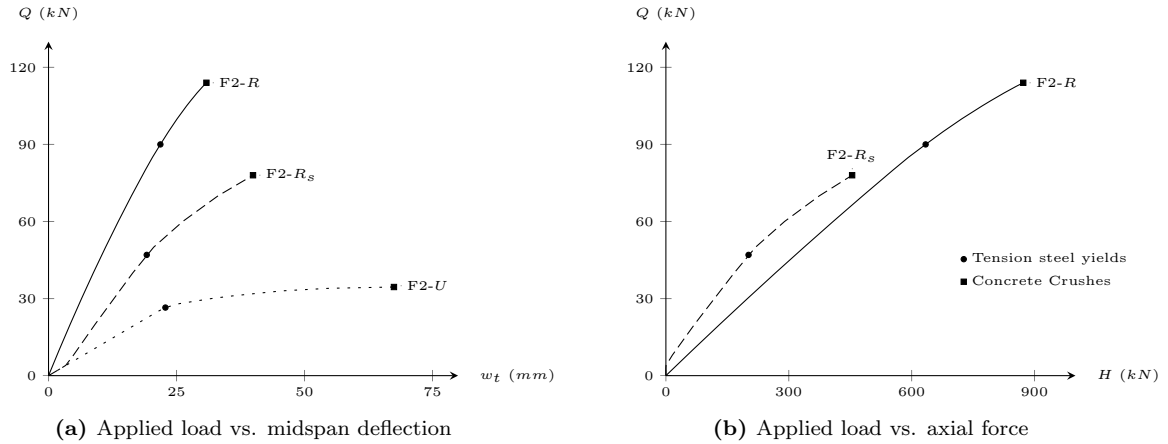


Figure 3.24: Influence of lateral slip on the response of beam F2.

3.3.2 Conclusion

The total lateral slip between the ends of a beam and its support is comprised of two components. The first component of slip occurs prior to the development of any lateral restraint force. The second component of slip accounts for any residual slip between the beam and its support. Relative slip between the ends of a beam and its supports can also cause a rotational slip to occur. The lateral and rotational

slip can be incorporated into the proposed analytical model by altering the compatibility conditions to allow for some lateral expansion and rotation of the ends of a beam.

As indicated in this section, lateral slip amounting to less than half a percent of the total length of a beam can have a significant influence on stiffness, capacity and deflection at failure. Based on the response from the sample analysis, allowing for lateral slip in beam *F2*:

1. Reduces the capacity by a factor of 1.5.
2. Reduces the peak axial compression by a factor of 1.9.
3. Increases the peak midspan deflection by a factor of 1.3.

It can therefore be concluded that accounting for the influence of any potential slip in the supports can increase the accuracy of the predicted response of a beam.

3.4 Bond Deterioration

The beam specimens tested by Su, Tian, and Song (2009) consist of three column stubs with two intermediate beam segments, representing a two-bay frame. The typical test setup for these specimens is presented in Figure 3.25.

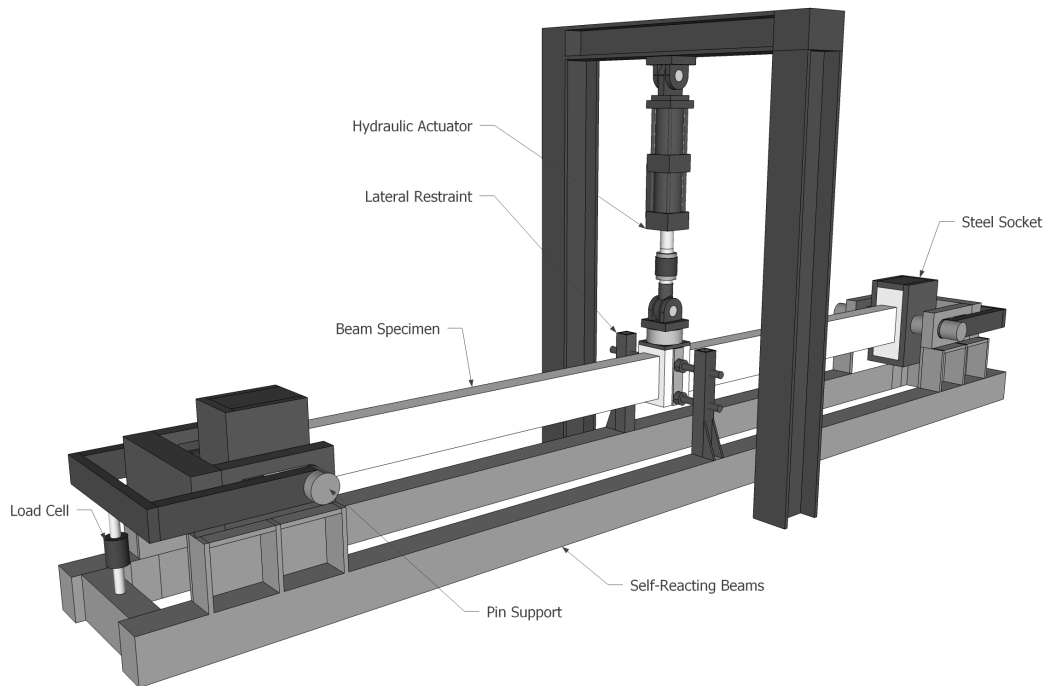


Figure 3.25: Test setup for S-Series experiment, adapted from Su(2009)

The column stubs at the midspan and support are internally reinforced with vertical bars and hoop reinforcement, as illustrated in Figure 3.26. This reinforcement confines the concrete in the column

stubs. The end column stubs are encased in a steel socket that clamps the beams, providing vertical and lateral support. Similarly, a loading plate is placed on top of the middle column stub, and steel plates are attached to each side for the out-of-plane restraints, illustrated in Figure 3.25. The testing conducted by Su, Tian, and Song (2009) found during testing, that the middle column stubs did not significantly deform. Therefore, the internal and external confinement provided by the reinforcement and the test setup limit the deformation of the concrete in the middle and end column stubs.

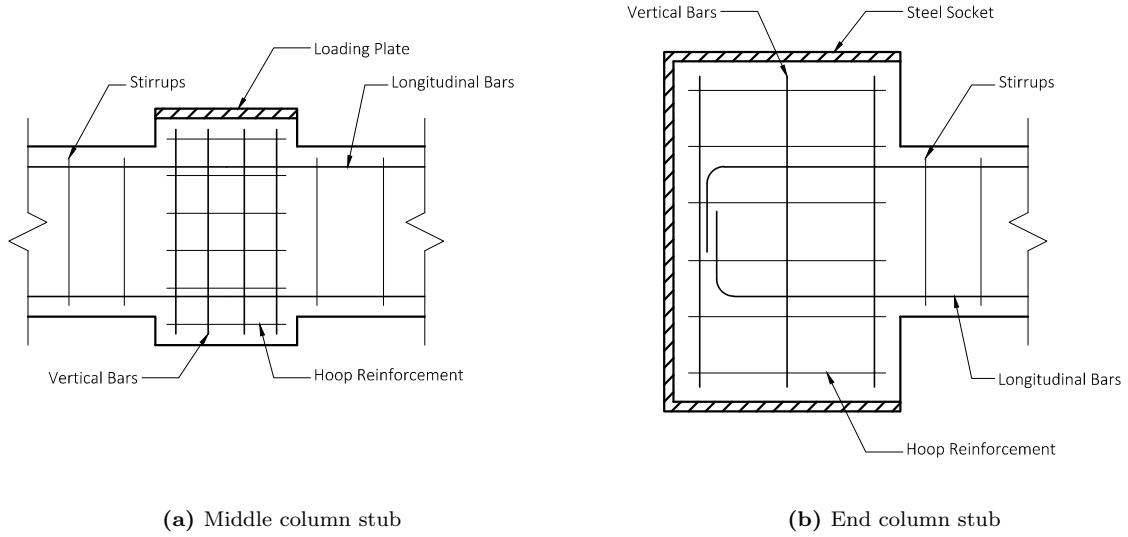


Figure 3.26: Reinforcement layout in the column stubs, adapted from Su (2009).

The beam segments that frame into the column stubs undergo large deformations prior to the failure of each specimen (Su, Tian, & Song, 2009). A truss model formulation for the middle column stub is presented in Figure 3.27a. The strain in the reinforcement, ε_s , increases gradually in the fan region up to a peak at approximately the interface of the beam segment and the column stub. This truss model formulation suggests that the strain in the reinforcement throughout the middle column stub will remain constant. The hoop reinforcement and loading plate, illustrated in Figure 3.26a, confine and prevent the expansion of the concrete. This reduces the relative magnitude of the strain in the concrete at the level of the steel, $\varepsilon_{c,s}$, as estimated in Figure 3.27a.

A truss model formulation for an end column stub is presented in Figure 3.27b. The tension force in the reinforcement increases throughout the fan region, up to a peak strain near the interface of the beam segment and column stub. The tensile stress in the reinforcement continues into the column stub for a length of d_{st} , which is discussed later in this section.

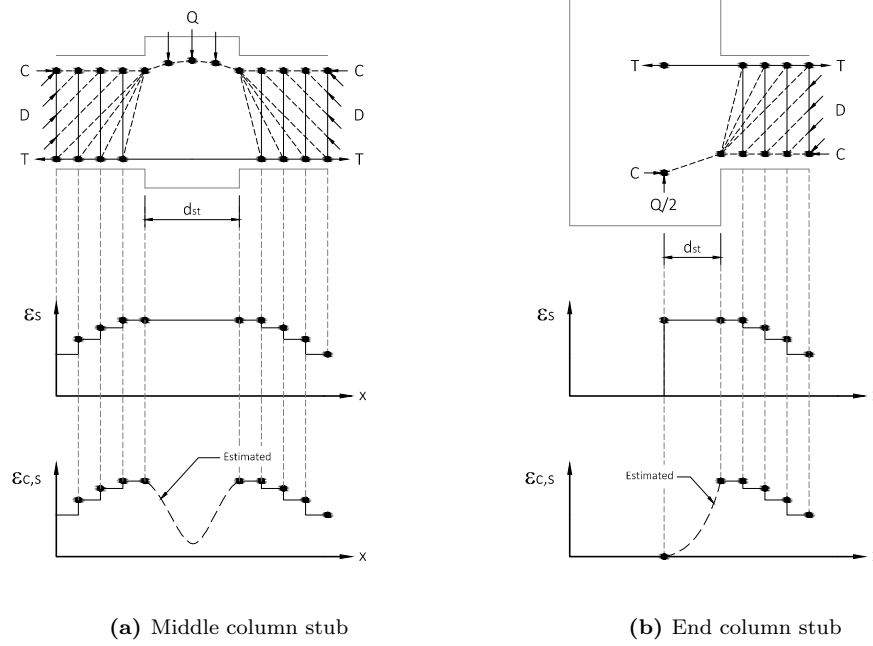


Figure 3.27: Strain penetration in the column stubs.

The variation between the strain in the concrete and the reinforcement indicates that the bond between the reinforcement and the concrete may degrade as the strain in the reinforcement increases. This bond degradation is often referred to as strain or yield penetration. Mayer and Eligehausen (1998) suggest that strain penetration increases the rotation of a beam that frames into a larger concrete section, resulting in a reduced stiffness and increased deflections of up to 35 percent. Similarly, Sritharan, Priestley, and Seible (2000) concluded that ignoring the influence of strain penetration will result in inaccurate predictions of strain contours, compression force flows, crack patterns and force transfers between elements used in finite element analysis formulations.

A number of empirical methods have been developed to quantify the effects of strain penetration (Mayer & Eligehausen, 1998). These methods are based on pull-out testing done on reinforcement with insufficient anchorage lengths. Failure in these tests is governed by slip in the anchorage at low, elastic strains. When the reinforcement is anchored well, slip will occur due to large inelastic strains within the reinforcement. Therefore the bond behaviour models traditionally used may not be appropriate for use in determining the effects of strain penetration, as suggested by Mayer and Eligehausen (1998) and Shima, Chou, and Okamura (1987).

3.4.1 Simplified Bond Deterioration Model

The proposed analytical model is formulated assuming a smeared crack model, which requires that the strain in the concrete at the level of the reinforcement, $\varepsilon_{c,s}$, be equal to the strain in the reinforcement, ε_s . This assumption of perfect bond remains true for most reinforced concrete structures. However in

structures with geometric irregularities, such as the beams tested by Su, Tian, and Song (2009), the bond between the concrete and the reinforcement can deteriorate. The implementation of a comprehensive bond model requires significant alterations to the current formulation to allow for discrete cracking, and would require that a bond-stress model be defined empirically.

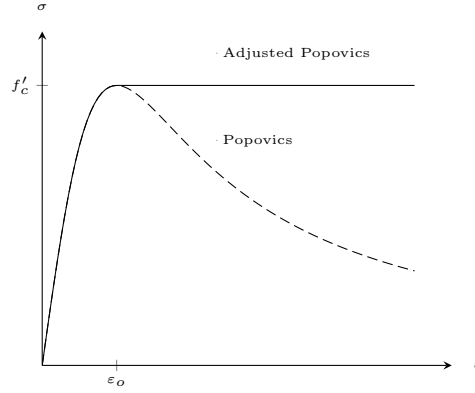
Alternatively, a simplified method of accounting for the effects of bond deterioration can be implemented into the proposed analytical method. The simplified method, developed specifically for the Su, Tian, and Song (2009) specimens, makes the following assumptions,

1. The beam segments are considered continuous throughout the middle stub, and extend a distance of d_{st} into the end column stubs.
2. The curvature at sections within the column stubs can be approximated by assuming $\varepsilon_{c,s} = \varepsilon_s$.
3. The concrete in the column stub regions maintains peak stress after peak strain.

At the middle column stub, the compression and tension chord remain within the geometry of the beam segment, as illustrated in Figure 3.27a. The depth of strain penetration at the middle column stub, d_{st} , is assumed to be equal to the width of the middle column stub. Similarly, the compression and tension chords from the beam segment extend into the end column stubs, as illustrated in Figure 3.27b. The depth of strain penetration, d_{st} , will vary based on the magnitude of inelastic strain in the reinforcement. To simplify the model, this length is assumed to be equal to the distance to the vertical pin support. Based on the test data presented in Chapter 4, this assumption is found to provide a reasonable representation of the depth of strain penetration.

The second assumption states that the curvature in the stub regions, determined assuming $\varepsilon_{c,s} = \varepsilon_s$, will be approximately the same as the curvature in the same segment when the expansion of the concrete on the tension side is prevented by internal and external confinement. The bond degradation only occurs over a short length relative to the length of the beam, and the bond is maintained on either end of the unbonded segment. Therefore, the strain in the reinforcement will be the approximately the same, regardless of whether the concrete expands, $\varepsilon_{c,s} = \varepsilon_s$, or does not deform with the reinforcement, $\varepsilon_{c,s} \neq \varepsilon_s$.

The third assumption states that the concrete in the stub regions maintain peak stress after peak strain, as illustrated in Figure 3.28. In the tests conducted by Su, Tian, and Song (2009), each specimen is supported at the end column stubs, and the load is applied to the middle column stub. This causes large bending moments to develop in the stub regions. The first assumption requires that the curvature in the stubs be determined based on the section properties of the beam segment. This would cause the model to predict that failure will occur within these regions. As indicated by Su, Tian, and Song (2009), the column stubs do not exhibit large deformations, and failure occurs at the interface of the beam segment and the column stub. As previously indicated, the stubs are heavily confined both internally and externally. It is likely that the concrete in the stub regions will be able to maintain stress at large strains. However, this cannot be quantified without more information. Therefore, the final assumption can be implemented into the proposed model to account for this confinement, and prevent failure from occurring in the stub regions.

Figure 3.28: Adjusted σ - ε response of concrete in the column stubs.

3.4.2 Influence of Bond Deterioration

The influence of bond deterioration can be understood by considering the response of beam BD, with properties summarized in Figure 3.29. The material and geometrical properties are based on specimen S1 from the Su, Tian, and Song (2009) experiments, discussed in detail in Chapter 4. The beam is assumed to be comprised of two beam segments, connected to three column stubs, similar to the specimen illustrated in Figure 3.25. The column stubs at the ends of the beam extend 150 mm from the support, and the stub at midspan extends 125 mm outwards from the applied load. Similar to the experiments by Su, Tian, and Song (2009), the load is assumed to be uniformly applied along the length of the middle stub.

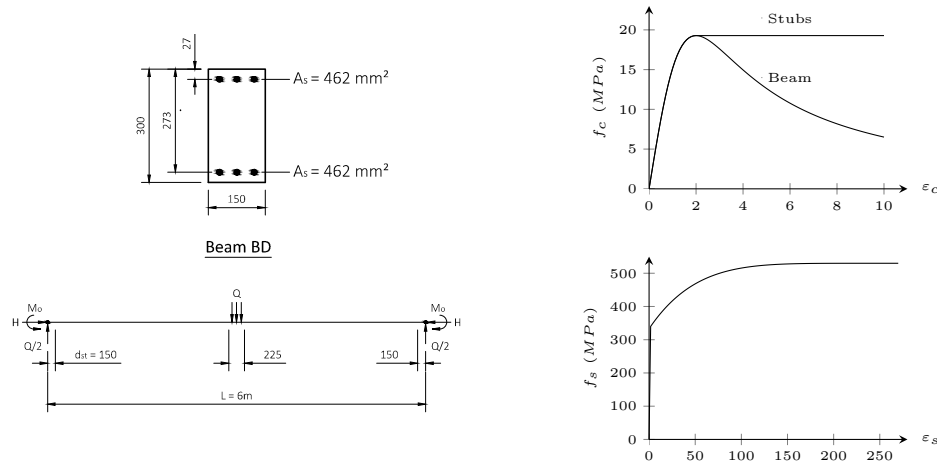


Figure 3.29: Properties of beam BD, used to study the influence of bond deterioration.

For this example, the analysis of beam BD is conducted as:

R: Base model, with no strain penetration. The beam remains perfectly rigid within $d_{st} = 150$ mm from the support, and $d_{st} = 125$ mm from the concentrated load.

B: Base model, with strain penetration. The simplified bond deterioration model is applied within $d_{st} = 150$ mm from the support, and $d_{st} = 125$ mm from the concentrated load.

The applied load vs. midspan deflection response of beam BD, with and without consideration of strain penetration, is presented in Figure 3.30a. Accounting for bond deterioration near the supports and the midspan of beam BD causes the peak applied load to reduce by a factor of 1.03, from 91 kN in beam BD-R to 88 kN in beam BD-B. Bond deterioration also causes the peak midspan deflection to increase by a factor of 1.8, from 17 mm in beam BD-R to 30 mm in beam BD-B. This response indicates that accounting for strain penetration has a significant influence on the rotation at the supports and at midspan, increasing the deformations throughout the beam. However, there is minimal influence on the capacity of the beam, as failure occurs at the interface of the beam segment and column stub in both beams.

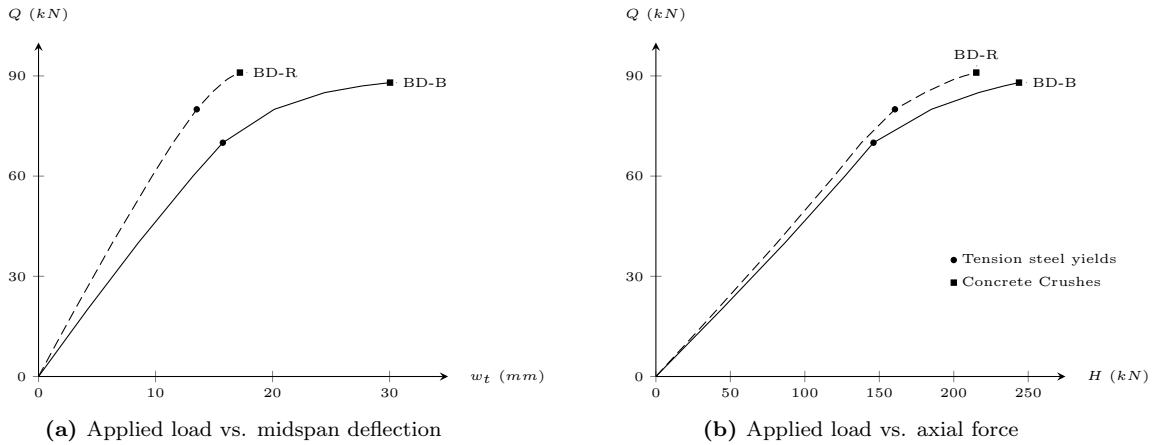


Figure 3.30: Influence of bond deterioration on the response of beam BD.

The applied load vs. axial restraint response of beams BD-B and BD-R is presented in Figure 3.30b. Accounting for bond deterioration increases the peak axial compression in the beam by a factor of 1.1, from 215 kN in beam BD-R to 244 kN in beam BD-B. The increased axial compression in the beam is caused by the additional lateral expansion within the stub regions, d_{st} . Based on the response, it can be concluded that the increased capacity caused by an increase in axial compression at each section is countered by the increased second-order effects caused by the larger midspan deflection of beam BD-B. This causes beam BD-B to have a slightly lower capacity, relative to beam BD-R.

The influence of the proposed bond model on the deflection of beam BD can be understood by considering the curvature throughout beams BD-B and BD-R, presented in Figure 3.31 for an applied load of $Q = 80$ kN. In beam BD-R, the middle and end column stubs are assumed to remain rigid, and therefore the curvature in these regions is equal to zero. Alternatively in beam BD-B, the curvature within the column stubs is determined using the simplified bond model. The increased curvature in the stub regions, caused by strain penetration, increases the deformations in the beam. For this example, the curvature is largest in the end column stubs, as a result of the uniformly applied load, and failure occurs at the interface of the beam segments and the end column stubs.

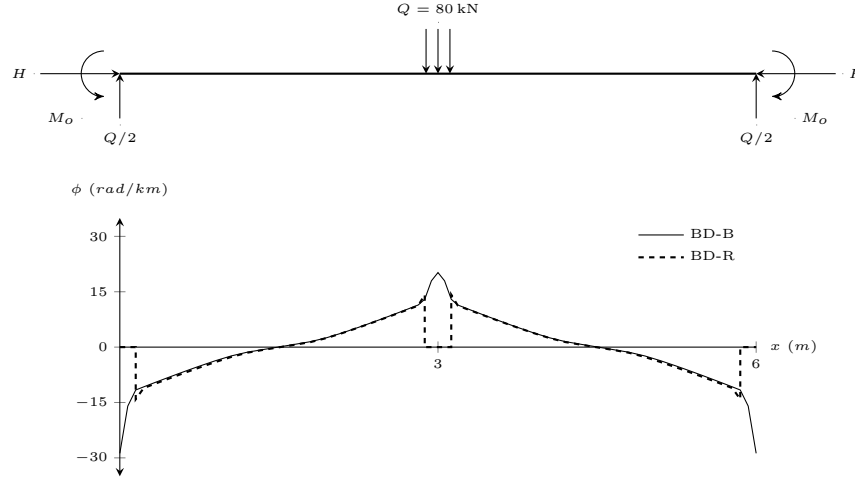


Figure 3.31: Influence of bond deterioration on the curvature in beam BD, at $Q = 80$ kN.

3.4.3 Conclusion

In the specimens tested by Su, Tian, and Song (2009), the reinforcement at the interface of the middle and end column stubs develop large inelastic strains. The concrete in the column stubs is confined internally by reinforcement, and externally by the test setup, limiting expansion. This results in bond degradation in the column stub regions. Accounting for bond deterioration using traditional methods, such as implementing a bond stress-slip model, would require significant alterations to the proposed analytical model, which is based on a smeared crack formulation. Therefore, a simplified method for accounting for strain penetration is developed based on the experiments conducted by Su, Tian, and Song (2009).

This method assumes that the additional rotation in the end and middle stubs can be approximated based on the curvature that would develop in the stub regions if the concrete was able to expand. This model requires that the concrete remain perfectly plastic after the peak compressive stress, to prevent failure from occurring in the column stubs. This is consistent with findings from the tests by Su, Tian, and Song (2009). Using a sample analysis, the bond deterioration model is shown to have minimal influence on capacity while increasing the deflection of a beam by 80 percent. The validity of this model is discussed in Chapter 4 where the predicted response of the proposed analytical model is compared to test data from experiments by Su, Tian, and Song (2009) and Yu and Tan (2013).

4

Experimental Validation

This chapter presents the results of an experimental validation conducted using test data from experiments by Su, Tian, and Song (2009) and Yu and Tan (2013). Both of these experiments investigate the progressive collapse mechanism of reinforced concrete frame beams. All the specimens tested consist of three column stubs separated by two beam segments. Each specimen is vertically, laterally and rotationally restrained at the outer column stubs, and a vertical load is applied monotonically on the middle column stub until failure. In both experiments, emphasis is placed on ensuring that the supports prevent any rotation or lateral displacement of the ends of each specimen.

Throughout this chapter, the Su, Tian, and Song (2009) experiment is referred to as the “S-Series”, and the Yu and Tan (2013) experiment is referred to as the “Y-Series”. For each experiment, the test setup of each specimen is first discussed. Following this, the properties of each specimen are presented, and the test data is discussed. Finally, the predicted response, generated using the proposed analytical model and Wu’s model, is compared to the test data from each specimen.

This validation is conducted using the refined version of the proposed analytical model. The refined model is based on the base model presented in Chapter 2, but accounts for the refinements presented in Chapter 3. These include:

1. The elastic rotational and lateral stiffness of the supports are incorporated using a rotational and linear spring, as indicated in Section 3.1.
2. The influence of diagonal compression field action is included to account for the horizontal component of the diagonal compression struts, based on the procedure presented in Section 3.2.
3. The slip at the end of each precast specimen, relative to the supports, is estimated based on the test data. This slip is incorporated using the procedure presented in Section 3.3.
4. The bond degradation between the reinforcement and concrete, caused by the internal and external confinement of the concrete in the column stubs, is incorporated into the analysis using the procedure presented in Section 3.4.

4.1 S-Series

This section presents and discusses the results of the restrained beam specimens tested by Su, Tian, and Song (2009). The proposed analytical model is used to predict the response of four out of the twelve reinforced concrete beams. These four beams are chosen to study the influence of varying span length, and concrete strength. To illustrate the importance of the model refinements presented in Chapter 3, the predicted response of each beam, generated using the refined model is compared to the predicted response generated using both the base model and Wu's model.

4.1.1 Test Setup

The S-Series experiment consisted of a total of twenty four precast reinforced concrete beam specimens with varying concrete strength, reinforcement ratio, span length, loading rate and support stiffness (Su, Wang, et al., 2009). The test data from twelve of these beams, which were laterally and rotationally restrained, were presented in the paper by Su, Tian, and Song (2009). The experimental test setup, illustrated in Figure 4.1, simulates the response of a two-bay frame after the middle column has been removed. Each beam specimen was cast separately, and placed into the support setup. The column stubs at each end of the specimen were anchored into steel sockets using steel plates and high strength bolts. Each socket was vertically supported by a pin assembly located near the inside face of the column stub. The bending restraint of the support was provided by a second vertical support located behind the end stub. The steel socket was rigidly attached to the support setup, which consisted of two self-reacting frame beams, to provide lateral restraint. Load cells were installed in both the vertical and horizontal supports to isolate and measure the reaction forces. Two supports were placed at the middle stub to prevent any out-of-plane rotation of the specimen during testing.

A displacement controlled load was applied at the center column stub using a servo-controlled actuator, reacting against a rigid loading frame. For each specimen, the displacement was increased monotonically until failure. A schematic of the test setup is presented in Figure 4.2. The clear distance between the middle and end column stub, L_n , represents the length of each beam segment. The end column stubs extend 400 mm into the steel sockets located at each support.

During testing, the elastic stiffness of the steel sockets was measured. The rotational stiffness, defined as the bending moment required to produce a unit rotation, was approximately equal to 17 500 kNm/rad. The axial stiffness, defined as the lateral force required to produce a horizontal unit displacement, was approximately equal to 1000 kN/mm. It is unclear if the measured stiffness accounts for the flexibility in the steel sockets, at what locations the rotations are referenced from, or how consistent the support stiffness was throughout the entire testing program.

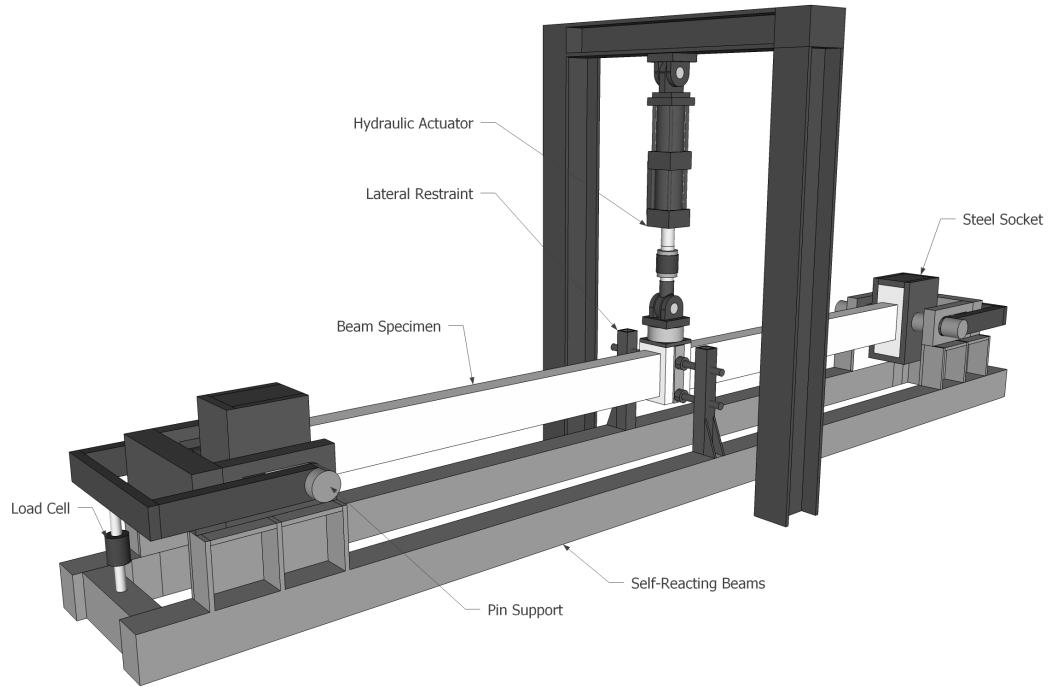


Figure 4.1: Test setup for S-Series experiment, adapted from Su (2009).

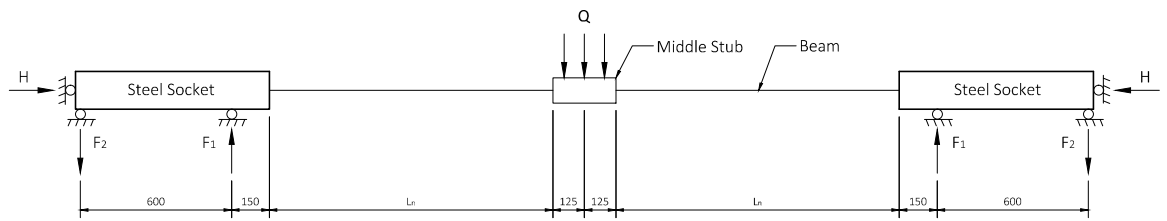


Figure 4.2: Schematic of the setup for each specimen, adapted from Su (2009).

4.1.2 Specimen Properties

The typical geometric layout of each test specimen from the S-Series experiments is presented in Figure 4.3. Each specimen consists of two beam segments, with a length of L_n , separated by column stubs at midspan and the supports. The typical reinforcement layout of each specimen is also included.

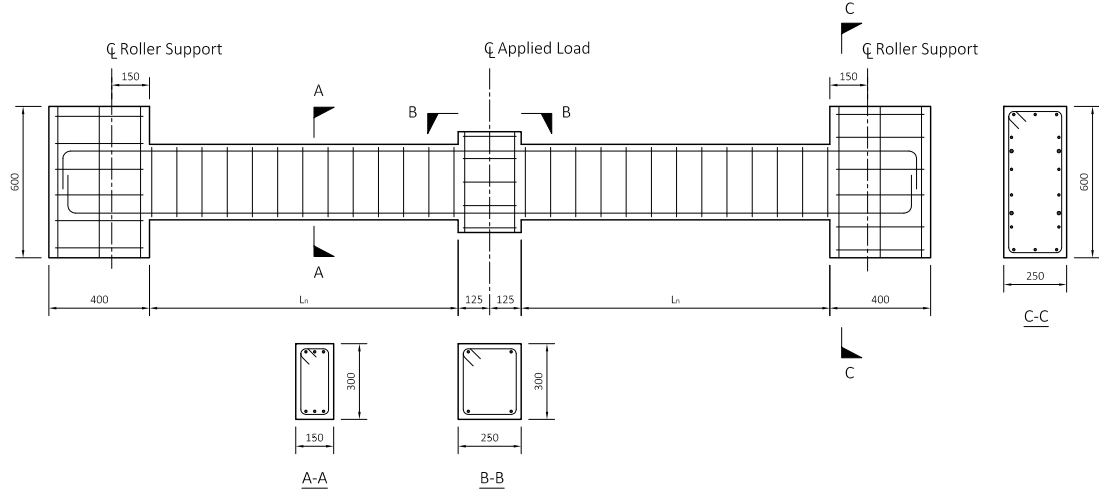


Figure 4.3: Geometric and reinforcement layout of specimens, adapted from Su (2009).

Of the twelve specimens tested by Su, Tian, and Song (2009), six were used to study the influence of reinforcement ratio, three were used to study the influence of span-to-depth ratio, and three were used to study the influence of increasing loading rate. Loading rate is not a consideration in the proposed analytical model, and therefore these specimens are not considered. To provide insight into the influence of varying concrete strength, reinforcement ratio and span-to-depth ratio, four of the beam specimens from these tests were selected for this validation. The properties of the selected beams are summarized in Table 4.1.

Table 4.1: S-Series beam properties, adapted from Su (2009).

Label	Ref.	L_n mm	L mm	L/h	f'_{cc} MPa	f'_c MPa	Longitudinal		Stirrups
							Top	Bottom	
S1	B2	2725	6000	20	24.1	19.3	3-14 ϕ	3-14 ϕ	8 ϕ @ 120 mm
S2	B3	2725	6000	20	26.4	21.1	3-14 ϕ	2-14 ϕ	8 ϕ @ 120 mm
S3	B1	1975	4500	15	23.2	18.6	3-14 ϕ	3-14 ϕ	8 ϕ @ 100 mm
S4	A3	1225	3000	10	39.0	31.2	3-14 ϕ	3-14 ϕ	8 ϕ @ 80 mm

The labels used by Su, Tian, and Song (2009) to identify each specimen are included for reference. The span length of each specimen, L , is defined as the total horizontal distance between the vertical roller supports. Therefore, the span-to-depth ratio is defined as the ratio of L to the height of the beam segment, equal to 300 mm in each specimen, as illustrated in Figure 4.3. The equivalent cylinder compressive strength of concrete in each specimen, f'_c , is assumed to be equal to 80% of the cube

compressive strength of concrete, f'_{cc} , provided by Su, Tian, and Song (2009). The concrete cover specified for each specimen is equal to 20 mm, measured to the longitudinal reinforcement.

As indicated by Su, Tian, and Song (2009), the beam segments consist of longitudinal reinforcement that is continuous through the center stub, as well as closely spaced stirrups, to avoid premature failure caused by reinforcement discontinuity and shear distress. The material properties for the longitudinal and transverse reinforcement specified in Table 4.1 are summarized in Table 4.2. The σ - ε response of the concrete and steel reinforcement is not provided by Su, Tian, and Song (2009).

Table 4.2: S-Series reinforcement properties, adapted from Su (2009).

Label	d_b	A_s	f_y	f_u	ε_u
	mm	mm ²	MPa	MPa	%
8ϕ	8	50	290	455	33
12ϕ	12	113	350	540	26
14ϕ	14	154	340	535	27

The stirrups consist of smooth steel bars with a diameter of 8 mm, while the longitudinal reinforcement consists of deformed steel bars with diameters of 12 and 14 mm. The longitudinal reinforcement is anchored into each end block using a standard hook with a development length specified based on ACI 318-05 (American Concrete Institute, 2005). The quantity and arrangement of the reinforcement in the middle and end column stubs is not discussed by Su, Tian, and Song (2009).

4.1.3 Measured Response of the Test Specimens

The test data used for this validation is based on the original experimental paper which was published in Chinese (Su, Wang, et al., 2009). The English translation of the paper, by Su, Tian, and Song (2009), presents test data that is inconsistent with the test data provided by the Chinese paper. Based on the predicted response of the analytical model, it is assumed that the test data provided by Su, Wang, et al. (2009) is correct.

The load-deflection and restraint-deflection response of the beams in the S-Series are presented in Figure 4.4. In beams S1, S2 and S3, the softening caused by second-order effects allows large deformations to occur prior to failure. The failure load of these three beams, Q_{fail} , is larger than the first peak in the applied load, Q_{peak} . Alternatively, beam S4 exhibits a sudden loss of capacity after the peak lateral restraint load, H_{peak} , causing Q_{fail} to be significantly lower than Q_{peak} .

In all specimens, Q_{peak} occurs prior to H_{peak} . This is consistent with the findings from Section 2.9, which suggest that the difference in the deflection at Q_{peak} and H_{peak} is caused by second-order effects. Increasing the span-to-depth ratio from 10 in beam S4, to 20 in beam S1, increases the difference between the midspan deflection at Q_{peak} and H_{peak} by a factor of 4.6, from $w_t/L = 0.05$ in beam S4 to $w_t/L = 0.23$ in beam S1. This indicates that increasing span-to-depth ratio increases the influence of second-order effects. In addition, reducing the span-to-depth ratio from 20 to 15 increases Q_{peak} by a factor of 1.5, from 82 kN in beam S1 to 126 kN in beam S3. Further reducing the span-to-depth ratio

from 15 to 10, in conjunction with a 70 percent increase in concrete strength, increases Q_{peak} by a factor of 1.9, from 126 kN in beam S3 to 245 kN in beam S4.

Reducing the span-to-depth ratio from 20 to 15 increases H_{peak} by a factor of 1.1, from 212 kN in beam S1 to 235 kN in beam S3. However, increasing the strength of the concrete by 70 percent, in addition to reducing the span-to-depth ratio from 15 to 10, increases H_{peak} by a factor of 1.3, from 235 kN in beam S3 to 304 kN in beam S4. This indicates that increasing the strength of concrete increases the lateral restraint force developed at the supports, which increases the beneficial effects of arching action. This is studied in detail in the parametric study presented in Chapter 5.

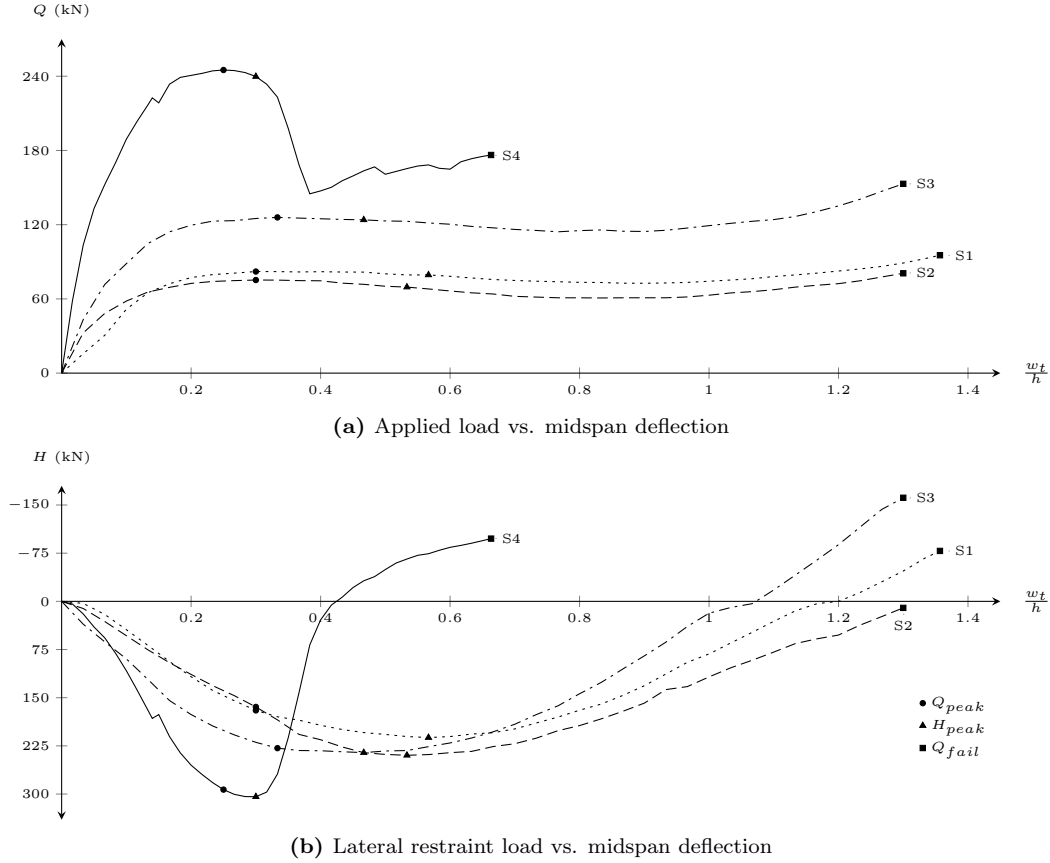


Figure 4.4: Response of specimens from S-Series experiment, adapted from Su (2009).

When the load is first applied, each specimen exhibits an initial softness in the load-deflection and restraint-deflection response. The softness in the load-deflection response is caused by some initial rotational slip between the end column stubs and the supporting steel socket. Similarly, the softness in the restraint-deflection response is assumed to be caused by some initial lateral slip between the end column stubs and the supporting steel socket. This behaviour is discussed individually for each specimen.

4.1.4 Predicted Response using the Proposed Analytical Model

The load-deflection and restraint-deflection response of each specimen in the S-Series validation is predicted using the refined version of the proposed analytical model. In this subsection, the model formulation and predicted response of beams S1, S2, S3 and S4 are presented.

Beam S1: Model Setup

The σ - ϵ response of the concrete used in the analytical model is presented in Figure 4.5. This response is based on the model developed by Popovics (1973), which only requires that the peak compressive stress of the concrete be known, as is the case for this experiment. Since this formulation is two-dimensional, the entire width of the cross section is assumed to be confined between the center of the reinforcement at the top and bottom of the beam. The cover concrete at the top and bottom of each section remains unconfined. The σ - ϵ response of the confined concrete is estimated using the model developed by Mander et al. (1988).

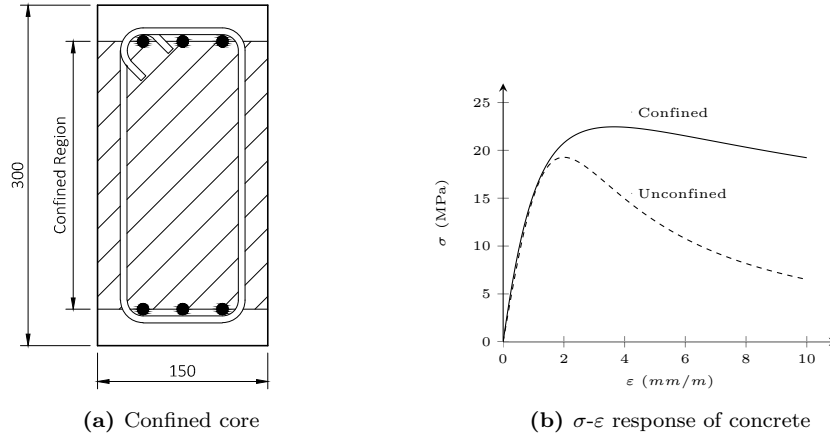
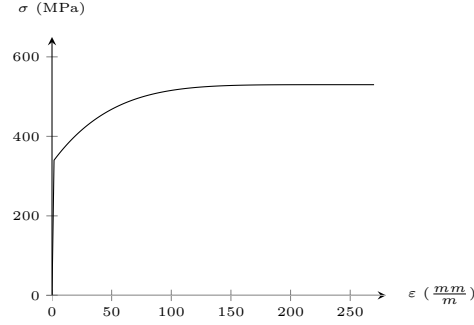


Figure 4.5: σ - ϵ response of concrete in specimen S1.

The behaviour of the reinforcement in tension and compression, presented in Figure 4.6, is estimated based on the model developed by Mander (1983). No information is provided regarding the existence of a yield plateau. As discussed in Section 2.9, incorporating a yield plateau in the σ - ϵ response of reinforcement can, in some cases, cause a numerical instability to occur. This instability is caused by a dip in the moment-curvature response, which cannot be modeled using the current formulation. However as indicated in Section 2.9, this slight dip in the moment-curvature response has little influence on the global response of the beam. Therefore, the reinforcement used in the S-Series validation is assumed to have no yield plateau.

Figure 4.6: σ - ε response of reinforcement in specimen S1.

As previously indicated, the elastic stiffness of each support was measured during testing. The little information provided by Su, Tian, and Song (2009) suggests that the rotational and lateral stiffness was based on the rotation and lateral displacement of the steel sockets, measured using a combination of load cells and linear variable differential transformers (LVDT). Since each specimen was cast outside of the steel socket, it is likely that some gaps and uneven surfaces existed between the concrete end block and the steel socket. This would allow some slip to occur at the ends of each specimen, resulting in a softening of the response at low loads.

The response of specimen S1, presented in Figure 4.4, suggests that the concrete end stub did slip, relative to the steel socket. This slip, which would not have been included in the measured elastic stiffness of the steel sockets, can be incorporated into the model using the formulation presented in Section 3.3. The lateral displacement vs. lateral restraint force of the steel socket is presented in Figure 4.7a, and is based on the measured values provided by Su, Tian, and Song (2009).

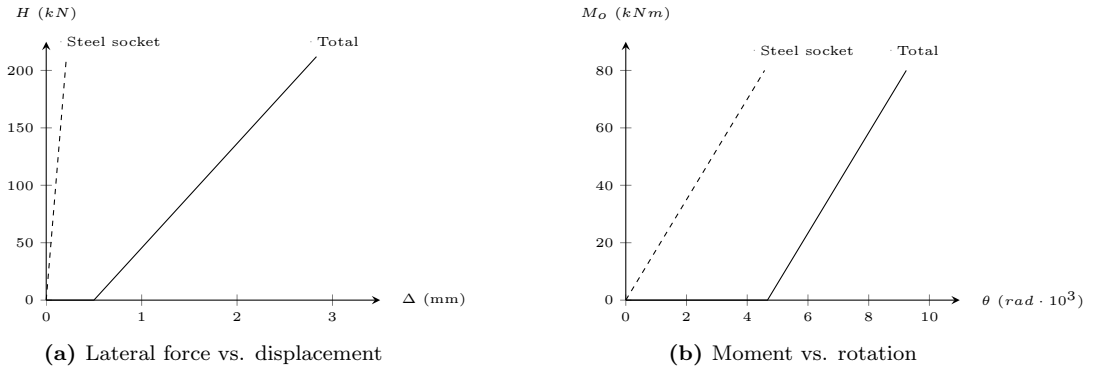


Figure 4.7: Lateral expansion and rotation of specimen S1.

The total slip between the concrete end block and the steel socket is assumed to be,

$$s_t = 0.5 \text{ mm} + \frac{H}{100 \text{ kN/mm}}$$

The amount of initial and residual slip was determined by adjusting the magnitudes to match the observed behaviour of the test specimen. The total lateral displacement vs. lateral restraint force of

the support, which includes the stiffness of the steel socket and the assumed lateral slip, is presented in Figure 4.7a. At the peak axial compression force of 212 kN, the total lateral expansion of the beam at each support is equal to 2.8 mm. Therefore, the total expansion of the entire beam is less than 0.1 percent of the length of the specimen, which is reasonable based on the test setup.

The bending moment vs. rotation of the steel socket is presented in Figure 4.7b. For specimen S1, the initial softness in the load-deflection response, illustrated in Figure 4.4, suggests that the end column stub rotated prior to the development of the rotational stiffness of the steel socket. The magnitude of the initial rotational slip, assumed to be equal to 0.0047 rad, corresponds with an initial displacement of 1.4 mm at the top and bottom of the concrete end column stub. This rotation was calibrated using the observed softness in the test data. The bending moment vs. total rotation of the end column stubs is presented in 4.7b.

To account for the influence of diagonal compression struts in each specimen, the diagonal compression field action model presented in Section 3.2 is incorporated into the analysis. This model is based on the truss model presented in Figure 4.8. The load applied to the middle column stub is assumed to transfer the shear force in the inclined struts located throughout the specimen. The compression chord in the column stubs is assumed to be inclined, allowing the shear force to transfer through the stub to the beam segment. The angle of inclination of the compressive chord is governed by the magnitude of the applied load. At the interface of each column stub and beam segment, the compression force fans out into multiple diagonal compression struts. A similar fan develops near the region where the entire depth of the beam is in compression, with length X_0 .

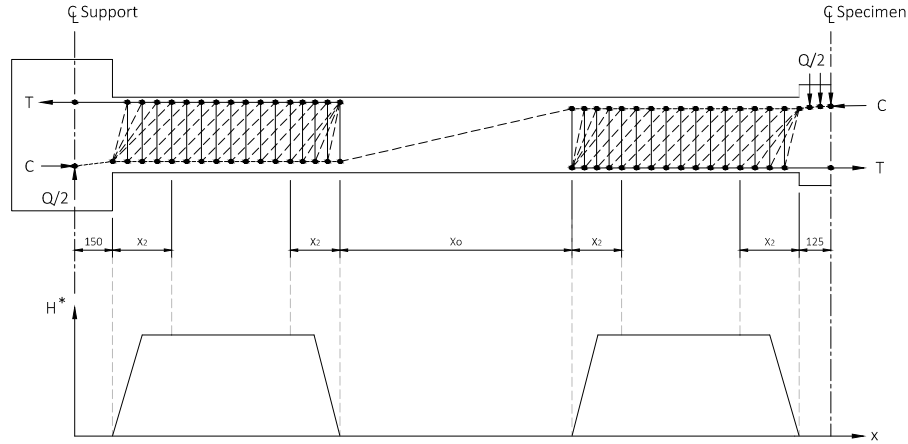


Figure 4.8: Truss model representation of specimen S1.

The horizontal component of the diagonal compression strut, H^* , is plotted along the length of specimen S1 in Figure 4.8. The length over which the entire depth of the beam is in compression is based on the vertical distance between the compression and tension resultant throughout the beam, the applied load, and the total axial compression force in the beam. The distance between the compression and tension resultant is based on the location of the resultant force predicted in the analysis, and is assumed to be

equal to 230 mm.

The diagonal struts in the B-regions are assumed to be inclined at 45° . Although there is uncertainty regarding the actual inclination of these struts, the response predicted using this assumption correlates well with test data. The influence of varying the inclination of the diagonal struts is discussed in detail in Section 5.5.

In the specimens tested by Su, Tian, and Song (2009), the reinforcement at the interface of the middle and end column stubs develop large inelastic strains. The concrete in the column stubs is confined internally by reinforcement, and externally by the test setup, limiting expansion. The quantity of reinforcement in the column stubs is unknown, but a layout of the reinforcement provided by Su, Tian, and Song (2009) indicates that both vertical bars and hoop reinforcement was provided, as illustrated in Figure 4.9. In addition, the test setup externally confines the concrete in the end column stubs, as illustrated in the test setup in Figure 4.1.

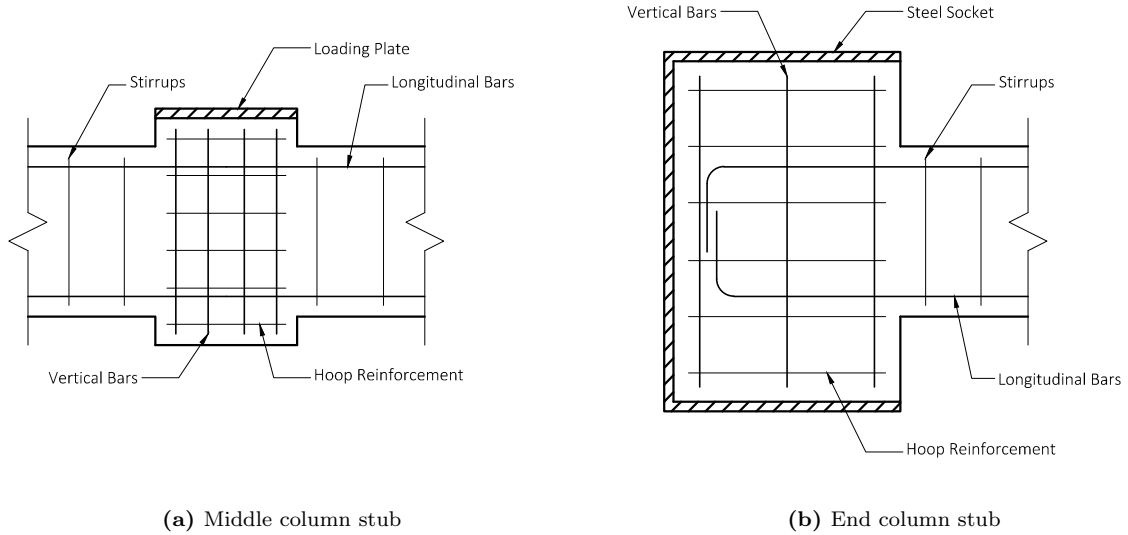


Figure 4.9: Reinforcement layout in the column stubs, adapted from Su (2009).

The large inelastic strain in the reinforcement, and the limited expansion of the concrete in the column stub, causes the bond between the reinforcement and concrete to degrade. This bond degradation, also referred to as strain penetration, is discussed in detail in Section 3.4. Accounting for bond deterioration using traditional methods, such as implementing a bond stress-slip model, would require significant alterations to the proposed analytical model, which is based on a smeared crack formulation. Therefore, a simplified method of accounting for strain penetration is developed and discussed in Section 3.4. This bond model is implemented into the proposed analytical model using the following assumptions:

1. The beam segments are considered continuous throughout the middle stub, and extend a distance of 150 mm into the end column stubs.
2. The curvature of sections within the column stubs are determined assuming $\varepsilon_{c,s} = \varepsilon_s$.

3. The concrete in the column stub regions maintains peak stress after peak strain.

This simplification provides a means to validate the proposed analytical model without having to significantly alter the formulation. However, this bond model is developed specifically for the specimens and test setup used in this experiment. Therefore, a more rigorous bond model should be developed to provide a more general formulation that can be applied in any situation. This is outside the scope of this research.

As indicated by Su, Tian, and Song (2009), the test data provided does not include the effect of self-weight. Therefore, the self-weight of each specimen is ignored in the model formulation.

Beam S1: Predicted Response of Model

The observed applied load vs. midspan deflection response of specimen S1 is presented in Figure 4.10a, alongside the predicted response generated using the refined model developed in Chapter 3, the base model developed in Chapter 2, and Wu's model developed by Wu (2013). Similarly the observed lateral restraint force vs. midspan deflection response is presented in Figure 4.10b, alongside the predictions from the three models.

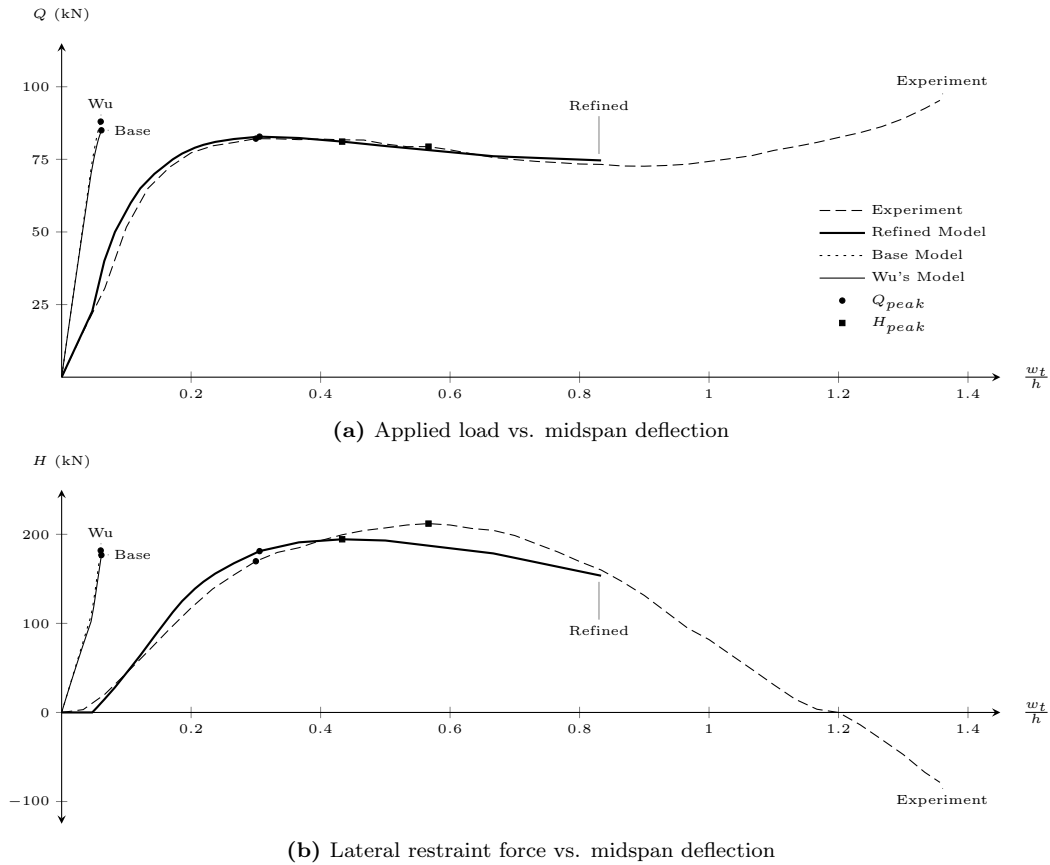


Figure 4.10: Predicted vs. observed response of specimen S1.

The peak applied load predicted by the base model and Wu's model, 85 kN and 88 kN, over-predict

the observed peak applied load, 82 kN, by a factor of 1.04 and 1.07, respectively. Similarly, the lateral restraint force at Q_{peak} predicted by the base model and Wu's model, 177 kN and 182 kN, over-predict the observed lateral restraint load at Q_{peak} , 170 kN, by a factor of 1.04 and 1.07, respectively. Both of these predictions are within ten percent of the observed behaviour of the specimen, and can be considered as reasonable predictions. However, the peak midspan deflection predicted by the base model and Wu's model, both equal to $w_t/L = 0.06$, under-predict the observed peak midspan deflection, $w_t/L = 0.3$, by a factor of 5. The lack of correlation between the predicted and observed stiffness and deflection of specimen S1 highlights the need for consideration of the refined model.

The peak applied load predicted by the refined model, 83 kN, is approximately equal to the observed Q_{peak} of 82 kN. In addition, the midspan deflection at Q_{peak} predicted by the refined model, $w_t/L = 0.31$, is within four percent of the observed deflection at Q_{peak} , $w_t/L = 0.3$. However the lateral restraint force at Q_{peak} predicted by refined model, 181 kN, over-predicts the actual magnitude of axial compression, 170 kN, by a factor of 1.06. Therefore, it can be concluded that the predicted response generated using the refined model up to Q_{peak} , correlates very well with the test data, and improves the midspan deflection at Q_{peak} predicted using Wu's method, by a factor of 5.

The predicted restraint-deflection response generated using the refined model correlates reasonably well with the observed response from the experiment. However the refined model, which predicts a peak axial compression of 194 kN, under-predicts the observed H_{peak} , 212 kN, by a factor of 1.09. More significantly, the refined model, which predicts that H_{peak} occurs at a midspan deflection of $w_t/L = 0.43$, under-predicts the observed midspan deflection, $w_t/L = 0.57$, by a factor of 1.3. Although the magnitude of the lateral restraint force is under-predicted by the refined model, the overall load-deflection and restraint-deflection response of specimen S1 correlates well with the test data.

As discussed in Chapter 2, the lateral restraint force is determined using a compatibility condition that defines the amount of lateral displacement of a beam at each support by integrating the strains along the length of the beam. In the refined model, bond deterioration is assumed to extend up to the location of the roller support. This assumption provides a reasonable estimate of the observed response of the specimen, up to the peak applied load. However, it is likely that the large in-elastic strain that develops in the reinforcement after Q_{peak} progressively deteriorates the bond between the reinforcement and the concrete beyond the location of the roller support. This increased depth of strain penetration would increase the strains in the concrete, and therefore increases the predicted lateral restraint force. However, there is a high degree of uncertainty with the state of bond in the end column stubs. With the very limited data provided by Su, Tian, and Song (2009), the actual depth of strain penetration beyond Q_{peak} cannot be predicted. However if a more rigorous bond deterioration model is adopted, then the proposed analytical model may be able to better predict the post-peak load-deflection and restraint-deflection response of the specimens in the S-Series experiment.

As discussed in Section 2.9, accounting for the combination of second-order effects and material nonlinearities can cause a numerical instability to occur. For specimen S1, this instability occurs at a midspan deflection of $w_t/L = 0.83$, limiting the ability of the refined model to predict the transition from arching action to tensile membrane action. This numerical instability can be understood by considering the family of moment-curvature diagrams for specimen S1, with increasing magnitudes of axial compression, presented in Figure 4.11. The moment-curvature response, assuming $H = 0$, indicates that after the

compression steel yields, the curvature increases by a factor of 4.5, while the bending moment only increases by a factor of 1.1 up to failure. The large increase in curvature corresponding with a small increase in bending moment increases the computational effort required to determine the actual curvature at each section. When the axial compression in the beam is increased to 150 kN, the curvature after the compression steel yields increases by a factor of 43.8, and the bending moment increases by a factor of 1.2 up to failure.

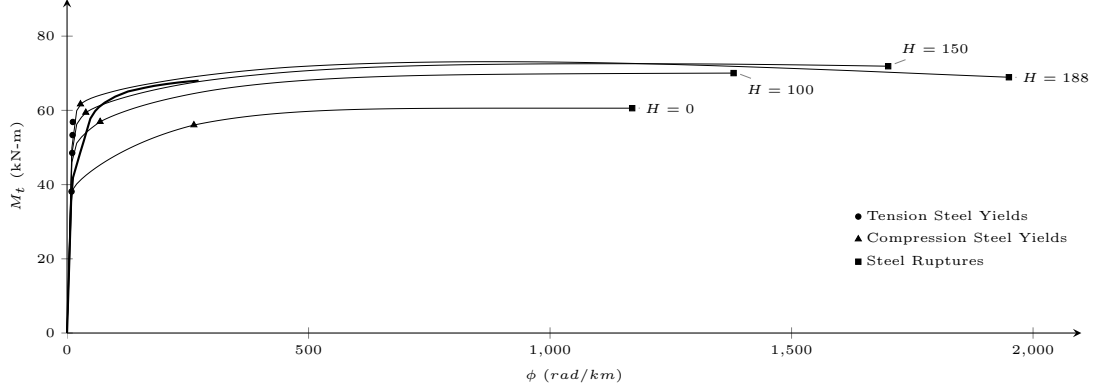
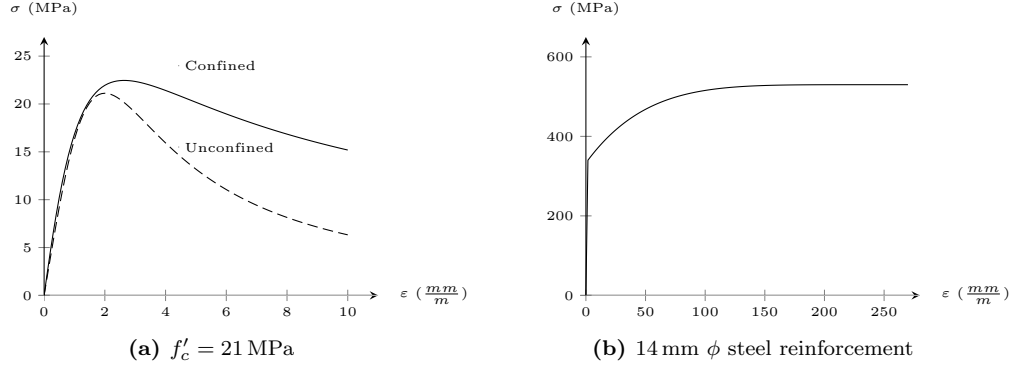


Figure 4.11: M - ϕ response of specimen S1.

The proposed analytical model determines the curvature based on the bending moment and axial compression force at each section. In cases where very small increments in bending moment cause large increases in curvature, the model becomes very unstable, particularly when predicting the response of the beam after the compression reinforcement has yielded. This is evident in the predicted moment-curvature response of specimen S1 at the interface of the beam segment and the middle column stub, presented in Figure 4.11. At a bending moment of 68 kN m, the model becomes very unstable and unable to predict the increased curvature in the beam associated with a very small increment in bending moment. To avoid this numerical instability, the proposed analytical model should be adjusted to allow for a curvature based prediction of bending moment at each section. This is outside the scope of this thesis.

Beam S2

As indicated for specimen S1, the numerical instability that develops in the analysis formulation limits the ability of the model to predict the post-peak response of the specimen. The proposed analytical model is, however, able to reasonably predict the response up to Q_{peak} . Therefore, the remaining specimens considered in this chapter are only modeled up to Q_{peak} . The constitutive material model assumed for both the concrete and reinforcement in specimen S2 is presented in Figure 4.12.

Figure 4.12: Material σ - ε response in specimen S2.

As indicated by Su, Tian, and Song (2009), the elastic stiffness of the steel socket is consistent for all specimens. The lateral restraint force vs. lateral displacement of the steel socket is presented in Figure 4.13a. However, each beam is precast and installed separately, which allows some slip to develop between the concrete end block and the steel socket. The total slip in specimen S2, estimated using the observed response, is equal to,

$$s_t = 0.5 \text{ mm} + \frac{H}{75 \text{ kN/mm}}$$

The lateral restraint force vs. total lateral displacement of the support is presented in Figure 4.13a. At a peak axial compression force of 165 kN, the total lateral expansion of the beam at each support is equal to 2.9 mm. Therefore, the total lateral expansion of the beam is approximately 0.2 percent of the length of the specimen, which is reasonable based on the test setup.

The observed response of specimen S2, presented in Figure 4.4, does not exhibit any softness in the load-deflection response. Therefore, the proposed analytical model only accounts for the elastic rotation of the steel sockets, which is based on the rotational stiffness provided by Su, Tian, and Song (2009). This is illustrated in the bending moment vs. total rotation of the sockets, presented in Figure 4.13b.

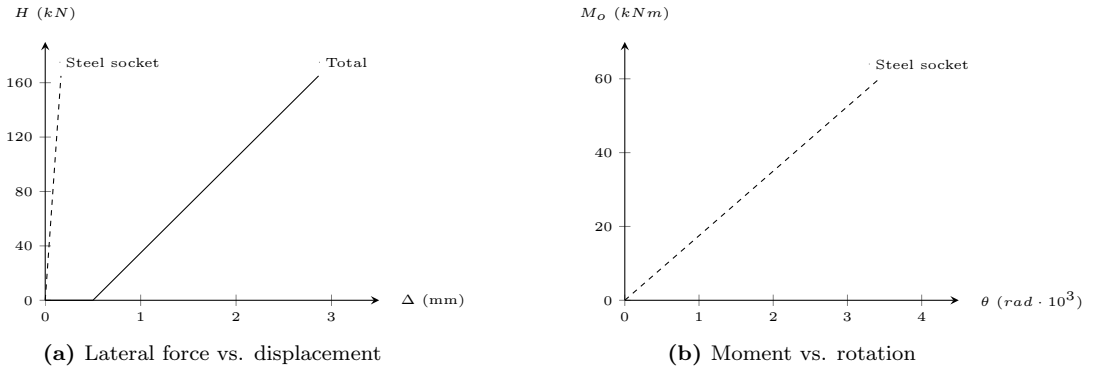


Figure 4.13: Lateral expansion and rotation of specimen S2.

The diagonal compression field action model used for specimen S2 is identical to that used for specimen

S1. In addition, the bond deterioration model developed for specimen S1 is adopted, but the depth of strain penetration into the end column stubs is assumed to be equal to 100 mm, which is two-thirds of the depth assumed for specimen S1. This adjustment was made to better fit the test data, and is reasonable based on the test setup.

The observed applied load vs. midspan deflection response of specimen S2 is presented in Figure 4.14a up to Q_{peak} , alongside the predicted response generated using the refined model, the base model and Wu's model. In addition, the lateral restraint force vs. midspan deflection response of the specimen is presented in Figure 4.14b, alongside the predicted response of the three models. The peak applied load predicted by the base model and Wu's model, 77 kN and 80 kN, over-predict the actual peak applied load, 75 kN, by a factor of 1.02 and 1.06, respectively. Both of these predictions are within ten percent of the observed behaviour of the specimen, and can be considered as reasonable predictions. The lateral restraint force at Q_{peak} predicted by the base model and Wu's model, 189 kN and 194 kN, over-predict the observed lateral restraint load at Q_{peak} , 164 kN, by a factor of 1.15 and 1.19, respectively. In addition, the peak midspan deflection predicted by the base model and Wu's model, both equal to $w_t/L = 0.053$, under-predict the observed peak midspan deflection, $w_t/L = 0.30$, by a factor of 5.66. Similar to specimen S1, the base model and Wu's model provide inaccurate predictions of the stiffness and deflection of specimen S2.

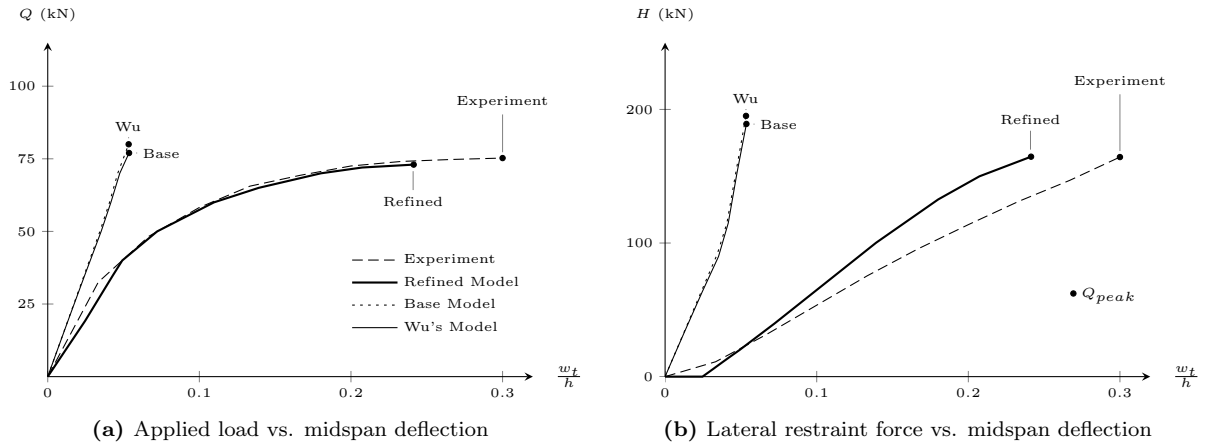


Figure 4.14: Predicted vs. observed response of specimen S2.

The peak applied load predicted by the refined model, 73 kN, is within five percent of the observed Q_{peak} of 75 kN. In addition, the lateral restraint force at Q_{peak} predicted by the refined model, 165 kN, is approximately equal to the observed lateral restraint at Q_{peak} . However, the midspan deflection at Q_{peak} predicted by the refined model, $w_t/L = 0.24$, under-predicts the observed deflection at Q_{peak} , $w_t/L = 0.30$, by a factor of 1.25. Despite the variation in the peak midspan deflection, the stiffness of the load-deflection response generated using the refined model correlates very well with the experiment. However, as previously discussed, the current formulation of the proposed analytical model becomes unstable when very small increases in applied load cause large increases in deflection. This helps to explain the under-predicted deflection.

Therefore, it can be concluded that the predicted response up to Q_{peak} , generated using the refined model, correlates well with the test data, and improves the prediction of the midspan deflection at

Q_{peak} , relative to Wu's method, by a factor of 4.5.

Beam S3

The constitutive material model assumed for both the concrete and reinforcement in specimen S3 is presented in Figure 4.15.

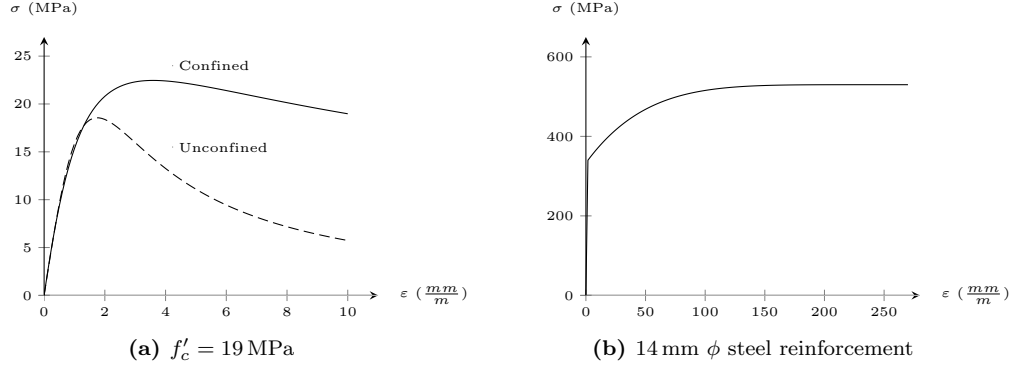


Figure 4.15: Material σ - ϵ response in specimen S3.

The total slip in specimen S3, estimated based on the test data, is equal to,

$$s_t = 0.0 \text{ mm} + \frac{H}{50 \text{ kN/mm}}$$

The lateral restraint force vs. total lateral displacement of each end stub, which includes the stiffness of the steel socket and the assumed lateral slip, is presented in Figure 4.16a.

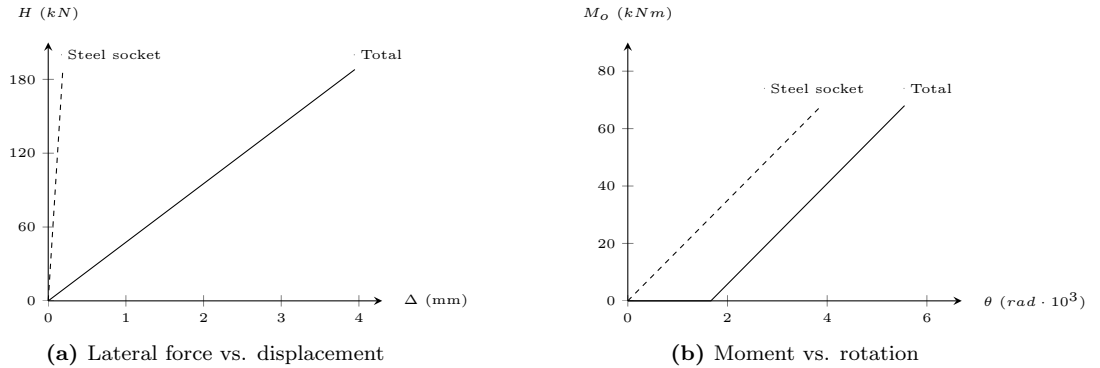


Figure 4.16: Lateral expansion and rotation of specimen S3.

At the peak axial compression force of 188 kN, the total lateral expansion of the beam at each support is equal to 3.9 mm. Therefore, the total expansion of the entire beam is less than 0.2 percent of the length of the specimen, which is reasonable based on the test setup.

The observed response of specimen S3, presented in Figure 4.4, exhibits an initial softness in the load-deflection response. The magnitude of the initial rotational slip is assumed to be equal to 0.0017 rad, which corresponds with an initial displacement of 0.5 mm at the top and bottom of the concrete end block. This rotation was calibrated based on the test data. The bending moment vs. total rotation of the end blocks is presented in 4.16b.

The diagonal compression field model, and the bond deterioration model used for specimen S3 are identical to that used for specimen S1.

The observed applied load vs. midspan deflection response of specimen S3 up to Q_{peak} , is presented in Figure 4.17a, alongside the predicted response generated using the refined model, the base model and Wu's model. In addition, the lateral restraint force vs. midspan deflection response of the specimen is presented in Figure 4.17b, alongside the predicted response of the three models.

The peak applied load predicted by the base model and Wu's model, 116 kN and 118 kN, under-predict the actual peak applied load, 126 kN, by a factor of 1.09 and 1.07, respectively. Both of these predictions are within ten percent of the observed behaviour of the specimen, and can be considered as reasonable predictions. The lateral restraint force at Q_{peak} predicted by the base model and Wu's model, 162 kN and 164 kN, under-predict the observed lateral restraint load at Q_{peak} , 229 kN, by a factor of 1.41 and 1.40, respectively. In addition, the peak midspan deflection predicted by the base model and Wu's model, both equal to $w_t/L = 0.031$, under-predicts the observed peak midspan deflection, $w_t/L = 0.33$, by a factor of 10.6. Therefore, the base model and Wu's model provide inaccurate predictions of the lateral restraint force, the stiffness, and the deflection of specimen S3 at Q_{peak} .

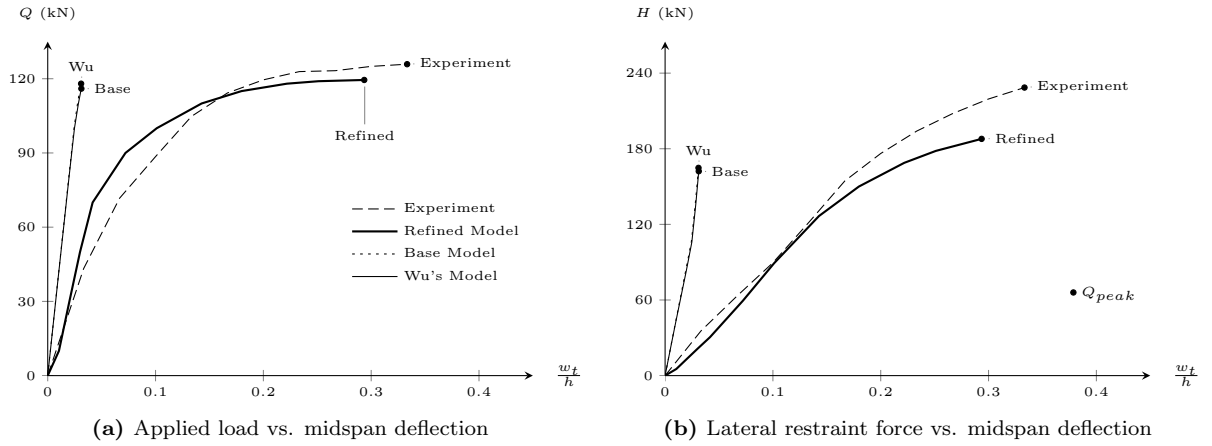


Figure 4.17: Predicted vs. observed response of specimen S3.

The peak applied load predicted by the refined model, 120 kN, is within five percent of the observed Q_{peak} of 126 kN. However, the lateral restraint force at Q_{peak} predicted by the refined model, 188 kN, under-predicts the observed lateral restraint force, 229 kN, by a factor of 1.22.

The magnitude of axial compression predicted by the refined model is dependent on the total expansion of the specimen prevented at each support. For specimens S1 and S2, which are six meters long, the bond deterioration model provides a reasonable prediction of the additional rotation and expansion of in the

column stubs, caused by strain penetration. However in shorter specimens, the bond model formulation under-predicts this rotation, causing a slight over-prediction of stiffness. Near the peak applied load, the bond model predicts a concentration of curvature in the column stubs, caused by large bending moments. This concentration of curvature causes the stiffness of the beam to degrade at an applied load that is lower than the observed response of specimen S3. In addition to causing a reduced prediction of capacity, this limits the amount of expansion in the beam segments prior to Q_{peak} , which limits the development of the lateral restraint force. As previously indicated, the development of a more comprehensive strain penetration model is outside the scope of this research. Therefore, for the purposes of this validation, the current bond deterioration model provides an adequate approximation of the response of the end stubs.

In addition, the midspan deflection at Q_{peak} predicted by the refined model, $w_t/L = 0.29$, under-predicts the observed deflection at Q_{peak} , $w_t/L = 0.33$, by a factor of 1.14. As previously discussed, the current formulation of the proposed analytical model becomes unstable around Q_{peak} , particularly in beams where small increases in applied load cause large increases in deflection. It can therefore be concluded that the predicted response generated using the refined model, up to Q_{peak} , correlates well with the test data, and improves the prediction of the midspan deflection at Q_{peak} generated using Wu's method, by a factor of 9.3.

Beam S4

The constitutive material model assumed for both the concrete and reinforcement in specimen S4 is presented in Figure 4.18.

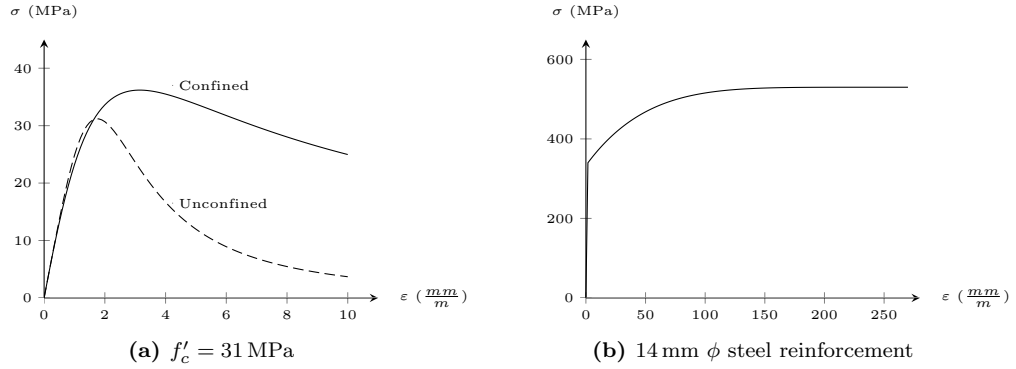


Figure 4.18: Material σ - ϵ response of specimen S4.

The total slip in specimen S4, estimated based on the test data, is equal to,

$$s_t = 0.5 \text{ mm} + \frac{H}{50 \text{ kN/mm}}$$

The lateral restraint force vs. total lateral displacement each end column stub, which includes the stiffness of the steel socket and the assumed lateral slip, is presented in Figure 4.19a. At the peak axial compression force of 249 kN, the total lateral expansion of the beam at each support is equal to 5.7 mm.

Therefore, the total expansion of the entire beam is less than 0.4 percent of the length of the specimen, which is reasonable based on the test setup.

The observed response of specimen S4, presented in Figure 4.4, exhibits some initial softness in the load-deflection response. The magnitude of the initial rotational slip is assumed to be equal to 0.0047 rad, which corresponds with an initial displacement of 1.4 mm at the top and bottom of the concrete end block. This rotation was estimated based on the observed softness in the test data. The bending moment vs. total rotation of each end block is presented in 4.19b.

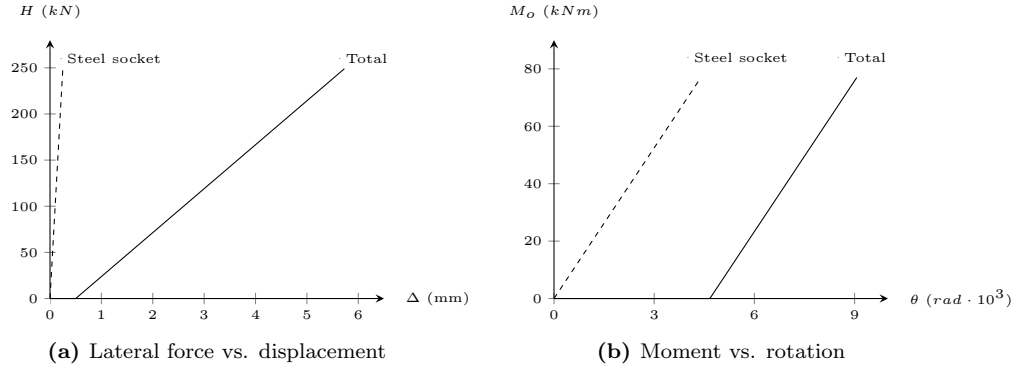


Figure 4.19: Lateral expansion and rotation of specimen S4.

The diagonal compression field model, and the bond deterioration model used for specimen S4 are identical to that used for specimen S1.

The observed applied load vs. midspan deflection response of specimen S4 up to Q_{peak} is presented in Figure 4.20a, alongside the predicted response generated using the refined model, the base model and Wu's model. In addition, the lateral restraint force vs. midspan deflection response of the specimen is presented in Figure 4.20b, alongside the predicted response of the three models.

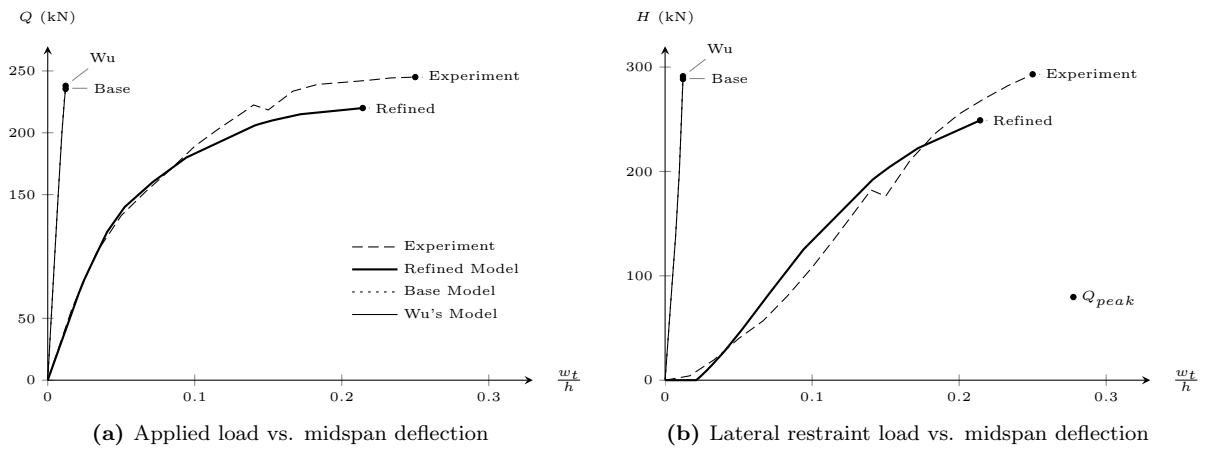


Figure 4.20: Predicted vs. observed response of specimen S4.

The peak applied load predicted by the base model and Wu's model, 236 kN and 238 kN, under-predict the actual peak applied load, 245 kN, by a factor of 1.04 and 1.03, respectively. The lateral restraint

force at Q_{peak} predicted by the base model and Wu's model, 289 kN and 291 kN, correlate well with the observed lateral restraint load at Q_{peak} , which is equal to 293 kN. Therefore, these two models are able to predict the capacity and lateral restraint force of the specimen quite well. However, the peak midspan deflection predicted by the base model and Wu's model, both equal to $w_t/L = 0.012$, under-predicts the observed peak midspan deflection, $w_t/L = 0.25$, by a factor of 20.8. Therefore, the base model and Wu's model provide inaccurate predictions of the stiffness and the deflection of specimen S4 at Q_{peak} .

The peak applied load predicted by the refined model, 220 kN, under-predicts the capacity of specimen S4, 245 kN, by a factor of 1.11. The lateral restraint force at Q_{peak} predicted by the refined model, 249 kN, under-predicts the observed lateral restraint force, 293 kN, by a factor of 1.17. In addition, the midspan deflection at Q_{peak} predicted by the refined model, $w_t/L = 0.21$, under-predicts the observed deflection at Q_{peak} , $w_t/L = 0.25$, by a factor of 1.19.

As previously discussed, the current formulation of the proposed analytical model becomes unstable around Q_{peak} , particularly in beams where large deflections correspond with small increases in applied load. It can therefore be concluded that the predicted response generated using the refined model, up to Q_{peak} , correlates well with the test data, and improves the prediction of the midspan deflection at Q_{peak} generated using Wu's method, by a factor of 17.5. In addition, the current formulation of the bond model causes an under-prediction of the axial compression force that develops in shorter beams. This results in a reduced prediction of the capacity of specimen S4. However for the purpose of this validation, the current bond deterioration model provides an adequate approximation of the response of the end stubs.

4.1.5 S-Series Conclusion

The predicted load-deflection and restraint-deflection response of specimens S1, S2, S3 and S4 correlate well with the experimental data provided by Su, Tian, and Song (2009). On average, the refined proposed analytical model predicts,

1. Q_{peak} within five percent.
2. Lateral restraint force at Q_{peak} within eleven percent.
3. Midspan deflection at Q_{peak} within sixteen percent.

The refined model improves the predicted capacity, lateral restraint and midspan deflection of all specimens, relative to the model developed by Wu (2013), by factors of 1.01, 1.04, and 9.05, respectively. Therefore, the refined analytical model significantly improves the correlation with test data. This good correlation between the analytical model and the test data builds confidence in the rational formulation proposed in this thesis.

4.2 Y-Series

This section presents and discusses the results of the restrained beam specimens tested by Yu and Tan (2013). The proposed analytical model is used to predict the response of the two reinforced concrete beams tested. The two beams are designed with and without consideration of seismic detailing requirements. To illustrate the importance of the model refinements presented in Chapter 3, the predicted response of each beam, generated using the refined model, is compared to the predicted response generated using both the base model and Wu's model.

4.2.1 Test Setup

The Y-Series experiment consists of two beam specimens tested by Yu and Tan (2013), designed to highlight the influence of seismic detailing on the development of arching and tensile membrane action. Each specimen represents a two-bay frame, and is comprised of three column stubs connected with two intermediate beam segments. The test setup used for both beams is illustrated in Figure 4.21.

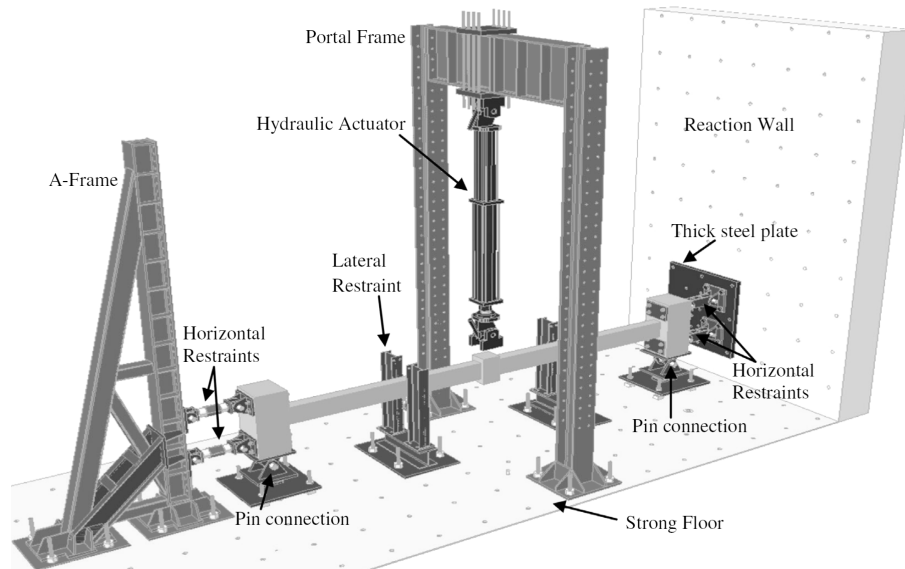


Figure 4.21: Test setup for Y-Series, adapted from Yu (2013).

The column stubs at each end were vertically supported with a pin-roller connection. Compression load cells were placed under these rollers to isolate and measure the vertical reaction forces. The horizontal and rotational restraint was provided at each end of the specimen by two struts acting in parallel. Each strut consisted of a two-pinned mechanism that prevented the transfer of bending and shear forces. On one end of the test setup, these restraints were anchored into a strong wall. On the other end, the struts were anchored onto an A-frame. On the A-frame side, the horizontal struts were instrumented with load cells to isolate and measure the lateral restraint force in each specimen. Out-of-plane lateral restraint was provided at the middle of each beam segment, in regions where minimal deformation was expected to occur.

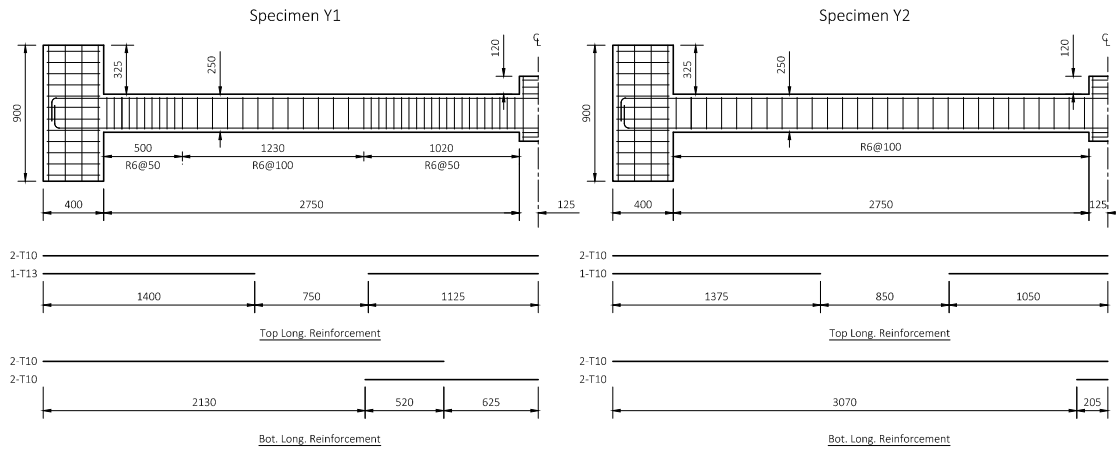


Figure 4.23: Geometric and reinforcement layout of specimens, adapted from Yu (2013).

In both specimens, one of the top reinforcing bars is curtailed near the halfway point of the beam segment, and the bottom reinforcement is lap spliced. For specimen Y1, this lap splice occurs away from the expected location of the plastic hinge, while in specimen Y2 it occurs near the expected location of the plastic hinge.

The general beam layout and typical cross-section of specimens Y1 and Y2 is presented in Figure 4.24. The span length of the beam, L , is defined as the distance between the two vertical roller supports. The concrete cover specified for each specimen is 20 mm, measured to the stirrups.

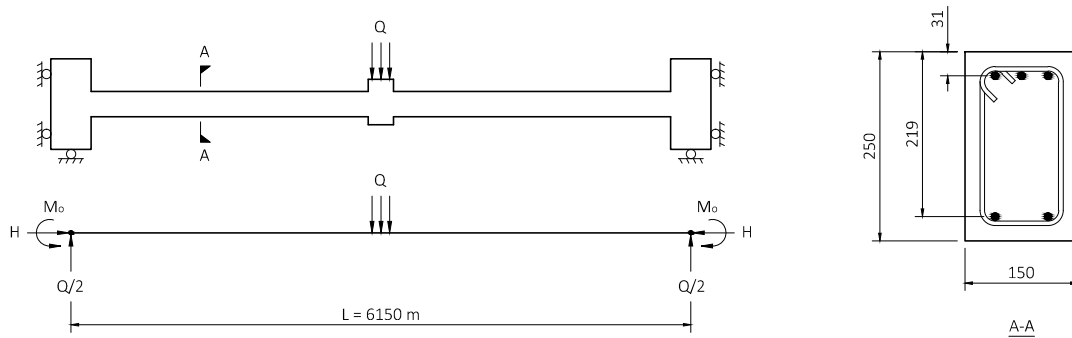


Figure 4.24: Typical beam layout and section, adapted from Yu (2013).

The material properties of the reinforcement used in each specimen are summarized in Table 4.3. The longitudinal reinforcement consists of deformed steel bars with diameters of 10 mm and 13 mm. These bars are anchored into the end blocks using a standard hook with a sufficient development length, determined based on ACI 318-05 (American Concrete Institute, 2005). The stirrups consist of two-legged, smooth steel bars with 135° hooks. The quantity and arrangement of reinforcement in the

middle and end column stubs is not provided (Yu & Tan, 2013).

Table 4.3: Y-Series reinforcement properties, adapted from Yu (2013).

Label	d_b	A_s	E_s	f_y	f_u	ε_u
	mm	mm ²	MPa	MPa	MPa	%
R6	6	28	178500	310	422	14
T10	10	79	182611	511	731	12
T13	13	133	185763	527	640	11

The σ - ε response of the concrete and steel reinforcement used for both specimens is presented in Figure 4.25. The response of concrete is based on the average of four cylinder tests, and the response of the reinforcement is based on coupon tests (Yu & Tan, 2013).

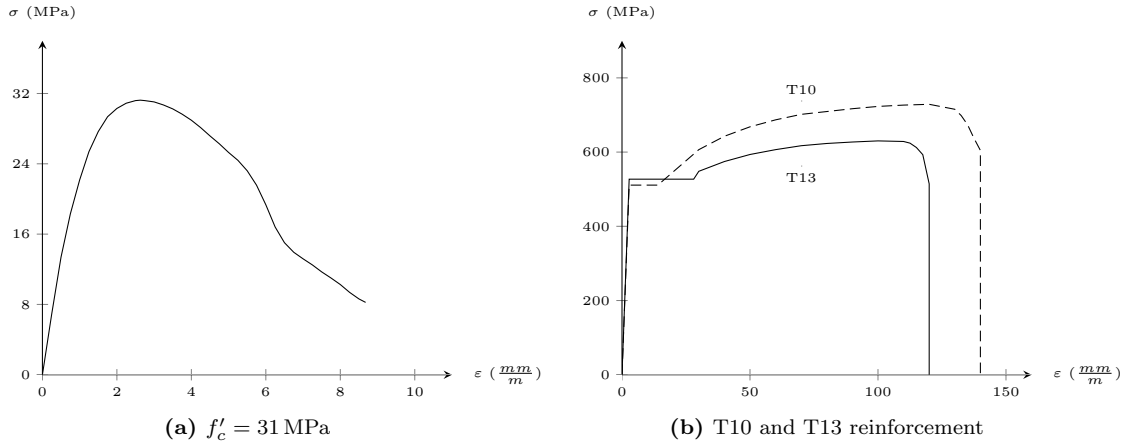


Figure 4.25: σ - ε response of concrete and steel, adapted from Yu (2013).

4.2.3 Measured Response of the Test Specimens

The load-deflection and restraint-deflection response of the two specimens tested by Yu and Tan (2013) is presented in Figure 4.26. Based on the observed response, it is found that the seismic design detailing provided in specimen Y1,

1. Increases the peak applied load, Q_{peak} , by a factor of 1.11, from 38 kN in beam Y2 to 42 kN in beam Y1.
2. Increases the midspan deflection at Q_{peak} by a factor of 1.07, from 73 mm in beam Y2 to 78 mm in beam Y1.
3. Increases the peak lateral restraint force, H_{peak} , by a factor of 1.14, from 155 kN in beam Y2 to 177 kN in beam Y1.

This indicates that accounting for the seismic detailing provisions provided in ACI 318-05 (American Concrete Institute, 2005) increases the influence of lateral restraint by 15 percent, up to Q_{peak} . The

sudden drops in applied load that occur at $Q_{rupture}$ are caused by rupturing of the reinforcement. In specimen Y1, which is designed based on seismic detailing provisions, the reinforcement first ruptures at a midspan deflection of $w_t/h = 0.88$. In contrast, specimen Y2, which is design based on standard detailing, does not have reinforcement rupture until a midspan deflection of $w_t/h = 1.52$. In both cases, rupture of reinforcement causes a drop in the applied load, but has little impact on the lateral restraint force. Therefore, rupturing of reinforcement does not alter the development of tensile membrane action, which increases the applied load up to Q_{fail} , caused by rupturing of the remaining reinforcement.

The initial softness in both the load-deflection and restraint-deflection response indicates the end column stubs slip relative to the supports, prior to the development of the elastic support stiffness. This is consistent with the observed response from the experiments by Su, Tian, and Song (2009), highlighting the difficulty associated with providing a fully rigid lateral and rotational restraint.

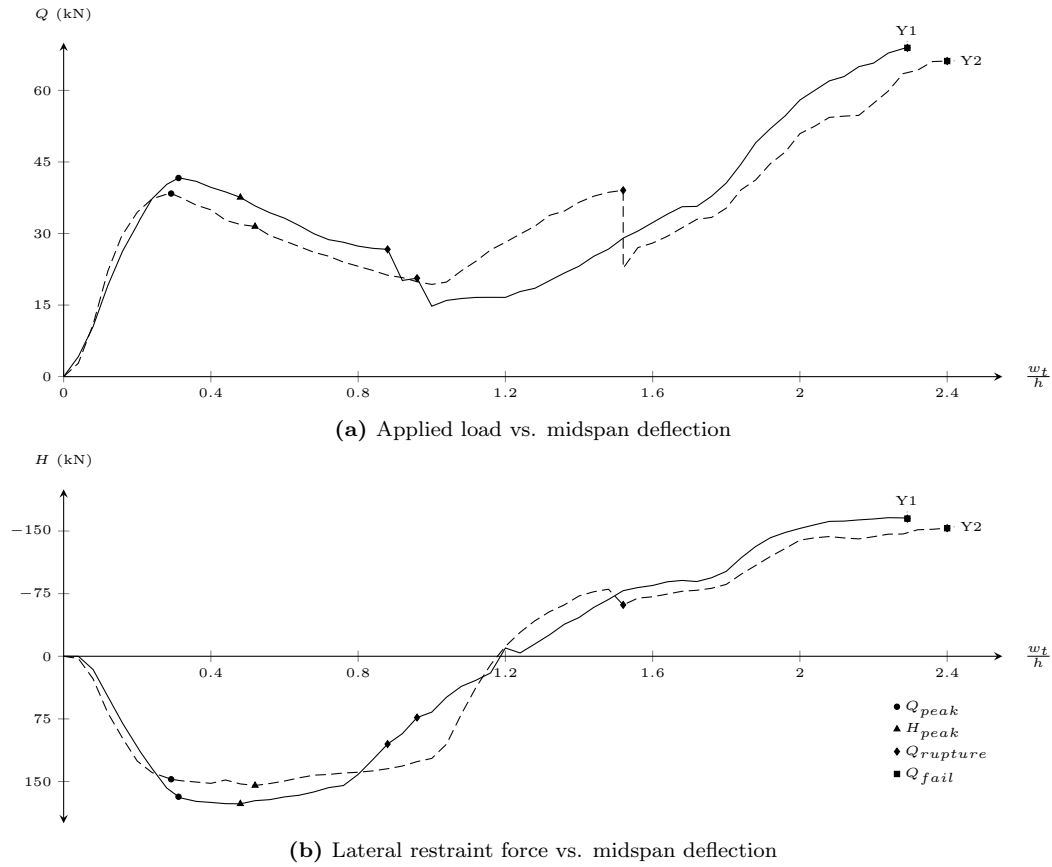


Figure 4.26: Response of specimens from Y-Series, adapted from Yu (2013).

The specimens tested by Su, Tian, and Song (2009) exhibit a gradual change in stiffness after Q_{peak} , allowing the lateral restraint force to continue to increase. In contrast, specimens Y1 and Y2 exhibit a sudden change in stiffness at Q_{peak} . This limits the increase in the lateral restraint force between Q_{peak} and H_{peak} , in specimens Y1 and Y2 to a factor of 1.05 and 1.03, in conjunction with an increase in the midspan deflection of 1.54 and 1.37, respectively.

This sudden change in stiffness is caused by the sudden rotation of the middle column stub, as indicated by Yu and Tan (2013). This rotation is illustrated in Figure 4.27 at Q_{peak} and at Q_{fail} .

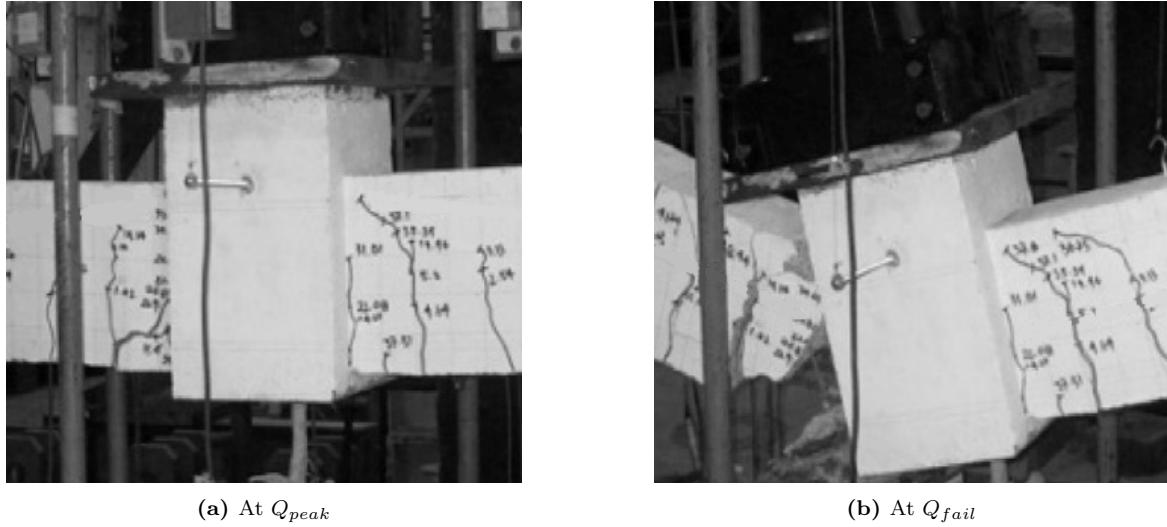


Figure 4.27: Failure mode of middle stub, adapted from Yu (2013).

The sudden rotation causes all additional deformations in the beam to concentrate on one side of the middle stub. This is evident in Figure 4.27, as the flexural cracks on the right side of the stub do not change between Q_{peak} and Q_{fail} . The likely cause of this rotation and concentration of deformation is the unsymmetrical lateral restraints provided. The lateral restraint used at the A-frame and the reaction wall are presented in Figure 4.28.

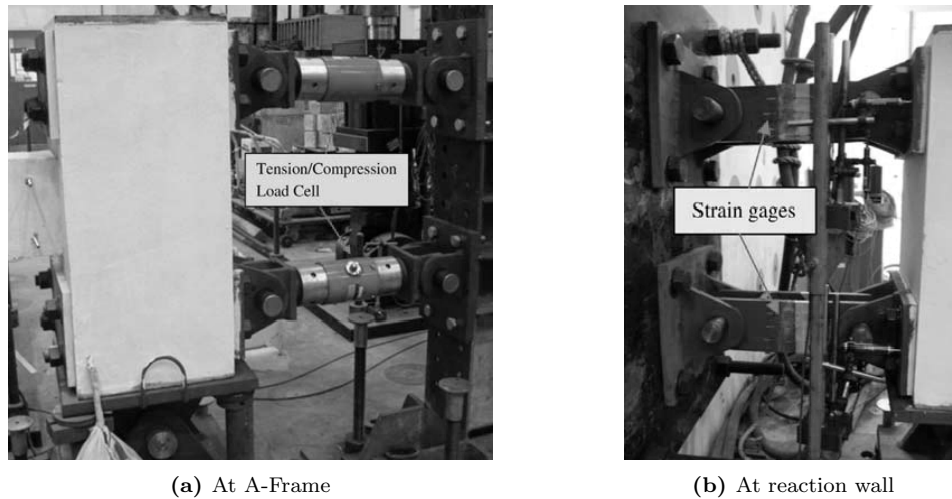


Figure 4.28: Lateral supports, adapted from Yu (2013).

At the A-frame side, the two horizontal struts that provide restraint have tension/compression load cells, allowing them to measure the reaction forces at each load stage. Using these reaction forces, along with the measured change in length of each strut, the stiffness of the support can be determined. At the

strong wall side, strain gauges are used to measure the change in length of the strut. Assuming that the axial force is constant throughout the beam will allow for an accurate determination of the lateral restraint stiffness using data from these strain gauges.

The magnitude of the rotational and axial stiffness of the supports, provided by Yu and Tan (2013), suggest that the stiffness is the same at both supports. However, this is unlikely as the supports at either side of each specimen use a different type of strut, with a unique stiffness. Since the applied load is symmetrical about midspan, the bending moment at each support, M_o , must be equal to maintain equilibrium. However, the reduced rotational stiffness at one end of the test setup will allow larger rotations to occur, relative to the other end of the test setup. This additional rotation is apparent when considering the deflected shape of specimen Y1, presented in Figure 4.29. The magnitude of vertical deflection at each point was measured by Yu and Tan (2013) using linear variable differential transformers (LVDT) that were installed at various intervals along the length of the beam.

The measured deflection at point A_a is approximately equal to 6.8 mm, while the measured deflection at point A_w is approximately equal to 6.3 mm. This deflection occurs over a length of 256 mm, indicating that the rotation at the end of the beam segment on the A-frame side, approximately equal to 1.52° , is 1.08 times larger than the rotation at the end of the beam segment on the strong wall side, approximately equal to 1.41° . This rotation increases the deflection of point B_a , relative to point B_w , by a factor of 1.04, from 64.7 mm at point B_w to 67.5 mm at point B_a .

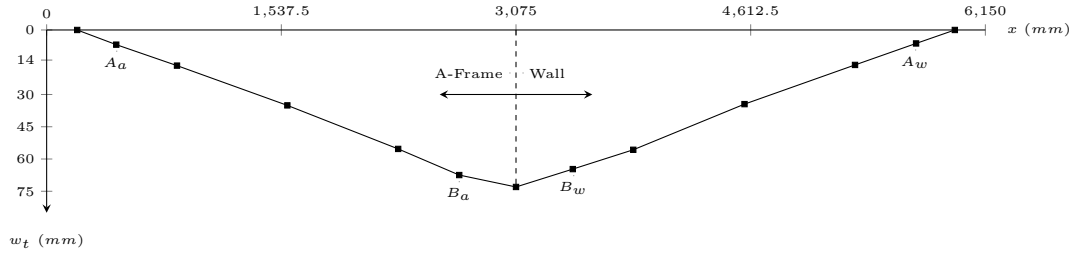


Figure 4.29: Deflection of specimen Y1, at Q_{peak} , adapted from Yu (2013).

Based on the deflected shape of specimen Y1, it can be concluded that the difference in stiffness at each support increases the amount of rotation on one side of each specimen. This additional rotation causes the middle stub to rotate, allowing deformations to concentrate in the beam segment located on the A-frame side of the specimen. This concentration of deformation is exacerbated after Q_{peak} , as indicated in Figure 4.27. Therefore, without more information regarding the nature of this deformation, the proposed analytical model can only be used to predict the response of each specimen up to Q_{peak} .

4.2.4 Predicted Response using the Proposed Analytical Model

The load-deflection and restraint-deflection response of each specimen in the Y-Series can be used to validate the refined version of the proposed analytical model.

Beam Y1: Model Setup

The location of the confined concrete in specimen Y1 is illustrated in Figure 4.30a. Since the formulation is two-dimensional, the entire width of the cross section is assumed to be confined between the center of the reinforcement at the top and bottom of the beam. The cover concrete at the top and bottom of the section remains unconfined. The σ - ε response of the unconfined concrete determined using the method developed by Popovics (1973), and the the confined concrete determined using the method developed by Mander et al. (1988), are presented in Figure 4.30b. The average σ - ε response from cylinder tests is included to illustrate the good correlation between the observed and predicted response of the concrete. Although the observed response of the concrete is provided for unconfined concrete, the use of the Popovics model corresponds with the predicted σ - ε response of the confined concrete, which is not provided.

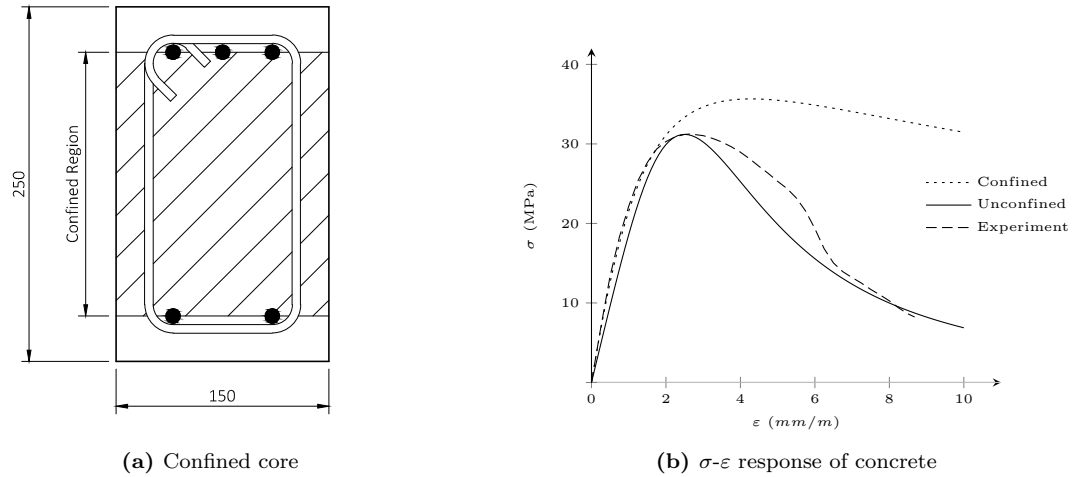
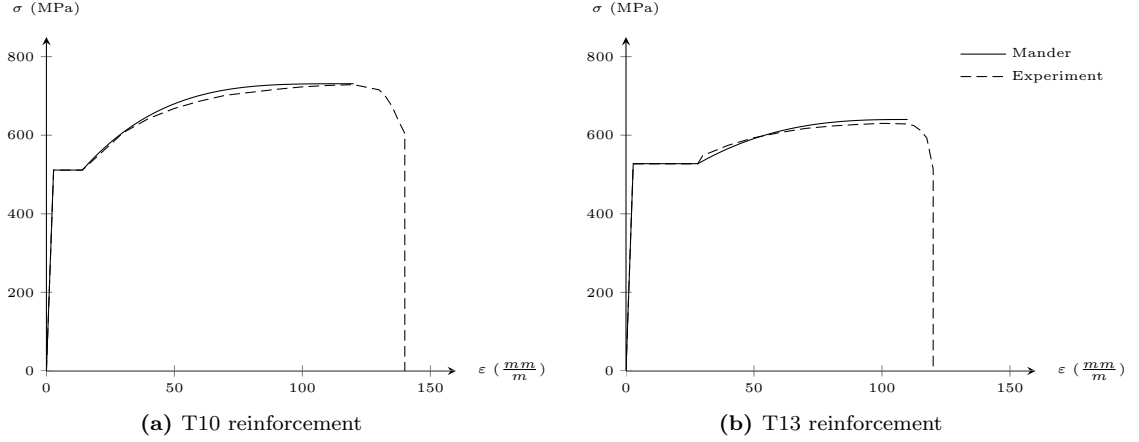


Figure 4.30: σ - ε response of concrete in specimen Y1.

The σ - ε response of the longitudinal reinforcement, presented in Figure 4.31, is based on the formulation developed by Mander (1983). The actual response of the reinforcement, provided by Yu and Tan (2013), correlates well with the predicted response. Therefore, the material model developed by Mander is used in the proposed analytical model.

Figure 4.31: σ - ε response of reinforcement in specimen Y1.

As previously discussed, the elastic lateral and rotational stiffness of the supports was measured during testing. Some uncertainty exists with the reported magnitude of stiffness, as the horizontal support struts attached to the A-frame differ from the horizontal support struts attached to the strong wall. Without more information regarding the possible variation in stiffness, the elastic support stiffness reported by Yu and Tan (2013) is assumed at both ends of the model developed for specimen Y1.

The test setup for each specimen, illustrated in Figure 4.21, indicates that the distance between the horizontal support struts is fixed. The specimens are precast prior to being installed in the test setup, and since the supporting struts do not contain jacks, the installation of the specimen will likely require the use of shims. In addition, the struts used to provide lateral and rotational restraint have two hinges, which may exhibit some slip. Therefore, it is possible that the concrete end blocks experience some lateral and rotational slip, relative to each support. This is consistent with the softness exhibited in the load-deflection and lateral restraint-deflection response of beam Y1, presented in Figure 4.26.

The lateral restraint force vs. lateral displacement of each end stub, based on the elastic stiffness of the support, is presented in Figure 4.32a.

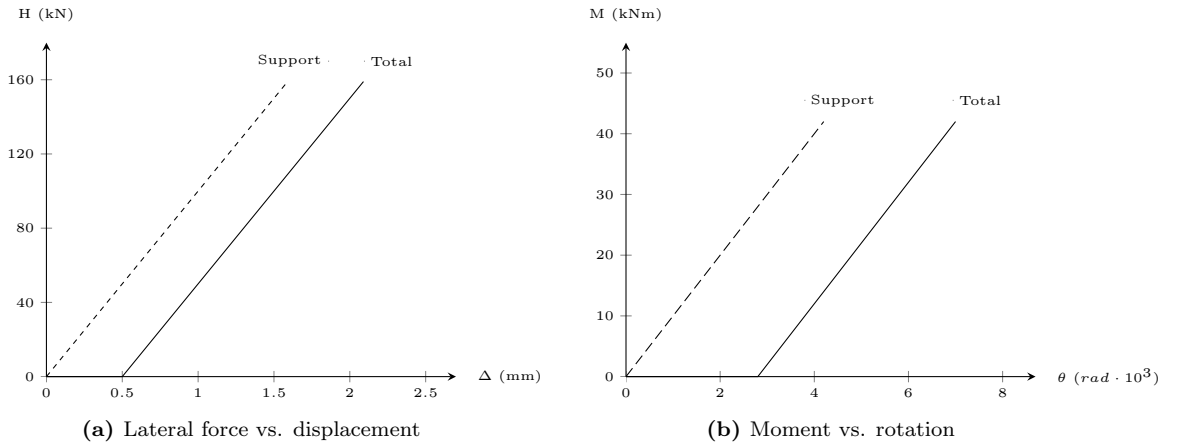


Figure 4.32: Lateral expansion and rotation of specimen Y1.

The initial lateral slip, calibrated based on the test data, is equal to,

$$s_t = 0.5 \text{ mm}$$

The lateral restraint force vs. total lateral displacement of the end block, which accounts for the initial lateral slip and the elastic stiffness of the support, is included in Figure 4.32a. The total lateral displacement at each support, equal to 2.1 mm, is less than 0.1 percent of the total length of the specimen. Therefore, the magnitude of slip is reasonable, based on the experimental test setup.

The initial softness exhibited in the load-deflection response of specimen Y1 indicates that some initial rotational slip occurs. The bending moment vs. rotation of the end block, based on the rotational elastic stiffness of the support, is presented in Figure 4.32b. The magnitude of the initial rotational slip, estimated based on the test data, is equal to 0.0028 rad. This rotation corresponds with a displacement of 0.7 mm at the top and bottom of the end column stubs. The bending moment vs. total rotational slip of the end blocks in specimen Y1 is presented in Figure 4.32b. The total rotational slip of the end blocks is approximately equal to 0.007 rad, which corresponds with a displacement of 3.2 mm at the top and bottom of the end column stubs. This rotation is within a reasonable range, based on the test setup.

Similar to the analysis conducted for the S-Series validation, the influence of the diagonal compression struts in the beam are incorporated using the diagonal compression field model proposed in Section 3.2. This model is applied over the length of the two beam segments, and assumes that the struts are inclined at 45°. For Specimen Y1, the lever arm between the compression and tension resultants in the truss model is assumed to be equal to 195 mm. This estimate is based on the depth of the compression zone and the effective depth of the reinforcement predicted in the analysis.

The concrete in each column stub is confined internally by reinforcement, and externally by the support setup, as illustrated in Figure 4.33. Similar to the specimens tested by Su, Tian, and Song (2009), this confinement prevents the concrete from expanding during testing. The lack of deformation in the middle column stub is evident in Figure 4.27, despite very large deformations in the adjacent beam segments. Therefore, the large tensile strain in the longitudinal reinforcement at the interface of each column stub and beam segment can cause bond deterioration to occur.

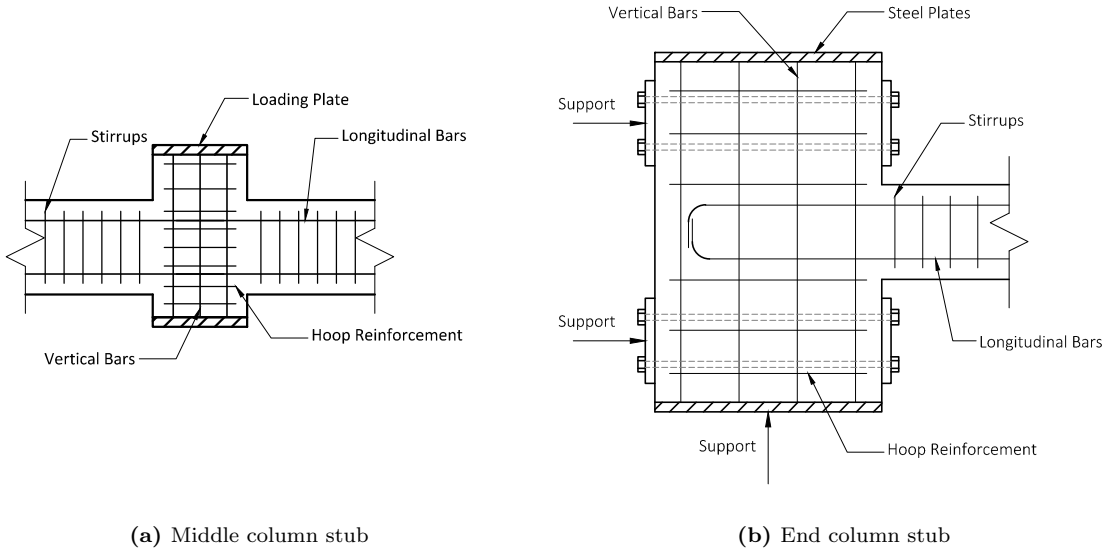


Figure 4.33: Reinforcement layout in the column stubs, adapted from Yu (2013).

The influence of strain penetration can be accounted for using the simplified method presented in Section 3.4. This bond model is implemented into the proposed analytical model using the following assumptions:

1. The beam segments are considered continuous throughout the middle stub, and extend a distance of 200 mm into the end column stubs.
2. The curvature of sections within the column stubs are determined assuming $\varepsilon_{c,s} = \varepsilon_s$.
3. The concrete in the column stub regions maintains peak stress after peak strain.

This simplification provides a means to validate the proposed analytical model without the need to alter the formulation significantly. However, this bond model is developed specifically for the specimens and test setup used in this experiment. Therefore, a more rigorous bond model should be developed to provide a more general formulation that can be applied in any situation. This is outside the scope of this thesis.

As indicated by Yu and Tan (2013), the test data provided does not include the effect of self-weight. Therefore, the self-weight of each specimen is ignored in the model formulation.

Beam Y1: Predicted Response of Model

The observed applied load vs. midspan deflection response of specimen Y1 is presented in Figure 4.34a up to Q_{peak} , alongside the predicted response generated using the refined model, the base model and Wu's model. In addition, the lateral restraint force vs. midspan deflection response of the specimen is presented in Figure 4.34b, alongside the predicted response of the three models.

The peak applied load predicted by the base model and Wu's model, 55 kN and 61 kN, over-predict the actual peak applied load, 42 kN, by a factor of 1.31 and 1.45, respectively. The lateral restraint force at Q_{peak} predicted by the base model and Wu's model, 223 kN and 241 kN, over-predict the observed lateral restraint load at Q_{peak} , 168 kN, by a factor of 1.33 and 1.44, respectively. In addition, the peak midspan deflection predicted by the base model and Wu's model, both equal to $w_t/L = 0.093$, under-predicts the observed peak midspan deflection, $w_t/L = 0.31$, by a factor of 3.33. Therefore, both the base model and Wu's model provide inaccurate predictions of the response of specimen Y1.

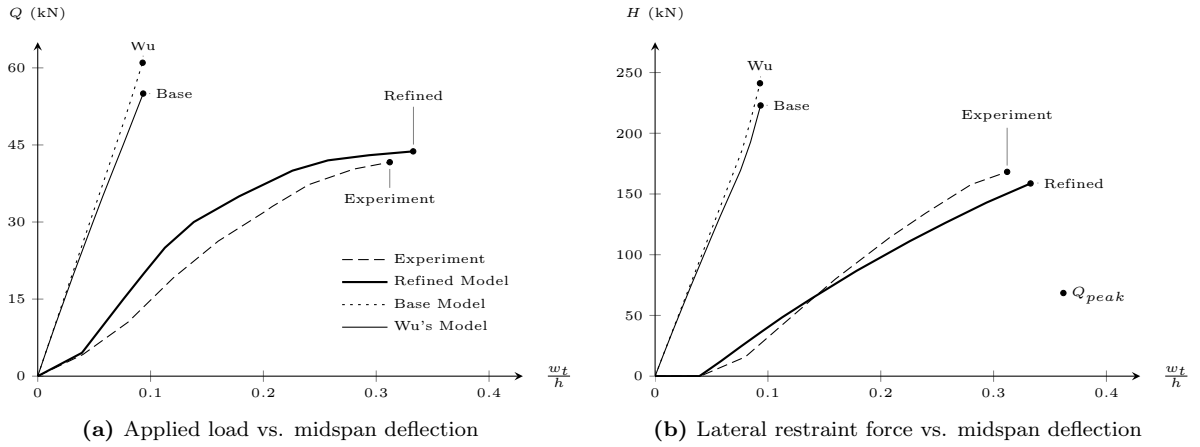


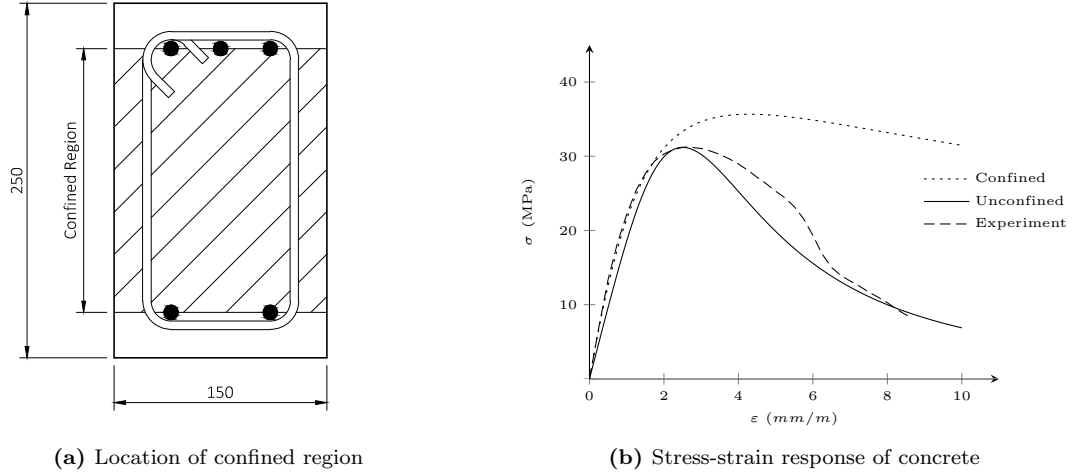
Figure 4.34: Predicted vs. observed response of specimen Y1.

The peak applied load predicted by the refined model, 44 kN, is within five percent of the observed Q_{peak} of 42 kN. The lateral restraint force at Q_{peak} predicted by the refined model, 159 kN, is within six percent of the observed lateral restraint, 168 kN. In addition, the midspan deflection at Q_{peak} predicted by the refined model, $w_t/L = 0.33$, over-predicts the observed deflection at Q_{peak} , $w_t/L = 0.31$, by a factor of 1.06.

The refined analytical model significantly improves the predicted capacity, lateral restraint and peak midspan deflection of specimen Y1 relative to Wu's model, by factors of 1.38, 1.36, and 3.14, respectively. However, the refined analytical model over-predicts the stiffness of the specimen, as illustrated in Figure 4.34a. The increased stiffness is likely caused by under-predicting the rotation in each column stub caused by bond deterioration. However, as previously indicated, the simplified bond deterioration model provides a reasonable prediction without the need of a rigorous model. It is also likely that the difference in the stiffness of the supports on either side of the specimen, which causes the sudden rotation of the middle stub, reduces the observed stiffness and capacity of specimen Y1. However without more information regarding the exact stiffness of each support, this cannot be confirmed using the proposed analytical model.

Beam Y2

The constitutive material model assumed for the unconfined and confined concrete in specimen Y2 is presented in Figure 4.35. The σ - ε response of the longitudinal reinforcement in specimen Y2 is equivalent to the reinforcement in Specimen Y1, and is presented in Figure 4.31.

Figure 4.35: σ - ϵ response of concrete in specimen Y2.

As indicated by Yu and Tan (2013), the elastic support stiffness is consistent for both specimens. However, each beam is precast and installed separately, which will allow the concrete end block to slip, relative to the lateral supporting struts. For specimen Y2, the total lateral slip is assumed to be equal to,

$$s_t = 0.35 \text{ mm}$$

The lateral restraint force vs. total lateral displacement of each end column stub, which includes the elastic support stiffness and assumed lateral slip, is presented in Figure 4.36a.

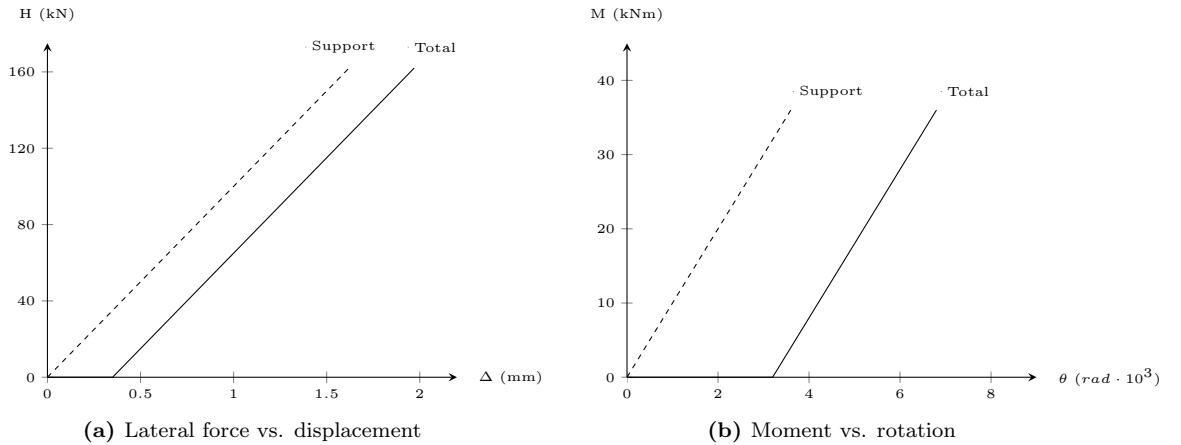


Figure 4.36: Lateral expansion and rotation of specimen Y2.

At the peak axial compression force of 162 kN, the total lateral expansion of the beam at each support is equal to 2.0 mm. Therefore, the total expansion of the entire beam is less than 0.1 percent of the length of the specimen, which is reasonable based on the test setup.

The initial softness exhibited in the load-deflection response of specimen Y2 indicates that some rotational slip may occur. The bending moment vs. rotation of the end block, based on the rotational elastic stiffness of the support, is presented in Figure 4.36b. The magnitude of the initial rotational slip, estimated based on the test data, is assumed to be equal to 0.0032 rad. The bending moment vs. total rotational slip of each column stub is presented in Figure 4.36b. The total rotational slip of the end blocks is approximately equal to 0.007 rad, which corresponds with a displacement of 3.2 mm at the top and bottom of the end column stubs. This rotation is within a reasonable range, based on the test setup.

The diagonal compression field model, and the bond deterioration model used for specimen Y2 are identical to that used for specimen Y1.

The observed applied load vs. midspan deflection response of specimen Y2 is presented in Figure 4.37a up to Q_{peak} , alongside the predicted response generated using the refined model, the base model and Wu's model. In addition, the lateral restraint force vs. midspan deflection response of the specimen is presented in Figure 4.37b, alongside the predicted response of the three models.

The peak applied load predicted by the base model and Wu's, 54 kN and 60 kN, over-predict the actual peak applied load, 38 kN, by a factor of 1.42 and 1.58, respectively. The lateral restraint force at Q_{peak} predicted by the base model and Wu's model, 227 kN and 244 kN, over-predict the observed lateral restraint load at Q_{peak} , 147 kN, by a factor of 1.54 and 1.66, respectively. In addition, the peak midspan deflection predicted by the base model and Wu's model, both equal to $w_t/L = 0.096$, under-predicts the observed peak midspan deflection, $w_t/L = 0.29$, by a factor of 3.02. Therefore, both the base model and Wu's model provide inaccurate predictions of the response of specimen Y2.

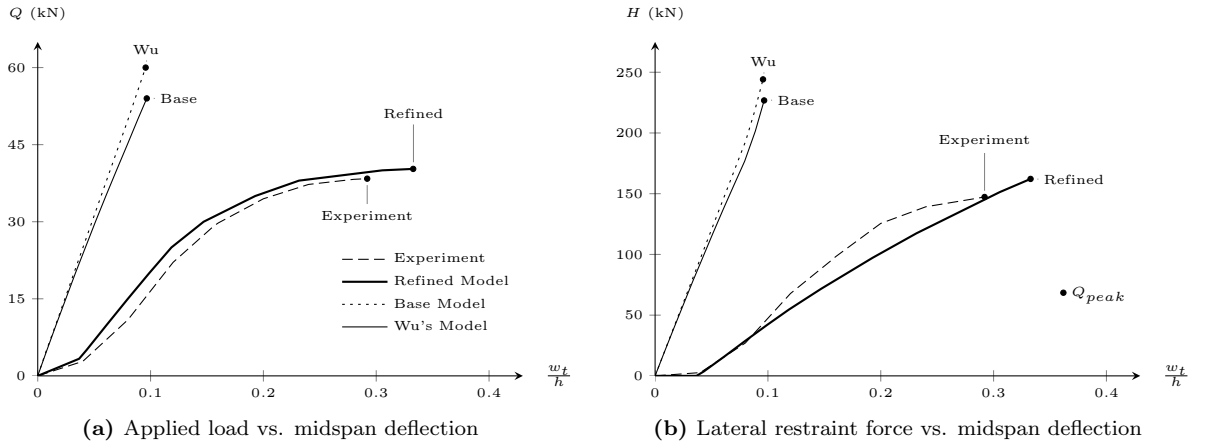


Figure 4.37: Predicted vs. observed response of specimen Y2.

The peak applied load predicted by the refined model, 40 kN, is within six percent of the observed Q_{peak} of 38 kN. The lateral restraint force at Q_{peak} predicted by the refined model, 162 kN, over-predicts the observed lateral restraint, 147 kN, by a factor of 1.1. In addition, the midspan deflection at Q_{peak} predicted by the refined model, $w_t/L = 0.33$, over-predicts the observed deflection at Q_{peak} , $w_t/L = 0.29$, by a factor of 1.14.

The refined analytical model significantly improves the predicted capacity, lateral restraint and peak

midspan deflection of specimen Y2, relative to Wu’s model, by factors of 1.49, 1.51, and 2.65, respectively. Similar to specimen Y1, the proposed analytical model over-predicts the stiffness and peak deflection of the beam. This is likely caused by the current formulation of the bond model, as well as the possible difference in stiffness between the supports on either end of the specimen. In addition, as previously suggested, the reinforcement layout in specimen Y2, which includes a lap splice that occurs through the middle stub, alters the amount of bond deterioration near the middle stub. Therefore, a more comprehensive bond model should be developed that can account for additional factors that may increase the influence of strain penetration. However for the purposes of this validation, the current bond deterioration formulation provides a reasonable prediction of the response of the two specimens.

4.2.5 Y-Series Conclusion

The predicted load-deflection and restraint-deflection response of specimens Y1 and Y2 correlate well with the experimental data provided by Yu and Tan (2013). On average, the refined version of the proposed analytical model predicts,

1. Q_{peak} within eight percent.
2. Lateral restraint force at Q_{peak} within ten percent.
3. Midspan deflection at Q_{peak} within ten percent.

The refined model improves the predicted capacity, lateral restraint and midspan deflection of both specimens, relative to the model developed by Wu (2013), by factors of 1.44, 1.44, and 2.90, respectively. Therefore, the refined analytical model significantly improves the correlation with test data. This good correlation between the analytical model and the test data builds confidence in the rational formulation proposed in this thesis.

4.3 Discussion of Results and Concluding Remarks

This chapter summarizes the results of an experimental validation conducted using data from experiments conducted by Su, Tian, and Song (2009) and Yu and Tan (2013), which investigate the progressive collapse mechanism of reinforced concrete frame beams. For specimens from both experiments, the proposed analytical model is able to predict, on average,

1. Q_{peak} within seven percent.
2. Lateral restraint force at Q_{peak} within eleven percent.
3. Midspan deflection at Q_{peak} within thirteen percent.

Therefore, the response predicted using the proposed analytical model is found to correlate well with the observed response of all specimens. As previously indicated, this represents a significant improvement over the model developed by Wu (2013).

Based on the results of this validation, a number of conclusions can be made. These include:

1. The stiffness of the support can have an impact on the response of restrained, reinforced concrete beams. Therefore, accurately measuring this stiffness is critical for predicting the response of a beam when using the proposed analytical model.
2. Any slip between a beam and its support, prior to the development of the lateral and rotational stiffness, delays the mobilization of the lateral restraint force, altering the stiffness, capacity and deflection of the beam.
3. The bond deterioration caused by geometric irregularities can have a significant influence on the stiffness of a beam, allowing larger deflections to occur, and increasing the influence of second-order effects.
4. The softening caused by second-order effects is governed by the geometry of the specimen. The response of each specimen, up to failure, confirms the behaviour of slender beams provided in Section 2.9.

This validation provides confidence in the rational formulation developed as part of the proposed analytical model. The current formulation, which accurately predicts the load-deflection and restraint-deflection response of each specimen up to the first peak in the applied load, can therefore be used in the development of a simplified analytical model that can be incorporated into design standards. In addition, the confidence afforded by this validation allows for the proposed analytical model to be used in the parametric study presented in Chapter 5.

5

Parametric Study

This chapter presents the results of five parameter studies aimed at determining the influence of critical parameters on the response of a laterally restrained reinforced concrete beam or slab strip. In Chapter 4, the proposed analytical model was shown to correlate well with test data from two experiments conducted on laterally restrained beams. Therefore, the proposed model provides a transparent, rational basis for predicting the influence of lateral restraint, and is used to conduct the parametric studies. In each study, a modified version of the basic model formulation is used. The modified version is defined as:

1. The σ - ε response of concrete is defined using the bi-linear response proposed by fib (2010).
2. The concrete is assumed to have zero tensile strength.
3. The σ - ε response of the reinforcement is defined using the model developed by Mander (1983). The reinforcement is assumed to have a yield stress of 400 MPa and a modulus of elasticity of 200 000 MPa.
4. The supports are assumed to be infinitely stiff.
5. The horizontal component of the diagonal compression struts, defined based on a truss model, are incorporated assuming a strut inclination of 45° . However in Section 5.5, the inclination is varied.
6. There is no slip between the beam and the support. However in Section 5.4, the compatibility conditions are adjusted to account for an initial lateral slip at the supports.

The parameters considered for each study are chosen based on the potential influence they have on the analysis of laterally restrained, reinforced concrete beams and slab strips. These parameters include:

1. Concrete compressive strength
2. Mechanical reinforcement ratio
3. Span-to-depth ratio
4. Initial lateral slip at the supports

5. Diagonal strut inclination assumed in the truss model

The beam considered for each parametric study is assumed to have a single point load applied at midspan, as illustrated in Figure 5.1.

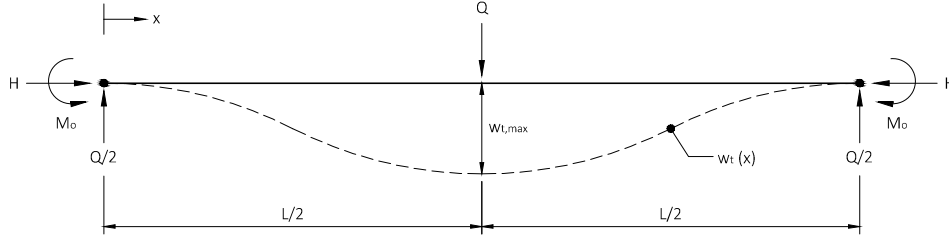


Figure 5.1: Beam layout for parametric studies.

5.1 Concrete Compressive Strength

A total of eight reinforced concrete beams, with properties summarized in Figure 5.2, are considered in this parametric study. Each beam is doubly reinforced, with an identical amount of reinforcement at the top and bottom of the beam. The beams are split into two series. The A-Series isolates the influence of varying the strength of concrete, while the B-Series studies the influence of varying reinforcement ratio in conjunction with the strength of concrete. For each beam, a subscript of R or U is added to classify the support condition as restrained or unrestrained, respectively.

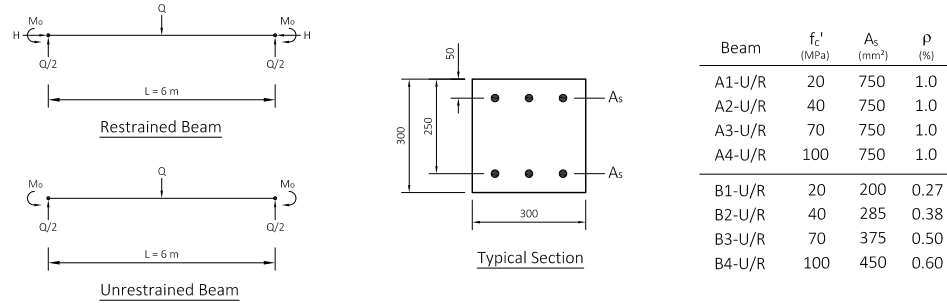


Figure 5.2: Beam properties for the concrete parametric study.

The reinforcement ratio is defined as,

$$\rho = \frac{A_s}{bd} \quad (5.1)$$

where A_s is the cross sectional area of the reinforcement at either the top or bottom of the beam, b is the width of the beam, and d is the effective depth of the reinforcement. All the beams in the A-Series

have a reinforcement ratio of 1 %. In the B-Series, the reinforcement ratio is varied from 0.27 % to 0.6 %, in conjunction with the strength of the concrete.

In both the A and B-Series, the compressive strength of concrete is varied from 20 MPa to 100 MPa. The variation in the σ - ε response of concrete used in each beam is presented in Figure 5.3.

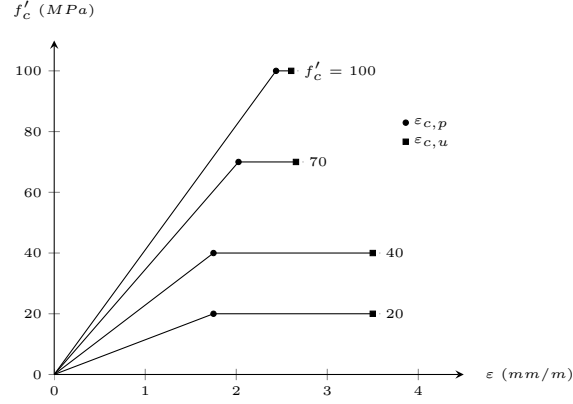


Figure 5.3: σ - ε response of concrete in parametric studies.

5.1.1 Unrestrained Beam Response

The applied load vs. midspan deflection of the A-Series beams, without lateral restraint, is summarized in Figure 5.4. For the A-Series beams, increasing the strength of concrete from 20 MPa to 100 MPa increases the capacity by a factor of 1.19, and increases the midspan deflection at failure by a factor of 1.67. Increasing the strength of concrete also increases the amount of deformation that occurs after the reinforcement yields, providing more warning of failure.

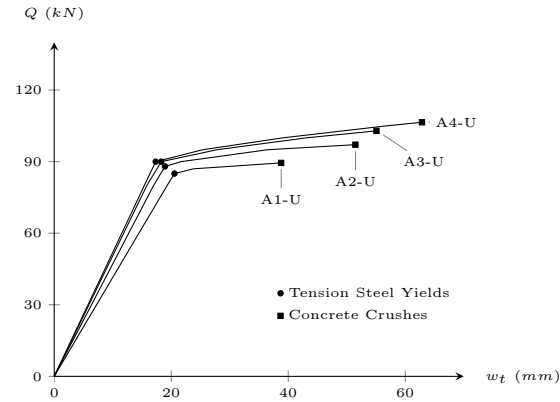


Figure 5.4: Load-deflection response of A-Series beams, without restraint.

The influence of concrete strength on the capacity of beams A1-U and A4-U can be understood by considering the plane of strain at the failure load of each beam, presented in Figure 5.5a. At each section, compressive strains are considered to be negative, and tensile strains are considered to be positive. The increased strength of concrete from beam A1-U to A4-U reduces the depth of the compression zone from

55 mm to 31 mm. This change allows the reinforcement at the top of the section, which is located at a depth of 50 mm, to transition from compression to tension. This allows the concrete resultant force, F_c , to increase from 250 kN in beam A1-U to 498 kN in beam A4-U. In addition, the reduced depth of compression in beam A4-U increases the lever arm of the concrete resultant force, e_c , from 128 mm in beam A1-U to 139 mm in beam A4-U. The increased magnitude and eccentricity of the compression resultant force increases the bending capacity of beam A4-U, relative to beam A1-U.

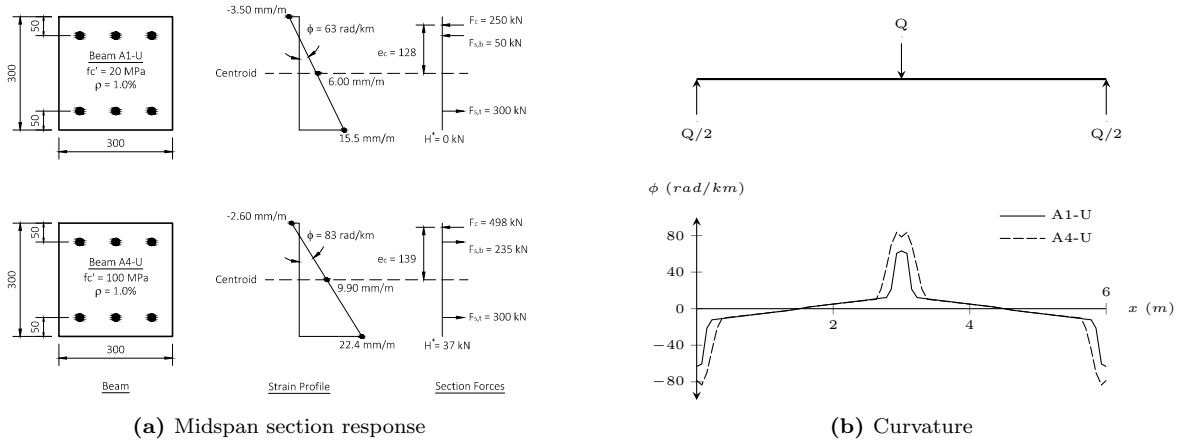


Figure 5.5: Section response of beams A1-U and A4-U, at failure.

The influence of concrete strength on the peak midspan deflection of beams A1-U and A4-U can be understood by considering the curvature along the length of each beam, presented in Figure 5.5b. Increasing the strength of concrete from beam A1-U to A4-U reduces the depth of compression at midspan from 55 mm to 32 mm, and reduces the peak compressive strain from 3.5 mm/m in beam A1-U to 2.6 mm/m in beam A4-U. The reduced compressive strains increase the peak curvature from 63 rad/km in beam A1-U to 83 rad/km in beam A4-U. This increase in curvature near the midspan and supports, which is caused by the reduced depth of compression in the concrete, increases the deformation of beam A4-U, relative to beam A1-U.

The peak values of applied load for beams in the A and B-Series, with no lateral restraint, are presented in Figure 5.6a. As previously suggested, increasing the strength of the concrete, from beam A1-U to beam A4-U, increases the beam's capacity by a factor of 1.19. In the B-Series, the reinforcement ratio is increased in conjunction with the strength of concrete. As a result, the beam's capacity increases by a factor of 2.3, from 29 kN in beam B1-U to 67 kN in beam B4-U. The additional increase in the capacity of beams in the B-Series is the result of the increasing quantity of reinforcement at the top and bottom of the beam, which increases the tension force resultant of the reinforcement, and therefore the bending capacity of the beam.

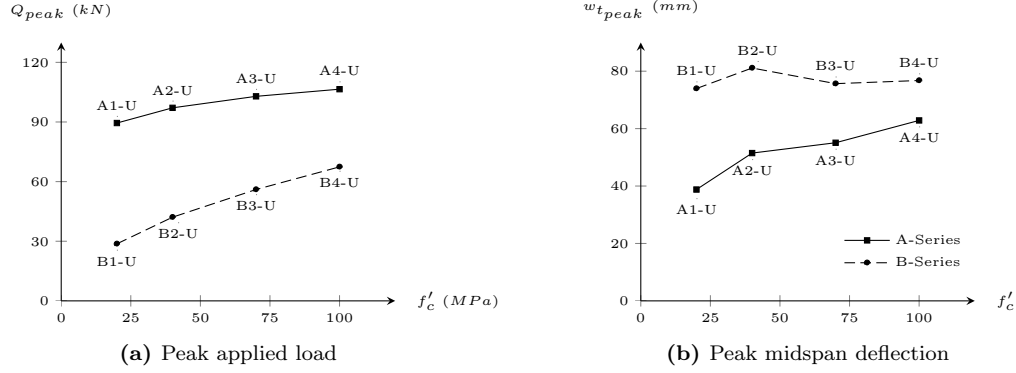


Figure 5.6: Response of beams in the A and B-Series, with no lateral restraint.

The peak midspan deflection of beams in the A and B-Series, with no lateral restraint, are presented in Figure 5.6b. As previously indicated, increasing the strength of concrete from beam A1-U to A4-U increases the peak midspan deflection by a factor of 1.67. However in the B-Series, the reinforcement ratio is increased in conjunction with the strength of concrete, and as a result, the peak midspan deflection of beam B2-U is greater than beams B1-U, B3-U and B4-U. This can be understood by considering the plane of strain presented in Figure 5.7a.

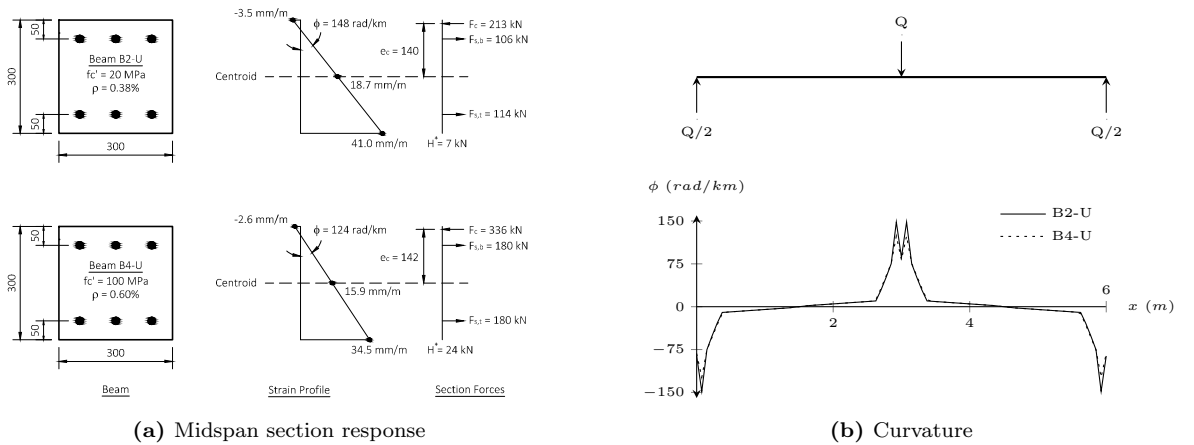


Figure 5.7: Section response of beams B2-U and B4-U, at failure.

If the strength of concrete was increased without varying the reinforcement ratio, the midspan curvature at peak load would increase. However, increasing the reinforcement ratio from 0.4 percent in beam B2-U to 0.6 percent in beam B4-U increases the tension force in the reinforcement from 114 kN to 180 kN. The increased tension force resultant in the reinforcement allows the compression force resultant of the concrete to increase. In the A-Series, increasing the strength of concrete reduces both the depth of compression and the peak compressive strain at the midspan of the beam. However in the B-Series, increasing the reinforcement ratio causes the depth of the compression zone to remain approximately equal. As a result, the curvature varies from 148 rad/km in beam B2-U to 124 rad/km in beam B4-U. The curvature at peak load is illustrated along the length of beams B2-U and B4-U in 5.7b. The increased

curvature in beam B2-U, near the midspan and support, increases the deflection of beam B2-U, relative to beam B4-U.

5.1.2 Restrained Beam Response

The load-deflection and load-restraint response of each beam in the A-Series, assuming full lateral restraint, is presented in Figure 5.8. These plots provide insight into the influence of concrete strength on the stiffness and capacity of laterally restrained, reinforced concrete beams. For the A-Series beams, increasing the concrete strength from 20 MPa to 100 MPa doubles the load capacity, and increases the peak axial compression by a factor of 3.5. In addition, increasing the strength of concrete from beam A1-R to A4-R reduces the peak midspan deflection by a factor of 1.10. This indicates that increasing the strength of concrete has little influence on a laterally restrained beam's midspan deflection at failure.

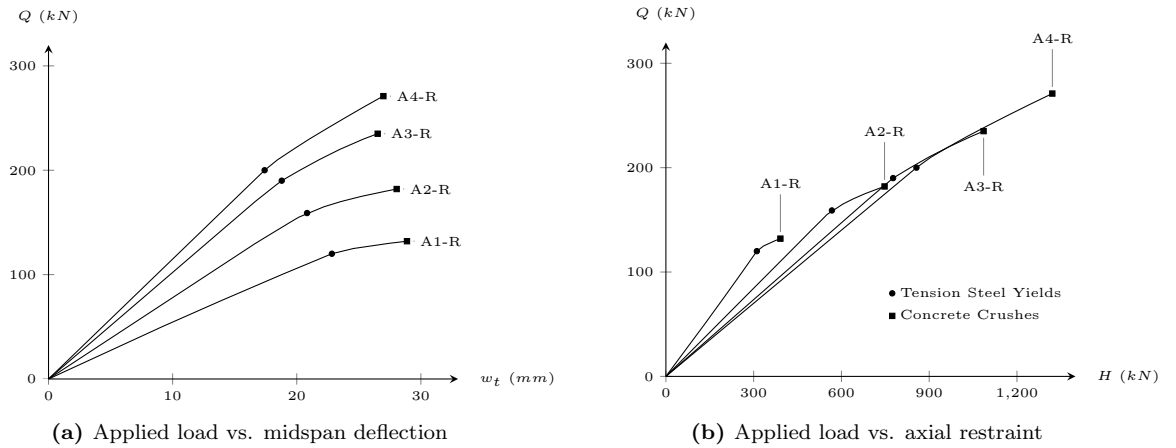
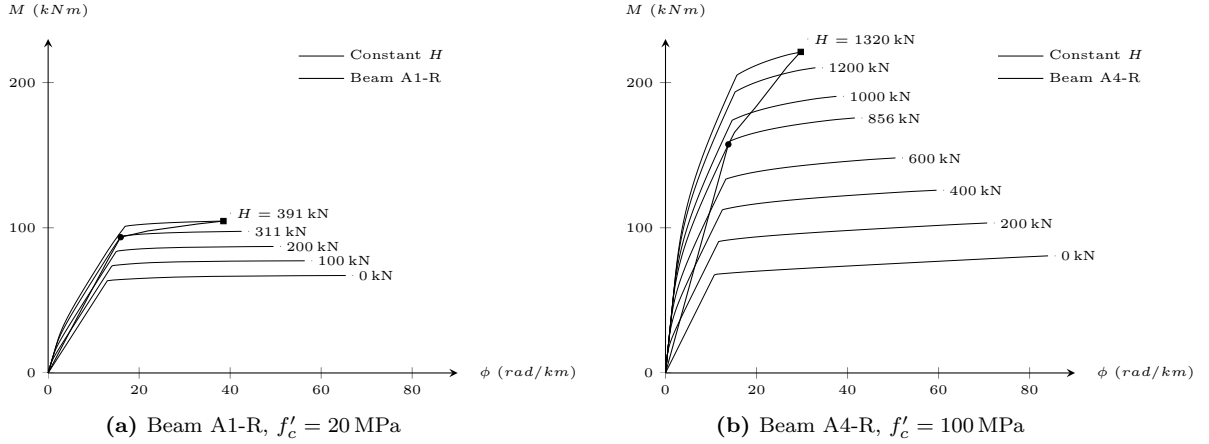


Figure 5.8: Response of A-Series beams, with lateral restraint.

A family of moment-curvature responses for beams A1-R and A4-R can be developed by varying the magnitude of axial compression in each beam. These curves, presented in Figure 5.9a for beam A1 and Figure 5.9b for beam A4, provide insight into how the axial compression force developed in a laterally restrained beam can increase the stiffness and capacity of a beam. The moment-curvature response of beams A1-R and A4-R, developed based on the family of moment-curvature responses of each beam, are included in Figure 5.9. Beam A4-R develops a larger magnitude of axial compression relative to beam A1-R, which increases the initial stiffness, delays the onset of yielding of the reinforcement, and increases the peak capacity. As a result, increasing the strength of concrete from beam A1-R to beam A4-R approximately doubles the yield moment and bending capacity.

Figure 5.9: $M-\phi$ response of beams A1-R and A4-R.

The lateral expansion at the support of beam A1-U is approximately equal to 1.5 mm, while the lateral expansion at the support of beam A4-U is approximately equal to 3.0 mm. The increased lateral expansion is caused by an increase in the compressive strength of concrete, which reduces the peak compressive strain in the concrete. This is illustrated in the midspan section response of beams A1-U and A4-U, presented in Figure 5.10a. The reduced peak compressive strain in beam A4-U increases the curvature of the response at the midspan, and at other sections in the beam, increasing the lateral expansion at the support. The increased outward expansion requires that a larger lateral restraint force be applied at the supports of beam A4-R, relative to beam A1-R. As illustrated in the midspan section response of beams A1-R and A4-R, presented in Figure 5.10b, the increased axial compression increases the magnitude of the resultant force in the concrete, which increases the beam's bending capacity.

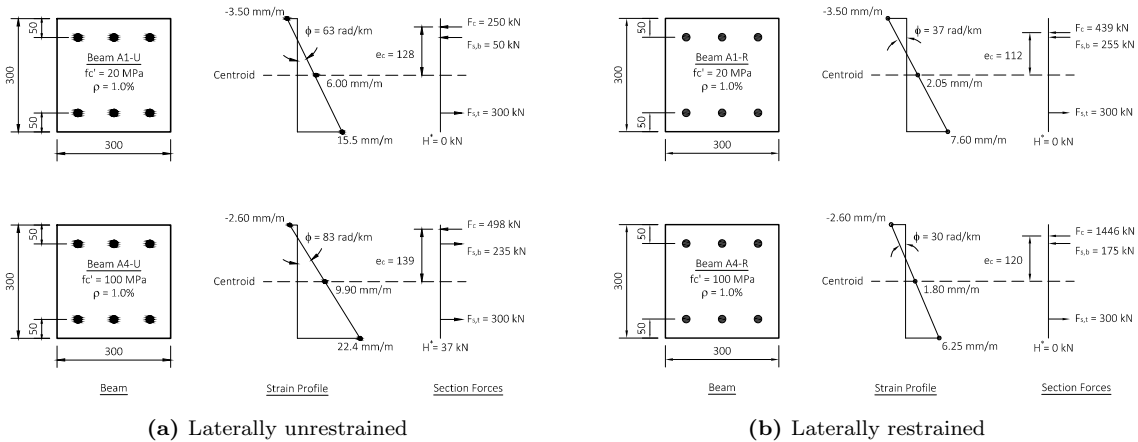


Figure 5.10: Section response of beams A1 and A4, at failure.

The curvature along the length of beams A1-R and A4-R is presented in Figure 5.11, at the failure load of each beam. The peak curvature in beam A1-R, equal to 37 rad/km, is 23 percent larger than the peak curvature in beam A4-R, equal to 30 rad/km. However, the peak applied load in beam A4-R, equal

to 271 kN, is more than twice the peak applied load in beam A1-R, equal to 132 kN. The increased capacity increases the magnitude of the shear force, which increases the horizontal component of the diagonal compression struts in the beam. As a result, the curvature near the midspan and supports spread out over a longer length. This spreading of curvature offsets the reduced peak curvature, limiting any changes in deflection.

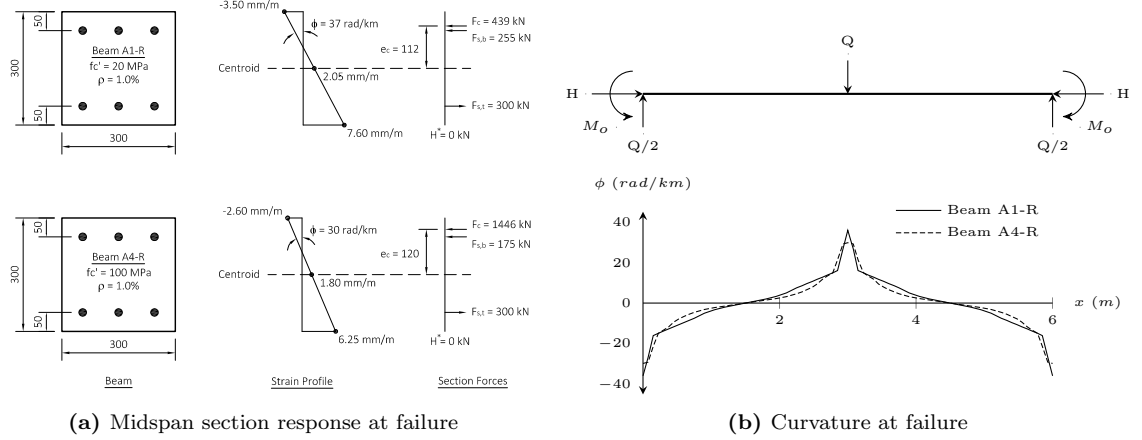


Figure 5.11: Section response of beams A1-R and A4-R, at failure.

The maximum values of applied load, axial compression and midspan deflection for all beams in the A and B-Series are presented in Figure 5.12. For beams in both the A and B-Series, increasing the strength of concrete increases the applied load and axial compression force at failure. The capacity of the B-Series beams is on average 1.5 times lower than the capacity of the A-Series beams, which have a larger reinforcement ratio. Since there is good correlation between the peak axial compression in the A and B-Series, it can be concluded that the reduced capacity in the B-Series is caused by the reduced resultant of the reinforcement. In addition, the midspan deflection of beams in the A and B-Series, presented in Figure 5.12c, indicate that increasing the strength of concrete has minimal influence on the total midspan deflection at failure.

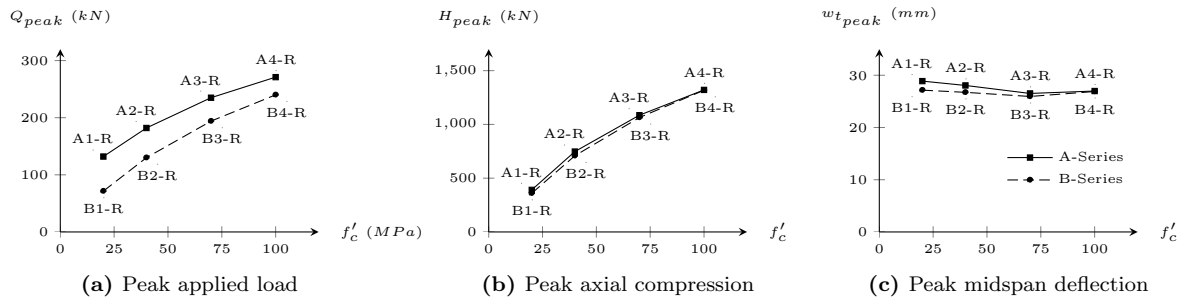


Figure 5.12: Response summary of beams in the A and B-Series, with lateral restraint.

5.1.3 Influence of Lateral Restraint

The capacity of the A-Series beams, with and without lateral restraint, is presented in Figure 5.13. When no lateral restraint is considered, increasing the compressive strength of concrete from 20 MPa to 100 MPa, for beams in the A-Series, increases the beam's capacity by a factor of 1.19. If lateral restraint is considered, increasing the compressive strength of concrete from 20 MPa to 100 MPa increases the beam's capacity by a factor of 2.05. This indicates that laterally restrained beams benefit more from an increased concrete strength than unrestrained beams. As previously discussed, increasing the strength of concrete increases the axial compression force developed, which increases the capacity of a restrained beam.

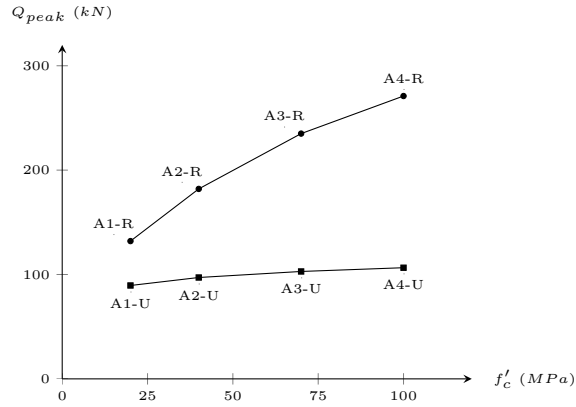


Figure 5.13: Influence of concrete strength on Q_{peak} in the A-Series.

The peak applied load for each beam in the A and B-Series is presented in Figure 5.14, with and without lateral restraint.

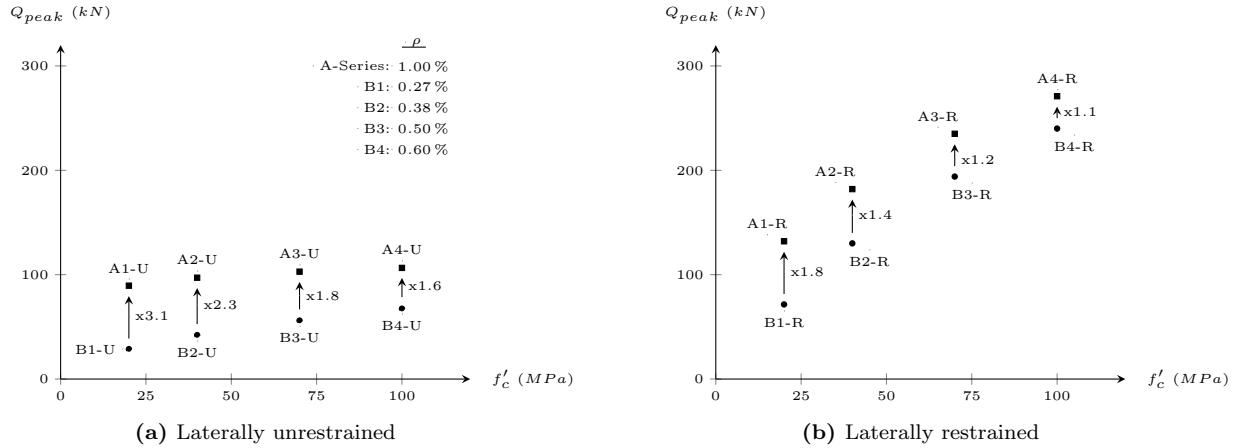


Figure 5.14: Influence of reinforcement ratio on Q_{peak} .

The factor that quantifies the increase in capacity of beams with the same concrete strength is included to highlight the influence of varying the reinforcement ratio. For unrestrained beams, increasing the reinforcement ratio increases the capacity of a beam by a factor ranging from 1.6 to 3.1. However for

restrained beams, increasing the reinforcement ratio only increases the capacity of a beam by a factor ranging from 1.1 to 1.8. This indicates that lateral restraint reduces the influence of reinforcement ratio on the capacity of a beam.

If a beam is laterally restrained, the axial compression force that develops increases the compressive force resultant in the concrete, F_c , relative to the force resultant in the reinforcement, F_s , at each section. This limits the influence of reinforcement on the response of laterally restrained beams. This is evident in the section response of beams A4-U and A4-R, presented in Figure 5.15.

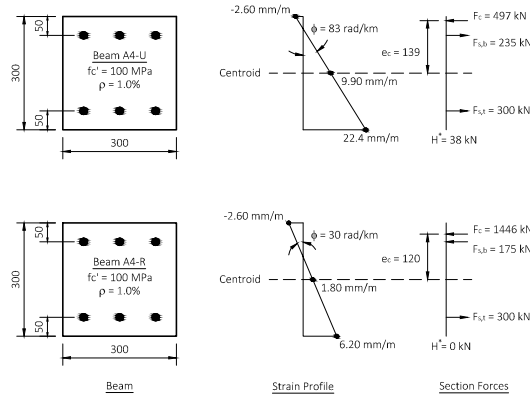


Figure 5.15: Section response of beams A4-U and A4-R.

The total bending moment at the midspan of beam A4, with and without lateral restraint, can be calculated as,

$$M_t = (F_c \cdot e_c) + (F_{s,b} \cdot e_{s,t}) + (F_{s,t} \cdot e_{s,t})$$

$$M_{tU} = (69) + (23.5) + (30) = 122.5 \text{ kN m}$$

$$M_{tR} = (174) + (18) + (30) = 222 \text{ kN m}$$

When the beam is laterally restrained, the compressive resultant force in the concrete increases by a factor of 2.9, from $F_c = 497 \text{ kN}$ in beam A4-U to $F_c = 1446 \text{ kN}$ in beam A4-R. This increases the influence of the concrete on capacity, relative to the reinforcement. In beam A4-U, the bending component of concrete is 61 percent of the total bending moment, while in beam A4-R, the bending component of concrete is 78 percent of the total bending moment. Therefore, when a beam is laterally restrained, varying reinforcement ratio has less of an impact on capacity, relative to unrestrained beams. However for both restrained and unrestrained beams, increasing the reinforcement ratio increases the capacity of a beam.

The benefit of lateral restraint can be quantified by considering the strength enhancement ratio due to arching action, α_c . This ratio is defined as,

$$\alpha_c = \frac{Q_{max_R}}{Q_{max_U}} \quad (5.2)$$

where Q_{max_U} is the peak capacity of a laterally unrestrained beam, and Q_{max_R} is the peak capacity of a laterally restrained beam. In addition, the deflection reduction ratio, α_d , can provide insight into the influence of lateral restraint on a beam's deflection at failure. This ratio is defined as,

$$\alpha_d = \frac{w_{t_{max,U}}}{w_{t_{max,R}}} \quad (5.3)$$

where $w_{t_{max,U}}$ is the peak midspan deflection of a laterally unrestrained beam, and $w_{t_{max,R}}$ is the peak midspan deflection of a laterally restrained beam.

The strength enhancement ratio for the A and B-Series beams is presented in Figure 5.16a. For the beams in the A-Series, the strength enhancement ranges from 1.5 in beam A1 to 2.5 in beam A4. This indicates that beams with a higher concrete strength will benefit more from lateral restraint. As previously discussed, increasing the compressive strength of concrete increases the axial compression developed in a restrained beam. This increased axial compression increases the capacity of a beam relative to the unrestrained case, which increases the strength enhancement due to lateral restraint.

This remains true for the beams in the B-Series, as increasing the compressive strength of concrete causes the strength enhancement to vary from 2.5 in beam B1 to 3.5 in beam B4. Therefore, reducing the reinforcement ratio increases the influence of lateral restraint on the peak capacity of a beam. As previously discussed, reducing the reinforcement ratio in restrained beams has less of an influence on capacity, relative to unrestrained beams. Therefore, reducing the reinforcement ratio increases the strength enhancement caused by the lateral restraint.

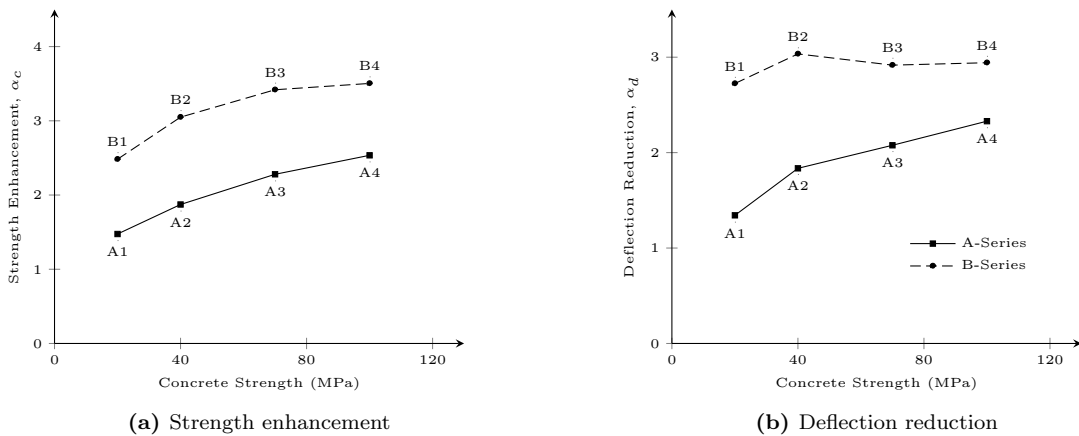


Figure 5.16: Influence of concrete strength on α_c and α_d .

The deflection reduction ratio is presented in Figure 5.16b for both the A and B-Series beams. For beam A1, the midspan deflection of the unrestrained beam is 1.3 times higher than the deflection of the

restrained beam. For beam A4, the midspan deflection of the unrestrained beam is 1.5 times higher than the deflection of the restrained beam. This indicates that increasing the strength of concrete increases the influence of lateral restraint on the midspan deflection at failure. As previously suggested, varying the strength of concrete has a minimal impact on the peak midspan deflection of restrained beams. However, increasing the strength of concrete in unrestrained beams increases the peak midspan deflection.

The influence of lateral restraint on the curvature in beams A1 and A4 is illustrated in Figure 5.17. The peak curvature at failure in beam A1-U is approximately 1.8 times greater than the curvature of beam A1-R, causing the peak midspan deflection to reduce by a factor of 1.3. In contrast, the peak curvature in beam A4-U is 2.8 times greater than the peak curvature in beam A4-R, causing the peak midspan deflection to reduce by a factor of 2.3. This response indicates that lateral restraint has a greater impact on the deflection of beams with higher concrete strength.

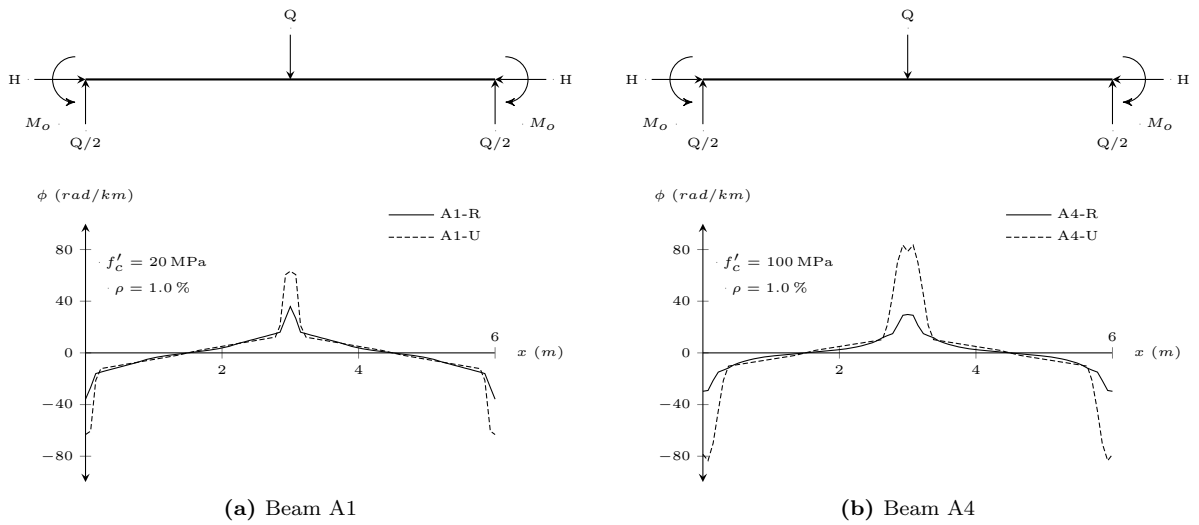


Figure 5.17: Curvature throughout beams A1 and A4, with and without lateral restraint.

In the B-Series beams, the deflection reduction ratio is equal to 2.7 in beam B1, and 3.0 in beams B2, B3 and B4. As previously discussed, increasing the strength of concrete has a minimal influence on the peak midspan deflection in restrained beams. Therefore, the consistent deflection reduction in beams B2, B3 and B4 is the result of the correlation in midspan deflection of each of the unrestrained beams. This relationship, presented in Figure 5.6, was discussed earlier in this section.

5.1.4 Reinforcement Limits

The Canadian Highway Bridge Design Code (CHBDC) specifies minimum and maximum reinforcement ratios for reinforced concrete bending members. To provide sufficient warning before the failure of a beam or slab strip, the flexural tension reinforcement must yield prior to the concrete crushing. The ratio of the depth of compression in the concrete, c , to the effective depth of the reinforcement, d , defines the relation between the peak compressive strain in the concrete and the tensile strain in the reinforcement. To ensure that the beam or slab slip will provide a sufficient warning of failure, the following limit, based on Clause 8.8.4.5 of the CHBDC, is recommended,

$$\frac{c}{d} \leq 0.5 \quad (5.4)$$

The c/d ratios for the beams in both the A and B-Series are presented in Figure 5.18a. This limit specifies the maximum reinforcement allowable in a beam or slab strip. In both series, increasing the strength of concrete causes an increase in the c/d ratio, which limits the warning provided prior to failure. The beams that consider a 100 MPa concrete strength exceed the recommended limit of 0.5, and therefore do not satisfy the CHBDC requirements. However, this limit is developed without consideration of axial compression caused by lateral restraint. For compression components, the maximum amount of reinforcement, based on Clause 8.8.5.6 of the CHBDC, is limited to,

$$\frac{A_s}{A_g} \leq 0.08 \quad (5.5)$$

where A_s is the total area of reinforcement on the flexural tension side, and A_g is the gross cross-sectional area of the beam (Canadian Standards Association, 2006). In a beam with lateral restraint, the magnitude of axial compression is dependent on the beam's geometry and material properties. As a result, increasing the reinforcement limit beyond the value prescribed for pure flexural members would need to be justified based on the consideration of each individual design.

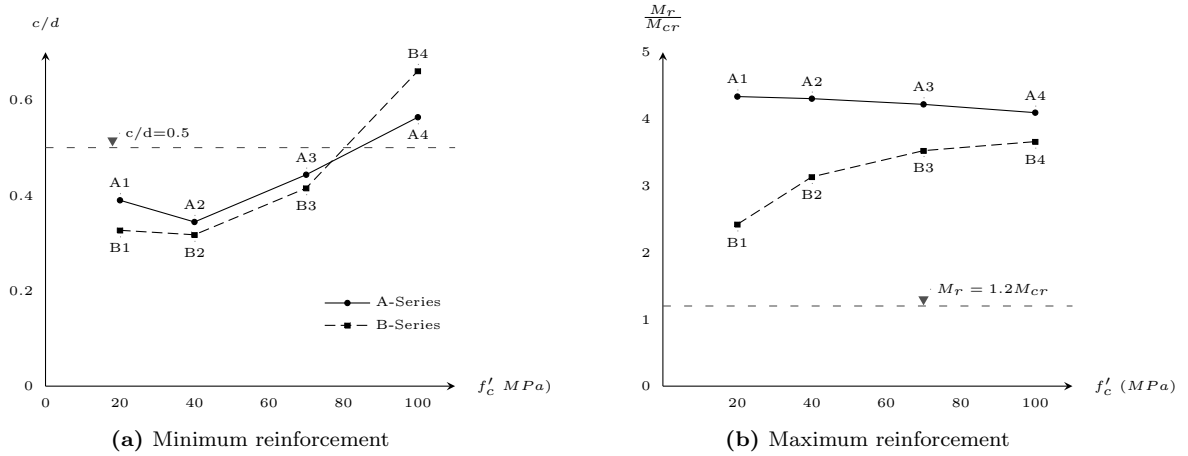


Figure 5.18: Reinforcement limits specified by the CHBDC (2006).

To prevent a brittle failure of the beam when it first cracks, the following limit, based on Clause 8.8.4.3 of the CHBDC, is recommended,

$$M_r \geq 1.2 M_{cr} \quad (5.6)$$

where M_r is the bending capacity of a laterally restrained beam, and M_{cr} is the bending moment at which cracking occurs (Canadian Standards Association, 2006). This limit specifies the minimum reinforcement required for a beam or slab. Prior to cracking, minimal axial compression will develop in a laterally restrained beam (Liebenberg, 1966). Therefore, the cracking moment can be determined

without consideration of axial compression. For the purpose of this stress check, the concrete is assumed to have a cracking strength of $f'_t = 0.4\sqrt{f'_c}$ (Canadian Standards Association, 2006). The ratio of bending capacity to the bending moment causing cracking, M_r/M_{cr} , for both A and B-Series beams, are presented in Figure 5.18b. When the reinforcement ratio is kept constant, increasing the strength of concrete has little influence on the ratio of bending capacity to the cracking moment. For beams in the B-Series, which have varied magnitudes of reinforcement, reducing the strength of concrete, in conjunction with a reduction in reinforcement ratio, reduces the ratio of bending capacity to bending moment causing cracking. However, all the beams considered in this study are above this threshold.

5.1.5 Summary of Results and Conclusions

The results from this study provide insight into the influence of concrete strength on laterally restrained (R) and unrestrained (U) beams, and can be summarized as:

1. Increasing the compressive strength of concrete from 20 MPa to 100 MPa in the A-Series:
 - (a) increases the load capacity by a factor of 2.1 (R), and 1.2 (U).
 - (b) increases the peak axial compression force by a factor of 3.4 (R).
 - (c) increases the strength enhancement caused by lateral restraint from 1.5 to 2.5.
 - (d) reduces the peak midspan deflection by a factor of 1.07 (R), and increases the peak midspan deflection by a factor of 1.62 (U).
2. Increasing the compressive strength of concrete from 20 MPa to 100 MPa in the B-Series:
 - (a) increases the load capacity by a factor of 3.4 (R), and 2.4 (U).
 - (b) increases the peak axial compression force by a factor of 3.7 (R).
 - (c) increases the strength enhancement caused by lateral restraint from 2.5 to 3.5.
 - (d) reduces the peak midspan deflection by a factor of 1.04 (R), and increases the peak midspan deflection by a factor of 1.04 (U).

In addition the results from this study provide insight into the influence of reinforcement ratio on laterally restrained (R) and unrestrained (U) beams, and can be summarized as:

3. Reducing the reinforcement ratio from 1.0 % to 0.60 %:
 - (a) increases the load capacity by a factor of 1.1 (R), and 1.6 (U).
 - (b) has little influence on the peak axial compression force developed in the beam.
 - (c) increases the strength enhancement caused by consideration of lateral restraint from 2.5 to 3.5.
 - (d) increases the peak midspan deflection by a factor of 1.2 (U) and has minimal influence on the peak midspan deflection in restrained beams.

4. Reducing the reinforcement ratio from 1.0 % to 0.27 %:
 - (a) increases the load capacity by a factor of 1.8 (R), and 3.1 (U).
 - (b) reduces the peak axial compression force by a factor of 1.08 (R).
 - (c) increases the strength enhancement caused by consideration of lateral restraint from 1.5 to 2.5.
 - (d) reduces the peak midspan deflection by a factor of 1.06 (R), and increases the peak midspan deflection by a factor of 1.9 (U).

Based on this parametric study, the following conclusions can be made:

1. Lateral restraint allows the compressive strength of concrete to be used more efficiently.
2. Increasing the reinforcement ratio decreases the effectiveness of arching action.

5.2 Mechanical Reinforcement Ratio

The combined influence of varying concrete strength and reinforcement ratio can be studied by considering the mechanical reinforcement ratio. The mechanical reinforcement ratio is defined as,

$$\omega = \frac{A_s f_y}{f'_c b d} \quad (5.7)$$

where A_s is the total area of reinforcement, f_y is the yield stress of the reinforcement, f'_c is the compressive strength of the concrete, b is the width of the beam, and d is the effective depth of the reinforcement. The properties of the beams considered in this study, which are identical to the beams used in the concrete parametric study, are presented in Figure 5.19. The beams in the A-Series have a mechanical reinforcement ratio ranging from 4.0 to 20 percent, while the beams in the B-Series have a mechanical reinforcement ratio ranging from 2.5 to 5.3 percent.

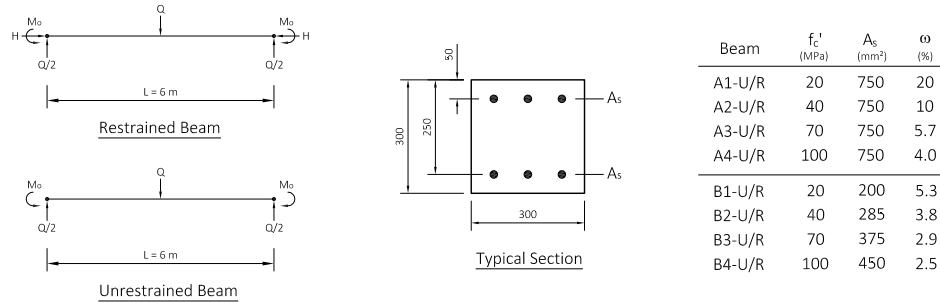


Figure 5.19: Beam properties for the mechanical reinforcement parametric study.

As indicated in the previous section, the majority of these beams meet the minimum and maximum reinforcement criteria recommended by the Canadian Highway Bridge Design Code.

5.2.1 Unrestrained Beam Response

The applied load vs. midspan deflection response for the A-Series beams, without lateral restraint, is presented in Figure 5.20. For the A-Series beams, reducing the mechanical reinforcement ratio from 20 percent in beam A1-U, to 4 percent in beam A4-U, increases the capacity by a factor of 1.19, and increases the peak midspan deflection by a factor of 1.62. In addition, reducing the mechanical reinforcement ratio increases the post-yielding deformation of each beam, providing more warning prior to failure. The behaviour of the unrestrained beams in the A-Series is discussed in detail in the previous section.

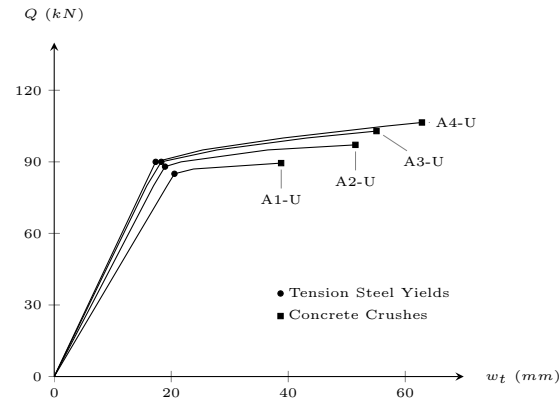


Figure 5.20: Load-deflection response of A-Series beams, without restraint.

The peak applied load of beams in the A and B-Series, with no lateral restraint, is presented in Figure 5.21a.

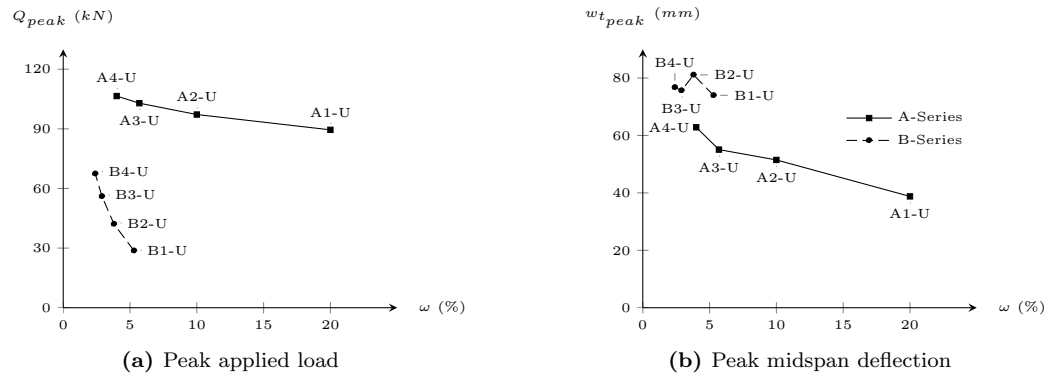


Figure 5.21: Response of the beams in the A and B-Series, with no lateral restraint.

In both the A and B-Series, increasing the mechanical reinforcement ratio reduces the capacity of the beam. However, the mechanical reinforcement ratio has a greater influence on the capacity of beams

in the B-Series, relative to the A-Series. In the A-Series, the mechanical reinforcement ratio is reduced by increasing the strength of concrete. However in the B-Series, the mechanical reinforcement ratio is reduced by increasing the strength of concrete and reducing the reinforcement ratio. As indicated in the previous section, altering the reinforcement ratio in an unrestrained beam has a greater influence on the response of a beam, relative to altering concrete strength.

In addition, the peak midspan deflection for beams in the A and B-Series, with no lateral restraint, is presented in Figure 5.21b. In the A-Series, increasing the mechanical reinforcement ratio reduces the peak midspan deflection of each beam. As discussed in the previous section, increasing the strength of concrete reduces the depth of compression in the concrete, which increases the curvature at each section. However, increasing the reinforcement ratio in conjunction with the strength of concrete limits this increased curvature, which limits the change in peak midspan deflection in beams in the B-Series.

5.2.2 Restrained Beam Response

The load-deflection and load-restraint response of each laterally restrained beam in the A-Series is presented in Figure 5.22. For the A-series, reducing the mechanical reinforcement ratio from 20 % to 4.0 % doubles the load capacity of the concrete, and increases the peak axial compression by a factor of 3.5. In addition, reducing the mechanical reinforcement ratio from beam A1-R to A4-R reduces the peak midspan deflection by a factor of 1.1.

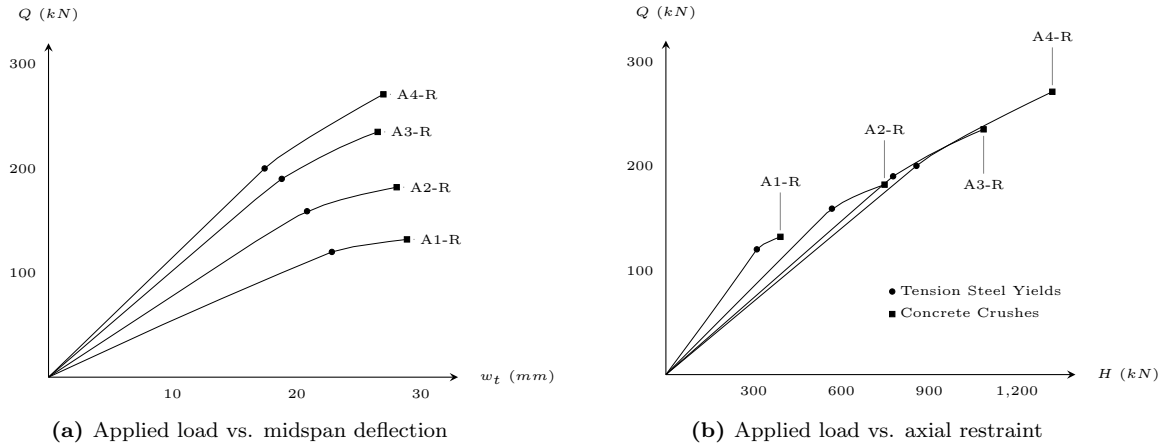


Figure 5.22: Response of B-Series beams, with lateral restraint.

In the A-Series, the mechanical reinforcement ratio is altered by varying the strength of the concrete. Therefore, the increase in capacity associated with a lower mechanical reinforcement ratio is caused by the development of a larger axial compression force in beams with higher strength concrete. In addition, altering the mechanical reinforcement ratio in the A-Series increases each beam's initial stiffness, but has a minimal impact on the peak midspan deflection. This relationship is consistent with the behaviour discussed in the previous section for A-Series beams with lateral restraint, which indicated that increasing the strength of concrete causes little change in the peak midspan deflection of a restrained beam.

The maximum values of applied load, axial compression force and midspan deflection for all beams in

the A and B-Series are presented in Figure 5.23. In both the A and B-Series, increasing the mechanical reinforcement ratio reduces the axial compression force, and capacity of each beam. In addition, the peak midspan deflection of the restrained beams in both the A and B-Series is presented in Figure 5.23c. This response indicates that varying the mechanical reinforcement ratio has minimal influence on the midspan deflection of a beam. This is consistent with the response of restrained beams with varying concrete strength, as discussed in the previous section.

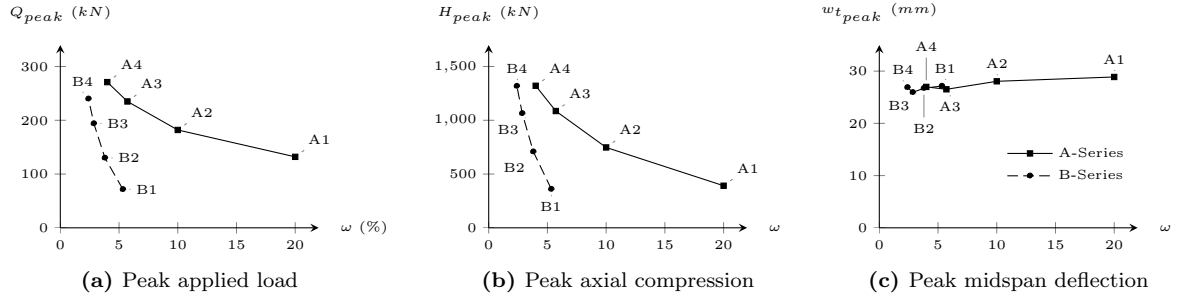


Figure 5.23: Response summary of beams in the A and B-Series, with lateral restraint.

In the B-Series, the mechanical reinforcement ratio is adjusted by simultaneously altering concrete strength and reinforcement ratio. Beams A4-R and B2-R, which have different combinations of concrete strength and reinforcement ratio, have approximately the same mechanical reinforcement ratio. However, the capacity and peak axial compression in beam A4-R are two times larger than beam B2-R. Therefore, simultaneously reducing concrete strength and reinforcement ratio, as in the B-Series, has more of an impact on the capacity of a beam than only altering the strength of concrete, as in the A-Series.

The midspan section response of beams A4-R and B2-R, at peak load, is summarized in Figure 5.24.

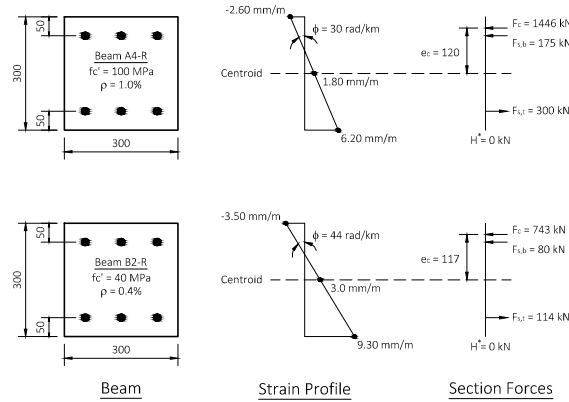


Figure 5.24: Midspan section response of beams A4-R and B2-R, at failure.

Although both beams have the same mechanical reinforcement ratio, the plane of strain, and resulting sectional forces, are different. Beam A4-R has a higher concrete strength, and as a result, a larger magnitude of axial compression at each section, relative to beam B2-R. The increased concrete strength

also reduces the peak compressive strain in the concrete from 3.5 mm/m to 2.6 mm/m. The reduced peak strain, along with a reduced reinforcement ratio, causes the peak curvature at midspan to reduce from 44 rad/km in beam B2-R to 30 rad/km in beam A4-R. As a result, the resultant forces in both the concrete and reinforcement in beam A4-R are greater than the resultant forces in beam B2-R. This allows beam A4-R to have a higher bending capacity than beam B2-R, without any change in the mechanical reinforcement ratio.

5.2.3 Influence of Lateral Restraint

The influence of mechanical reinforcement ratio on strength enhancement, caused by lateral restraint, is illustrated in Figure 5.25a. The response of both the A and B-Series beams suggest that reducing the mechanical reinforcement ratio of a beam increases the beneficial influence of lateral restraint on beam capacity. In the A-Series, reducing the mechanical reinforcement ratio from 2 percent to 0.4 percent increases the strength enhancement from 1.5 in beam A1 to 2.5 in beam A4. This corresponds with the relationship between concrete strength and strength enhancement discussed in the previous section. In the B-Series, reducing the mechanical reinforcement ratio from 5.3 percent to 2.4 percent increases the strength enhancement from 2.5 in beam B1 to 3.5 in beam B4. This indicates, as suggested in the previous section, that reducing the reinforcement ratio, in conjunction with increasing concrete strength, increases the benefits of lateral restraint.

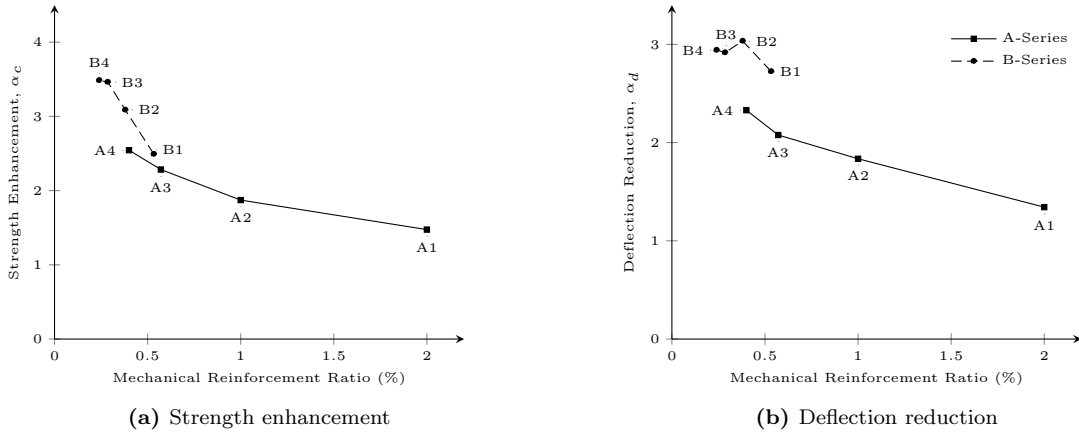


Figure 5.25: Influence of mechanical reinforcement ratio on α_c and α_d .

In addition, the influence of mechanical reinforcement ratio on the deflection reduction ratio, caused by lateral restraint, is illustrated in Figure 5.25b. The response of both the A and B-Series suggest that reducing the mechanical reinforcement ratio causes the peak midspan deflection of a restrained beam to deviate from the response of an unrestrained beam. For restrained beams in both series, varying the mechanical reinforcement ratio has minimal influence on peak midspan deflection. On the other hand, reducing the mechanical reinforcement ratio in unrestrained beams causes the peak midspan deflection to increase. Therefore the deviation in peak midspan deflection is caused by variations in the peak midspan deflection of the unrestrained beams, relative to the restrained beams. The similarities in peak midspan deflection in beams B2, B3 and B4 are caused by the increased axial compression in the beam,

as well as the reduced peak compressive strain in higher strength concrete. This was discussed in detail in the previous section.

5.2.4 Summary of Results and Conclusions

The results of this study provide insight into the influence of mechanical reinforcement ratio on laterally restrained (R) and unrestrained (U) beams, and can be summarized as:

1. Reducing the mechanical reinforcement ratio from 20 percent to 4 percent in the A-Series:
 - (a) increases the load capacity by a factor of 2.1 (R), and 1.19 (U).
 - (b) increases the peak axial compression force by a factor of 3.4 (R).
 - (c) increases the strength enhancement caused by lateral restraint from 1.5 to 2.5.
 - (d) the peak midspan deflection is reduced by a factor of 1.07 (R), and increased by a factor of 1.62 (U).
2. Reducing the mechanical reinforcement ratio from 5.3 percent to 2.4 percent in the B-Series:
 - (a) increases the load capacity by a factor of 3.4 (R), and 2.4 (U).
 - (b) increases the peak axial compression force by a factor of 3.7 (R).
 - (c) increases the strength enhancement caused by lateral restraint from 2.5 to 3.5.
 - (d) the peak midspan deflection is reduced by a factor of 1.04 (R), and increased by a factor of 1.04 (U).

Based on this parametric study, it can be concluded that:

1. Reducing mechanical reinforcement ratio increases the beneficial effects of lateral restraint.

5.3 Second-Order Effects

A total of ten reinforced concrete beams, with properties summarized in Figure 5.26, are considered in this parametric study. The results from the parametric studies conducted in the previous sections indicate that a beam with a higher concrete strength, and lower reinforcement ratio, will benefit more from lateral restraint. Therefore, the beams considered in this study are split into two series. The C-Series looks at the response of beams with a low concrete strength and high reinforcement ratio, while the D-Series looks at the response of beams with a high concrete strength and a low reinforcement ratio. To study the influence of second-order effects on the response of beams in both series, the span-to-depth ratio, L/h , is varied from 7 to 47.

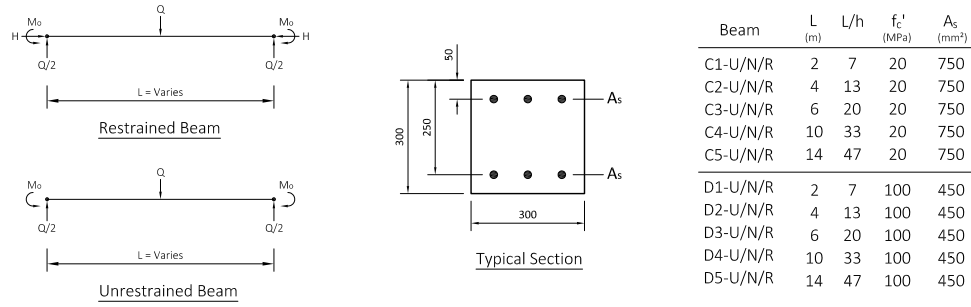


Figure 5.26: Beam properties for the second-order effects parametric study.

The analysis of each beam is conducted using the basic configuration of the proposed analytical model, with consideration of the spreading of load by diagonal compression struts. The three support conditions considered for each beam are:

U: Beam has no lateral restraint.

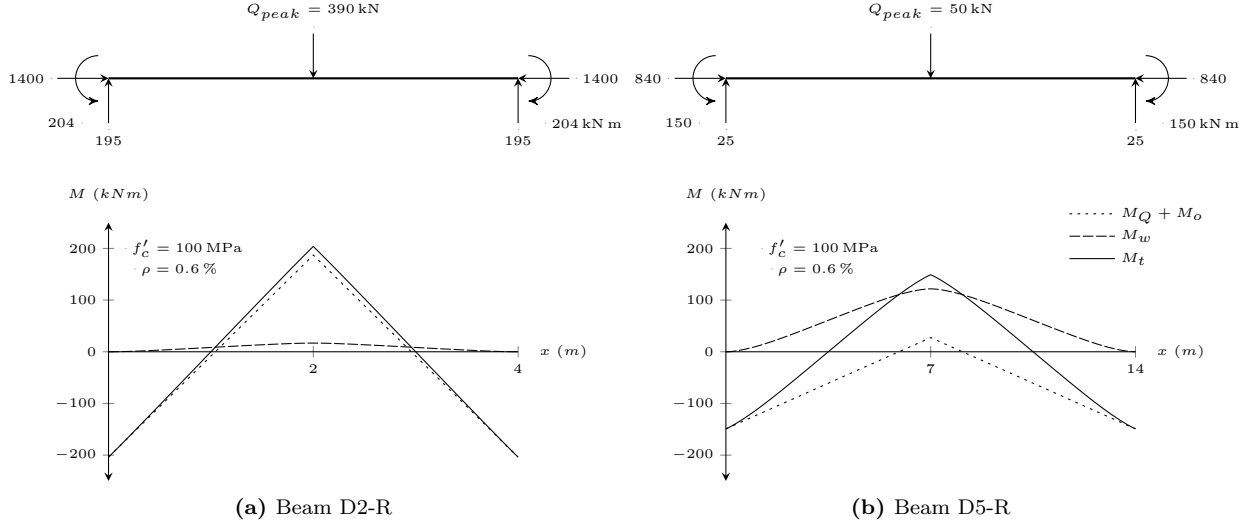
N: Beam has an infinitely stiff lateral restraint, but the contribution of second-order effects is ignored.

R: Beam has an infinitely stiff lateral restraint, and second-order effects are included in the analysis.

5.3.1 Influence of Second-Order Effects on Bending Moment

The total bending moment in a beam or slab strip, M_t , is comprised of the bending moment caused by the applied load and end restraint, $M_Q + M_o$, and the bending moment caused by consideration of second-order effects, M_w . The bending moment caused by second-order effects is equal to the product of the axial compression force in the beam, H , and the total deflection of the beam, w_t . Therefore, consideration of second-order effects is important in beams that developed a large axial compression force and deflection, prior to failure.

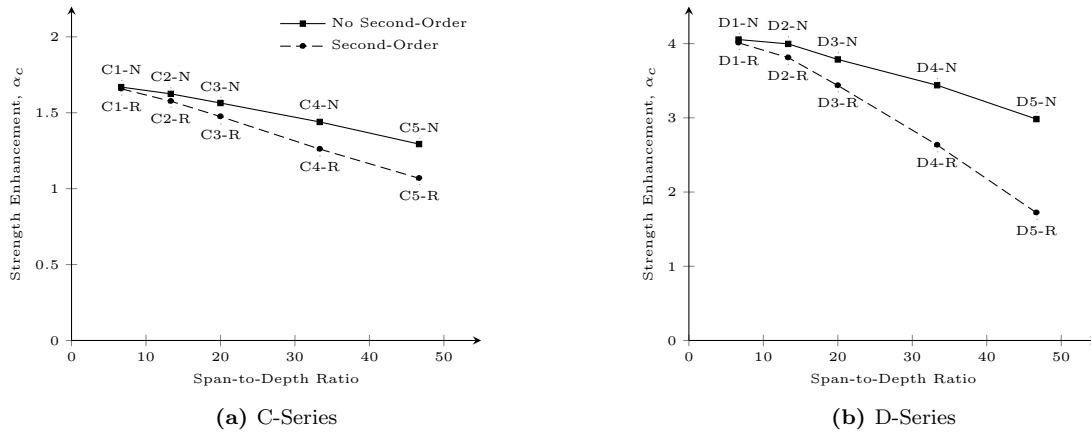
The calculated values of $M_Q + M_o$, M_w and M_t for beams D2-R and D5-R are presented in Figure 5.27, at failure load. In beam D2-R, the bending moment caused by second-order effects at failure load, 17 kN m, is less than ten percent of the total bending moment in the beam, 200 kN m. Therefore the consideration of M_w in beam D2-R, which has a span-to-depth ratio of 13, has little influence on the response of beam D2-R. This is evident in Figure 5.27a, where the response of M_t closely matches the response of $M_Q + M_o$.

Figure 5.27: Bending moment diagram in beams D2-R and D5-R, at Q_{peak} .

In beam D5-R however, the bending moment caused by second-order effects at failure, 120 kN m, is 80 percent of the total bending moment in the beam, 150 kN m. Therefore the consideration of M_w in beam D5-R, which has a span-to-depth ratio of 47, is important as it governs the response of the beam. This is evident in Figure 5.27b where the response of M_t diverges from the response of $M_Q + M_o$, as a result of the larger magnitude of M_w . The response of beams D2-R and beam D5-R indicate that increasing the span-to-depth ratio of a beam will increase the magnitude of M_w , relative to M_t , and as a result, increase the influence of second-order effects.

5.3.2 Influence of Lateral Restraint

The influence of lateral restraint on the strength enhancement of beams in both the C and D-Series is presented in Figure 5.28, with and without consideration of second-order effects.

Figure 5.28: Influence of second-order bending moment on α_c .

If second-order effects are considered for the C-Series beams, which have a low concrete strength and high reinforcement ratio, the strength enhancement varies from 1.7 in beam C1-R to 1.1 in beam C5-R. If second-order effects are not considered, the strength enhancement varies from 1.7 in beam C1-N to 1.3 in beam C1-N. Therefore, increasing the span-to-depth ratio from 7 to 47 increases the influence of second-order effects on strength enhancement from less than one percent in beam C1, to 20 percent in beam C5.

When second-order effects are considered for the D-Series beams, which have a high concrete strength and low reinforcement ratio, the strength enhancement varies from 4.0 in beam D1-R to 1.7 in beam D5-R. When second-order effects are not considered, the strength enhancement varies from 4.0 in beam D1-N to 3.0 in beam D5-N. This response is similar to that of the beams in the C-Series, as increasing the span-to-depth ratio from 7 to 47 causes the difference in strength enhancement between beams, with and without second-order effects, to vary from 1 percent to 73 percent. The divergence in the response between the C and D series beams indicates that considering the influence of second-order effects is more important for beams with a higher concrete strength and lower reinforcement ratio. In addition, the strength enhancement is, on average, two times higher in the D-Series than the C-Series. This supports the finding from the previous sections, that beams with a high concrete strength and low reinforcement ratio benefit more from lateral restraint.

5.3.3 Influence of Second-Order Effects on Beam Response

The influence of second-order effects can be studied by considering the ratio of the peak load predicted for each beam with consideration of second-order effects, $Q_{R_{peak}}$, and without consideration of second-order effects, $Q_{N_{peak}}$. This ratio is presented in Figure 5.29 for beams in the C and D-Series. In both series, increasing the span-to-depth ratio causes the capacity of a beam without consideration of second-order effects to increase relative to the capacity of a beam with consideration of second-order effects. For the C-Series beams, the ratio between the peak load, with and without considering second-order effects, varies from less than one percent in beam C1 to 21 percent in beam C5. However for the D-Series beams, this ratio varies from 1 percent in beam D1 to 73 percent in beam D5. This indicates that increasing the span-to-depth ratio, increasing the strength of the concrete, and reducing the reinforcement ratio increases the influence of second-order effects on the capacity of a beam.

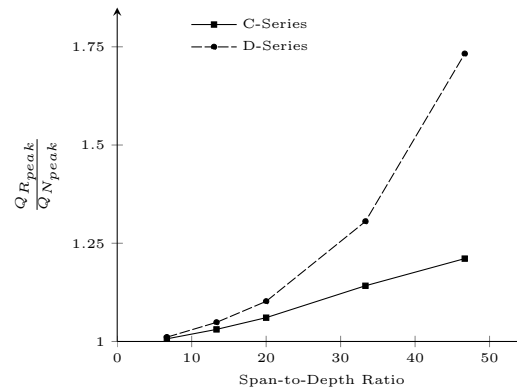


Figure 5.29: Influence of second-order bending moment on Q_{peak} .

In the previous sections, it was found that increasing the strength of concrete, and reducing the reinforcement ratio, increases the magnitude of the peak axial compression force developed in a beam, but has minimal influence on the midspan deflection at peak load. Therefore, beams in the D-Series develop a larger axial compression with little change to each beam's deflection, relative to beams in the C-Series. This increases the magnitude of the bending moment due to second-order effects, relative to the total bending moment developed in the beam, which increases the importance of considering second-order effects. The bending moment in beams C5-R and D5-R are presented in Figure 5.30. The peak axial compression force developed in beam D5-R, 840 kN, is 4.2 times larger than the peak axial compression developed in beam C5-R, 200 kN. However, the capacity of beam D5-R, 50 kN, is only 1.25 times larger than the capacity of beam C5-R, 40 kN. Therefore, the relative magnitude of M_w to M_t increases by a factor of 2.5, from 34 percent in beam C5-R to 84 percent in beam D5-R. This increase indicates that considering a beam with a high concrete strength and low reinforcement ratio increases the influence of second-order effects on the response.

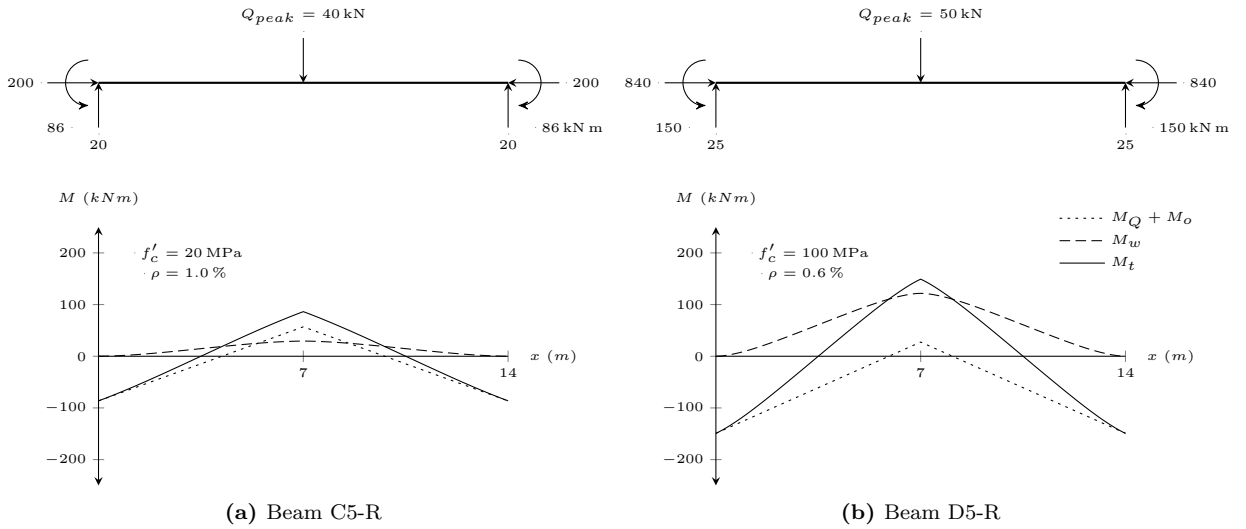


Figure 5.30: Bending moment in beams C5-R and D5-R, at Q_{peak} .

The influence of second-order effects on the axial compression force developed in a laterally restrained beam can be quantified by looking at the ratio of the peak axial compression in a beam with second-order effects, $H_{R_{peak}}$, to the peak axial compression in a beam without second-order effects, $H_{N_{peak}}$. This ratio is presented in Figure 5.31a for beams in the C and D-Series. The response from these beams indicate that varying the span-to-depth ratio does not change the influence of second-order effects on the axial compression force developed at failure.

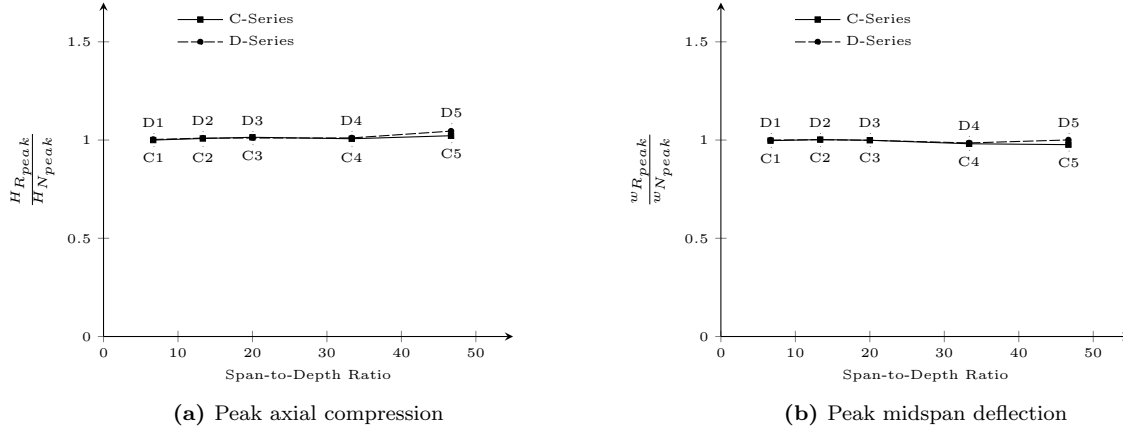
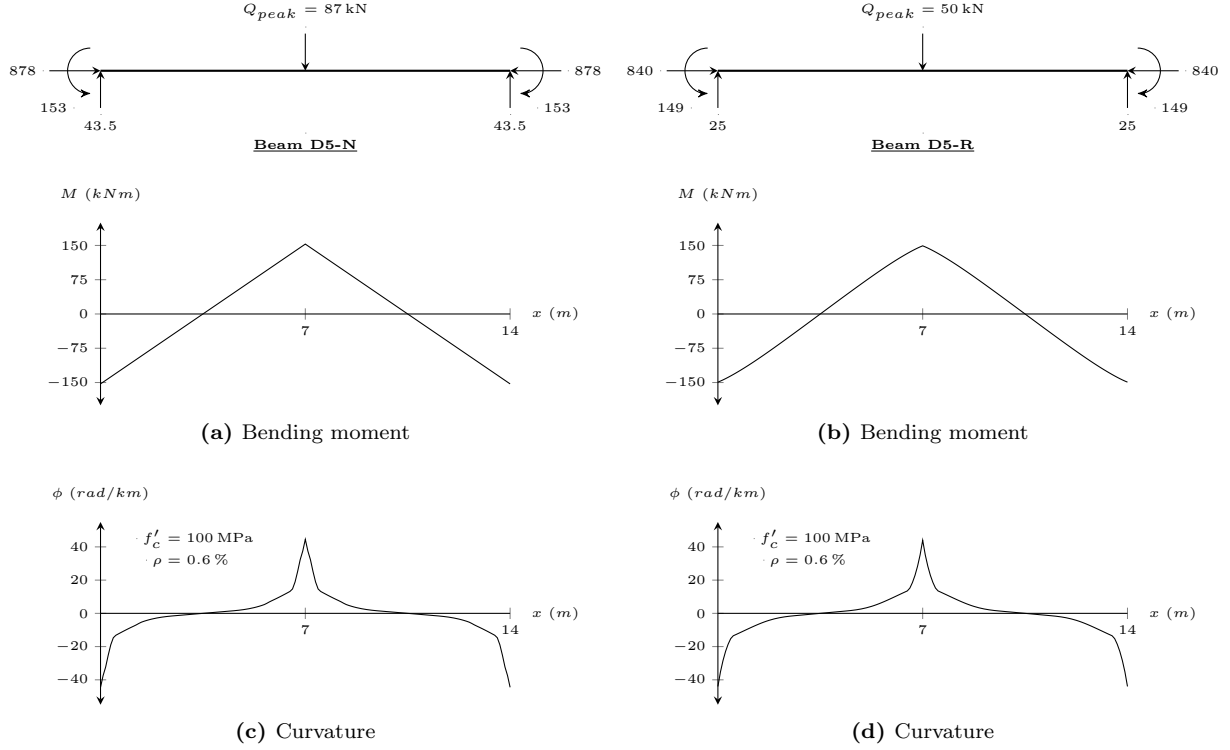


Figure 5.31: Influence of second-order bending moment on H_{peak} and $w_{t_{peak}}$.

Similarly, the influence of second-order effects on the peak midspan deflection developed in a laterally restrained beam can be quantified by considering the ratio of the peak midspan deflection in a beam with second-order effects, $w_{R_{peak}}$, to the peak midspan deflection in a beam without second-order effects, $w_{N_{peak}}$. This ratio is presented in Figure 5.31b for beams in the C and D-Series. The response from these beams indicate that varying the span-to-depth ratio does not change the influence of second-order effects on the midspan deflection at failure.

Therefore, it can be concluded that second-order effects have a minimal influence on the peak axial compression and peak midspan deflection developed in a laterally restrained beam. This can be explained by considering the bending moment and curvature response of beam D5-R and D5-N, presented in Figure 5.32. Since the section properties for both beams are the same, they will have the same bending moment capacity. In beam D5-R, the total bending moment is equal to the sum of the bending moment due to the applied load, M_Q , the bending moment due to the support restraint, M_o , and the bending moment caused by second-order effects, M_w . Therefore, the total bending moment in beam D5-R will be nonlinear. In contrast the bending moment in Beam D5-N, which does not consider M_w , remains linear. As a result of not considering M_w , the magnitude of M_Q and M_o increases to achieve a section's bending capacity. As a result, the load capacity of beam D5-N, 87 kN, is 1.7 times larger than the load capacity of beam D5-R, 50 kN.

The second condition of compatibility specified for the proposed model, presented in Chapter 2, states that for a beam supported by an infinitely stiff rotational restraint, the total rotation at each support must be equal to zero. To achieve this, the moment area theorem requires that the integral of the curvature along half of a beam be equal to zero. This requirement applies to the analysis of beams with and without second-order effects. Since the peak bending moment in both beams is very similar, and the beams do not rotate at the supports, the curvature response of beam D5-R is very similar to the curvature response of beam D5-N. Therefore, the magnitude of the axial compression force and the deflection of each beam, at failure, is not significantly altered by second-order effects.

Figure 5.32: Bending moment and curvature throughout beam D5, at Q_{peak} .

5.3.4 Summary of Results and Conclusions

The results of this study provides insight into the influence of second-order effects on the response of laterally restrained beams, and can be summarized as:

1. Increasing the span-to-depth ratio from 7 to 47 in the C-Series:
 - (a) reduces the strength enhancement caused by lateral restraint from 1.7 to 1.1 (R) and from 1.7 to 1.3 (N).
 - (b) increases the magnitude of $\frac{Q_{N_{peak}}}{Q_{R_{peak}}}$ by less than one percent to 21 percent.
 - (c) has minimal influence on the axial compression force and midspan deflection at Q_{peak} .
2. Increasing the span-to-depth ratio from 7 to 47 in the D-Series:
 - (a) reduces the strength enhancement caused by lateral restraint from 4.0 to 1.7 (R) and from 4.1 to 3.0 (N).
 - (b) increases the magnitude of $\frac{Q_{N_{peak}}}{Q_{R_{peak}}}$ by 1 percent to 73 percent.
 - (c) has minimal influence on the axial compression force and midspan deflection at Q_{peak} .

Based on this parametric study, it can be concluded that:

1. Increasing the span-to-depth ratio of a laterally restrained beam increases the influence of second-order effects on load capacity.
2. Increasing the concrete strength and reducing the reinforcement ratio of a laterally restrained beam increases the influence of second-order effects on load capacity.
3. For every value of span-to-depth ratio, accounting for second-order effects has minimal influence on the axial compression and beam deflection at Q_{peak} .
4. Based on the response in Figure 5.29, and assuming that the allowable variation in the predicted capacity of a beam is $\pm 10\%$, it can be concluded that analysis of beams with a span-to-depth ratio above 20 should account for second-order effects.

5.4 Lateral Slip at Supports

The lateral slip that can develop between the ends of a beam and its supports delays the onset of axial compression. This slip will typically only occur in beams that are precast and mechanically attached to a support, such as in the experiments conducted by Su, Tian, and Song (2009), and Yu and Tan (2013).

The influence of this initial lateral slip can be studied by considering the response of beams A1 and B4, as summarized in Figure 5.33. The parametric studies presented in the previous sections indicate that beam A1, which has a lower concrete strength and higher reinforcement ratio relative to beam B4, will benefit less from lateral restraint than beam B4. Therefore, beams A1 and B4 represent the upper and lower bound of strength enhancement, for the beams in the A and B-Series. To study the influence of initial lateral slip, the magnitude of the total slip at both supports, S , is varied from 0 mm to 3 mm. Throughout this study, the amount of slip is referred to non-dimensionally as the ratio of the total slip to the length of the beam, S/L .

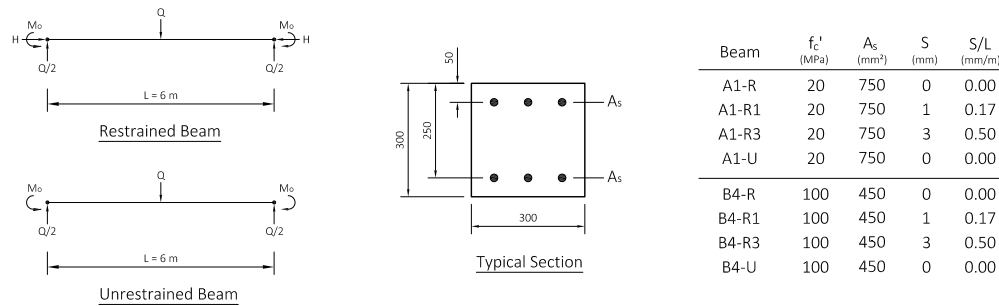


Figure 5.33: Beam properties for the slip parametric study.

The analysis for each beam is conducted using the basic configuration of the proposed analytical model, with consideration of the spreading of load by diagonal compression struts. The two support conditions considered for each beam are:

U: Beam has no lateral restraint.

R: Beam has an infinitely stiff lateral restraint.

5.4.1 Restrained Beam Response

The applied load vs. midspan deflection response of beam A1-R, with varying magnitudes of slip, is presented in Figure 5.34a. When there is no lateral slip at the supports, the potential expansion of the beam is prevented by the lateral restraint, causing an axial compression force to develop in the beam. As the magnitude of slip is increased, the beam expands prior to engaging the lateral support, delaying the onset of axial compression. In beam A1-R1, the initial response of the beam follows the response of a beam with no lateral restraint, A1-U. When the lateral restraint is engaged, at a midspan deflection of 8 mm, an axial compression force develops causing the response to deviate from A1-U. In contrast, the reinforcement in beam A1-R3 yields prior to engaging the lateral restraint. As a result, the response of beam A1-R3 is identical to the response of beam A1-U up to a midspan deflection of 25 mm, after which the development of axial compression causes the stiffness of the beam to increase.

Increasing the total lateral slip in a beam from 0 mm/m to 0.5 mm/m reduces the capacity by a factor of 1.3, from 132 kN in beam A1-R to 101.5 kN in beam A1-R3. In addition, increasing the total lateral slip in a beam from 0 mm/m to 0.5 mm/m increases the peak midspan deflection by a factor of 1.2, from 29 mm in beam A1-R to 34 mm in beam A1-R3.

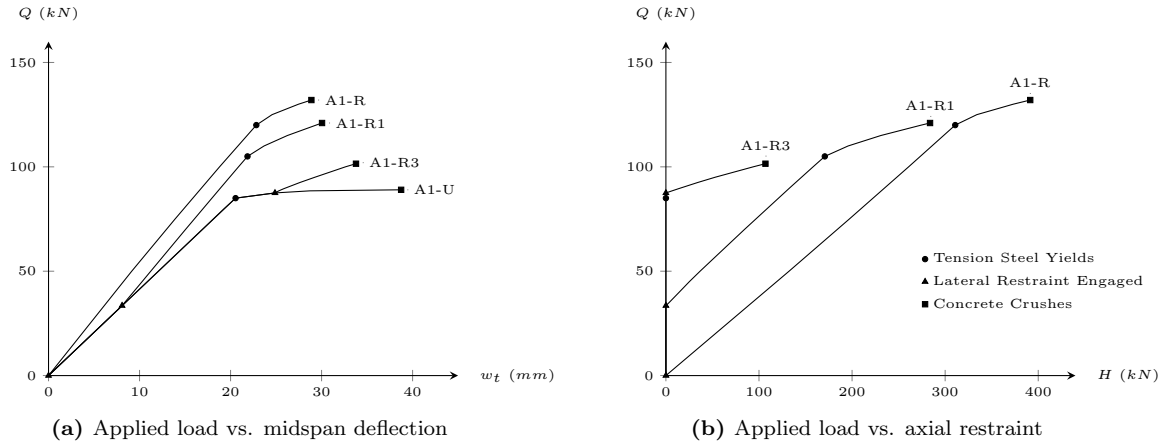


Figure 5.34: Influence of slip on Q , H and w_t for beam A1.

The applied load vs. axial compression force of beams A1-R, with varying magnitudes of slip, is presented in Figure 5.34b. Beam A1-R, which does not slip, immediately engages the lateral support, allowing an axial compression force to develop. The slip that occurs in beam A1-R1 delays the development of axial compression in the beam. This offsets the response of beam A1-R1, relative to A1-R. However once the lateral restraint is engaged, the stiffness of the response, before and after the reinforcement has yield, are identical in both beams. This remains true for beam A1-R3, as the post-yield stiffness of the response is equal to that of beams A1-R1 and A1-R. This indicates that any lateral slip at the supports delays the onset of axial compression in each beam, which limits the peak axial compression developed at failure. Therefore, increasing the total lateral slip in a beam from 0 mm/m to 0.5 mm/m reduces the

peak axial compression force developed by a factor of 3.7, from 391 kN in beam A1-R to 107 kN in beam A1-R3.

The lateral restraint force vs. total lateral expansion of beams A1-R1 and A1-R3 is presented in Figure 5.35. Prior to engaging the lateral restraint, no axial compression develops in either beam. Once the lateral restraint is engaged, the infinitely stiff lateral support prevents any further outward expansion of the beam at the supports, allowing an axial compression force to develop. As previously suggested, increasing the magnitude of slip prior to the development of axial compression reduces both the capacity and peak axial compression force.

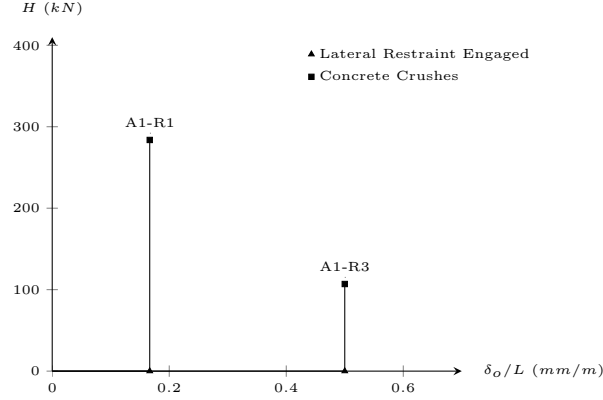


Figure 5.35: Lateral restraint force vs. slip in beams A1-R1 and A1-R3.

The peak values of applied load, axial compression force and midspan deflection are presented in Figure 5.36 for both beams A1 and B4, with varying magnitude of initial lateral slip. Similar to the response of beam A1, increasing the total lateral slip in beam B4 from 0 mm/m to 0.5 mm/m reduces the capacity by a factor of 1.5, from 235 kN in beam B4-R to 160 kN in beam B4-R3. In addition, increasing the total lateral slip in beam B4 from 0 mm/m to 0.5 mm/m reduces the peak axial compression force developed by a factor of 1.9, from 1280 kN in beam B4-R to 691 kN in beam B4-R3.

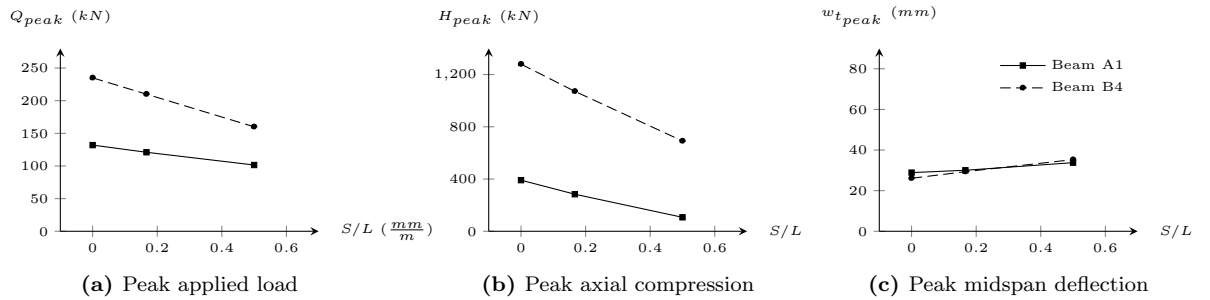


Figure 5.36: Response summary of beams A1 and B4, with varying lateral slip.

As indicated in the parametric studies presented in previous sections, increasing the strength of concrete and reducing the reinforcement ratio increases the capacity and peak axial compression force of beam B4, relative to beam A1. In addition, varying the strength of concrete and reinforcement ratio has little

influence on total midspan deflection at failure. Therefore, the peak midspan deflection of beam B4 is approximately equal to the peak midspan deflection developed in beam A1.

5.4.2 Influence of Lateral Restraint

The strength enhancement ratio is presented in Figure 5.37a for various magnitudes of lateral slip in beams A1 and B4. For beam A1, increasing the initial lateral slip from 0 mm/m to 0.5 mm/m reduces the strength enhancement caused by lateral restraint by a factor of 1.4, from 1.5 in beam A1-R to 1.1 in beam A1-R3. Similarly for beam B4, increasing the initial lateral slip from 0 mm/m to 0.5 mm/m reduces the strength enhancement ratio by a factor of 1.5, from 3.5 in beam B4-R to 2.4 in beam B4-R3. This indicates that for beams A1 and B4, increasing the magnitude of the initial slip at the supports reduces the influence of lateral restraint.

As previously indicated, allowing the beam to expand by a very small magnitude, relative to the length of the beam, delays the development of axial compression. This reduces the capacity of the beam, bringing it closer to the response of a beam with no lateral restraint. Therefore, any lateral slip of the beam, relative to the supports, will reduce the influence of lateral restraint on capacity.

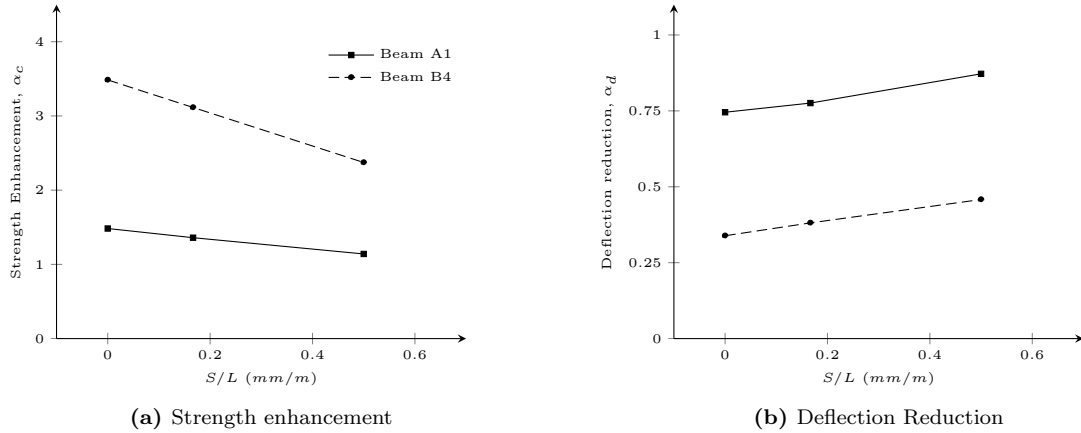


Figure 5.37: Influence of lateral slip on α_c and α_d .

The deflection reduction ratio is presented in Figure 5.37b for various magnitudes of lateral slip in beams A1 and B4. For beam A1, increasing the initial lateral slip from 0 mm/m to 0.5 mm/m increases the deflection reduction ratio caused by lateral restraint by a factor of 1.2, from 0.75 in beam A1-R to 0.87 in beam A1-R3. Similarly, increasing the initial lateral slip in beam B4 from 0 mm/m to 0.5 mm/m increases the deflection reduction ratio by a factor of 1.4, from 0.34 in beam B4-R to 0.46 in beam B4-R3. This indicates that increasing the magnitude of lateral slip in both beams reduces the influence of lateral restraint on deflection.

5.4.3 Summary of Results and Conclusions

The results of this study provide insight into the influence of initial lateral slip on the response of laterally restrained beams, and can be summarized as:

1. Increasing the lateral slip from 0 mm/m to 0.5 mm/m in beam A1:
 - (a) reduces capacity by a factor of 1.3.
 - (b) reduces the peak axial compression force by a factor of 3.7.
 - (c) increases the peak midspan deflection by a factor of 1.2.
 - (d) reduces the strength enhancement, caused by lateral restraint, by a factor of 1.4.
 - (e) increases the deflection reduction ratio, caused by lateral restraint, by a factor of 1.2.
2. Increasing the lateral slip from 0 mm/m to 0.5 mm/m in beam B4:
 - (a) reduces capacity by a factor of 1.5.
 - (b) reduces the peak axial compression force by a factor of 1.9.
 - (c) increases the peak midspan deflection by a factor of 1.2.
 - (d) reduces the strength enhancement, caused by lateral restraint, by a factor of 1.5.
 - (e) increases the deflection reduction ratio, caused by lateral restraint, by a factor of 1.4.

Based on this parametric study, it can be concluded that:

1. Lateral slip delays the development of axial compression, reducing the influence of arching action on the response of laterally restrained beams.
2. An initial lateral slip, of less than 0.02 % of L , can impact the response of a laterally restrained beam, and should be considered as part of the analysis.

5.5 Diagonal Strut Inclination

The importance of considering the horizontal component of diagonal compression struts in both laterally unrestrained and restrained beams was discussed in Chapter 3. The diagonal compression field action model, used throughout this thesis, assumes that the diagonal struts are inclined at an angle of 45° . The actual angle of inclination, θ , is dependent on the length of the beam, the distance between the compression and tension resultants, and the spacing of stirrups. Therefore, the strut inclination angles considered in this study range from 30° and 60° , providing a reasonable range of θ expected in a beam. This range provides insight into the influence of varying strut inclination, and does not identify the maximum and minimum angles possible.

The beams considered in this parametric study are presented in Figure 5.38. For all beams, the angle of inclination of each strut is equal to 30° , 45° , and 60° . The parametric studies summarized in the

previous sections indicate that beams with lower concrete strength and higher reinforcement ratio will benefit less from lateral restraint. Therefore, beams T1 and T2 represent an upper and lower bound of strength enhancement for laterally restrained beams.

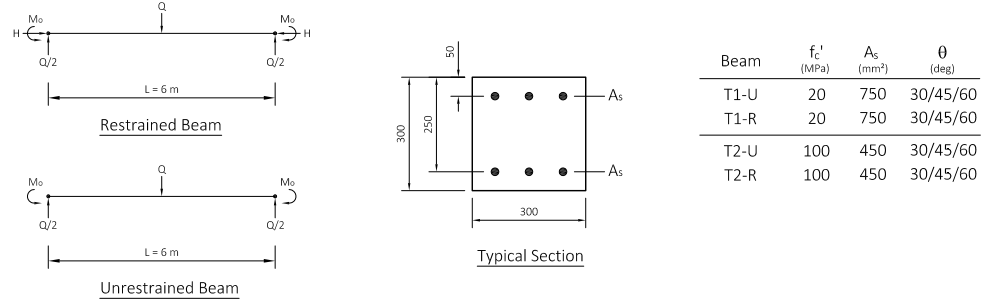


Figure 5.38: Beam properties for the strut inclination parametric study.

The analysis of each beam is conducted using the basic configuration of the proposed analytical model, with consideration of the spreading of load caused by diagonal compression struts. The two support conditions considered for each beam are:

U: Beam has no lateral restraint.

R: Beam has an infinitely stiff lateral restraint.

Varying the angle of inclination of a strut varies the total length of the fan region, L_{fan} . In the diagonal compression field action model, proposed in Chapter 3, this angle is assumed equal to 45° . As a result of this assumption, the length of the fan region is equal to z . Altering the inclination of the struts in this region will change the length of the fan region to,

$$L_{fan} = \frac{z}{\tan \theta} \quad (5.8)$$

where z is the lever arm between the compression and tension resultant, and θ is the assumed inclination of the diagonal compression strut in the beam. The influence of varying θ on the length of the fan region is illustrated in Figure 5.39. This figure indicates that reducing the angle of strut inclination increases the length of the fan region, while increasing the angle of inclination reduces the length of the fan region.

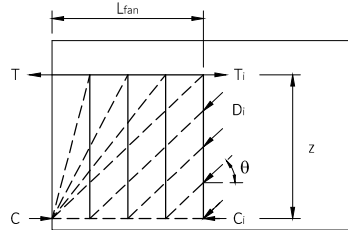


Figure 5.39: Influence of strut inclination on L_{fan} .

5.5.1 Unrestrained Beam Response

The influence of varying the angle of inclination on the capacity and peak midspan deflection of beams T1-U and T2-U is presented in Figure 5.40. The peak applied load, Q_{peak} , and peak midspan deflection, $w_{t_{peak}}$, are presented relative to the response of beams T1-U and T2-U, assuming a truss inclination of 45° . In beam T1-U, varying θ has no influence on capacity as failure occurs at the location of peak bending moment, where there are no diagonal struts. In beam T2-U however, assuming $\theta = 30^\circ$ reduces the capacity by a factor of 1.01, while assuming $\theta = 60^\circ$ increases the capacity by a factor of 1.01. The difference between the response of beams T1-U and T2-U is caused by variation in the location of failure. In beam T2-U, increasing the angle of inclination increases the distance between the section where concrete crushes and the peak bending moment, which reduces the load capacity. However for both beams, varying the angle of inclination of the diagonal struts has little influence on the capacity of a laterally unrestrained beam.

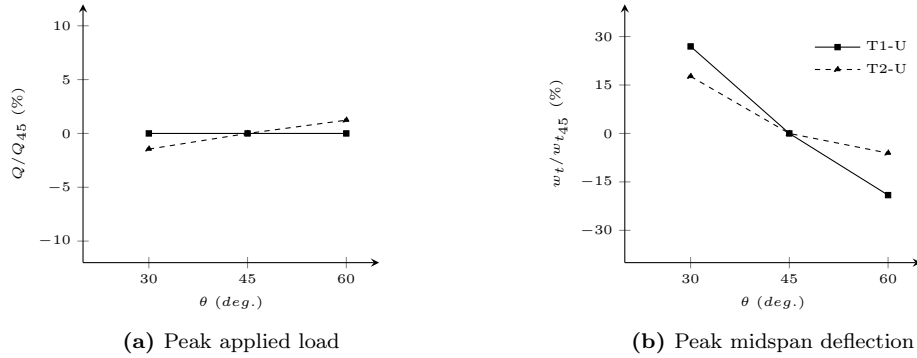


Figure 5.40: Influence of varying θ on the response of laterally unrestrained beams.

In beam T1-U, assuming $\theta = 30^\circ$ increases the peak midspan deflection by a factor of 1.27, while assuming $\theta = 60^\circ$ reduces the peak midspan deflection by a factor of 1.19. Similarly for beam T2-U, assuming $\theta = 30^\circ$ increases the peak midspan deflection by a factor of 1.18, while assuming $\theta = 60^\circ$ reduces the peak midspan deflection by a factor of 1.06. In both beams, reducing θ increases H^* , which increases the curvature at every section in both beams. This increased curvature causes the peak midspan deflection to increase. However in beam T2-U, reducing θ also shifts the location of peak curvature away from the location of peak bending. This shift is caused by the increased H^* in each section, and is discussed in detail in Chapter 3. This shift brings the peak curvature closer to the supports, which reduces the influence of reducing θ , relative to beam T1-U, where the peak curvature always coincides with peak bending moment.

Therefore, the assumption of $\theta = 45^\circ$ is valid for predicting the capacity of laterally unrestrained beams. However, varying θ has a significant influence on the predicted deflection in each beam. Since the main purpose of this thesis is to understand the influence of lateral restraint on the response of reinforced concrete beams, an inclination angle of 45° provides a consistent base line for comparison between restrained and unrestrained beams.

5.5.2 Restrained Beam Response

The influence of varying strut inclination on the capacity, peak axial compression force and peak midspan deflection of beams T1-R and T2-R is presented in Figure 5.41. For beams T1-R and T2-R, assuming $\theta = 30^\circ$ increases the capacity by a factor of 1.02, while assuming $\theta = 60^\circ$ reduces the capacity by a factor of 1.02. The increased capacity in beams with a smaller magnitude of θ corresponds with an increased peak axial compression force, H_{peak} . For beam T1-R, assuming $\theta = 30^\circ$ increases the peak axial compression by a factor of 1.08, while assuming $\theta = 60^\circ$ reduces the peak axial compression by 1.08. Similarly for beam T2-R, assuming $\theta = 30^\circ$ increases the peak axial compression by a factor of 1.04, while assuming $\theta = 60^\circ$ reduces the peak axial compression by a factor of 1.04.

As previously indicated, reducing θ increases the peak magnitude of H^* , which increases the curvature throughout the beam. This increase in curvature corresponds with an increase in the lateral expansion of the beam, requiring that a larger axial compression force develop at the support. This increased axial compression increases capacity, relative to a laterally unrestrained beam. Beam T2-R, which has a high concrete strength, develops a larger axial compression force than beam T1-R. Therefore, the change in H^* has less of an influence on beam T2-R.

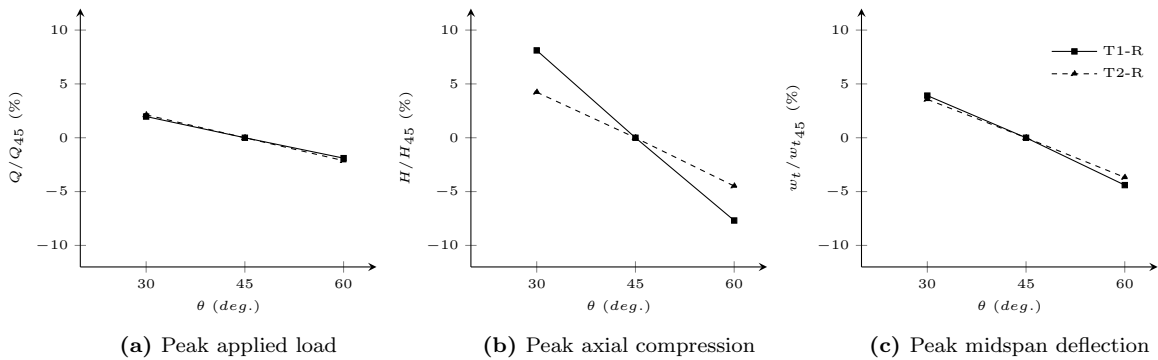


Figure 5.41: Influence of varying θ on the response of laterally restrained beams.

In beams T1-R and T2-R, assuming $\theta = 30^\circ$ increases the peak midspan deflection by a factor of 1.04, while assuming $\theta = 60^\circ$ reduces the peak midspan deflection by a factor of 1.04. As previously indicated, reducing the inclination angle of a strut increases curvature throughout the beam, which increases the magnitude of midspan deflection at failure load.

The response presented in Figure 5.41 indicates that varying θ in laterally restrained beams varies the response by $\pm 5\%$. Therefore, the assumption that $\theta = 45^\circ$, made throughout this thesis, does not significantly influence the accuracy of the predicted response of a laterally restrained beam.

5.5.3 Summary of Results and Conclusions

The results of this study provides insight into the influence of varying strut inclination, used as part of the diagonal compression field action model implemented in the proposed analytical model, on the response of laterally restrained (R) and unrestrained (U) beams, and can be summarized as:

1. For beam T1, varying θ from 45° to 30° and 60° :
 - (a) varies the capacity by approximately $\pm 2\%$ (R) and $\pm 0\%$ (U).
 - (b) varies the peak axial compression force by approximately $\pm 8\%$ (R).
 - (c) varies the peak midspan deflection by approximately $\pm 4\%$ (R), and $\pm 25\%$ (U).
2. For beam T2, varying θ from 45° to 30° and 60° :
 - (a) varies the capacity by approximately $\pm 2\%$ (R) and $\pm 1\%$ (U).
 - (b) varies the peak axial compression force by approximately $\pm 4\%$ (R).
 - (c) varies the peak midspan deflection by approximately $\pm 4\%$ (R), and $\pm 15\%$ (U).

Based on this parametric study, it can be concluded that:

1. Altering the assumed angle of strut inclination, used as part of the diagonal compression field action model, does not significantly alter the capacity, axial compression force and deflection of laterally restrained beams.
2. Altering the assumed angle of strut inclination, used as part of the diagonal compression field action model, does not significantly alter the capacity of laterally unrestrained beams, but can cause a significant change in the peak midspan deflection.

5.6 Discussion of Results and Concluding Remarks

This chapter presents the results of five parametric studies that highlight the influence of critical parameters on the response of restrained, reinforced concrete beams and slab strips. The proposed analytical model, presented in Chapter 2, is used to conduct each study. The parameters considered for each parametric study are (i) concrete compressive strength, (ii) mechanical reinforcement ratio, (iii) span-to-depth ratio, (iv) lateral slip at supports, and (v) diagonal strut inclination. The results of each study highlight the influence of these parameters on the stiffness, capacity and deflection of beams, with and without lateral restraint. The important findings of these studies include:

1. *Lateral restraint increases the benefit of higher strength concrete.* In an unrestrained beam, increasing the strength of concrete increases the amount of lateral expansion. If the beam is laterally restrained, the increased lateral expansion is prevented by an increased lateral restraint force. Therefore, the increased axial compression force increases the capacity of the laterally restrained beam.
2. *Increasing reinforcement ratio decreases the effectiveness of arching action.* Reducing the reinforcement ratio in a laterally unrestrained beam increases the magnitude of lateral expansion. Therefore in a laterally restrained beam, reducing reinforcement ratio will increase the magnitude of axial compression. The increased axial compression increases the capacity of the beam.
3. *Reducing mechanical reinforcement ratio increases the benefits of lateral restraint.* Reducing mechanical reinforcement ratio, achieved by increasing concrete strength and reducing reinforcement

ratio, increases the lateral expansion of a laterally unrestrained beam. In a laterally restrained beam, this expansion is prevented by the lateral supports, increasing the axial compression force. The increased axial compression force increases the capacity of the beam.

4. *Increasing the span-to-depth ratio increases the influence of second-order effects on the capacity of a laterally restrained beam.* As the span-to-depth ratio is increased, the deflection and axial compression force in each beam increases. This increases the magnitude of the bending moment caused by second-order effects, relative to the total bending moment in the beam.
5. *Increasing concrete strength and reducing reinforcement ratio increases the influence of second-order effects on the capacity of a laterally restrained beam.* As previously indicated, increasing concrete strength and reducing reinforcement ratio increase the axial compression developed, which increases the magnitude of the bending moment caused by second-order effects.
6. *For all values of span-to-depth ratio, second-order effects have a minimal influence on the axial compression force and midspan deflection at peak load.* Increasing the bending moment due to second-order effects reduces the bending moment caused by the applied load, without altering the total bending moment in the system. Therefore, accounting for second-order effects has little influence on the curvature throughout a beam, which limits any changes in deflection or axial compression.
7. *Lateral slip delays the development of axial compression, reducing the influence of laterally restraint.* Prior to engaging the lateral stiffness of the supports, the beam behaves identically to a laterally unrestrained beam. Delaying the onset of lateral restraint therefore reduces the axial compression developed in the beam at each magnitude of applied load, reducing capacity and increasing deflection.
8. *Varying the inclination of the diagonal struts used in the diagonal compression field action model does not significantly alter the response of laterally restrained beams.* Reducing the angle of inclination increases the horizontal component of the diagonal compression strut. However, the axial compression force that develops in the beam is much larger, relative to the horizontal component of the strut, and therefore has minimal influence on the response of a beam.

These studies provide insight into how various parameters influence the development of arching action in laterally restrained, reinforced concrete beams or slab strips. This insight builds on the current understanding of lateral restraint by identifying the importance of considering second-order effects, as well as lateral slip between the beam and its support. Based on this study, and assuming that the allowable variation in the predicted capacity of a beam is $\pm 10\%$, it can be concluded that the analysis beams with a span-to-depth ratio above 20 should account for second-order effects. In addition, lateral slip, equal to less than 0.02% of the length of the beam, can have a significant influence on the capacity of laterally restrained beams and slab strips, and should be accounted for in an analysis.

6

Conclusions and Summary

This chapter summarizes the key findings of this thesis related to the behaviour of laterally restrained, reinforced concrete slab strips and beams. These findings are presented in Section 6.1, and include the conclusions from the parametric studies. A summary of the proposed analytical model, including four supplementary refinements to the model, is presented in Section 6.2. This is followed by a summary of the model validation conducted using test data from two experiments on laterally restrained, reinforced concrete beams in Section 6.3. Finally, recommendations for future work in developing a simplified version of the model, for use in design standards, are presented in Section 6.4.

6.1 Key Findings from this Thesis

The primary conclusions from the development and validation of the rational analytical model are:

1. For beams with a span-to-depth ratio greater than 20, second-order effects should be considered. For beams with a span-to-depth ratio lower than 20, variation in capacity caused by second-order effects is less than ten percent, and may be ignored. Secondary conclusions include:
 - (a) Increasing span-to-depth ratio of a beam from 7 to 47 reduces the strength enhancement caused by lateral restraint, by a factor of approximately two.
 - (b) Increasing concrete strength from 20 MPa to 100 MPa, and reducing reinforcement ratio from 1.0 % to 0.6 %, increases the influence of second-order effects on load capacity. As a result, varying the span-to-depth ratio from 7 to 47 increases in the influence of second-order effects, by a factor of 3.5.
 - (c) Varying span-to-depth ratio has little influence on the axial compression force and midspan deflection at peak load.
2. Lateral slip between the ends of a beam and its supports delays the development of the lateral restraint force, reducing the influence of arching action on the response of laterally restrained

beams. If the lateral slip is greater than 0.01 % of the length of the beam, then it should be considered. Secondary conclusions include:

- (a) Increasing slip from 0 mm/m to 0.5 mm/m reduces the strength enhancement caused by lateral restraint, by a factor of 1.5.
 - (b) Increasing slip from 0 mm/m to 0.5 mm/m, on average, reduces capacity by a factor of 1.3, reduces the peak axial compression by a factor of 2.8, and increases the peak midspan deflection, by a factor of 1.2.
3. Increasing concrete strength from 20 MPa to 100 MPa increases the strength enhancement caused by lateral restraint, by a factor of 1.5. Secondary conclusions include:
- (a) Increasing concrete strength from 20 MPa to 100 MPa, on average, increases the capacity of a restrained beam by a factor of 2.8, and increases the peak axial compression by a factor of 3.6.
 - (b) Increasing concrete strength from 20 MPa to 100 MPa has little influence on the midspan deflection at failure.
4. Reducing the mechanical reinforcement ratio increases the strength enhancement caused by lateral restraint, by a factor of 1.5. Secondary conclusions include:
- (a) Reducing the mechanical reinforcement ratio from 20 % to 4 %, with a concrete strength of 20 MPa, increases the load capacity by a factor of 2.1, and increases peak axial compression force by a factor of 3.4.
 - (b) Reducing the mechanical reinforcement ratio from 5.3 % to 2.4 %, with a concrete strength of 100 MPa, increases the load capacity by a factor of 3.4, and increases peak axial compression force by a factor of 3.7.
5. The effects of strain penetration should be considered when a beam is cast monolithically with a supporting structure that is confined. This confinement prevents expansion of the concrete, causing the bond between the reinforcement and the concrete to deteriorate. The amount of confinement required to cause significant bond deterioration cannot be quantified in this thesis, as a comprehensive bond model is not employed. However, the test data used for the experimental validation indicates that strain penetration can reduce capacity by a factor of 1.03, and increase the peak midspan deflection by a factor of 1.8.

6.2 Proposed Analytical Model

The proposed analytical model is based on the assumption that plane sections remain plane. This assumption provides a basis for relating the bending moment and axial compression to the curvature at any section along the length of the beam, using a layered analysis approach. The layered analysis approach relates the strain in the concrete and steel reinforcement to the stress and force resultant, using nonlinear constitutive material models.

The compatibility condition for a beam with rigid supports states that no lateral expansion or rotation will occur at the supports. The analytical model developed by Wu (2013) suggests that the total expansion and rotation of a beam at the supports can be quantified by integrating the strains at the top and bottom of each section, along the length of a given beam,

$$L_{c,ce} = L + \int_0^L \varepsilon_{ce} dx$$

where $L_{c,ce}$ is the chord length of the centroidal axis, L is the undeformed length of a beam, and ε_{ce} is the strain at the centroid of each section. Wu's model assumes that the chord length of the centroidal axis is always equal to the arc length of the centroidal axis, $L_{a,ce}$. This assumption limits the applicability of the model to beams with minimal deflections. To provide a more comprehensive formulation, the proposed analytical model differentiates the chord and arc length of the centroid as,

$$L_{a,ce} = L + \int_0^L \varepsilon_{ce} dx$$

$$L_{c,ce} = \frac{L \cdot L_{a,ce}}{L_w}$$

where L_w is the arc length of the deflected shape. Therefore, the two compatibility conditions used in the proposed analytical model are:

1. No lateral expansion at the supports:

$$L_{c,ce} = L$$

2. No rotation at the supports:

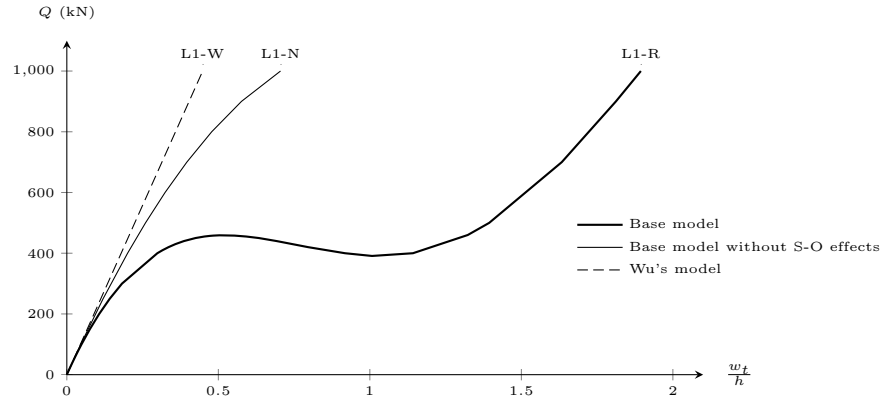
$$\int_0^L \varepsilon_t = \int_0^L \varepsilon_b$$

where ε_t and ε_b are the strains along the top and bottom of a given beam.

The proposed analytical model uses three levels of iteration to determine the deformed shape of the beam, the bending moment applied at the ends of the beam, and the axial compression in the beam. First, second-order effects are incorporated into the analysis by assuming a deflected shape, based on the previous load stage. The bending moment at each section is then determined based on the applied load, the bending moment caused by second-order effects, and the assumed bending moment at the supports. Using the bending moment and the assumed axial compression in the beam, the strain profile at each section is found. This strain profile is used to quantify the outward expansion of the support, the rotation of the beam at the support, and the deflected shape. The magnitude of axial compression and bending moment applied to the beam by the support is then quantified by considering the two compatibility conditions, through an iterative procedure. Finally, the assumed deflected shape is updated based on

the calculated deflected shape of the beam, and the analysis is repeated until the magnitude of midspan deflection converges.

The importance of considering second-order effects is highlighted in the response of beam *L1*, presented in Section 2.9. This analysis assumes that the concrete remains linear elastic in compression, and the reinforcement remains linear elastic in both compression and tension. The load-deflection response of beam *L1* predicted using the base model, *L1-R*, the base model without consideration of second-order effects, *L1-N*, and Wu's model, *L1-W*, is presented in Figure 2.26. The difference between the chord length and arc length of the centroidal axis causes the peak midspan deflection of beam *L1-W* and *L1-N*, to differ by a factor of 1.6. In addition, accounting for the bending moment caused by second-order effects causes significant softening to occur in the beam, resulting in the formation of two peaks in the applied load. This causes the maximum midspan deflection to increase by a factor of 2.7.

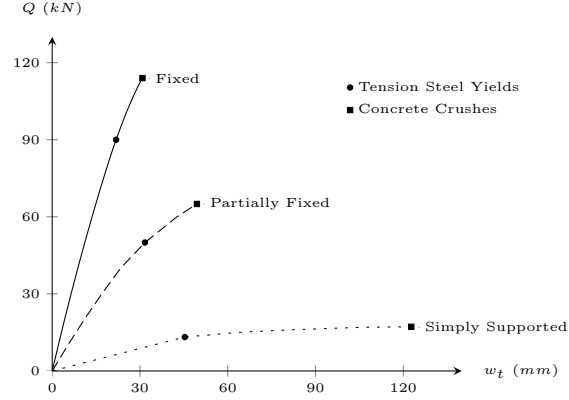


Partial reprint of Figure 2.26: Influence of second-order effects.

The model developed in Chapter 2 is defined as the Base model. The test-data from experiments conducted by Su, Tian, and Song (2009) and Yu and Tan (2013) highlight the importance of considering the influence of the test setup. These influences can be accounted for in the proposed analytical model using four supplementary refinements. Therefore, the refined version of the model includes:

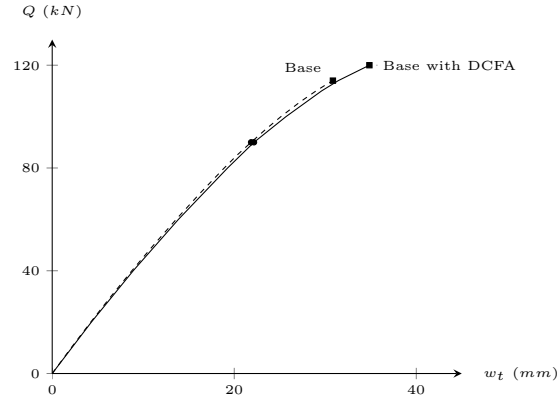
1. The elastic stiffness of a support.
2. The horizontal component of the diagonal compression struts throughout the beam.
3. Lateral and rotational slip between the beam and the support.
4. Strain penetration caused by bond deterioration in regions with geometric irregularities.

First, the compatibility condition is updated to allow for expansion and rotation of the supports based on the properties of a linear and rotational spring, respectively. The stiffness of each spring is based on the measured stiffness of the support. The influence of varying rotational and lateral restraint, studied in Section 3.1, is illustrated in the load-deflection response presented in Figure 3.6. For the partially restrained beam, $K_{axial} = 500 \text{ kN/mm}$ and $K_{rot} = 5000 \text{ kNm/rad}$. For this example, accounting for partial restraints reduces capacity by a factor of 1.8 and increases the peak midspan deflection by a factor of 1.6.



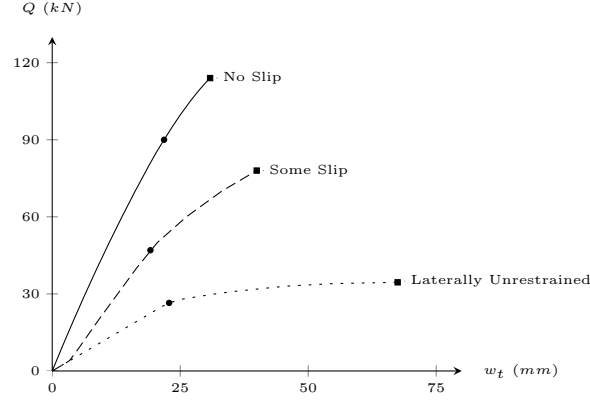
Partial reprint of Figure 3.6: Influence of partial end restraints.

Second, the influence of the diagonal compression struts that carry the shear force throughout a beam is accounted for by applying a horizontal force resultant, H^* , at every section. The magnitude of H^* is dependent on the inclination of the strut, and the magnitude of the shear force at each section. The proposed diagonal compression field action (DCFA) model provides a simplified way to incorporate this effect, without having to develop a truss model at every load stage for every beam. The influence of H^* on the response of the beam studied in Section 3.2, is illustrated in Figure 3.18. For this example, accounting for DCFA increases capacity by a factor of 1.05, and increases the peak midspan deflection by a factor of 1.13.



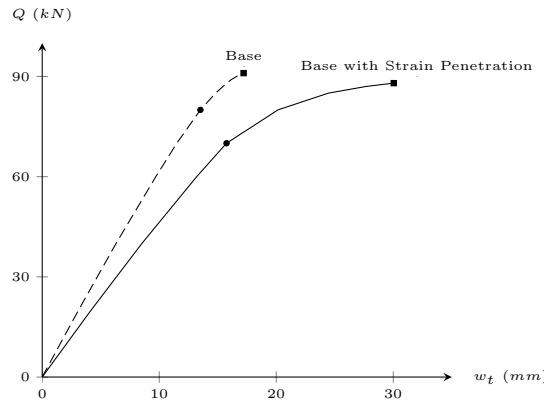
Partial reprint of Figure 3.18: Influence of H^* .

The third supplementary approach adjusts the compatibility conditions to account for any initial lateral or rotational slip between the beam and the supports. Slip can occur in beams that are precast and later attached to the supports, as in the experiments by Su, Tian, and Song (2009) and Yu and Tan (2013). The influence of lateral slip is illustrated in Figure 3.24, for the beam studied in Section 3.3, which assumes a total slip of $s_t = (0.5 \text{ mm}) + (H/(1000 \text{ kN/mm}))$. In this example, lateral slip causes the capacity to reduce by a factor of 1.5, and increases the peak midspan deflection by a factor of 1.3.



Partial reprint of Figure 3.24: Influence of lateral slip.

Finally, an approach to account for bond deterioration between the continuous reinforcement in a beam and the supporting structure is proposed. This deterioration occurs in regions where the reinforcement has large inelastic strains, and confinement limits the expansion of the concrete, such as the column stubs in the experiments conducted by Su, Tian, and Song (2009) and Yu and Tan (2013). The simplified approach proposed for this thesis assumes that the additional deformation caused by bond deterioration can be approximated by calculating the additional curvature in the regions with bond deterioration using the assumption that plane sections remain plane. The influence of strain penetration on the response of the beam studied in Section 3.4, is illustrated in Figure 3.30. For this example, accounting for strain penetration reduces the capacity by a factor of 1.03, and increases the peak midspan deflection by a factor of 1.8.

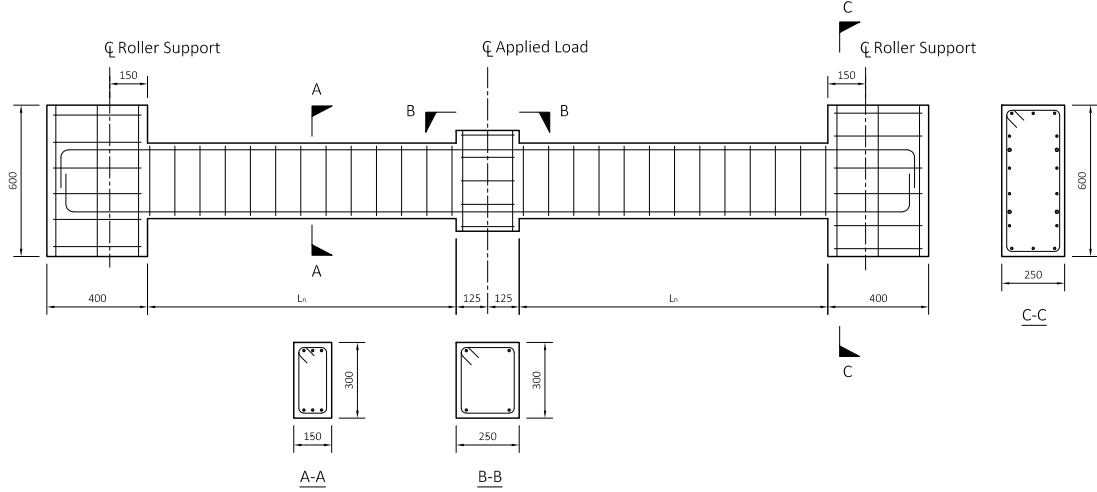


Partial reprint of Figure 3.30: Influence of bond deterioration.

The four model refinements, presented in Chapter 3, significantly improve the correlation between the proposed analytical model and the results from the experiments conducted by Su, Tian, and Song (2009) and Yu and Tan (2013). This correlation, presented in Chapter 4, is summarized in the next section.

6.3 Experimental Validation of the Proposed Model

Test data from experiments conducted by Su, Tian, and Song (2009) and Yu and Tan (2013) is used to validate the proposed analytical model. Both experiments investigate the progressive collapse mechanism of reinforced concrete frame beams, and specimens consist of three column stubs separated by two beam segments. A typical specimen from the experiment conducted by Su, Tian, and Song (2009) is illustrated in Figure 4.2. Each specimen is vertically, laterally and rotationally restrained at the outer column stubs, and a vertical load is applied monotonically on the middle column stub until failure.



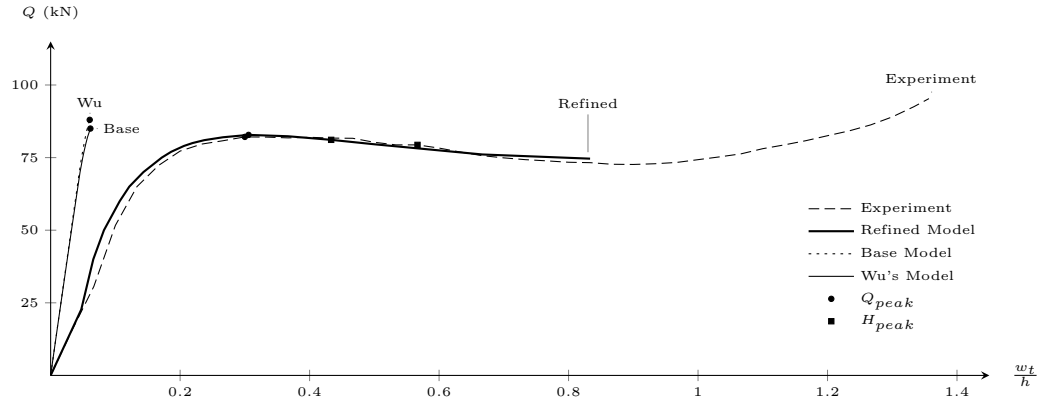
Reprint of Figure 4.3: Geometric layout of the specimens tested by Su (2009).

The test data from four beams from the S-Series, and two beams from the Y-Series, are considered as part of an experimental validation of the proposed analytical model. In all the beams considered, the peak applied load, Q_{peak} , occurs prior to the peak axial compression force, H_{peak} . This is caused by second-order effects, which reduces the bending capacity of each beam. In addition, when the load is first applied, each specimen exhibits an initial softness in the load-deflection and restraint-deflection response. This softness is caused by slip between the ends of each specimen and the supports.

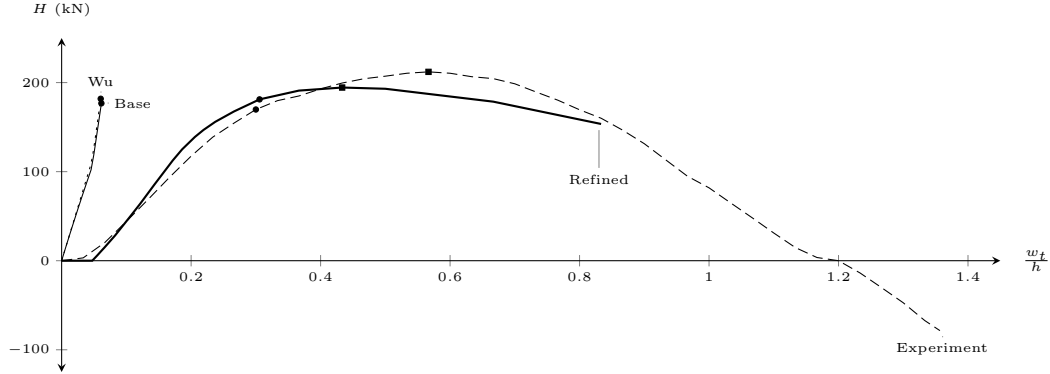
The load-deflection and restraint-deflection response of beam S1, part of the S-Series validation, is presented in Figure 4.10. At low magnitudes of applied load, beam S1 exhibits an initial softness caused by lateral and rotational slip of the beam, relative to the support. The midspan deflection of beam S1 at Q_{peak} , $w_t/L = 0.30$, is 1.9 times smaller than the peak midspan deflection at H_{peak} , $w_t/L = 0.57$. This suggests that second-order effects reduce the stiffness of a beam at higher loads, which reduces capacity. As the specimen is loaded beyond H_{peak} , the applied load begins to increase. At a midspan deflection of $w_t/L = 1.2$, the axial force in the beam transitions from compression to tension, signaling the onset of tensile membrane action. The failure load of the beam, 95 kN, is 1.2 times higher than the first peak in the applied load, 82 kN. This suggests that in some cases, the capacity of a beam can increase during tensile membrane action. However, this does not occur in beam S4, which has a lower span-to-depth

ratio of 10.

The refined version of the proposed analytical model can be adapted to predict the response of each specimen in both experiments. For each specimen, the refinements that account for slip, diagonal compression field action and bond degradation are adjusted to better fit the observed behaviour. The predicted response generated using the refined model, the base model, and Wu's model are included for comparison in Figure 4.10. For specimen S1, the base model and Wu's model are able to predict Q_{peak} and the axial compression at Q_{peak} within ten percent. However, both models over predict the midspan deflection at Q_{peak} by a factor of 5. In contrast, the refined model is able to predict Q_{peak} within one percent, the axial compression at Q_{peak} within ten percent, and the midspan deflection at Q_{peak} within four percent. The refined model improves the predicted load, axial compression force and deflection of beam S1 at Q_{peak} , relative to Wu's model, by factors of 1.07, 1.01, and 5. Therefore, the refined model provides a significantly improved prediction of the response of specimen S1.



(a) Applied load vs. midspan deflection



(b) Lateral restraint force vs. midspan deflection

Reprint of Figure 4.10: Predicted vs. observed response of specimen S1.

The proposed analytical model is able to provide an accurate prediction of the response of beam S1, up to Q_{peak} . However, simultaneously accounting for second-order effects and material nonlinearities causes a numerical instability to form at a midspan deflection of $w_t/L = 0.83$. Although a simplified model is adopted for bond degradation, it is found to provide a reasonably accurate representation of the strain penetration in the column stubs. In addition, the assumed magnitude of slip is found to be reasonable, as it is equal to less than 0.1 % of the length of each beam.

For all specimens, the proposed analytical model is able to predict, on average:

1. Q_{peak} within seven percent.
2. Lateral restraint force at Q_{peak} within eleven percent.
3. Midspan deflection at Q_{peak} within thirteen percent.

As a result of this validation, the following conclusions can be made:

1. Varying the lateral and rotational stiffness of the support has a significant impact on the capacity and deflection of a beam.
2. A lateral slip of less than 0.1 percent of the overall length of a beam, between the beam and its supports, can significantly alter the capacity and deflection of a laterally restrained beam.
3. The bond deterioration caused by geometric irregularities can have a significant influence on the capacity and deflection of a beam.
4. The softening caused by second-order effects is governed by the geometry of the beam, and allows for the development of two peaks in the applied load.

6.4 Final Conclusions and Recommendations for Future Work

This thesis presents a rational analytical model that is able to predict the influence of lateral restraint on the response of reinforced concrete beams and slab strips. The model has been validated using test data from two experiments conducted on laterally restrained beams. The parametric study conducted using the analytical model provides insight into the behaviour and capacity of laterally restrained beams. An important aspect of the analytical model is the intuitive and rational nature of the equilibrium and compatibility conditions, which are developed using simple formulations that are based on traditional sectional analysis. However, the current formulation is computationally intensive and requires three levels of iteration. As a result, it cannot, in its present form, be implemented in design standards, and must therefore be simplified before it can be implemented into design practice.

A number of recommendations are provided as a basis for future work in the development of a simplified analytical method that can predict the capacity of laterally restrained, reinforced concrete beams and slabs. These recommendations are presented in a chronological development of the simplified model, and include:

1. An experimental program be conducted on laterally and rotationally restrained, reinforced concrete beams. Contrary to previous experimentation, the influence of arching action should be isolated from external factors caused by the testing setup, including non-rigid lateral and rotational restraint, bond deterioration and slip relative to the supports. The results of this experiment will provide further verification of the proposed analytical model.
2. A detailed analytical study aimed at simplifying the current analytical model be conducted using this experimental data. Based on this, a simplified approach to accounting for second-order effects in slender beams should be developed to reduce the number of iterations required in the analysis.

3. The importance of considering slip and bond deterioration will be based on the specific application for the simplified model. If significant bond deterioration is expected to occur, a more comprehensive strain penetration model should be developed and implemented into the current formulation.
4. A comprehensive study be undertaken on the rotational and axial stiffness provided by various configurations of concrete slabs and beams. This list can then be used to simplify the treatment of the lateral and rotational stiffness of the supports.
5. A series of experiments be conducted on a number of small scale bridge deck slabs with varying reinforcement and support stiffness to verify this simplified model. This test can potentially provide the basis for implementing the simplified analytical model in design standards.

The proposed analytical model improves the current understanding of the influence of lateral restraint on reinforced concrete structures, and this thesis highlights the importance of considering second-order effects, bond deterioration and slip relative to the support. The analytical model provides the basis for the development of a simplified model that can be implemented in design standards. The rational treatment of arching action in the analysis of reinforced concrete beams and slabs is critical for improving the economy of reinforced concrete construction. In the future, this rational formulation can be adapted for use in bridges, buildings, power plants and dams. Therefore the potential impact of this research, and future research conducted on this basis, are limitless.

References

- American Concrete Institute. (2005). *Building Code Requirements for Structure Concrete* (ACI 318-05 ed.). Farmington Hills, MI: American Concrete Institute.
- Batchelor, B. V., Hewitt, B. E., Csagoly, P. F., & Holowka, M. (1985). Load carrying capacity of concrete deck slabs. *Ontario Ministry of Transportation Research and Development Branch*, 85(03).
- Botticchio, R. M. (2014). *Determining and validating the three-dimensional load path induced by arching action in bridge deck slabs* (MAsc. Thesis). University of Toronto.
- Canadian Standards Association. (2006). *Canadian Highway Bridge Design Code*. Mississauga: Standards Council of Canada.
- Christiansen, K. P. (1963). The effect of membrane stresses on the ultimate strength of the interior panel in a reinforced concrete slab. *The Structural Engineer*, 41(08).
- Department of Regional Development for Northern Ireland. (1986). *Design of M-Beam Bridge Decks - Amendment No. 3 to Bridge Design Code*. Northern Ireland Roads Service Headquarters.
- Einsfeld, R. A., Martha, L. F., & Bittencourt, T. N. (2000). Combination of smeared and discrete approaches with the use of interface elements. *European Congress on Computational Methods in Applied Sciences and Engineering*(1–8).
- Eyre, J. R. (1997). Direct assessment of safe strengths of reinforced concrete slabs under membrane action. *Journal of Structural Engineering*, 123(1331–1338).
- Eyre, J. R., & Kemp, K. O. (1994). In-plane stiffness of reinforced concrete slabs under compressive membrane action. *Magazine of Concrete Research*, 46(166)(66–77).
- FarhangVesali, N., Valipour, H., Samali, B., & Foster, S. (2013). Development of arching action in longitudinally-restrained reinforced concrete beams. *Elsevier: Construction and Building Materials*, 47(7–19).
- Federation Internationale du Beton (fib). (2010). *fib Bulletin 66: Model Code* (Final Draft Volume 2 ed.). Switzerland: Federation Internationale du Beton.
- Gauvreau, D. P. (1993). *Ultimate limit state of concrete girders prestressed with unbonded tendons* (PHD. Thesis). ETH Zurich.
- Guice, L. K., & Rhomberg, E. J. (1988). Membrane action in partially restrained slabs. *American Concrete Institute Structural Journal*, 85(4)(365–373).
- Johansen, K. W. (1962). Yield line theory. *Cement and Concrete Association*.
- Khanna, O. S., Mufti, A. A., & Bakht, B. (2000). Experimental investigation of the role of reinforcement in the strength of concrete deck slabs. *Canadian Journal of Civil Engineering*, 27(03)(475–480).
- Liebenberg, A. C. (1966). Arch action in concrete slabs. *Council for Scientific and Industrial Research Report*, 234(40)(1–35).

- Mander, J. B. (1983). *Seismic design of bridge piers* (PHD. Thesis). University of Canterbury.
- Mander, J. B., Priestley, M. J. N., & Park, R. (1988). Theoretical stress-strain model for confined concrete. *ASCE Journal of Structural Engineering*, 114(8)(1804-1826).
- Mayer, U., & Eligehausen, R. (1998). Bond behaviour of ribbed bars at inelastic steel strains. *Proc. 2nd Int. PhD Symposium in Civil Engineering, Technical University of Budapest*, 33(10)(304-322).
- McDowell, E. L., McKee, K. E., & Sevin, E. (1956). Bond behaviour of ribbed bars at inelastic steel strains. *Proceedings of the American Society of Civil Engineers, Structural Division*, 82(2)(1-18).
- Menn, C. (1990). *Prestressed Concrete Bridges* (P. Gauvreau, Trans.). Basel, Switzerland: Birkhauser Verlag.
- Ockleston, A. J. (1955). Load tests on a three storey reinforced concrete building in johannesburg. *The Structural Engineer*(39-46).
- Ontario Ministry of Transportation and Communications. (1979). *The Ontario Highway Bridge Design Code*. Toronto, Ontario.
- Park, R. (1964). Ultimate strength of rectangular concrete slabs under short term uniform loading with edges restrained against lateral movement. *Proceedings, Institution of Civil Engineers*, 28(125-150).
- Popovics, S. (1973). A numerical approach to the complete stress-strain curve of concrete. *Cement and Concrete Research*, 3(5)(583-599).
- Rankin, G. I. B. (1982). *Punching failure and compressive membrane action in reinforced concrete slabs* (PHD. Thesis). Queens University of Belfast.
- Rankin, G. I. B. (1997). Arching action strength enhancement in laterally-restrained slab strips. *Proceedings of the Institute of Civil Engineers*, 122(461-467).
- Ruddle, M. E. (1989). *Arching action and the ultimate capacity of reinforced concrete beams* (PHD. Thesis). Queens University of Belfast.
- Schlaich, J., Schafer, K., & Jennewein, M. (1987). Toward a consistent design of structural concrete. *PCI Journal*, 32(3)(74-150).
- Shima, H., Chou, L., & Okamura, H. (1987). Bond-slip-strain relationship of deformed bars embedded in massive concrete. *Concrete Library of JSCE*, 10(79-94).
- Sritharan, S., Priestley, M., & Seible, F. (2000). Nonlinear finite element analyses of concrete bridge joint systems subjected to seismic actions. *Elsevier: Finite Elements in Analysis and Design*, 36(215-233).
- Su, Y., Tian, Y., & Song, X. (2009). Progressive collapse resistance of axially-restrained frame beams. *ACI Structural Journal*, 106-S55(600-607).
- Su, Y., Wang, X., Song, X., NI, M. C. . N., & Wang, N. (2009). Experimental investigation on the arching action in reinforced concrete frame-beams. *J.Xi'an University of Architecture and Technology, Natural Science Edition*, 41(4)(477-484).
- Taylor, S. E., Rankin, G. I. B., & Cleland, D. J. (2001). Arching action in high-strength concrete slabs. *Proceedings of the Institution of Civil Engineers, Structures and Buildings Issue*, 146(4)(353-362).
- UK Highways Agency. (2002). *Use of Compressive Membrane Action in Bridge Decks*. London, UK: Manual for Roads and Bridges.
- Valipour, H. R., Vesali, N., Samali, B., & Foster, S. (2014). Reserve of strength in reinforced concrete frames: analysis of arching action. *Australian Journal of Structural Engineering*, 15(2)(161-175).
- Vecchio, F., & Tang, K. (1990). Membrane action in reinforced concrete slabs. *Canadian Journal of*

- Civil Engineering*, 17(5)(686–697).
- Westergaard, H. M., & Slater, W. A. (1921). Moments and stresses in slabs. *American Concrete Institute Journal*, 17(415–538).
- Wu, A. (2013). *Rational modelling of arching action in laterally restrained beams* (MAsc. Thesis). University of Toronto.
- Yu, J., & Tan, K. (2013). Experimental and numerical investigation on progressive collapse resistance of concrete beam column sub-assemblages. *Elsevier: Engineering Structures*, 55(90–106).
- Zheng, Y., Robinson, D., Taylor, S., Cleland, D., & Shaat, A. (2009). Analysis of compressive membrane action in concrete slabs. *Proceedings of the Institution of Civil Engineers, Bridge Engineering*, 161(21–31).

Appendix A

Sample Calculations

Proposed Model Sample Calculation

The following sample calculation is taken from the analysis of beam F2, presented in Section 2.8. The layout of beam F2 is presented in Figure A.1. The procedure for this analysis is based on the proposed procedure of the “base” model formulation, summarized in Section 2.7.

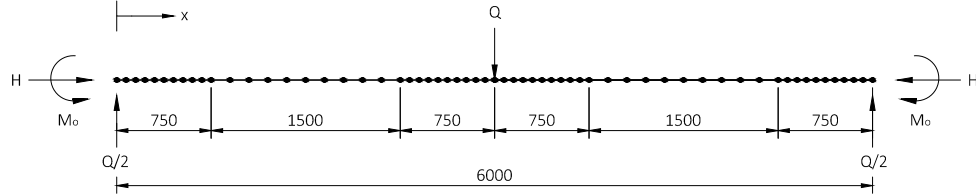


Figure A.1: Layout of sections in beam F2.

1. Input the section properties of beam F2, presented in Figure A.2.

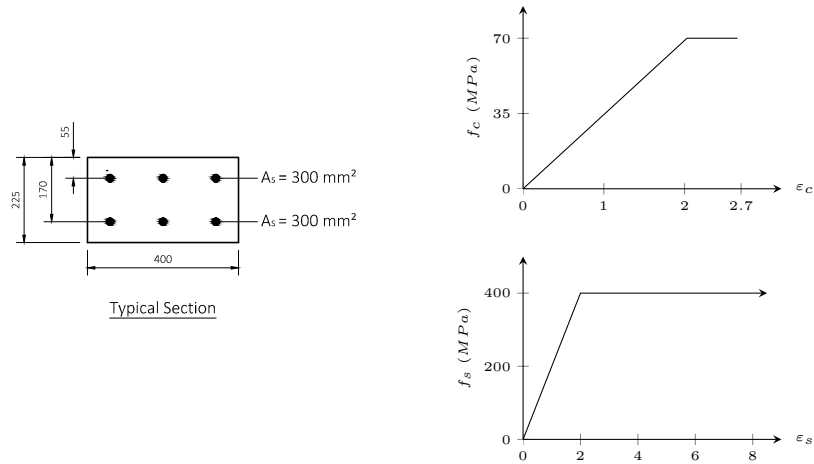


Figure A.2: Properties of beam F2, used for sample analysis.

2. For this load stage, $Q = 95kN$.
3. Assume a deflection, w_o , for each section along the length of the beam. In this case, the deflected shape from the previous load stage, presented in Figure A.3, is used as the initial estimate. The midspan deflection is equal to 22 mm.

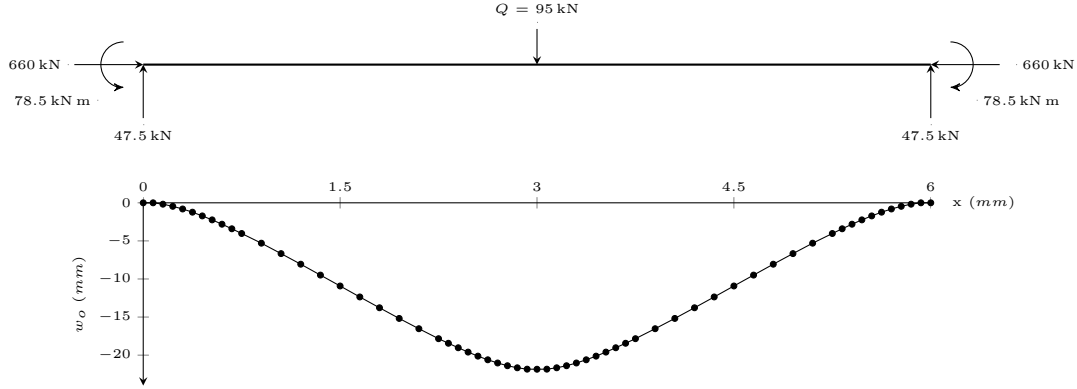


Figure A.3: Assumed initial deflected shape of beam F2.

4. Assume a magnitude of negative bending moment applied at the supports, required to provide rotational compatibility. The bending moment from the previous load stage, $M_o = -78.5 \text{ kN m}$, can be used as the initial estimate.
5. Assume a lateral restraint force, required to provide lateral compatibility. The lateral restraint force from the previous load stage, $H = 660 \text{ kN}$, can be used as the initial estimate.
6. Determine the bending moment due to the applied load, presented in Figure A.4. For a concentrated load, the peak bending moment at midspan is equal to $M_{Q,max} = 142.5 \text{ kN m}$.

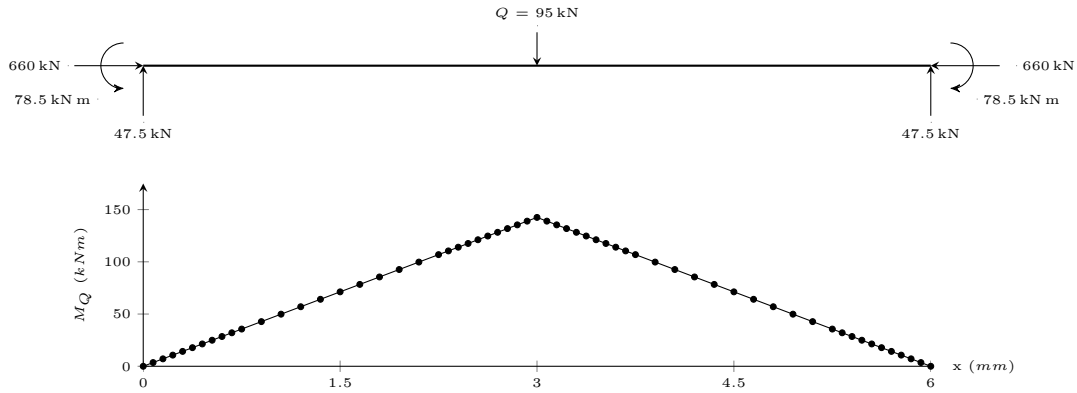


Figure A.4: Bending moment in beam F2, due to the applied load.

7. Determine the bending moment caused by second-order effects, presented in Figure A.5. The bending moment due to second-order effects is defined as $M_w = H \cdot w_o(x)$. The magnitude of M_w at midspan is 14 kN m .

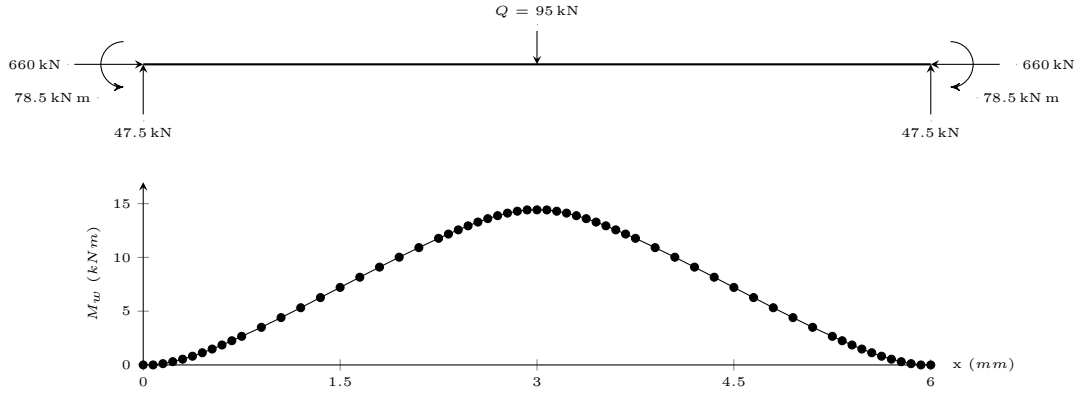


Figure A.5: Bending moment in beam F2, due to second-order effects.

8. Determine the total bending moment by combining the three bending moment components. The total bending moment, $M_t = M_Q + M_o + M_w$, is presented in Figure A.6. The magnitude of M_t at midspan is 78 kN m.

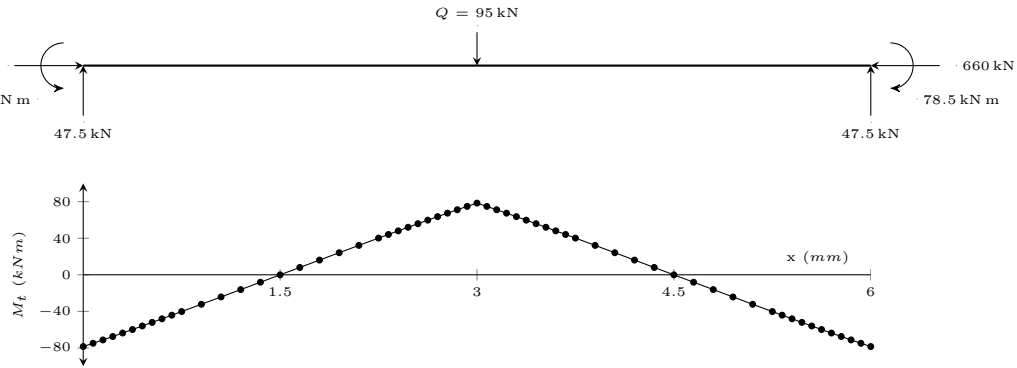


Figure A.6: Total bending moment in beam F2.

9. Determine the curvature throughout beam F2, ϕ , based on the total bending moment and axial compression at each section. The curvature of the beam, presented in Figure A.7, is calculated using a layered analysis approach. The curvature at midspan and the supports is equal to 30 rad/km.

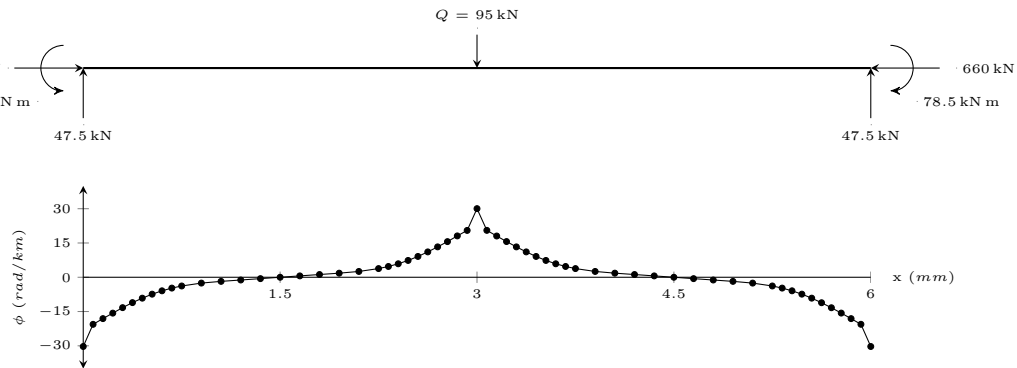


Figure A.7: Total curvature in beam F2.

10. Based on the curvature through beam F2, calculate w_t , L_w , $L_{a,ce}$ and $L_{c,ce}$. The values for this iteration are summarized in Table A.1.

Table A.1: Results from first iteration.

Assumed Variables			Moment and Curvature			Beam Deformation		
$w_{o,mid}$	-21.85	mm	$M_{t,sup}$	-78.5	kNm	$w_{t,mid}$	-23.90	mm
M_o	-78.5	kNm	$M_{t,mid}$	78.4	kNm	L_w	6000.22	mm
H	660	kN	ϕ_{sup}	-30.0	rad/km	$L_{a,ce}$	6000.32	mm
			ϕ_{mid}	30.3	rad/km	$L_{c,ce}$	6000.10	mm

11. Check if the assumed value of axial compression is correct. Since $L_{c,ce}$ is larger than the undeformed length of the beam, return to step 5 and increase the magnitude of the axial compression force. After conducting a number of iterations, it is determined that the axial compression force that provides lateral compatibility is $H = -671$ kN. The results of the iteration are summarized in Table A.2.

Table A.2: Results from second iteration.

Assumed Variables			Moment and Curvature			Beam Deformation		
$w_{o,mid}$	-21.85	mm	$M_{t,sup}$	-78.7	kNm	$w_{t,mid}$	-23.40	mm
M_o	-78.5	kNm	$M_{t,mid}$	78.5	kNm	L_w	6000.20	mm
H	671.36	kN	ϕ_{sup}	-27.9	rad/km	$L_{a,ce}$	6000.20	mm
			ϕ_{mid}	27.4	rad/km	$L_{c,ce}$	6000.00	mm

12. Determine the rotation of the beam at the supports. Based on moment area theorem, the rotation is equal to $\theta_o = 0.881 \cdot 10^{-6}$ rad.
13. Check if the assumed value of M_o is correct. Since θ_o is greater than zero, return to step 4 and increase the magnitude of M_o . After conducting a number of iterations, it is determined that the negative bending moment that provides rotational compatibility is $M_o = -70$ kNm. The results of this iteration are summarized in Table A.3.

Table A.3: Results from third iteration.

Assumed Variables			Moment and Curvature			Beam Deformation		
$w_{o,mid}$	-21.85	mm	$M_{t,sup}$	-78.6	kNm	$w_{t,mid}$	-23.20	mm
M_o	-78.6	kNm	$M_{t,mid}$	78.6	kNm	L_w	6000.20	mm
H	671.36	kN	ϕ_{sup}	-27.6	rad/km	$L_{a,ce}$	6000.20	mm
			ϕ_{mid}	27.6	rad/km	$L_{c,ce}$	6000.00	mm

14. Check if the assumed deflection of beam F2 is equal to the calculated deflection, $w_o = w_t$. Since w_t is greater than w_o , return to step 3 and set $w_o = w_t$. After conducting a number of iterations,

the deflected shape of the beam is found, as presented in Figure A.8. The results of this iteration are summarized in Table A.4.

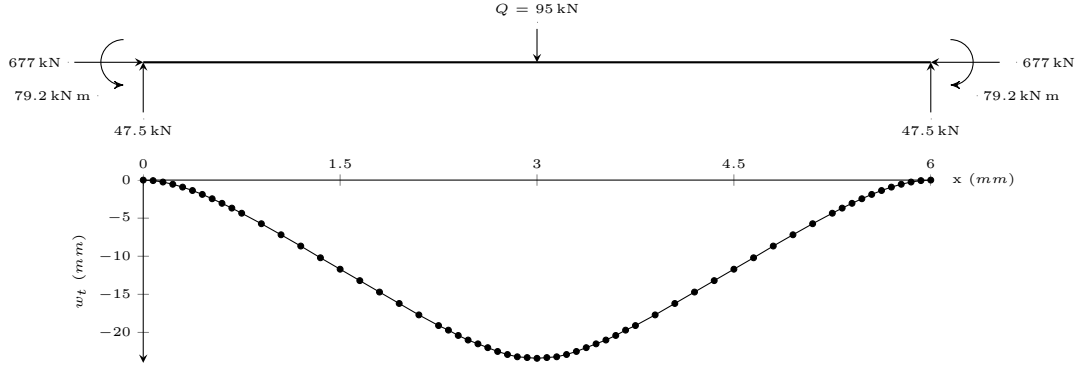


Figure A.8: Final deflected shape of beam F2

Table A.4: Results from final iteration.

Assumed Variables			Moment and Curvature			Beam Deformation		
$w_{o,mid}$	-23.39	mm	$M_{t,sup}$	-79.2	kNm	$w_{t,mid}$	-23.40	mm
M_o	-79.2	kNm	$M_{t,mid}$	79.2	kNm	L_w	6000.20	mm
H	676.97	kN	ϕ_{sup}	-28.1	rad/km	$L_{a,ce}$	6000.20	mm
			ϕ_{mid}	28.1	rad/km	$L_{c,ce}$	6000.00	mm

The results presented in Table A.4 is the final solution of the proposed analysis model for $Q = 95$ kN. These steps can be repeated with an incrementally increasing load to determine the response of the beam up to failure. Alternatively, the response at any load stage can be determined without consideration of previous load stages. The full response of beam F2 is summarized in Section 2.8.

Layered Analysis Sample Calculation

The following sample calculation outlines the iterative procedure used to determine the strain profile at each section, based on a known bending moment and an axial compression force. This calculation is based on the layered analysis procedure summarized in Section 2.5.2. The properties of beam F2 are summarized in Figure A.9.

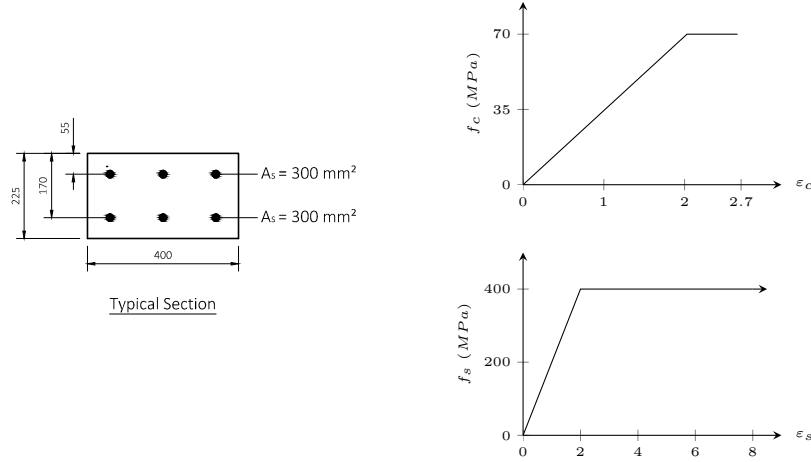


Figure A.9: Properties of beam F2, used for layered sample analysis.

1. Given: $M_t = 78.5 \text{ kN m}$ and $H = 660 \text{ kN}$.
2. Assume $\varepsilon_t = -2.0 \text{ mm/m}$.
3. Assume $\varepsilon_b = 5.0 \text{ mm/m}$.
4. Calculate the curvature, $\phi = 31.1 \text{ rad/km}$, and centroidal strain, $\varepsilon_{ce} = 1.5 \text{ mm/m}$.
5. Calculate the resultant force in the top reinforcement, $F_{s,t} = -17.3 \text{ kN}$, and bottom reinforcement, $F_{s,b} = 120 \text{ kN}$.
6. Calculate the resultant force in the concrete, $F_c = -889 \text{ kN}$, and the eccentricity of this force, $e_c = 91 \text{ mm}$.
7. Determine the axial compression force at the section using horizontal equilibrium.

$$H_o = F_c + F_{s,t} + F_{s,b} = -786 \text{ kN}$$

8. Check if the assumed bottom strain in the section is correct. Since H_o is greater in magnitude than H , return to step 3 and increase the magnitude of ε_b . After conducting a number of iterations, the bottom strain based on horizontal equilibrium is found to be $\varepsilon_b = 6.0 \text{ mm/m}$. The results of this iteration are summarized in Table A.5.

Table A.5: Results from first iteration of layered analysis.

Assumed Variables			Resultant Forces			Force Eccentricity		
ε_t	-2.0	mm/m	F_c	-777	kN	e_c	93.2	mm
ε_b	6.0	mm/m	$F_{s,t}$	-2.6	kN	$e_{s,t}$	57.5	mm
			$F_{s,b}$	120	kN	$e_{s,b}$	-57.5	mm

9. Determine the bending moment at the section, based on rotational equilibrium.

$$M_o = F_c(e_c) + F_{s,t}(e_{s,t}) + F_{s,b}(e_{s,b}) = -79.9 \text{ kN m}$$

10. Check if the assumed top strain in the section is correct. Since M_o is greater in magnitude than M_t , return to step 2 and reduce the magnitude of ε_t . After conducting a number of iterations, the top strain based on rotational equilibrium is found to be $\varepsilon_t = -1.8 \text{ mm/m}$. The results of this iteration are summarized in Table A.6.

Table A.6: Results from final iteration of layered analysis.

Assumed Variables			Resultant Forces			Force Eccentricity		
ε_t	-1.8	mm/m	F_c	-770	kN	e_c	92.2	mm
ε_b	5.0	mm/m	$F_{s,t}$	-10.2	kN	$e_{s,t}$	57.5	mm
			$F_{s,b}$	120	kN	$e_{s,b}$	-57.5	mm

The strain profile summarized in Table A.6 relates the bending moment and axial compression force at the section to the curvature, $\phi = 30.3 \text{ rad/km}$, and the centroidal strain, $\varepsilon_{ce} = 1.57 \text{ mm/m}$.

Appendix B

Additional Notes on the Proposed Model

Concrete Confinement

The influence of confinement on the σ - ε response of concrete can be quantified based on the model developed by Mander et al. (1988). This model assumes that confinement is provided by stirrups, as illustrated in Figure B.1.

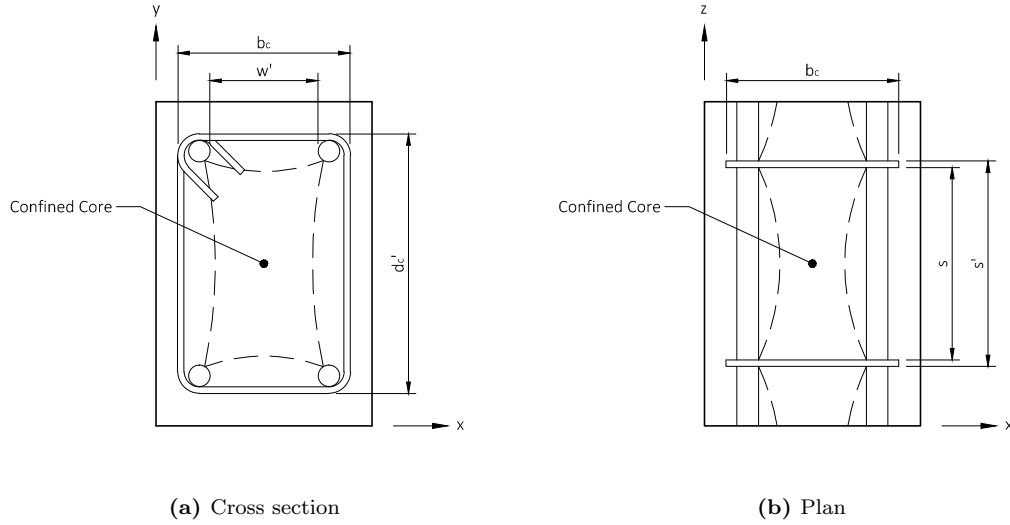


Figure B.1: Geometrical properties of a confined core.

Based on Mander's model, the compressive stress of concrete in a confined core is defined as,

$$f_c = \frac{f'_{cc} x r}{r - 1 + x^r} \quad (\text{B.1})$$

where f'_{cc} is the peak compressive strength defined based on the geometry of the confined core and the amount of confining reinforcement. The variable x is defined as,

$$x = \frac{\varepsilon_o}{\varepsilon_{cc}} \quad (\text{B.2})$$

where ε_o is the peak compressive strain in the unconfined concrete, and ε_{cc} is the peak compressive strain in the confined core. The variable r is defined as,

$$r = \frac{E_c}{E_c - E_{sec}} \quad (\text{B.3})$$

where E_c is the tangent modulus of elasticity in the concrete, and E_{sec} is the secant stiffness of the concrete. The increased peak strain in confined concrete is defined as,

$$\varepsilon_{cc} = \varepsilon_o \left[1 + 5 \left(\frac{f'_{cc}}{f'_c} - 1 \right) \right] \quad (\text{B.4})$$

The magnitude of the tangent and secant stiffness in the concrete is assumed to be as,

$$E_c = 5000\sqrt{f'_c} \quad (\text{B.5})$$

$$E_{sec} = \frac{f'_{cc}}{\varepsilon_{cc}} \quad (\text{B.6})$$

The increase in compressive stress capacity caused by confinement is based on the confinement effectiveness coefficient, k_e . The magnitude of the confinement coefficient can be estimated as,

$$k_e = \frac{\left(1 - \sum_{i=1}^n \frac{(w'_i)^2}{6b_c d_c}\right) \left(1 - \frac{s'}{2b_c}\right) \left(1 - \frac{s'}{2d_c}\right)}{(1 - \rho_{cc})} \quad (\text{B.7})$$

where w'_i is the clear transverse spacing between longitudinal bars, b_c is the concrete core dimension defined from center to center of the stirrups in the out-of-plane direction, d_c is the concrete core dimension defined from center to center of the stirrups in the transverse direction, s' is the clear spacing between stirrups, and ρ_{cc} is the ratio of the area of longitudinal steel to the core area of the section.

The confinement effectiveness coefficient is used to define the effective lateral confining pressure, f_1 , provided by the reinforcement in both the transverse (x) and out-of-plane (y) directions. The magnitude of confining pressure in both directions is defined as,

$$f'_{1x} = k_e \rho_x f_{yh} \quad (\text{B.8})$$

$$f'_{1y} = k_e \rho_y f_{yh} \quad (\text{B.9})$$

where ρ_x and ρ_y are the reinforcement ratios for the transverse and out-of-plane reinforcement, respectively, and f_{yh} is the yield strength of the stirrups. The confined strength ratio, f'_{cc}/f'_c , based on the calculated lateral confining stress, is determined using the multi-axial failure criterion presented graphically in the paper by Mander et al. (1988).

The ultimate compressive strain in the confined concrete core, $\varepsilon_{c,u}$, is defined as the strain causing the transverse reinforcement to fracture. The ultimate compressive strain in confined concrete can be determined using a strain energy balance approach, where the increased strain energy developed in the confined concrete must be provided by the strain energy capacity of the confining reinforcement as it yields in tension. This approach is summarized as,

$$U_{sh} = U_{cc} + U_{sc} - U_{co} \quad (\text{B.10})$$

where U_{cc} is the strain energy stored by confined concrete per unit volume, U_{co} is the strain energy stored by unconfined concrete per unit volume, U_{sc} is the strain energy capacity stored by longitudinal

reinforcing steel in compression per unit volume of concrete core, and U_{sh} is the strain energy capacity of transverse confining steel per unit volume of concrete core.

The area under a σ - ε curve represents the total strain energy per unit volume. Therefore, the strain energy of each material can be determined by numerically integrating the material's σ - ε response. Alternatively, the ultimate compressive strain in the confined concrete can be estimated as,

$$110\rho_s = \int_0^{\varepsilon_{c,u}} f_c d\varepsilon_c + \rho_{cc} \int_0^{\varepsilon_{c,u}} f_{sl} d\varepsilon_c - 0.017\sqrt{f'_c} \quad (\text{B.11})$$

where ρ_s is the ratio of the volume of hoop reinforcement to the volume of concrete core, f_c is the longitudinal compressive stress in the concrete, ε_c is the longitudinal compressive strain in the concrete, f_{sl} is the compressive stress in the longitudinal reinforcement, and f'_c is the unconfined compressive strength of the concrete.

Moment Area Theorem

The moment area theorem, illustrated in Figure B.2, states that the vertical deviation of point A from the tangent at point B is equal to the second moment of area under the curvature diagram.

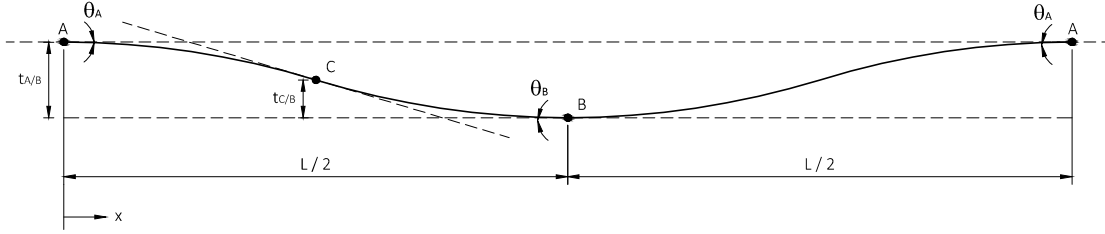


Figure B.2: Beam deflection, based on Moment Area Theorem.

The magnitude of deflection at point B, relative to point A, is defined as,

$$t_{A/B} = \int_A^B \phi \cdot x \cdot dx \quad (\text{B.12})$$

where $t_{A/B}$ is the vertical distance from point A to the tangent at point B, ϕ is the curvature at each section, and x is the horizontal distance between section A and B. This procedure can be used to find the relative deflection between any two point along the length of a beam.

For the proposed analytical model, a numerical integration approach is used to calculate deflection. The maximum deflection, at the midspan of the beams considered throughout this thesis, $w_{t,max}$, is defined as,

$$w_{t,max} = \sum_{i=1}^{n-1} \left(\frac{\phi(i) + \phi(i+1)}{2} \right) \left(x(i+1) - x(i) \right) \left(\left(\frac{x(i+1) + x(i)}{2} \right) \right) \quad (\text{B.13})$$

where n is the total number of sections, ϕ is the curvature at each section, and x is the distance from each section to the support. The magnitude of deflection at any section, $w_{t,m}$, is determined as,

$$w_{t,m} = w_{t,max} + \sum_{i=m}^{n-1} \left(\frac{\phi(i) + \phi(i+1)}{2} \right) \left(x(i+1) - x(i) \right) \left(\left(\frac{x(i+1) + x(i)}{2} \right) - x(m) \right) \quad (\text{B.14})$$

where m is the section considered. By calculating the deflection at each section, the deformed shape of the beam can be found.

The second compatibility condition proposed for the analytical procedure requires that the ends of a

beam do not rotate. The rotation of the beam ends can be determined from the curvature response at each section using the moment area theorem. The theorem states that the change in slope between any two points is equal to the area under the curvature diagram, between the two points. The magnitude of rotation at point A, relative to point B, is defined as,

$$\theta_{AB} = \int_A^B \phi \, dx \quad (\text{B.15})$$

Alternatively, a numerical integration approach can be taken to find the rotation at the end of a beam, θ_o ,

$$\theta_o = \sum_{i=1}^{n-1} \left(\frac{\phi(i) + \phi(i+1)}{2} \right) \left(x(i+1) - x(i) \right) \quad (\text{B.16})$$

Appendix C

Proposed Experiment

Overview

The proposed analytical model presented in Chapter 2 is based on the response of a reinforced concrete beam with infinitely rigid supports. This theoretical boundary condition is very difficult to achieve as the majority of restrained beams or slabs have supports that allow for some rotation and lateral expansion. As a result, few experiments in the literature adequately study the effect of arching action in reinforced concrete beams with stiff support conditions. The majority of the experiments that do exist are based on the study of two-bay frames with the middle column removed. This requires that column stubs be constructed at the midspan and at the supports, causing geometric irregularities. These stubs introduce a high degree of complexity and uncertainty into the analysis, and their behaviour is difficult to predict. In Chapter 4, the analytical model is validated using the test data from six reinforced concrete beams with stiff supports, from two experiments. However, a number of approximations are required to account for the complexity in the test setup. Therefore, the development of a simple testing program that isolates the behaviour of arching action in reinforced concrete beams is desired to provide further validation of the proposed model.

This chapter proposes an original experimental setup that isolates the behaviour of arching action in reinforced concrete beams. This setup is based on the equipment and testing space available in the Structural Engineering Laboratory at the University of Toronto. A fully rigid boundary condition is provided using two hydraulic actuators acting in parallel at each end of the beam. The actuators are servo-controlled, and can therefore adjust in length to prevent any outward expansion or rotation of the beams. The ends of each beam are cast onto a steel end plate. The reinforcement in each beam is mechanically anchored to the back of each plate, allowing for the full development of the capacity of the reinforcement, limiting strain penetration. Based on this experimental setup, four test specimens are proposed to provide insight into the influence of rigid restraints on the stiffness and capacity of reinforced concrete beams. The material properties of each specimen are varied to study the influence of concrete strength, reinforcement ratio and span-to-depth ratio. Following this, the response of each specimen, predicted using the proposed analytical model, is summarized.

Support Setup

The main goal of the proposed experiment is to provide a fully fixed support. The reactions at each end of the support must be isolated to accurately measure the vertical, horizontal and bending moment reactions. The rotational restraint can be provided using two stiff struts acting in parallel, arranged either vertically or horizontally at the end of each specimen. This arrangement is likely governed by the limitations of space and available equipment in the laboratory. For the proposed experiment, the support couple that provides rotational restraint is positioned horizontally, as illustrated in Figure C.1. In addition to providing rotational restraint, this force couple also provides the required lateral restraint.

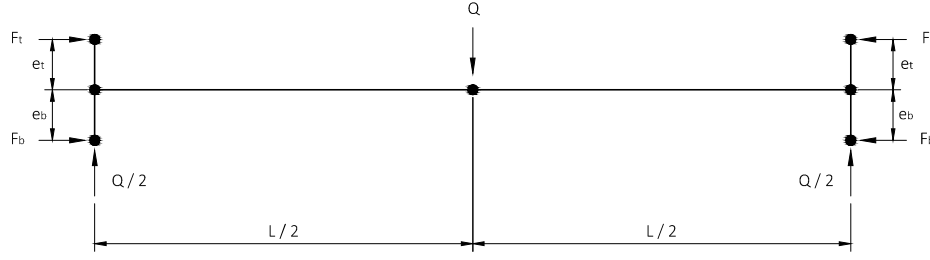


Figure C.1: Lateral and rotational restraint schematic.

During the experiment, the magnitude of the force in the top strut, F_t , and the bottom strut, F_b , will be measured. Based on the respective eccentricity of each strut from the centroid of the beam specimen, e , the total bending moment and lateral restraint force can be calculated as,

$$M_o = (F_b \cdot e_b) + (F_t \cdot e_t) \quad (C.1)$$

$$H = F_b + F_t \quad (C.2)$$

The lateral stiffness of each support is defined as the lateral load required to produce a unit displacement. If the strut is assumed to remain elastic throughout testing, then the axial stiffness of each strut can be determined as,

$$K_{axial} = \frac{Q}{\Delta} = \frac{AE}{L} \quad (C.3)$$

where A is the cross section area, E is the modulus of elasticity of the material, and L is the total length of the strut. Therefore, the stiffness of each strut can be increased by increasing the cross sectional area of the support, using a material with a larger stiffness, or reducing the length of the strut.

The rotational stiffness provided at each support is defined as the bending moment required to develop a unit rotation, and can be determined as,

$$K_{rot} = \frac{M_o}{\theta} = \frac{K_{axial}(e_t + e_b)^2}{2} \quad (C.4)$$

The rotational stiffness of a support, provided by two struts acting in parallel, is governed by the axial stiffness and the lever arm between the struts. Therefore, the rotational stiffness of a support can be increased by either increasing the distance between the struts, or increasing the stiffness of the struts.

The experimental studies previously conducted on reinforced concrete beams provide a rigid boundary condition by isolating the reaction forces using passive struts. The reaction force in each passive strut

is compared to the measured axial deformation of the strut, to determine the elastic stiffness of the support. Due to limitations in the size of the setup and available laboratory equipment, these struts allow for some lateral expansion and rotation of the beam at the supports. In addition, the use of passive struts at each support results in a fixed specimen length that cannot be easily adjusted. If the specimen length is not exactly the right size, then connecting the specimen to the struts will induce an initial tension or compression resultant, prior to testing.

Alternatively, the stiffness of each strut can be increased by using active struts. The length of these struts can be adjusted by actively measuring the lateral expansion and rotation of the beam ends. An example of an active strut is a servo-controlled hydraulic actuator, illustrated in Figure C.2. The actuator consists of a load cell, a strain gauge and a jack located within a double hinged mechanism that prevents the transfer of bending and shear forces. By actively measuring and adjusting for lateral expansion and rotation at the supports, the actuators provide a fully fixed boundary condition.

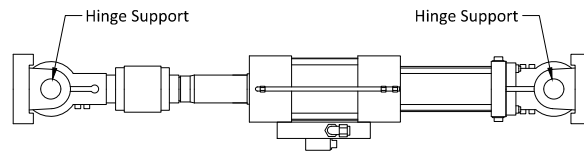


Figure C.2: Proposed actuator supports, drawn by David Hubbell.

The axial force in each of the actuators can be transferred to the strong floor using a massive concrete block. These blocks must be large enough to provide a significantly stiff bearing support for the actuators. The stiffness of these blocks can be increased by post-tensioning them into the strong floor using four threaded steel rods, placed through ducts cast into the blocks. This ensures that the block will not slip when exposed to the large compression and tension forces from the actuators. To provide stiffness in tension, the actuators are anchored in the block using threaded rods with sufficient embedment, defined based on recommendations from the Canadian Standards Association (2006). To prevent the end plates of the actuator from lifting off the surface of the concrete when subjected to large tensile forces, a torque wrench should be used to tighten the end plates to the surface of the concrete.

The rotational stiffness of a support is governed by the distance between the two parallel actuators. This separation requires that either the beam specimen be sufficiently deep, or the beams be connected to larger blocks on either end that can spread out the reaction forces. Increasing the depth of the specimen can cause significant difficulties, particularly when considering slender beams. It is often more practical to provide end blocks that are much larger than the beam's cross section. In previous experiments, concrete end blocks have been cast monolithically at the ends of each beam specimen. This allows the reinforcement to remain continuous at the ends of the beam, and simplifies the support setup. However, the use of concrete end blocks increases the complexity of the behaviour at the critical regions located at the supports. As previously described, these geometric irregularities cause the bond between the reinforcement and the concrete in the end blocks to deteriorate, causing the strain in the steel to penetrate out from the blocks. Therefore, an alternative solution is required for the proposed experiment to prevent the development of strain penetration.

The reaction forces from the beam can be spread into each of the actuators without increasing complexity by considering an externally attached, rigid steel block. Two alternatives for these blocks are presented in Figure C.3.

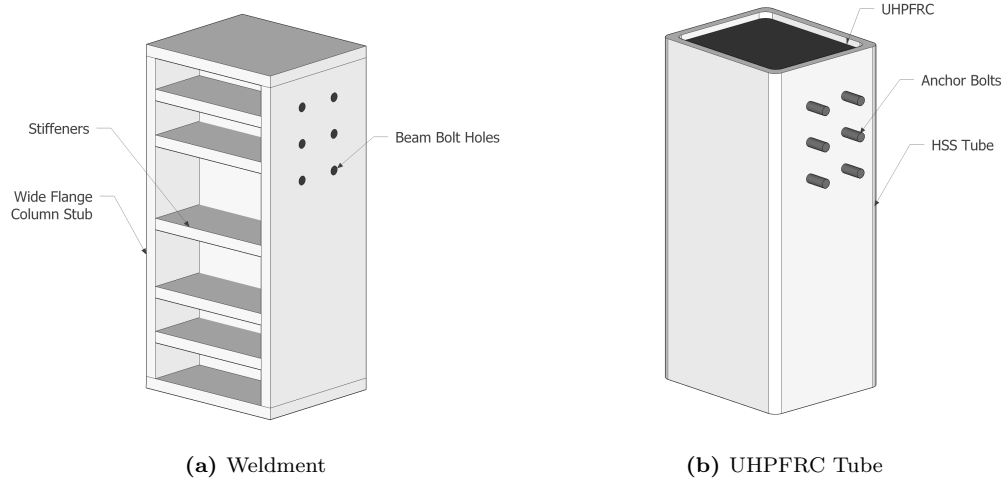


Figure C.3: Options for the steel end block at each support.

Both alternatives provide a sufficient amount of rigidity as part of the test setup. Therefore, the difference between the two will likely depend on the available materials and fabrication costs. The first option is to construct a steel weldment composed of a stocky wide flange column reinforced with steel stiffeners. This option requires a significant amount of fabrication and welding be done to ensure the column remains rigid. If it is difficult to source the heavy column, the section can be fabricated using thick steel plates. The second option is to fill a steel rectangular hollow tube with Ultra High Performance Fiber Reinforced Concrete (UHPFRC). This option requires that threaded steel rods be embedded into the concrete to provide anchors for the beam and actuators. In addition, this option requires a sufficient understanding of the mix composition and casting techniques required for UHPFRC.

The two vertical reactions in the system are located at the base of the steel end blocks. A horizontal roller is used to prevent the transfer of horizontal loads into the vertical restraint. Therefore, the shear force at each support is isolated and can be measured using load cells located between the roller and the strong floor. At each support, two load cells are used in parallel to provide out-of-plane lateral stability. The proposed support setup for the experiment is presented in Figure C.4.

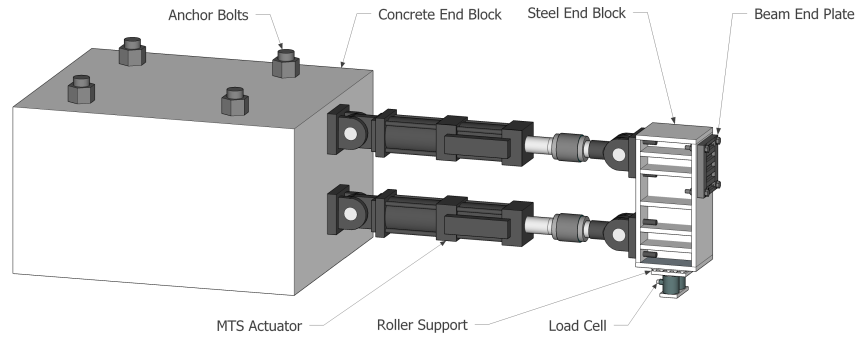


Figure C.4: Experimental support setup.

Beam Specimens

The test specimens for the proposed experiment consist of rectangular, doubly reinforced concrete beams with no geometric irregularities along their length. The ends of each beam are cast onto a steel end plate, which is attached to the rigid steel block prior to testing. Shear keys welded onto each steel plate allow the shear force in the concrete to transfer through to the support. The reinforcement in the beam is continuous through the end plates, with a mechanical connection at the back allowing for the full development of the reinforcement's capacity. The full development of the reinforcement at the support is critical to this experiment, as the peak bending moment is expected to occur near the interface of the concrete beam and the steel end plate. The steel end plates proposed for this experiment are illustrated in Figure C.5.

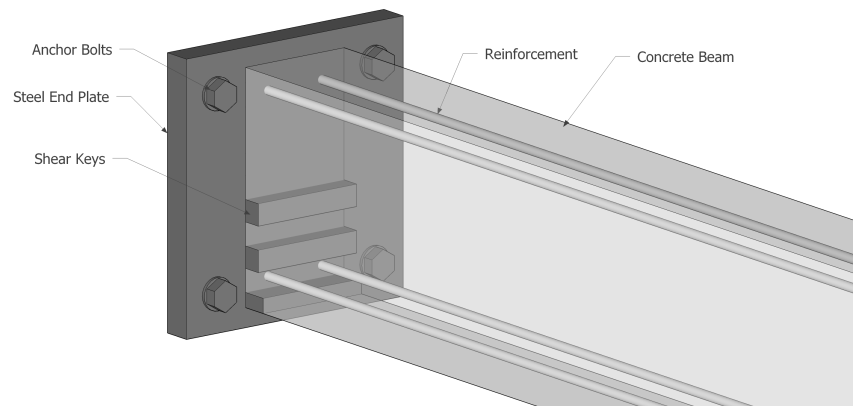


Figure C.5: Steel end plates.

The goal of the proposed experiment is to provide insight into the influence of concrete strength, reinforcement ratio and span-to-depth ratio on the strength enhancement caused by arching action. This

experiment also provides a means to verify and further develop the proposed analytical model. A summary of the proposed specimens and their respective properties are presented in Table C.1. The length of the specimens are kept constant to simplify the support setup. Therefore to study the effects of slenderness, the height of the beam is varied. The width of each specimen is governed by the capacity of the available actuators, as increasing the width increases the magnitude of the lateral restraint force.

Table C.1: Properties of the beams in the proposed experiment.

Label	L <i>mm</i>	h <i>mm</i>	L/h	b <i>mm</i>	f'_c <i>MPa</i>	$A_{s,t}$ <i>mm²</i>	$A_{s,b}$ <i>mm²</i>	f_y <i>MPa</i>	f_u <i>MPa</i>	d <i>mm</i>	d' <i>mm</i>
B1	3000	300	10	150	30	200	200	400	550	266	34
B2	3000	300	10	150	30	103	103	553	600	268	32
B3	3000	150	20	150	30	52	52	553	600	120	30
B4	3000	150	20	150	70	52	52	553	600	120	30

Predicted Beam Response

The response of each beam can be predicted using the proposed analytical model. The beam is assumed to have fully rigid support conditions. In addition, no bond deterioration is considered as the reinforcement is mechanically anchored to the back of the steel end plates. The ability of the actuators to adjust in length according to the actual length of the specimen provides a means of preventing any initial slip in the specimen. Therefore, the model does not consider the influence of slip. The diagonal compression field action model is incorporated into the analysis to account for the influence of the diagonal compression struts throughout the beam. The behaviour of concrete in compression is predicted using the model developed by Popovics (1973). The tensile strength of the concrete is assumed to be equal to zero, and the effects of confinement are not considered. The behaviour of the reinforcement is based on the model developed by Mander (1983), with $E_s = 200$ GPa.

The applied load vs. midspan deflection prediction for each beam is presented in Figure C.6a. The proposed analytical model predicts that all four specimens will fail as a result of crushing simultaneously at midspan and the support, with the reinforcement yielding just before failure. Increasing the depth of the beam results in an increased stiffness and capacity. However, this also causes a reduction in the total deflection of the beam. Increasing the reinforcement ratio from specimen B2 to B1 causes a stiffer response and a larger peak load. However, the additional deflections exhibited by beam B1 are likely caused by the less stiff reinforcement specified. This highlights the importance of reinforcement yield strength on the response of reinforced concrete beams. In addition, the increase in concrete strength between beams B3 and B4 results in a stiffer response and an increased capacity, but with little impact on the deflection of the beam. This signifies the importance of using higher strength concrete to increase the enhancement caused by arching action.

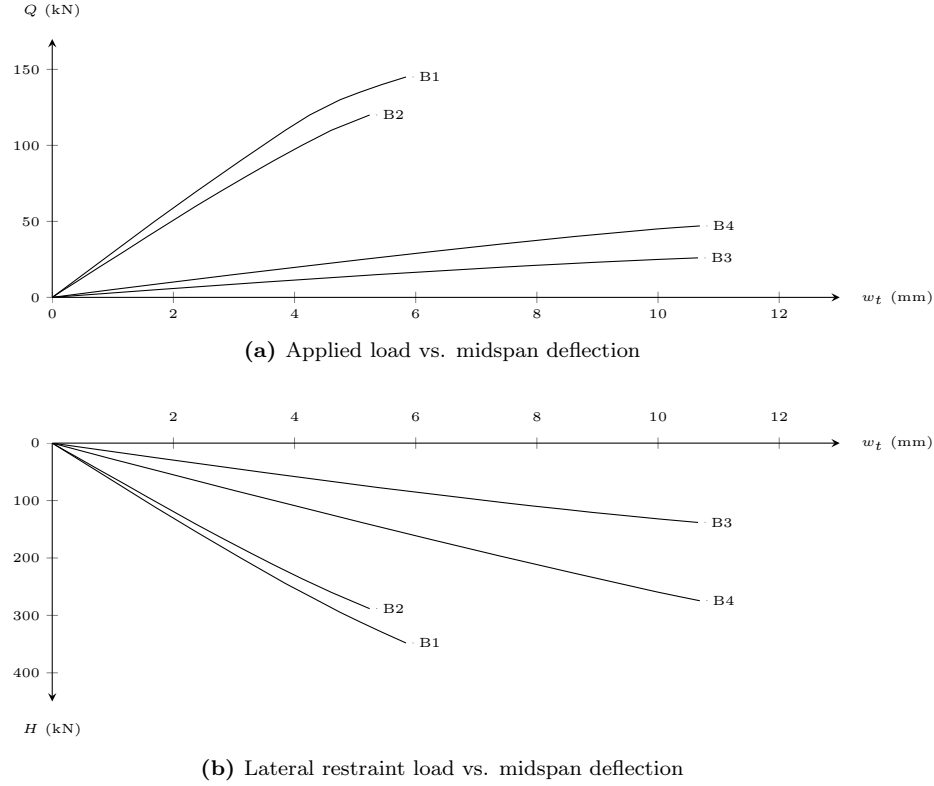


Figure C.6: Predicted response of the beams in the proposed experiment.

The relationship between the axial compression force and the midspan deflection is presented in Figure C.6b. Increasing the slenderness of a beam reduces the total axial compression developed. Alternatively, increasing the reinforcement ratio has little effect on the response, but does increase the axial compression at failure, likely due to the development of a larger applied load. Increasing the concrete strength from beam B3 to B4 causes a significant increase in the axial compression force developed in the section, accounting for the increased capacity in the beam.

Discussion of Results and Concluding Remarks

The proposed experimental setup uses two hydraulic actuators acting in parallel at each end of the specimen to provide the rotational and axial restraint. The length of each actuator is adjusted during the test to prevent the lateral expansion and rotation of the ends of the beam, providing a fully fixed connection. The axial compression and bending moment from the beam is spread out into each actuator using a rigid steel block. This steel block can be constructed using a stiff I-beam column or by filling a rectangular steel tube with Ultra High Performance Fiber Reinforced Concrete. The beam specimens can then be cast onto steel end plates, and the reinforcement mechanically anchored to the back of each plate. This prevents the development of strain penetration in the beam specimens.

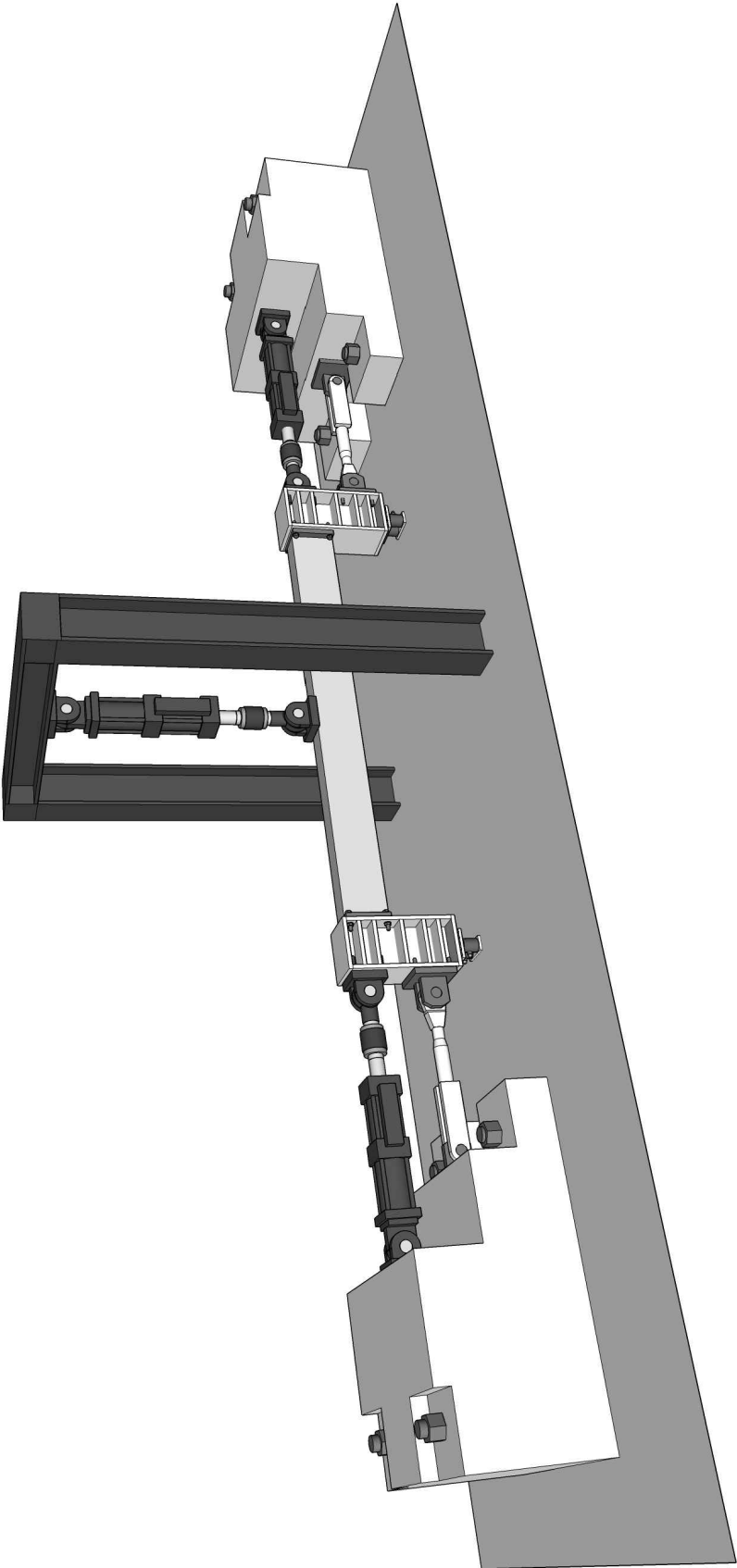
The proposed experiment consists of four doubly reinforced concrete beams. The properties of each beam are varied to study the influence of concrete strength, reinforcement ratio, and span-to-depth ratio. A prediction of the behaviour of each beam specimen is generated using the proposed analytical model.

These predictions result in a number of conclusions, including:

1. Increasing the slenderness of a beam reduces the magnitude of axial compression developed. This also causes a reduction in the stiffness and capacity of a beam, corresponding with an increase in deflection.
2. Increasing the strength of concrete increases the stiffness and capacity of the beam without a significant reduction in deflection.
3. The yield strength of reinforcement can impact the deflection of a reinforced concrete beam.

The next step in the progression of this research is to conduct a series of experiments that focus on isolating the response of arching action in reinforced concrete beams. The proposed setup provides a basis for developing these experiments by providing a fully rigid boundary condition. These experiments will provide a means to validate the proposed analytical model without the need for the simplifying assumptions used in the current experimental validation. This will increase confidence in the rational approach. In addition, the experiments can provide valuable insight into the influence of various beam parameters, which is critical in the development of a simplified analytical procedure that can be adopted in future design codes.

A full set of drawings, for the proposed experiment, is presented in the following pages.



Drawing Title:

Proposed Experiment 3D Model

Date:

08/17/15

Drawn By:

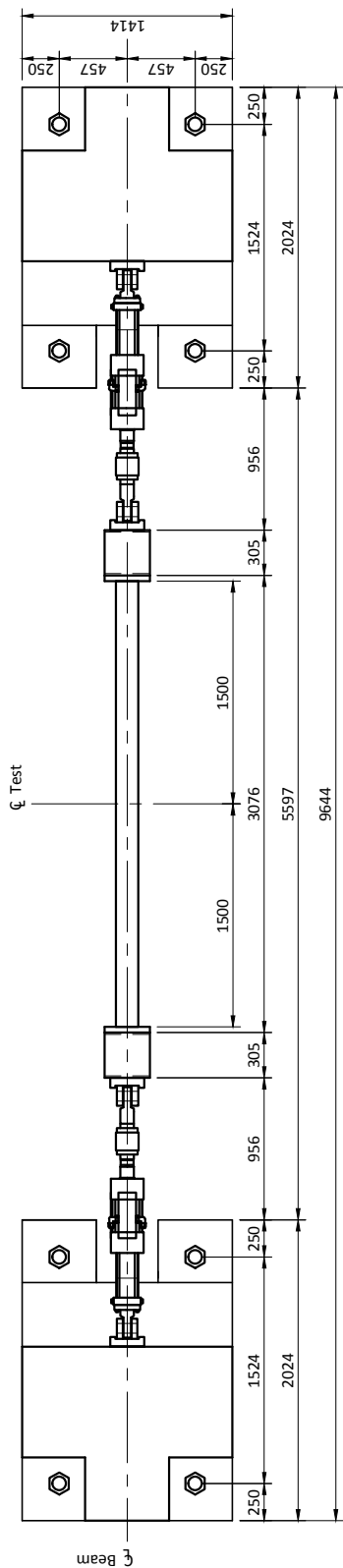
RM

DWG #:

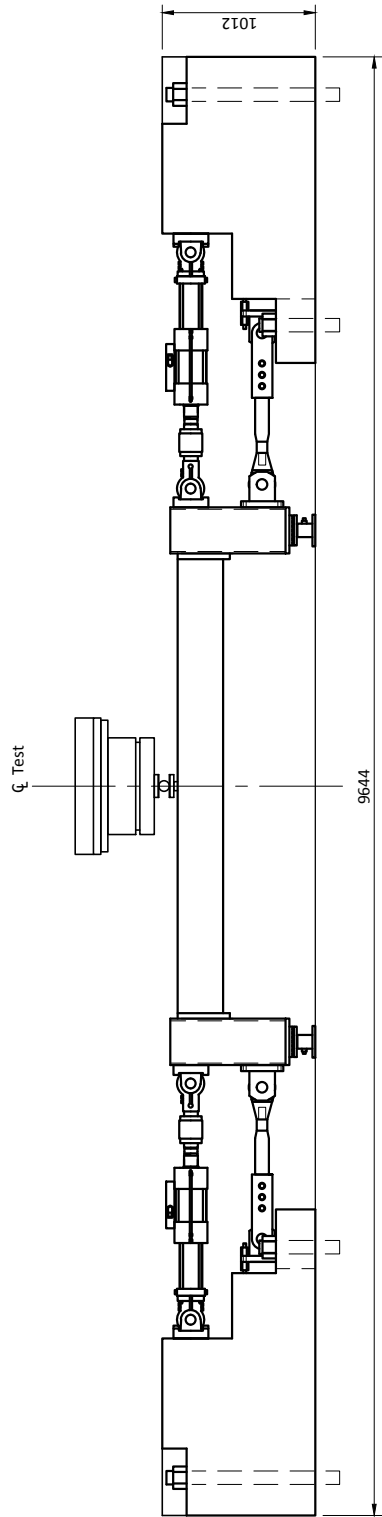
SD - 00

NOTES:

1) THIS DRAWING SET IS BASED ON THE PROPOSED EXPERIMENT SUMMARIZED IN APPENDIX C. THE SETUP IS DEVELOPED USING THE AVAILABLE EQUIPMENT IN STRUCTURAL TESTING FACILITY AT THE UNIVERSITY OF TORONTO

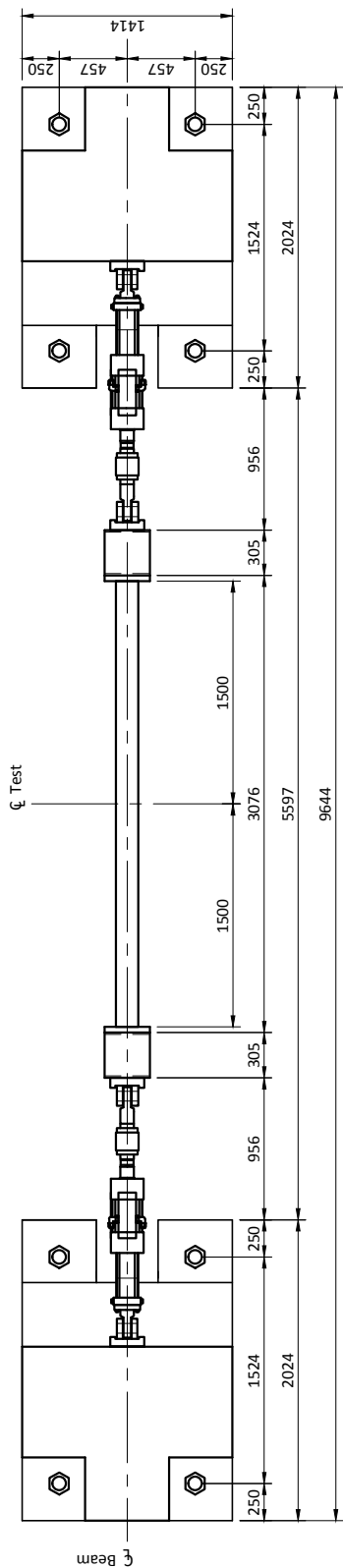


TEST SETUP PLAN
SCALE 1:50

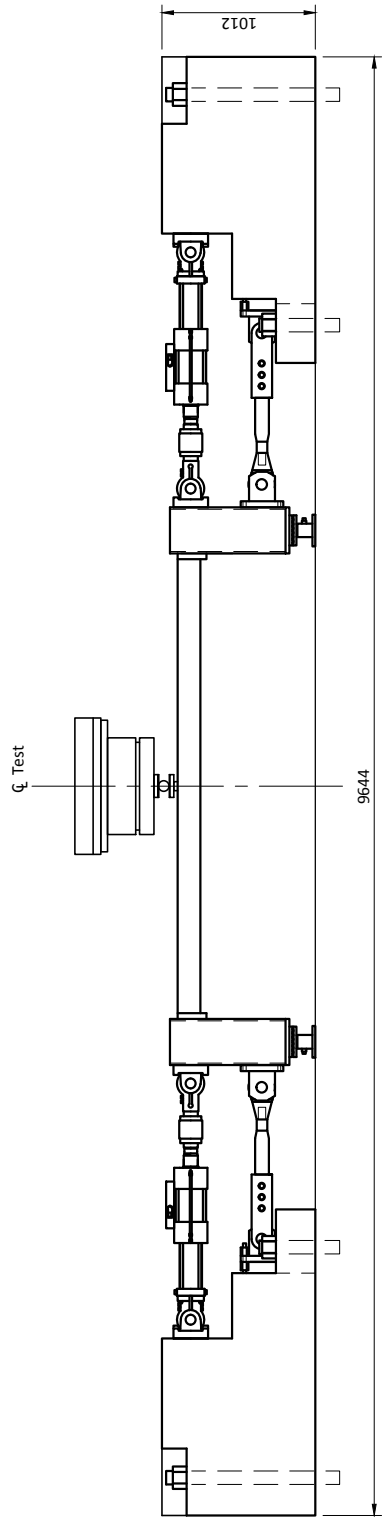


TEST SETUP ELEVATION
SCALE 1:50

Drawing Title: Plan and Elevation Beams B1 and B2			DWG #:	SD - 01
Date:	08/17/15	Drawn By:	RM	

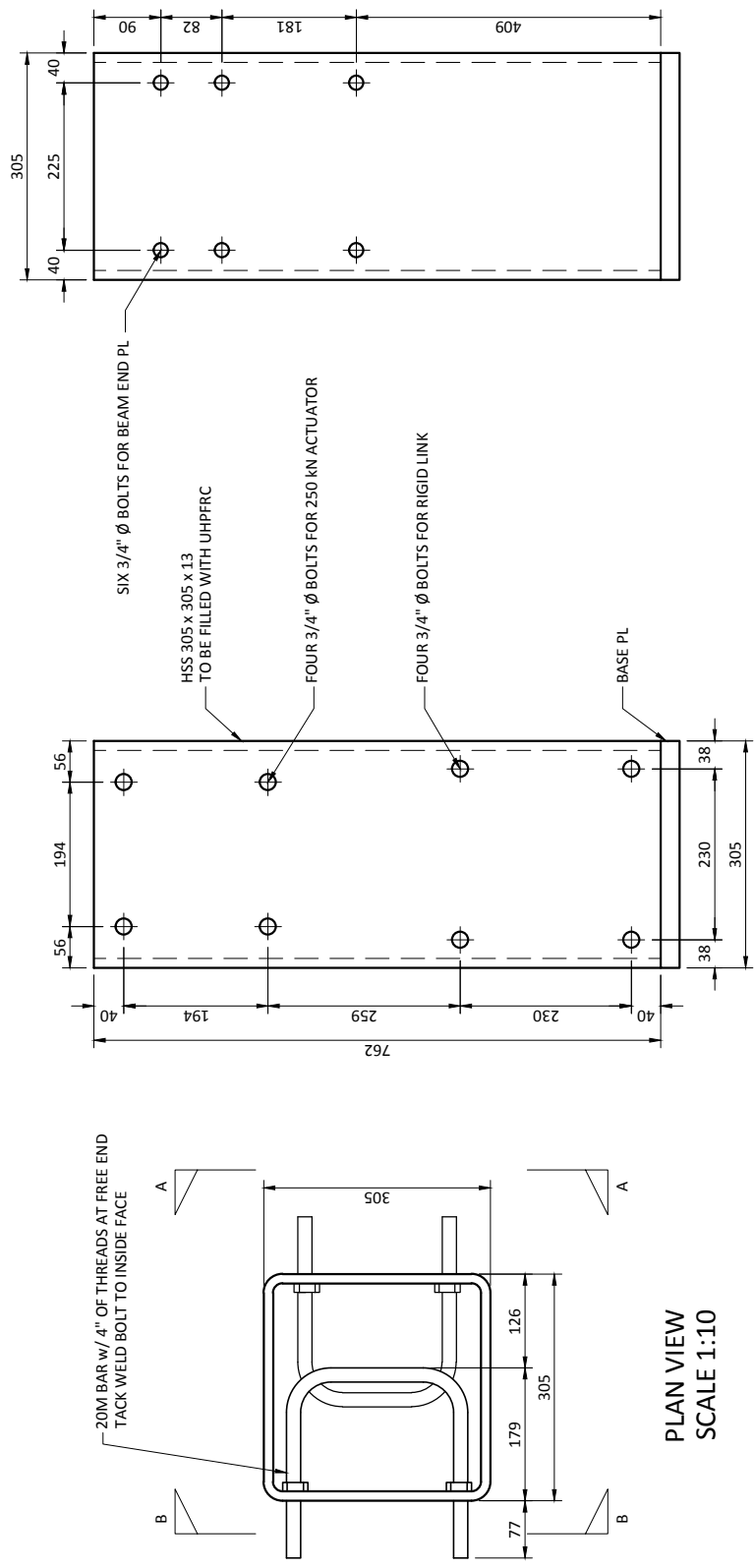


TEST SETUP PLAN
SCALE 1:50



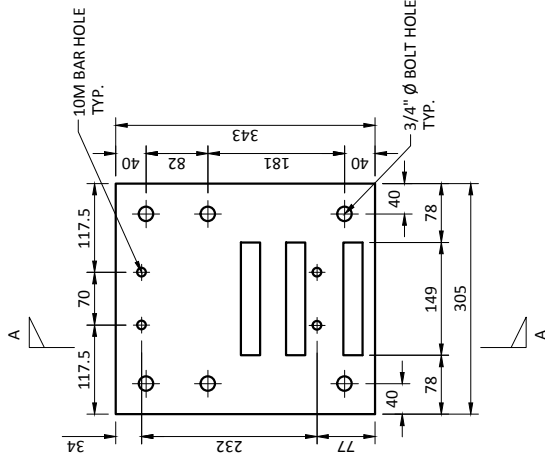
TEST SETUP ELEVATION
SCALE 1:50

Drawing Title: Plan and Elevation Beams B3 and B4			DWG #:	SD - 02
Date:	08/17/15	Drawn By:	RM	

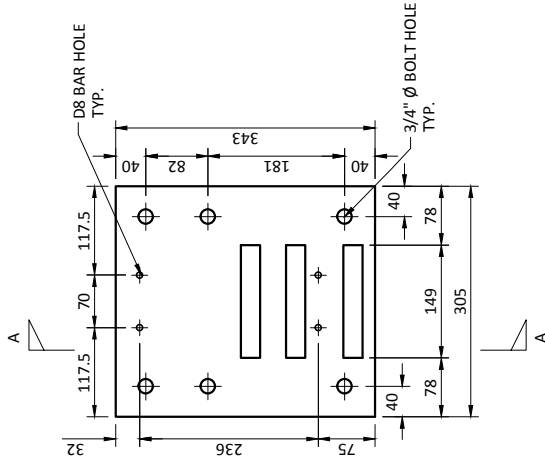


- NOTES:
- 1) ALL BOLTS ARE TO BE TORQUED TO 200 lbf USING TORQUE WRENCH
 - 2) THE UHPFRC PROVIDED IS BASED ON A MIX DEVELOPED AT THE UNIVERSITY OF TORONTO

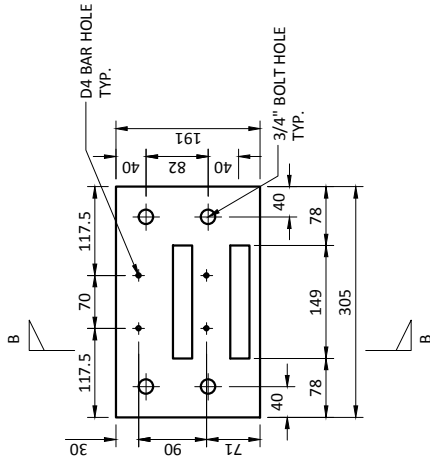
Drawing Title: Steel End Block Details		
Date: 08/17/15	Drawn By: RM	DWG #: SD - 03



BEAM B1 END PL
SCALE 1:10



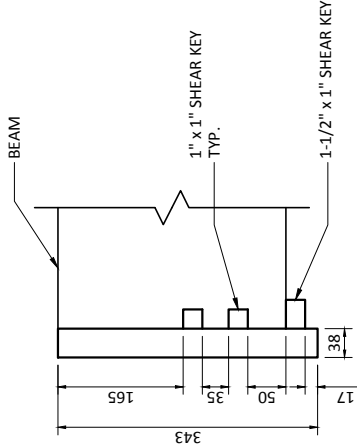
BEAM B2 END PL
SCALE 1:10



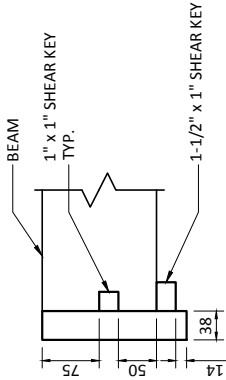
BEAM B3/B4 END PL
SCALE 1:10

NOTES:

- 1) ALL BOLTS ARE TO BE TORQUED TO 200 lbf USING TORQUE WRENCH
- 2) THE ENDS OF THE REINFORCING BARS ARE TO BE PEENED TO PROVIDE A MECHANICAL CONNECTION
- 3) SHEAR KEYS ARE TO BE WELDED TOP AND BOTTOM, BUT NOT SIDES. THIS ALLOWS FORMWORK TO SIT FLUSH ON BOTH SIDES



DETAIL A-A
SCALE 1:10



DETAIL B-B
SCALE 1:10

Beam End Plate Details

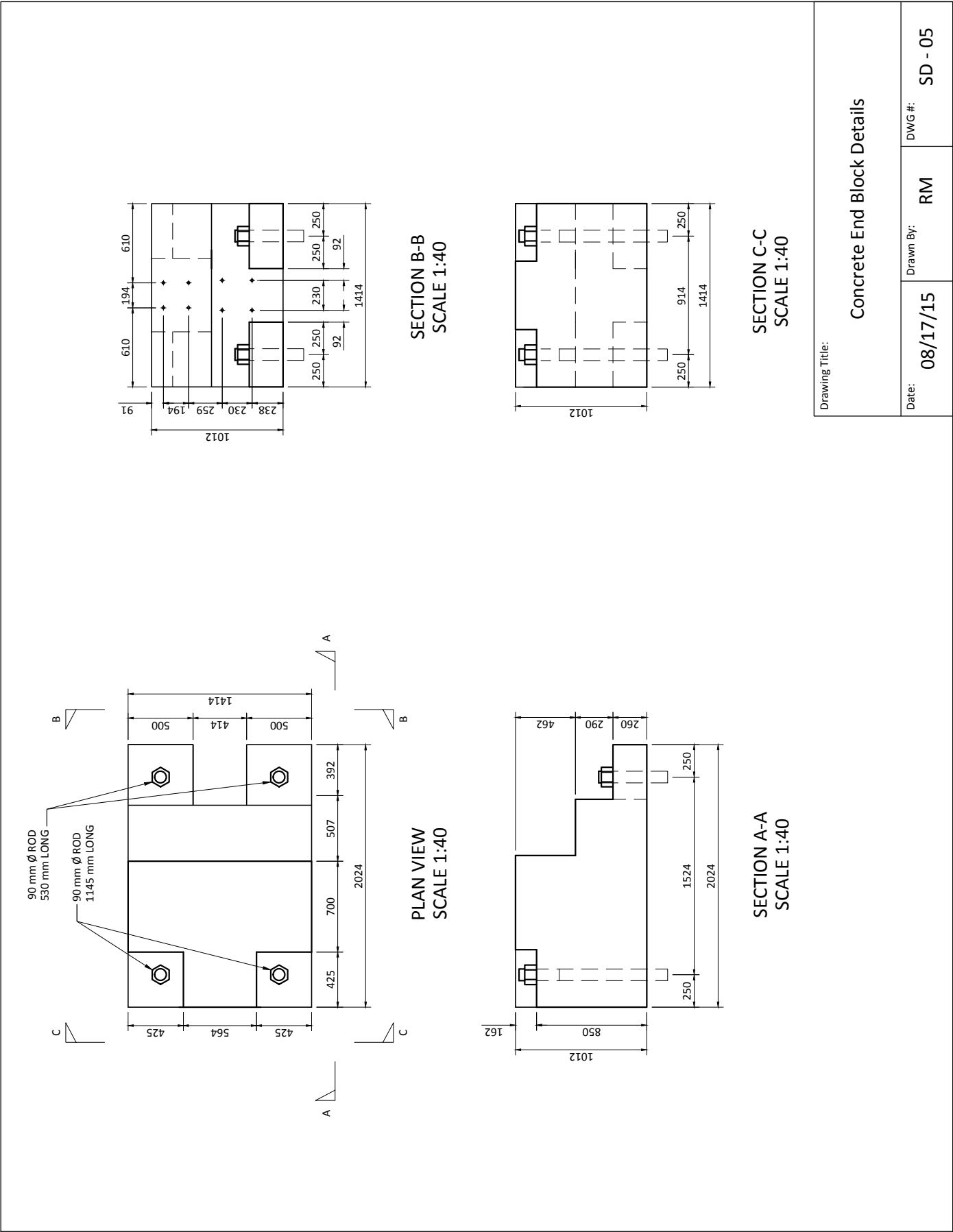
Drawing Title:

Date: 08/17/15

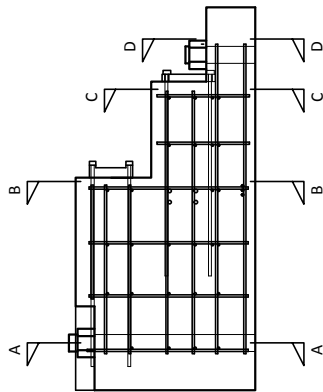
Drawn By: RM

DWG #:

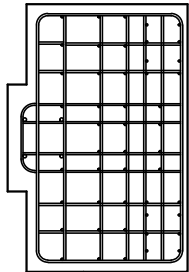
SD - 04



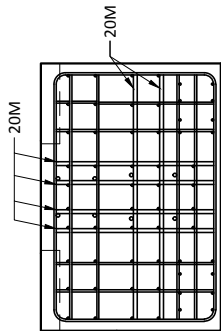
Drawing Title:			
Concrete End Block Details			
Date:	08/17/15	Drawn By:	RM
		DWG #:	SD - 05



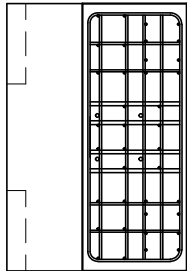
REINFORCEMENT LAYOUT
SCALE 1:40



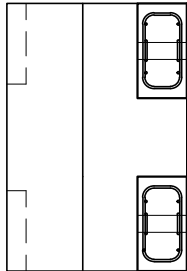
SECTION A-A
SCALE 1:40



SECTION B-B
SCALE 1:40



SECTION C-C
SCALE 1:40



SECTION D-D
SCALE 1:40

NOTES:

1) ALL REINFORCEMENT IS 10M, UNLESS NOTED OTHERWISE

Drawing Title:

End Block Reinforcement Layout

Date:

08/17/15

Drawn By:

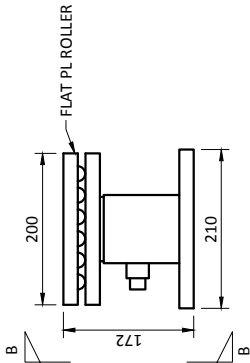
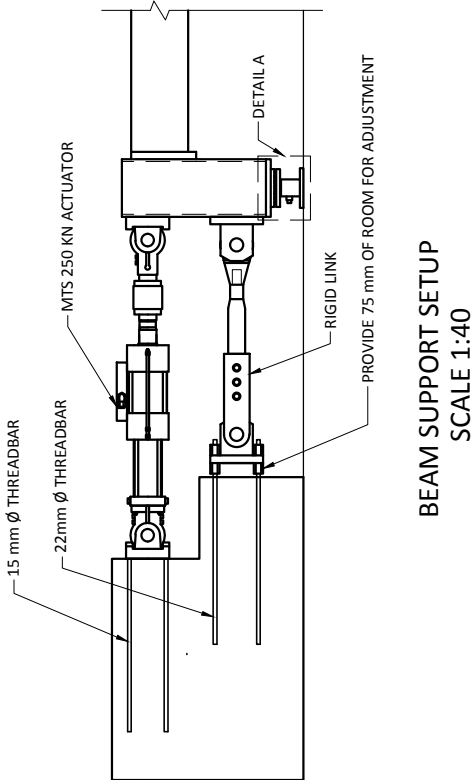
RM

DWG #:

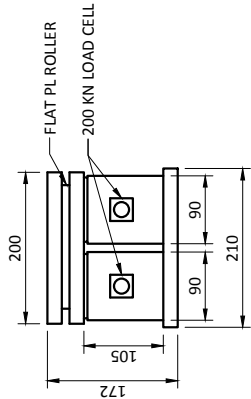
SD - 06

SETUP PROCEDURE:

- 1) POST-TENSION END CONCRETE BLOCK TO BALDWIN STRONG FLOOR. BOLTS ARE TO BE TORQUED TO A PRESSURE EQUIVALENT TO 80 TONS
- 2) FASTEN ACTUATOR TO THE END CONCRETE BLOCKS AT BOTH ENDS, USING A TEMPORARY SUPPORT AT THE FREE END
- 3) FASTEN THE RIGID LINKS TO THE END CONCRETE BLOCKS AT BOTH ENDS, PROVIDING 45 mm OF ADJUSTMENT ROOM MEASURED FROM THE FACE OF THE CONCRETE TO THE OUTER FACE OF THE RIGID LINK
- 4) INSTALL THE ROLLER SUPPORTS AT BOTH ENDS
- 5) PLACE THE STEEL END BLOCKS ONTO THE ROLLER SUPPORT, USING A TEMPORARY SUPPORT FOR STABILITY AS REQUIRED
- 5) FASTEN BOTH THE ACTUATOR AND THE RIGID LINK TO THE STEEL END BLOCKS
- 6) ADJUST THE LENGTH OF THE ACTUATOR AND RIGID LINK TO ENSURE THE CLEAR DISTANCE BETWEEN THE STEEL BLOCKS IS EXACTLY 3038 mm. ENSURE THAT THE INSIDE FACE OF THE STEEL END BLOCKS ARE PERPENDICULAR TO THE GROUND
- 7) RETRACT THE ACTUATOR TO ALLOW FOR PLACEMENT OF THE TEST SPECIMEN
- 8) PLACE THE TEST SPECIMEN INTO POSITION. ADJUSTING THE LENGTH OF THE ACTUATOR AS REQUIRED. FASTEN THE BEAM END PLATES TO THE STEEL END BLOCKS WITH THE SPECIFIED TORQUE
- 9) INSTALL TEST INSTRUMENTATION, AND APPLY LOAD MONOTONICALLY TO THE SPECIMEN UNTIL FAILURE OCCURS
- 10) AFTER TESTING, THE SPECIMEN CAN BE REMOVED BY RETRACTING THE ACTUATOR, AND THE NEXT SPECIMEN CAN BE INSTALLED



DETAIL A
SCALE 1:10



SECTION B-B
SCALE 1:10

Drawing Title:

Test Setup Details

Date:

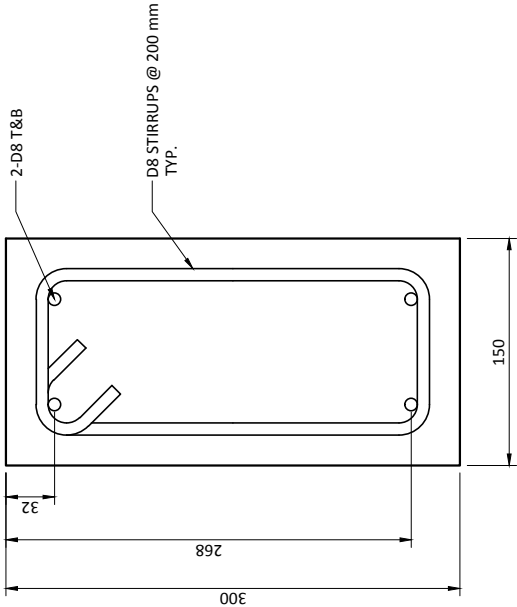
08/17/15

Drawn By:

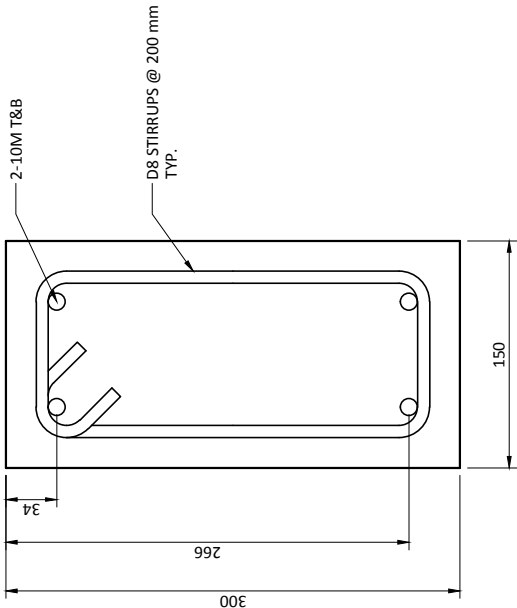
RM

DWG #:

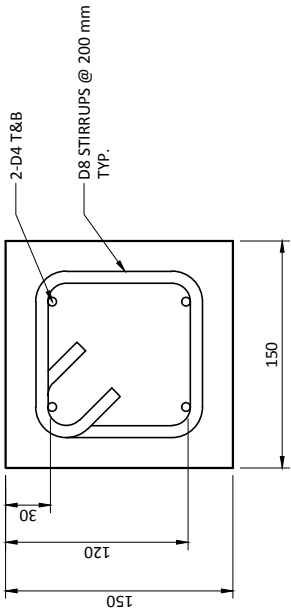
SD - 07



BEAM B2 SECTION
SCALE 1:5



BEAM B1 SECTION
SCALE 1:5



BEAM B3/B4 SECTION
SCALE 1:5

Drawing Title: Test Specimen Details			
Date: 08/17/15	Drawn By: RM	DWG #: SD - 08	